Semiconductors, Vol. 35, No. 4, 2001, pp. 371–373. Translated from Fizika i Tekhnika Poluprovodnikov, Vol. 35, No. 4, 2001, pp. 385–386.

ATOMIC STRUCTURE AND NONELECTRONIC PROPERTIES OF SEMICONDUCTORS

The Effect of Various Types of Shallow Impurities and Their Concentration on Microhardness and Photomechanical Properties of Semiconductors

A. B. Gerasimov and G. D. Chiradze*

Kutaisi Tsereteli State University, Kutaisi, 384000 Georgia

** e-mail: irpdd@sanetk.net.ge*

Submitted August 17, 2000; accepted for publication September 26, 2000

Abstract—The results of studying the influence of various types of shallow-level impurities and their concentrations on the microhardness and photomagnetic effect in silicon single crystals are reported. It is shown that an increase in impurity concentration results in a decrease of both the dark microhardness and the magnitude of the photomagnetic effect. The effect of the acceptor impurities is found to be more efficient in comparison with the donor ones. The data obtained are explained on the basis of the mechanism according to which the decrease of microhardness in semiconductors is caused by free charge carriers (antibonding quasiparticles) occurring in relevant energy bands. © *2001 MAIK "Nauka/Interperiodica".*

The influence of shallow-level impurities on microhardness and the photomechanical effect (a change of microhardness under illumination [1]) has been reported in a number of publications [2–6]. Their analysis shows that in some cases the experimental results not only disagree but even contradict each other. A possible cause of such a contradiction can be related to different experimental conditions. The absence of a common opinion about the mechanism of formation of the impressions in the course of indentation, as well as about the mechanism of photomechanical effect at a microscopic level, is a reason why the physical nature of these effects has not yet been clarified.

The physical nature of the influence of the type and concentration of shallow-level impurities on the microhardness and photomagnetic effect is clarified in this study on the basis of the mechanism proposed in [7, 8], which allows the explanation of all specific features of photomechanical [9–12], electromechanical [13], and thermomechanical [14] effects. According to this mechanism, the observed decrease in microhardness under the effects of light, electric field, and temperature on a semiconductor is caused by the formation of antibonding quasiparticles (free electrons and holes).

We studied dislocation-free single crystals of silicon with (100)-oriented surfaces doped with phosphorus and boron within the concentration range N from 10^{13} to 10^{19} cm^{-3} to introduce shallow-level donors and acceptors, respectively. The preparation of the surfaces of the samples and the methods for observation of microhardness in the dark and under irradiation with white light of various intensities have been described previously [9]. The loading was chosen equal to 25 g. In all measurements, the major diagonal of Knoop's pyramid coincided with the ⟨100⟩ direction in the (100) plane.

The microhardness measured in the dark and under illumination for Si samples as a function of impurity concentration is shown in the figure. It can be seen that an increase in the shallow-level impurity concentration results in a decrease in both the dark microhardness and the magnitude of the photomechanical effect. It can also be seen that the influence of the acceptor impurity on the dark microhardness is more efficient in comparison with the donor impurities. Qualitatively, the same impact of impurities is typical for the photomechanical effect.

The decrease in dark microhardness with increasing concentration of shallow-level impurities is caused by the formation of free electrons and holes in relevant energy bands (antibonding quasiparticles). They weaken the interatomic bonds [8] and facilitate the motion of atoms in the mechanical field produced by the indenter. This is also supported by the fact that the impurity atoms do not affect the dark microhardness in compensated Si samples.

A stronger influence of the acceptor impurities in comparison with that of donors is caused by the fact that the top of the bonding (valence) band lies at a larger energy distance from the level of an isolated atom than the bottom of the antibonding (conduction) band (see Fig. 3.3 in [15]). Therefore, a hole in the

1063-7826/01/3504-0371$21.00

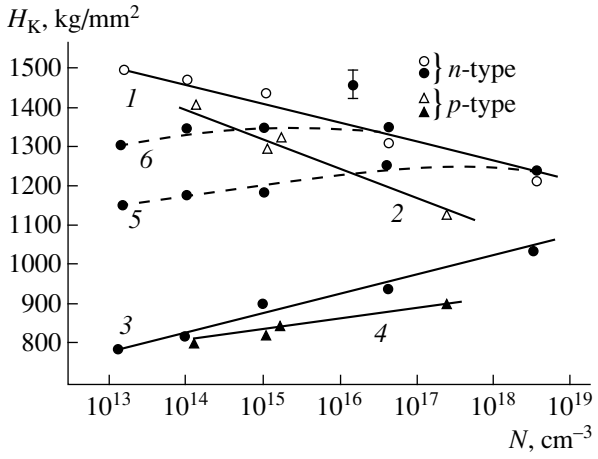

Microhardness measured (*1*, *2*) in the dark and (*3*–*6*) under illumination H_K as a function of impurity concentration in Si. The illumination intensities were (*1*, *2*) 0, (*3*, *4*) 1, (*5*) 1/2, and (*6*) 1/4 in arbitrary units.

bonding band weakens the chemical bonds to a greater extent than a free electron located in the antibonding band. It should also be pointed out that the bond-weakening effect of the antibonding quasiparticles, which are formed due to the ionization of impurities, is considerably smaller than of the quasiparticles formed as a result of the band-to-band transitions. In the latter case, the chemical bond weakens by an energy equal to the band gap [16]. If the antibonding quasiparticles are formed by the electron and hole transitions from the impurity levels to relevant energy bands, the weakening of the chemical bonds is controlled by the energy depth of these impurity levels. Thus, in order to attain the same degree of weakening of chemical bonds, the number of antibonding quasiparticles generated in the level-to-band transitions should be an order of magnitude greater than the number of these quasiparticles resulting from band-to-band transitions.

It is also easy to explain the decrease in the magnitude of the photomechanical effect with increasing impurity concentration in Si. This occurs because of the decrease in the lifetime of the charge carriers excited by light, which leads to the reduction of the steady-state concentration of antibonding quasiparticles at a given illumination intensity. A comparatively large reduction of the photomechanical effect in the crystals with acceptor impurities is observed, because the softening action of antibonding quasiparticles induced by light is the same for both types of samples, whereas the dark microhardness for acceptor impurities is lower.

The effect of illumination becomes unobservable if the bond-weakening effect of antibonding quasiparticles formed by the ionization of impurities becomes considerably stronger than that of the quasiparticles formed by the illumination (i.e. by the band-to-band transitions). This corresponds to the impurity concentration region where the curves *1*, *5* and *1*, *6* in the figure merged together. Such an explanation is supported by the fact that the regions in which the concentration dependences of microhardness measured in the dark and under illumination merge together shift to higher concentrations of the antibonding quasiparticles formed by the ionization of impurities.

The presence of shallow-level impurity atoms manifests itself in the residual photomechanical effect (the residual softening of the subsurface layer of the material after turning off the illumination [10]). The increase in impurity concentration causes the reduction not only of the charge carrier lifetime, but also of the Debye screening length [17]; as a result, the width of the barrier arising due to inhomogeneous bending of energy bands along the sample surface decreases [18]. This causes an increase in the concentration of antibonding quasiparticles stored in corresponding spatially separated minima and, therefore, reduces the influence of antibonding quasiparticles produced by light and enhances their recombination rate. All these factors reduce both the magnitude of the residual photomechanical effect and its lifetime.

REFERENCES

1. G. C. Kuczynsky and R. H. Hochman, Phys. Rev. **108**, 946 (1957).
2. M. S. Ablova and A. R. Regel', Fiz. Tverd. Tela (Leningrad) **4**, 1053 (1962) [Sov. Phys. Solid State **4**, 775 (1962)].
3. M. G. Mil'vidskiĭ, V. B. Osvenskiĭ, O. G. Stolyarov, and D. B. Shlyakova, Fiz. Met. Metalloved. **20**, 150 (1965).
4. S. S. Gorelik, Yu. M. Litvinov, M. G. Lozinskiĭ, and T. G. Tereshchenkova, Izv. Akad. Nauk SSSR, Neorg. Mater. **2**, 1689 (1966).
5. Yu. Kh. Vekilov, M. G. Mil'vidskiĭ, V. B. Osvenskiĭ, *et al.*, Izv. Akad. Nauk SSSR, Neorg. Mater. **2**, 636 (1966).
6. P. P. Kuz'menko, N. N. Novikov, N. Ya. Gorid'ko, and K. I. Fedorenko, Fiz. Tverd. Tela (Leningrad) **8**, 1732 (1966) [Sov. Phys. Solid State **8**, 1381 (1966)].
7. A. B. Gerasimov, V. B. Golubkov, É. R. Kuteliya, *et al.*, Pis'ma Zh. Tekh. Fiz. **6**, 58 (1980) [Sov. Tech. Phys. Lett. **6**, 25 (1980)].
8. A. B. Gerasimov, Mater. Sci. Forum **65–66**, 47 (1990).
9. A. B. Gerasimov, G. D. Chiradze, N. G. Kutivadze, *et al.*, Fiz. Tverd. Tela (St. Petersburg) **40**, 503 (1998) [Phys. Solid State **40**, 462 (1998)].
10. A. B. Gerasimov, G. D. Chiradze, N. G. Kutivadze, *et al.*, Fiz. Tverd. Tela (St. Petersburg) **41**, 1225 (1999) [Phys. Solid State **41**, 1115 (1999)].
11. A. B. Gerasimov, G. D. Chiradze, N. G. Kutivadze, *et al.*, Fiz. Tverd. Tela (St. Petersburg) **42**, 683 (2000) [Phys. Solid State **42**, 701 (2000)].

12. A. B. Gerasimov, G. D. Chiradze, and N. G. Kutivadze, Fiz. Tekh. Poluprovodn. (St. Petersburg) **35** (1), 70 (2001) [Semiconductors **35**, 72 (2001)].

13. A. B. Gerasimov, G. D. Chiradze, and N. G. Kutivadze, Sb. Nauchn. Tr. "Intelekti" **3**, 24 (1998).

14. A. B. Gerasimov, G. D. Chiradze, N. G. Kutivadze, *et al.*, Proc. Tbilisi Univ., Ser. Phys. **34**, 79 (1999).

15. W. A. Harrison, in *Electronic Structure and the Properties of Solids: The Physics of the Chemical Bond* (Freeman, San Francisco, 1980; Mir, Moscow, 1983), Vol. 1.

16. A. B. Gerasimov, G. D. Chiradze, N. G. Kutivadze, *et al.*, Proc. Tbilisi Univ., Ser. Phys. **34**, 73 (1999).

17. S. M. Ryvkin, *Photoelectric Effects in Semiconductors* (Fizmatgiz, Leningrad, 1963; Consultants Bureau, New York, 1964).

18. *Problems of Radiotechnology of Semiconductors*, Ed. by L. S. Smirnov (Nauka, Novosibirsk, 1980), p. 149.

Translated by A. Zalesskiĭ

Semiconductors, Vol. 35, No. 4, 2001, pp. 374–376. Translated from Fizika i Tekhnika Poluprovodnikov, Vol. 35, No. 4, 2001, pp. 387–389.

ATOMIC STRUCTURE AND NONELECTRONIC PROPERTIES OF SEMICONDUCTORS

Laser Beam Epitaxy of HgCdTe/Si Heterostructures

S. V. Plyatsko* and N. N. Bergush

Institute of Semiconductor Physics, National Academy of Sciences of Ukraine, Kiev, 03028 Ukraine

** e-mail: plyatsko@laser.semicond.kiev.ua*

Submitted July 26, 2000; accepted for publication October 6, 2000

Abstract—Laser-induced deposition was employed to grow HgCdTe thin films on Si substrate at a temperature of ≲190°C. Auger spectroscopy and optical and electrical measurements demonstrate that the quality of films obtained is strongly dependent on the type of source and quality of the Si substrates. © *2001 MAIK "Nauka/Interperiodica".*

In this study, we measured and analyzed the Auger electron spectra, and the structural, electrical and optical properties of HgCdTe layers grown on (001)- and (111)-oriented Si substrates by modulated laser beam epitaxy, i.e., by sputtering the target material with a modulated infrared laser beam. During the HgCdTe epitaxy, the temperature of substrates did not exceed 190°C. As source materials, we chose HgCdTe single crystals of specific composition and ground material in the form of pellets prepared by cold pressing. No additional source of Hg vapor was used. The following are the parameters of laser radiation we employed: modulation frequency f ranged from 10 to 100 Hz, photon energy $\hbar\omega$ was 0.118 eV, and the power density W was varied from 10^4 to 10^5 W/cm^2. The scanning geometry, the step size, and the sputtering time were set and controlled by a computer. In view of the high temperature conductivity of HgCdTe (2.2×10^{-2} cm^2/s), the neighboring irradiated areas of the target were not allowed to overlap, in order to exclude heat accumulation somewhere on the target. Owing to this, the convective thermal evaporation from the areas adjacent to the laser-irradiated region was reduced. Composition of the grown layers was determined by Auger electron spectroscopy, by energy-dispersive X-ray analysis (EDAX), and from the optical absorption spectra.

The results of Auger spectrometry indicate the presence of C, S, and Cl on the film surface. The concentration of these elements decreases rapidly with the distance from the surface and nearly vanishes at a depth of about 1 nm. To determine the content of components in the layer, we resorted to a comparison of the samples with a material of known composition. Using the elemental-sensitivity coefficients for HgCdTe seems incorrect here, since these coefficients are generally determined from comparison between intensities of Auger transitions in differential spectra of an element (I_i) and those of a pure silver or silicon target ($I_{Ag(Si)}$), the effect of the host material and the specific features of the analyzer disregarding [1]. Moreover, the determination of the coefficient of component response for Hg is ambiguous.

Concentrations of Hg, Cd, and Te atoms are nearly constant throughout the surface layer including the surface. This is also confirmed by the EDAX data.

The comparison of Auger spectra of the studied layers with those of the single-crystal material of the target (Fig. 1) shows, in contrast with [2, 3], an excess of mercury in the layers at any temperature of epitaxy. We note also that in HgCdTe layers grown on Si substrates at moderate temperatures $T_s \approx 190$°C, the resulting composition depends on the volume purity of the substrate and on the carbon content in particular. Thus, in layers grown on a Si substrate with a large concentration of carbon, the diffused C atoms are detected throughout the entire layer with thickness $h \lesssim 5$ μm.

The X-ray structural analysis of HgCdTe/Si heterostructures has revealed that, regardless of the substrate temperature, at a medium growth rate $v \approx 20$ Å/s (growth rate during the laser-pulse passage is 240 Å/s), the layers obtained are polycrystalline with (111) preferred orientation. In addition, the spectrum has a peak corresponding to (100) orientation. The ratio of peak intensities corresponding to (111) and (100) orientations increases with decreasing growth rate.

The morphology of the film surface is defined to a smaller extent by the density of laser radiation at the target. Under the condition that the laser beam diameter considerably exceeds the crater depth ($d \gg h_{cr}$) and with W = const, we always obtain a film with both mirror surfaces: the free one and the other adjacent to the substrate. Sputtering of the same site on the target up to the formation of a crater ($d \lesssim h_{cr}$) leads to the production of spherical inclusions on the free surface. The density of inclusions grows with h_{cr} and the film becomes diffuse-reflecting. As this takes place, the inclusion size remains constant, and the surface adjacent to the substrate remains ideally smooth. The surface of the crater bears traces of the melt.

The liquid-phase inclusions observed on the film surface provide evidence for considerable heating of the crater walls with vapor flux and subsequent ejection of the liquid matter into the condensation zone. This

fact is also confirmed by the dependence of the density of inclusions on the distance between the source and the substrate: as the distance increases, the density noticeably decreases.

Morphology of the grown films was also examined by scanning atomic force microscopy (AFM) at room temperature. Every AFM image gives us a view of the surface area of 1.5×1.5 μm^2 in size. The film structure turns out to be polycrystalline, with columnar crystallites increasing in size with a decrease in the growth rate, which agrees well with X-ray structural studies.

With the exception of the liquid-phase inclusions, the same morphology of the surface was observed for CdTe layers deposited on the Si substrate in a wide range of growth temperatures. Therefore, it is most probable that the inclusions in HgCdTe contain mercury. Such inclusions can cause a significant error in HgCdTe content determined from Auger spectroscopy and EDAX measurements. In this circumstance, the optical absorption spectra seem to provide the most reliable information. The corresponding study was performed at a temperature of $T = 340$ K with an IKS-31 spectrometer. The band gap E_g was determined at the absorption level $\alpha = 700$ cm^{-1} and the film content turned out to coincide with that of the single-crystal target, specifically, $Hg_{1-x}Cd_xTe$ ($x = 0.22$).

We also studied the electrical properties of HgCdTe films on the Si substrate in the temperature range from 77 to 310 K (Fig. 2). For all of the samples obtained, *n*-type conduction was observed. To invert the conduction type, we have to increase the growth temperature to $T_s > 190$°C, where reevaporation of Hg accompanies the growth and cooling of the film. At $T = 77$ K, the carrier mobility μ was in the range between 10^3 and 7×10^3 cm^2/(V s). These values are an order of magnitude smaller than those determined for HgCdTe layers grown on Si by molecular beam epitaxy (MBE), but are comparable to similar parameters obtained in [2]. The low mobility once again supports the conclusion about the polycrystalline structure of the films.

Regardless of the conduction type of the semiconductor crystal, the films had *n*-type conduction. When the target is single-crystalline, the carrier concentration $N_D - N_A$ is no lower than 9×10^{15} cm^{-3} and increases considerably with temperature, whereas with the target from pressed materials, $N_D - N_A \approx 5 \times 10^{18}$ cm^{-3} ($77 \le T \le 350$ K). Temperature dependences of the Hall coefficient (R_H), resistivity (ρ), and mobility (μ) are shown in Fig. 2.

The difference between the $N_D - N_A$ values for targets of different types cannot be uniquely related to the pressing-induced contamination, since the sputtering conditions (W = const) are different for a single crystal and finely dispersed matter. Sputtering of a pellet gives rise to a flux of particles with higher energies, which enables soft implantation and the generation of donor centers.

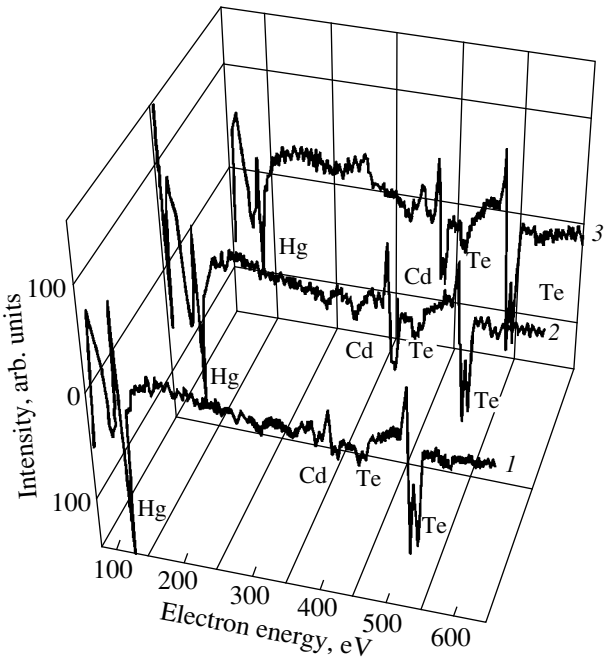

Fig. 1. Auger spectra of HgCdTe films grown on Si by sputtering (*1*) a single-crystal target and (*2*) the pressed pellet. (*3*) Auger spectrum of the bulk single-crystal source material.

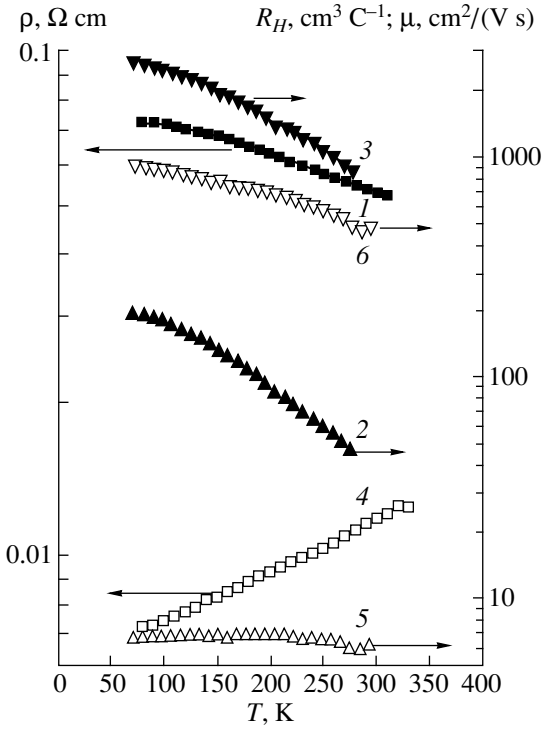

Fig. 2. Temperature dependence of (*1*, *4*) resistivity ρ, (*2*, *5*) Hall coefficients R_H, and (*3*, *6*) mobility μ for *n*-HdCdTe films grown on Si from (*1–3*) $Hg_{1-x}Cd_xTe$ ($x = 0.2$) single-crystal target and (*4–6*) the pressed pellet.

The results considered above apparently follow from significant supersaturation arising near the substrate during laser sputtering. Under this condition, the film becomes continuous even at an early stage of growth; however, the numerous nuclei, which appear but do not reach Ostwald ripening, have a significantly disordered orientation. It seems that in the range of epitaxial temperatures used, the crystallites cannot be ordered without a considerable decrease in the growth rate if congruent evaporation is retained. This conclusion is confirmed by the results of [4, 5], in which laser sputtering of a target was used to deposit CdTe/CdMnTe superlattices and epilayers.

The epitaxial growth of II–VI compounds on the Si substrate presents a real challenge, not only because of differences in the lattice constants and thermal expansion coefficients, but also due to a difference in the layer and substrate surface free energies [6, 7]. The surface free energy of (111) Si is higher than that of the II–VI compounds, HgCdTe among them. For the (111) orientation, this difference amounts to as much as $\Delta\sigma(111) \approx 500$ erg/cm^2, which promotes continuous film condensation [8] but does not stimulate the epitaxial growth of continuous single-crystal layers.

Thus, in contrast to MBE and laser molecular beam epitaxy [9], laser sputtering with moderate energy density $W \approx 10^5$ W/cm^2, which does not give rise to highly energy-dispersed gas–plasma fluxes ($E \ll 2 \times 10^3$ eV), enables the epitaxial growth of HgCdTe in a vacuum without adding Hg. Therefore, the search for surfactants to the (II–VI)/Si heteropair is a topical problem, especially important for nonequilibrium film growth, which to a different extent is realized both during MBE and laser epitaxy. As compared with MBE, laser sputtering of the target provides a considerably higher energy of particles in gas flux, thus ensuring a higher lateral mobility on the surface. This fact can also be used to facilitate heteroepitaxy on silicon substrates.

REFERENCES

1. A. M. Tas'kov, I. M. Malinskiĭ, D. G. Rodionov, and A. E. Gukaĭlo, Zh. Anal. Khim. **45** (5), 1001 (1990).
2. J. T. Cheung and D. T. Cheung, J. Vac. Sci. Technol. **21** (1), 182 (1982).
3. J. T. Cheung and H. Sankur, Crit. Rev. Solid State Mater. Sci. **15** (1), 63 (1988).
4. J. M. Wrobel and J. J. Dubowski, Appl. Phys. Lett. **55** (5), 469 (1989).
5. J. J. Dubowski, A. P. Roth, E. Teleporte, *et al.*, J. Cryst. Growth **117**, 862 (1992).
6. S. V. Plyatsko, Fiz. Tekh. Poluprovodn. (St. Petersburg) **32**, 257 (1998) [Semiconductors **32**, 231 (1998)].
7. R. Sporken, M. D. Lange, S. Sivananthan, and J. T. Faurie, Appl. Phys. Lett. **59** (1), 81 (1991).
8. S. A. Kukushkin and A. V. Osipov, Usp. Fiz. Nauk **168** (10), 1083 (1998) [Phys. Usp. **41**, 983 (1998)].
9. J. T. Cheung and J. Madden, J. Vac. Sci. Technol. B **5** (3), 705 (1987).

Translated by A. Sidorova-Biryukova

Semiconductors, Vol. 35, No. 4, 2001, pp. 377–383. Translated from Fizika i Tekhnika Poluprovodnikov, Vol. 35, No. 4, 2001, pp. 390–395.

ELECTRONIC AND OPTICAL PROPERTIES OF SEMICONDUCTORS

Emission from Hot Charge Carriers during the Formation of High-Field Autosolitons in Electron–Hole Plasma in *n*-Ge

M. N. Vinoslavskiĭ* and A. V. Kravchenko

Institute of Physics, National Academy of Sciences of Ukraine, pr. Nauki 46, Kiev, 03028 Ukraine

** e-mail: mvinos@iop.kiev.ua*

Submitted July 18, 2000; accepted for publication August 2, 2000

Abstract—The evolution of the spatial distribution of photogenerated electron–hole plasma in *n*-Ge samples during charge-carrier heating by an electric field at $T = 77$ K was studied. A multiprobe system was used, and the infrared emission from the sample in the wavelength range of $\lambda = 1.65$–10 μm was measured to clarify the processes of contact exclusion, direction reversal in the bipolar plasma drift, the formation of high-field thermal-diffusion autosolitons, and lattice heating in the vicinity of an autosoliton. © *2001 MAIK "Nauka/Interperiodica".*

1. INTRODUCTION

Current instabilities accompanied by stratification of the charge-carrier density and formation of spatially inhomogeneous structures emerge as a result of intense charge-carrier heating by an electric field ($E \geq 1500$ V/cm) in monopolar-conduction semiconductors that typically feature either *N*- or *S*-shaped differential-conductivity curves (see, e.g., [1]). As this takes place, the effective temperature of charge carriers in a crystal far exceeds the lattice temperature.

In semiconductors with bipolar electrical conduction, the stratification of quasi-neutral electron–hole plasma during current instabilities may also occur under conditions of positive differential conductivity [2, 3], for much lower levels of the charge-carrier heating and at much lower electric fields. In a bipolar system, a steady and highly nonequilibrium high-amplitude autostructure may emerge even if the average heating of the charge carriers is slight as long as there is a local higher level excitation for a short time; this autostructure may feature a high temperature or a high charge-carrier density. This class of autostructures includes, in particular, thermal-diffusion autosolitons that may manifest themselves either as current filaments or as high-field domains [3–7]. Observations of luminous spots in GaAs films [3, 4, 7], filaments in α-SiC *p*–*n* junctions [6], and *S*-shaped current–voltage characteristics in InSb crystals [8] are related to the emergence of such autosolitons.

We previously detected the above high-field autosolitons in *n*-Ge electron–hole plasma generated by light and heated by an electric field [9–12]. We used a multiprobe contact system to study the dynamics of formation and subsequent evolution of various types of autosolitons in relation to the crystallographic orientation of the samples; these types include the static, traveling, pulsating, and individual autosolutions, and those following each other.

The objective of this study was to gain insight into the modification dynamics of spatial distribution of electron–hole plasma in the course of it being heated by an electric field, to compare these dynamics with those of variation in the infrared (IR) emission from the hot charge carriers, and to estimate the Joule heating of the crystal lattice in the vicinity of an autosoliton.

2. EXPERIMENTAL

We used samples of high-resistivity *n*-Ge⟨111⟩ with a resistivity of ~40 Ω cm and a donor concentration of $N_d \sim 1 \times 10^{13}$ cm^{-3}; the samples were 0.05 cm in thickness and 0.1×0.8 cm in area, were provided with two n^+–*n* contacts at the end faces, and were installed in a liquid-nitrogen cryostat together with an 18-probe head. The cryostat had two transmitting IR windows (the inner cold windows made of ZnSe and the outer warm windows made of BaF_2) and a single quartz window oriented at an angle of 45° to the axis of the output IR window.

The wide face of the sample was oriented parallel to the IR windows along their horizontal axes. Two lenses made of BaF_2 were used to focus the IR emission from the samples onto a Ge:Au photodetector installed in another liquid-nitrogen cryostat with an IR window. The spectral-sensitivity curve for the photodetector in the wavelength range of $\lambda = 1.6$–10 μm is shown in

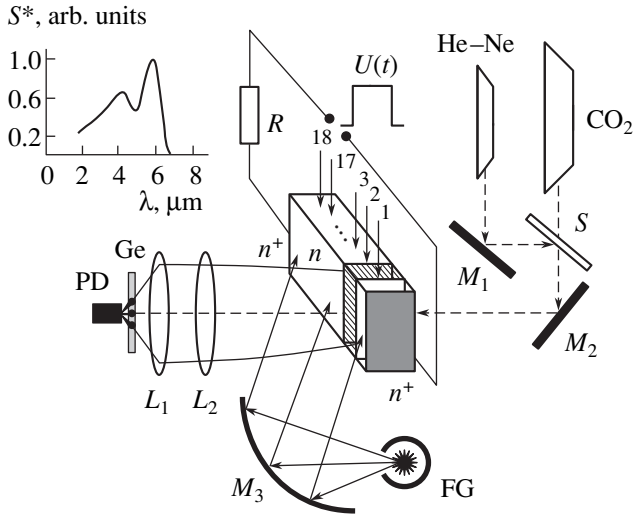

Fig. 1. A schematic representation of the setup for measuring the distributions of the electric-field strength over the sample and the IR emission from the n^+–n–n^+ structure in the n-Ge sample. 1–18 correspond to the numbers of contact probes; PD stands for a Ge:Au photodetector; L_1 and L_2 stand for BaF_2 lenses; M_1 and M_2 stand for the plane mirrors; M_3 stands for a spherical mirror; S stands for a BaF_2 plate; and FG denotes a flash lamp for generating the electron–hole plasma. The inset shows the spectral-sensitivity curve S^* for a Ge:Au photodetector.

Fig. 1 (see the inset). In addition, the IR emission from the sample was cut from the short-wavelength side (λ = 1.65 μm) using a Ge plate in order to eliminate the signal corresponding to the flash-lamp light reflected from the sample.

The photodetector was set at the desired area of the sample using the CO_2-laser radiation that passed through the second IR window, penetrated through the sample, and reached the photodetector. The electron–hole plasma with electron and hole concentrations as high as $n = p \approx 1 \times 10^{16}$ cm^{-3} was generated by a single bell-shaped pulse of light with a duration of $\tau_I \approx 230$ μs. The light was introduced into the cryostat through a quartz window; the generation was uniform over the large-area sample surface facing the exit IR window. A rectangular voltage pulse with an amplitude as large as 300 V and duration of τ_U = 10–250 μs was fed to the n^+–n contacts of the sample either simultaneously with the onset of the optical pulse or with a delay (at the point in time corresponding to the peak of the intensity of light). The storage oscilloscopes were used to record the pulse signals of light $I(t)$, current $J(t)$, voltage $U(t)$, and emission from the sample $IR(t)$; the voltages at the probes were fed to differential inputs of the oscilloscopes, which made it possible to detect local electric-field strengths in various regions of the sample and determine the electric-field distributions over the sample at the desired points in time.

In the absence of illumination, a virtually uniform electric-field distribution ($E_h = U/l$ = 5–400 V/cm, where l is the sample length) is obtained in the sample subjected to a rectangular voltage pulse, except for slight nonuniformities either at the contacts or in the middle part of the sample; the latter nonuniformities are caused by inherent inhomogeneities of the sample resistivity due to impurities, defects, surface quality, etc.

In illuminated samples, three spatial–temporal phenomena are observed as the applied voltage increases. In what follows, we describe the typical data using one of the samples as an example.

3. RESULTS AND DISCUSSION

3.1. Contact Exclusion

As the intensity of illumination of the sample increases for moderate applied voltages ($U \le 80$ V, lower than the autosoliton-formation threshold, see [9, 10]), the current first increases steadily, attains its maximum value before the peak of illumination intensity is reached, and then decreases steadily (Fig. 2). As this takes place, the electric-field strength $E_{0-1}(t)$ at the positively biased contact (within the interval of l_{0-1}) rapidly increases from $E_{av} \sim 100$ V/cm to a maximum value of $E_{0-1} \sim 550$ V/cm; at the same time, in other parts of the sample (l_{1-2}, l_{2-3}, etc.), the electric-field strengths $E_{1-2}(t)$, $E_{2-3}(t)$, and so on, decrease first (after a slight initial increase) to a certain minimum value $E_{min} \sim 30$ V/cm, which is constant for most of the sample, owing to the development of exclusion, i.e., to the field-induced shift of the electron–hole plasma from the positively biased contact to the negatively biased contact in the direction coinciding with the minority-carrier (hole) drift.

The signal of integrated IR emission (IR) from the exclusion region in the sample emerges for certain values of illumination intensity and field strength in this region, increases steadily to a maximum, and then decreases to zero as I decreases (Fig. 2). The IR signal was eliminated by installing a glass platelet between the sample and the photodetector. This indicates that the main emission is concentrated in the IR region of the spectrum beyond the glass-transparence cutoff. It is easy to verify that, in this situation, the temperature of the emitting electron–hole plasma does not exceed 300 K.

However, calculations of the electron and hole temperatures in the heating electric field performed on the basis of the energy-balance equation with allowance made for various mechanisms of scattering [11, 12] yield almost the same temperatures for electrons ($T_e \sim$ 200–250 K) and for holes ($T_h \sim$ 150–180 K) for the fields of $E_{ex} \sim$ 500–700 V/cm. The Joule heating of the crystal in the exclusion region as obtained from the thermal-balance equation does not exceed $\Delta T \sim 50$ K

and only slightly affects the dynamics of the IR signals and the local fields E_{i-j}.

3.2. Direction Reversal for Bipolar Drift

For a higher applied voltage ($U > 100$ V), the current first increases steadily with increasing illumination intensity. As this takes place, the fields $E_{0-1}(t)$ and $E_{1-2}(t)$ in the two near-contact regions also increase to a maximum value owing to extension of the exclusion region; simultaneously, the IR emission signal appears due to heating of the charge carriers by the field in the exclusion region (Fig. 3, the time interval t_1–t_2). Subsequently, beginning with a certain threshold illumination intensity, the current increases steeply; this is accompanied with a decrease in the near-contact field and a steep increase in the amplitude of the IR emission signal (Fig. 3, the time interval being t_2–t_3) as a result of the bipolar-drift direction being reversed (the latter phenomenon has been described elsewhere [13, 14]). The aforementioned phenomenon occurs since, for a high density of electron–hole plasma, the electron mobility becomes higher than the hole mobility in a heating electric field as the illumination intensity increases. As a result, the plasma flux controlled by bipolar drift, which is related to the gradient of the ratio between the electron and hole mobilities, exceeds the counter plasma flux caused by the drift related to the carrier-concentration gradient. Electrons and holes leave the low-field ("cold") accumulation region for the near-contact region with a higher field. As a result, although the field strength decreases in the latter region, the number of free charge carriers increases drastically, which brings about an abrupt increase in both the current and the signal of IR emission from the charge carriers in the exclusion region.

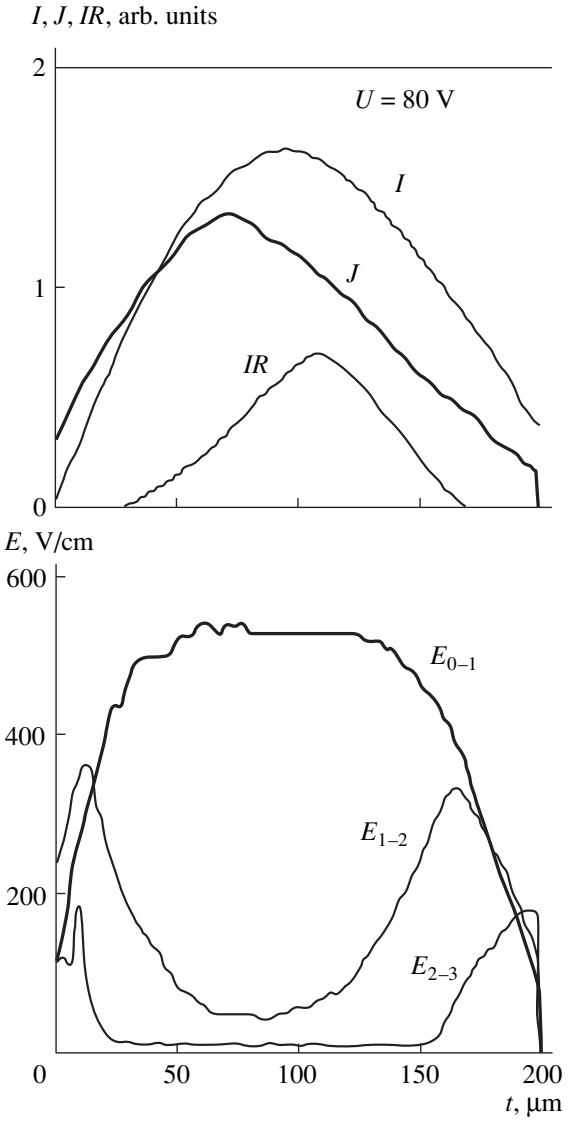

Fig. 2. Evolution of the contact-exclusion process: the shapes of the optical I and current J pulses of the signals of the total IR emission under a voltage of 80 V and of local electric-field strengths at the positively biased contact (E_{0-1}, E_{1-2}, and E_{2-3}). Sample 1 with l_{0-1} = 0.07 mm, l_{1-2} = 0.07 mm, and l_{2-3} = 0.06 mm.

3.3. Formation of a High-Field Autosoliton

As the illumination intensity increases further (for a voltage exceeding the threshold value; i.e., for $U \geq 120$ V), the increase in the current is replaced by a slight abrupt decrease and oscillations that are accompanied with an abrupt increase in the field in the exclusion region $E_{1-2}(t)$ (Fig. 3, the time interval being t_3–t_4), which is due to the formation of a high-field autosoliton [9, 10]. If the autosoliton emerges in the near-contact region to which the photodetector is set at, three portions are observed in the $IR(t)$ curve. The IR-emission signal first steadily increases owing to exclusion; in the second portion, a steeper increase in the signal occurs, which is related to the drift-direction reversal; finally, the signal increases abruptly owing to intense heating of charge carriers in the autosoliton region where the field may be as high as E_{AS} = 1000–5000 V/cm. A glass filter reduced the IR-emission signal by 30–50%, which indicated, according to estimations, that the plasma temperature was no lower than 1000 K. Calculations based on the energy-balance equations for the electron temperature differing from the hole temperature [11, 12] and for the fields E_{AS} = 2000–5000 V/cm yielded electron temperatures close to those mentioned above, whereas the hole temperatures were found to be lower by about a factor of 2.

It is noteworthy that the peak related to the emergence of an autosoliton appears in the $IR(t)$ curve (Fig. 3, see the interval t_3–t_4) corresponding to the IR radiation passed through the glass filter (IR_{glass}) that transmitted the emission from the hottest charge carriers. The first abrupt IR_{glass} signal decrease subsequent to

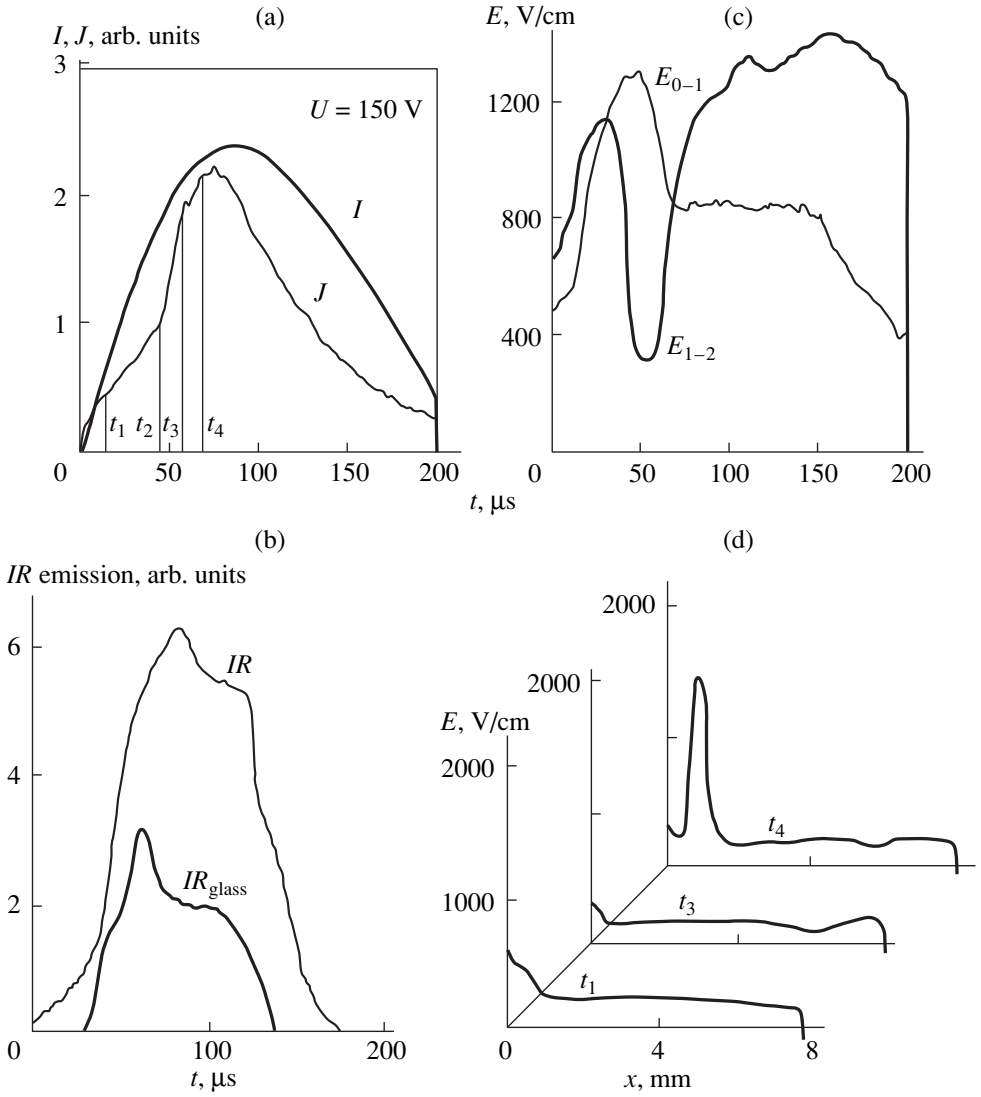

Fig. 3. Dynamics of formation of a single static autosoliton and its shift to a positively biased contact under conditions of increasing illumination intensity. (a) The shapes of the optical I and current J pulses for voltage $U = 150$ V. (b) The time dependences of the total IR emission ($\lambda = 1.65$–10 μm) and the IR emission IR_{glass} that passed through a glass filter and originated in the near-contact region of the sample. (c) The time dependences of the local electric-field strengths in the near-contact regions E_{0-1} and E_{1-2}; sample 1 with $l_{0-1} = l_{1-2} = 0.07$ mm. (d) The distribution of the electric-field strength over the sample at the consecutive points in time that correspond to the contact exclusion (t_1), the direction reversal for the bipolar plasma drift (t_3), and the high-field soliton formation (t_4). Sample 1.

the above peak may be attributed, first, to a transition of hot electrons from hot valleys with small effective mass to a cold valley with a large effective mass in a high autosoliton field directed along the ⟨111⟩ axis. Second, a decrease in the IR_{glass} signal may be caused by cooling of the charge carriers due to an intense lattice heating in the autosoliton region, which manifests itself in the continuing increase in the total IR-emission signal during the autosoliton lifetime.

As the illumination intensity decreases during the optical pulse, autosoliton decay occurs for a certain value of I, after which the IR and IR_{glass} signal amplitudes decrease abruptly. The $IR(t)$ curve then flattens, whereupon it descends to zero. The IR_{glass} signal both emerges later than the IR signal does (Fig. 3, at the point in time $t_2 \approx 40$ μs) and ceases to exist at an earlier time. A delay of the IR signal in reference to the IR_{glass} signal indicates that the crystal lattice is found to be appreciably heated in the region of a collapsed autosoliton.

For some of the samples and for a fairly high applied voltage ($U = 220$ V), a consecutive emergence of two to three autosolitons was observed with increasing illumination intensity (with increasing density of the elec-

tron–hole plasma) at a certain distance from the positively biased contact; these autosolitons were then shifted to the positively biased contact [in the direction of the drift of the majority charge carriers (electrons) due to the reversal in the direction of the bipolar plasma drift] where the autosolitons came to rest and coalesced to a single static autosoliton. This process was also accompanied by both a slight decrease and oscillations in the current, and the emergence of both peaks in the signal of IR emission in the photodetector, which was set at the sample region $l_{2–3}$, and the local fields $E_{0–1}$, $E_{1–2}$, and $E_{2–3}$ (Fig. 4) in the region of formation and motion of the autosoliton in the vicinity of the contact. In this situation, the processes consisting in the contact exclusion and the reversal in the direction of the bipolar plasma drift, preceding the autosoliton emergence and occurring in the vicinity of the contact ($l_{0–1}$ and $l_{1–2}$), were not detected by the photodetector because these processes were out of its "field of view."

It is worth noting that sample regions making the most significant contributions to the signal of the total IR emission are often separated in space, depending on the electron–hole plasma density and the actual distribution of the field in the sample; the above regions include (i) the exclusion region with the highest field at the positively biased contact, (ii) the exclusion region where the bipolar-drift reversal occurs, and (iii) the autosoliton formation region. Therefore, the amplitude of the IR-emission signal corresponding to contributions made by the aforementioned processes depends on the sample region at which the photodetector is set. If the photodetector is set at the autosoliton-formation region for a sample with the ⟨111⟩ orientation, a steplike signal of IR emission is observed. If the photodetector is set at an area away from the contact and from the autosoliton-formation region, the IR emission signal appears abruptly when the autosoliton comes to the chosen point of the sample. Thus, due to a strong localization of the electric field in the bipolar plasma, the IR emission from the sample is markedly nonuniform over its surface and the peak of the IR emission signal shifts with time. In addition, in contrast to uniform emission from a hot monopolar plasma in an electric field in *n*- and *p*-Ge [15, 16], we also observed experimentally IR emission with shorter wavelengths ($\lambda \approx 2$ μm) as a result of higher local electric-field strengths in the autosoliton region.

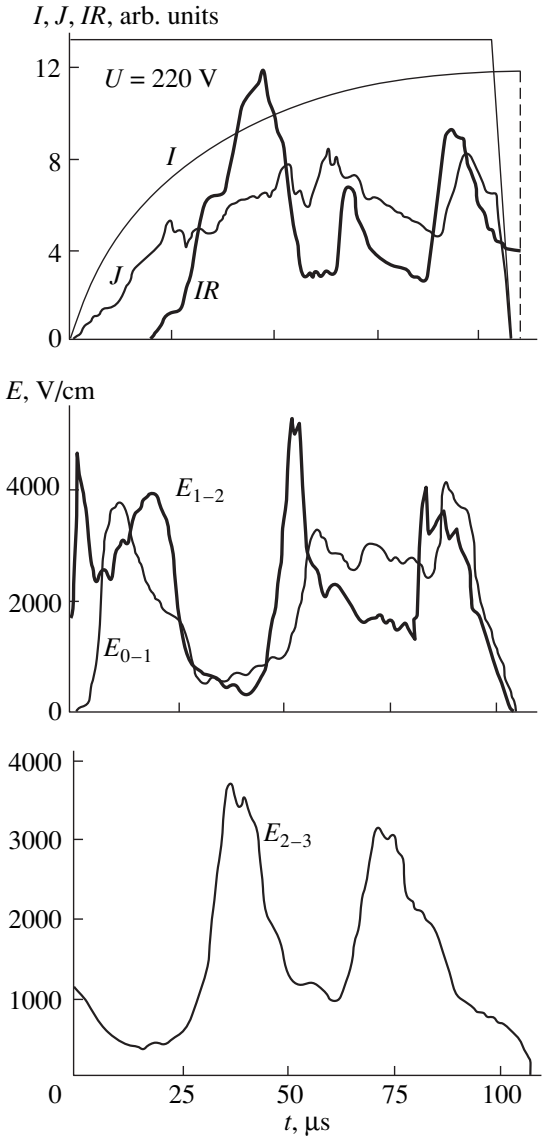

Fig. 4. The formation dynamics and motion to the positively biased contact for two autosolitons under conditions of increasing illumination intensity I and for a high applied voltage of U = 220 V; the time dependences of the total IR emission, current J, and local fields $E_{0–1}$, $E_{1–2}$, and $E_{2–3}$ are shown. Sample 2 with $l_{0–1} = l_{1–2}$ = 0.02 mm and $l_{2–3}$ = 0.04 mm.

If a rectangular voltage pulse with a large amplitude (U = 190–300 V) is applied in the time interval corresponding to the optical-pulse peak ($I \sim I_{max}$, see Fig. 5), the autosoliton is formed from the outset of the voltage pulse in the exclusion region close to the positively biased contact. This is evidenced by our observation, at the voltage-pulse onset, of (i) a characteristic narrow current peak followed by oscillations; (ii) a peak of a high field $E_{0–1} \sim 2000$ V/cm at the positively biased contact (as this takes place, the field in the autosoliton region is certain to be higher than the field $E_{0–1}$ because, in this case, the autosoliton width $L_{AS} \sim 0.3$ mm $< l_{0–1}$ = 0.7 mm); and (iii) a small-amplitude peak of the IR_{glass} emission that comes from the autosoliton is observed through a glass plate, is incident in part on the photodetector (which, in this experiment, is mainly set at the $l_{3–4}$ region), and is indicative of a high charge-carrier temperature ($T_e \sim 1000$ K) in the autosoliton region. In addition, on the one hand, the autosoliton starts to move to the negatively biased contact [11, 12] under the effect of bipolar drift in the sample with the field orientation of $E \parallel \langle 111 \rangle$ and leaves the $l_{0–1}$ region, which

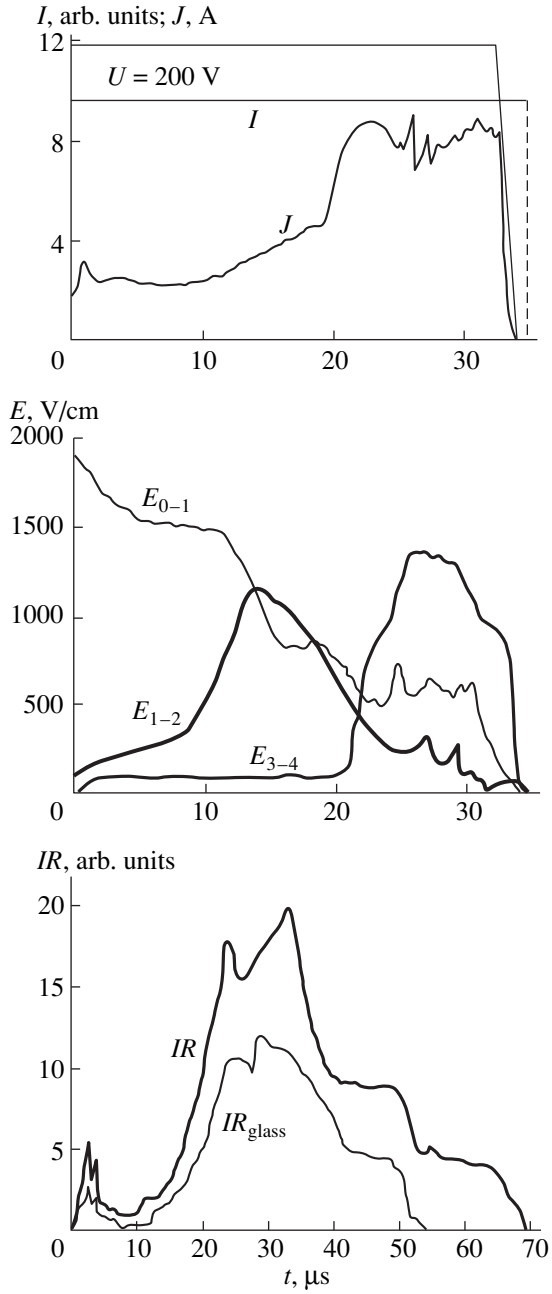

Fig. 5. Formation and motion of an autosoliton to the negatively biased contact for a constant illumination intensity (I) and a high applied voltage (U = 200 V). A steplike decay of signals corresponding to the IR and IR_{glass} emission from the autosoliton region in the sample after termination of the voltage pulse and collapse of the autosoliton is shown. Sample 1 with $l_{0-1} = l_{1-2} = 0.07$ mm and $l_{3-4} = 0.05$ mm.

results in a decrease in the field E_{0-1} (Fig. 5). On the other hand, a high power $W = JE \geq 3000$ W/cm is immediately released in the autosoliton region, which results in a rapid Joule heating of the crystal to temperatures exceeding 400 K in the vicinity of the autosoliton. This, in turn, gives rise to a high-rate thermal generation of nonequilibrium electrons and holes and results in an additional decrease in the electric field in the exclusion region l_{0-1} and brings about an increase in the current (Fig. 5). An abrupt increase in the signals of emission IR and IR_{glass} from the autosoliton is observed when the autosoliton comes to the l_{3-4} region at which the photodetector is set.

After termination of the large-amplitude ($U \sim$ 200 V) voltage pulse, we observed a two-stage decay of the IR-emission signal and a single-stage decay of the IR_{glass} signal from the autosoliton region of the illuminated sample (Fig. 5). The first rapid decay of the IR and IR_{glass} signals is related to the autosoliton decomposition. The duration of subsequent plateaus was about 5–10 μs, and their existence may be caused by an intense heating of the autosoliton region and by extension of the emitting hot zone to the entire photodetector-sensed region where the photogenerated electrons and holes are scattered. The precise origin of plateaus in the IR-signal decay curves is yet to be clarified.

ACKNOWLEDGMENTS

We are indebted to O.G. Sarbeĭ for his productive participation in discussing the results. We also thank V.N. Poroshin and V.M. Vasetskiĭ for their help with preparing the experiments.

This study was supported by the State Foundation for Basic Research (project no. 2.4/816), the International Scientific Foundation CRDF (grant no. UP1-368), and the Ukraine–Israel Scientific Project (grant no. 2M/1807-97).

REFERENCES

1. V. L. Bonch-Bruevich, I. P. Zvyagin, and A. G. Mironov, *Domain Electrical Instabilities in Semiconductors* (Nauka, Moscow, 1972; Consultants Bureau, New York, 1975).
2. B. S. Kerner and V. V. Osipov, Fiz. Tverd. Tela (Leningrad) **21** (8), 2342 (1979) [Sov. Phys. Solid State **21**, 1348 (1979)].
3. B. S. Kerner and V. V. Osipov, Usp. Fiz. Nauk **157** (2), 201 (1989) [Sov. Phys. Usp. **32**, 101 (1989)].
4. B. S. Kerner and V. F. Sinkevich, Pis'ma Zh. Éksp. Teor. Fiz. **36** (10), 359 (1982) [JETP Lett. **36**, 436 (1982)].
5. V. V. Gafiĭchuk, B. S. Kerner, and V. V. Osipov, Fiz. Tekh. Poluprovodn. (Leningrad) **15** (11), 2171 (1981) [Sov. Phys. Semicond. **15**, 1261 (1981)].
6. B. S. Kerner, D. P. Litvin, and V. I. Sankin, Pis'ma Zh. Tekh. Fiz. **13**, 819 (1987) [Sov. Tech. Phys. Lett. **13**, 342 (1987)].
7. I. A. Vashchenko, B. S. Kerner, V. V. Osipov, and V. F. Sinkevich, Fiz. Tekh. Poluprovodn. (Leningrad) **23** (8), 1378 (1989) [Sov. Phys. Semicond. **23**, 857 (1989)].
8. I. K. Kamilov, A. A. Stepurenko, and A. S. Kovalev, Fiz. Tekh. Poluprovodn. (St. Petersburg) **34** (4), 433 (2000) [Semiconductors **34**, 418 (2000)].

9. M. N. Vinoslavskiĭ, Fiz. Tverd. Tela (Leningrad) **31** (8), 315 (1989) [Sov. Phys. Solid State **31**, 1461 (1989)].
10. M. N. Vinoslavskiy, B. S. Kerner, V. V. Osipov, and O. G. Sarbei, J. Phys.: Condens. Matter **2**, 2863 (1990).
11. M. N. Vinoslavskiy and O. G. Sarbei, in *Proceedings of the 23rd International Conference "The Physics of Semiconductors," Berlin, 1996*, Ed. by M. Scheffler and R. Zimmermann, p. 117.
12. O. G. Sarbeĭ, M. M. Vinoslavskiĭ, and A. V. Kravchenko, Ukr. Fiz. Zh. **44** (1–2), 190 (1999).
13. A. C. Prior, Proc. Phys. Soc. London **76**, 465 (1960).
14. A. A. Akopyan and Z. S. Gribnikov, Fiz. Tekh. Poluprovodn. (Leningrad) **9** (8), 1485 (1975) [Sov. Phys. Semicond. **9**, 981 (1975)].
15. L. E. Vorob'ev and V. N. Stafeev, Fiz. Tekh. Poluprovodn. (Leningrad) **1** (8), 1429 (1967) [Sov. Phys. Semicond. **1**, 1190 (1968)].
16. L. E. Vorob'ev and V. N. Stafeev, Fiz. Tekh. Poluprovodn. (Leningrad) **2** (7), 1045 (1968) [Sov. Phys. Semicond. **2**, 875 (1969)].

Translated by A. Spitsyn

Semiconductors, Vol. 35, No. 4, 2001, pp. 384–390. Translated from Fizika i Tekhnika Poluprovodnikov, Vol. 35, No. 4, 2001, pp. 396–402.

ELECTRONIC AND OPTICAL PROPERTIES OF SEMICONDUCTORS

An Analysis of the Shape of a Luminescence Band Induced by Transitions of Free Electrons to Carbon Atoms in Semi-Insulating Undoped GaAs Crystals

K. D. Glinchuk*, N. M. Litovchenko, A. V. Prokhorovich, and O. N. Stril'chuk

Institute of Semiconductor Physics, National Academy of Sciences of Ukraine, Kiev, 03028 Ukraine

**e-mail: ria@isp.kiev.ua*

Submitted June 20, 2000; accepted for publication August 22, 2000

Abstract—The shape of a photoluminescence band observed due to recombination of free electrons at shallow-level acceptors (carbon atoms) in semi-insulating undoped GaAs crystals was analyzed at various temperatures (T = 4.8–77 K). It is shown that at low temperatures the shape observed essentially differs from the theoretical one, while at high temperatures theory and experiment agree closely for radiative transitions of free electrons to isolated shallow-level acceptors. The difference between the experimental and theoretical shapes of the photoluminescence band is associated with the broadening of carbon-induced acceptor levels (i.e., with the formation of the acceptor impurity band), resulting from the effect of electric fields of randomly distributed ionized acceptors and donors on "isolated" carbon atoms. Coincidence of the shapes is associated with a considerable increase in the energy of free carriers (to values up to and above the width of the acceptor impurity band).

1. INTRODUCTION

It is known that an intense photoluminescence (PL) band with emission peak position $h\nu_m$ = 1.4935 ± 0.0005 eV is observed in GaAs at the temperature of T = 4.2 K; this band is caused by free electron e transition to shallow-level acceptors, i.e., neutral carbon C^0_{As} atoms (having an ionization energy of ε_a = 26 meV) [1–3]. Studying the luminescent characteristics of semi-insulating undoped gallium arsenide crystals (henceforth, SI GaAs crystals), we have found that the shape of the low-temperature PL band observed in them, which appeared due to the transitions $e \longrightarrow C^0_{As}$ indicated above (henceforth, PL carbon band), cannot be explained by the theoretical concepts of radiative transitions of free electrons to isolated shallow-level acceptor (the photon energy emitted is equal to $h\nu$). It is necessary to assume for its explanation that the carbon atoms in SI undoped GaAs crystals are not isolated; rather, they interact with each other and with shallow- and deep-level acceptors. This assumption will be discussed below.

2. SHAPE OF THE LUMINESCENCE BAND INDUCED BY THE RADIATIVE RECOMBINATION OF FREE ELECTRONS AT SHALLOW-LEVEL ACCEPTORS IN DIRECT-GAP PHOTOCONDUCTORS (THEORY)

A further theoretical consideration of the spectral intensity of emission $I_{ca}(h\nu)$ will be carried out for a typical representative of direct-gap semiconductors—photoconducting GaAs crystals, whose conductivity at low temperatures ($T \le 200$ K) is completely controlled by photoelectrons (with concentration Δn), photoholes (with concentration Δp), and by the band gap E_g. These crystals contain partially compensated deep-level defects and also randomly distributed shallow-level (hydrogen-like) donors and acceptors. Concentrations of the latter are relatively low (the wave functions both of electrons localized at donors and of holes localized at acceptors do not overlap). In a thermal equilibrium, the shallow-level donors are completely filled by holes, and acceptors, by electrons (the holes at acceptors and the electrons at donors appear only under illumination).

1063-7826/01/3504-0384$21.00 © 2001 MAIK "Nauka/Interperiodica"

2.1. Isolated Acceptors (Model 1)

This situation occurs for low concentrations of acceptors and donors when each acceptor can be treated as an isolated atom (neither the acceptor force fields nor the wave function of holes are localized at the acceptor overlap; the same is true of the donor force fields) forming a discrete level with ionization energy ε_a in the band gap. Then, the shape of the luminescence band induced by the recombination of free electrons (with kinetic energy $\varepsilon = h\nu - E_g + \varepsilon_a$) at shallow-level isolated acceptors is controlled only by their energy distribution $\Delta n(\varepsilon)$ (obviously, $\Delta n(\varepsilon) \sim \rho_e(\varepsilon)\varphi_e(\varepsilon)$), where $\rho_e(\varepsilon) \sim \varepsilon^{1/2}$ is the density of states in the conduction band, and $\varphi_e(\varepsilon)$ is the probability of their occupation by electrons, and in the nondegenerate semiconductors (in which $\varphi_e(\varepsilon) \sim \exp(-\varepsilon/kT)$) it is described by the relation [3–5]

$$I_{ca}(h\nu) \propto \Delta n(\varepsilon) \propto \rho_e(\varepsilon)\varphi_e(\varepsilon) \propto (h\nu - E_g + \varepsilon_a)^{1/2} \times \exp\left(-\frac{h\nu - E_g + \varepsilon_a}{kT}\right), \quad (1)$$

where the energy of photons emitted is $h\nu = \varepsilon + E_g - \varepsilon_a$.

Obviously, the peak position of the emission band considered is

$$h\nu_{m1} = E_g - \varepsilon_a + 0.5kT, \quad (2)$$

and its half-width is

$$w_1 \cong 1.8kT. \quad (3)$$

As follows from (1)–(3), the luminescence spectrum under consideration at $T \longrightarrow 0$ K consists of a narrow line with $h\nu_{m1} \cong E_g - \varepsilon_a$, and, as the temperature increases, this spectrum broadens and shifts towards lower or higher energies depending on E_g and ε_a dependences on T.

2.2. Interacting Acceptors (Model 2)

This situation occurs for relatively high concentrations of acceptor and/or donors. Here, the overlap of electric fields of isolated acceptors and of fields produced by randomly arranged donors and/or by similar (or other) acceptors is possible (obviously, this results in the transformation of previously isolated acceptors (see Subsection 2.1) into interacting acceptors [5–10]). In addition, this situation occurs when the isolated acceptors reside in the fields of internal stresses, which are produced by chaotically distributed point or extended defects in the crystal lattice [5, 6, 11]. This situation occurs also if an electric field is generated by piezoelectric phonons [11] in a disordered crystal or if the wave functions of holes localized at isolated acceptors overlap [4, 9, 10].

One should expect that, in photoconductors, the interaction of isolated acceptors with charged donors and/or acceptors will be dominant due to the relatively high concentrations of compensating impurities in these materials [9]. It is this case that will be considered by us below.

The disorder in the distribution of ionized impurities throughout the crystal results in the isolated acceptors occurring in force fields of different magnitudes. As a consequence, broadening of levels formed by acceptors takes place; i.e., an acceptor impurity band with a half-width of w_h is formed [7–10]. This band is characterized by a spectrum of closely spaced discrete acceptor levels (the wave functions of holes at these levels remain localized) with various ionization energies $\varepsilon_{a1}, \varepsilon_{a2} \ldots \varepsilon_{ai}$ and densities of states $\rho_h(\varepsilon_{ai})$ (their density is maximal ($\rho_h = \rho_{h\max}$) at the energy $\varepsilon_{ai} = \varepsilon_a$); the probability of their occupation by holes is $\Delta\varphi_h(\varepsilon_{ai})$, and the concentration of holes at them is $\Delta p_h(\varepsilon_{ai}) = \rho_h(\varepsilon_{ai})\Delta\varphi_h(\varepsilon_{ai})$ [7–10]. Obviously, in this case, when calculating the spectral intensity of emission caused by the transition of free electrons (whose kinetic energy is $\varepsilon = h\nu - E_g + \varepsilon_{ai}$) to the acceptor impurity band, one should take into account that disorder in the arrangement of ionized donors and acceptors results in the appearance of impurity-potential fluctuations (the rms depth of a potential well is γ) [8, 9]. However, in nongenerate compensated semiconductors with a small effective electron mass (in particular, in the SI GaAs crystals under consideration), fluctuations of the impurity composition in fact do not distort the conduction band; i.e., the position of the conduction band bottom is the same for the entire crystal [4, 8]. Therefore, in this case, the PL spectrum is governed only by the energy distribution of free electrons $\Delta n(\varepsilon) \sim \varepsilon^{1/2}\exp(-\varepsilon/kT)$ and holes $\Delta p_h(\varepsilon_{ai})$ localized at the acceptors, since the probability of the radiative recombination of free electrons and holes localized at the acceptors is in fact independent of their energies [4, 8]. The spectrum shape is defined by the relation [8]

$$I_{ca}(h\nu) \propto \int_{E_g - h\nu}^{\infty} (h\nu - E_g + \varepsilon_{ai})^{1/2} \times \exp\left(-\frac{(h\nu - E_g + \varepsilon_{ai})}{kT}\right)\rho_h(\varepsilon_{ai})\Delta\varphi_h(\varepsilon_{ai})d\varepsilon_{ai}, \quad (4)$$

where the energy of emitted photons is given by $h\nu = \varepsilon + E_g - \varepsilon_{ai}$.

It is obvious that the position of the peak for the PL band under consideration is $h\nu_{m2} \geq h\nu_{m1}$, and its half-width is $w_2 \geq w_1$ (undoubtedly, $w_2 \cong w_1 + w_h$ if $\Delta\varphi_h \neq f(\varepsilon_{ai})$).

We may conclude the following from the analysis of relation (4).

At low temperatures ($T \longrightarrow 0$ K), the PL spectrum shape is controlled only by the energy distribution of levels in the acceptor impurity band $\rho_h(\varepsilon_{ai})$, since, at the above temperatures, they are approximately similarly

filled with holes, i.e., $\Delta\varphi_h \neq f(\varepsilon_{ai})$ (this takes place if the coefficients of electron and hole capture by the acceptors with various ionization energies ε_{ai} differ only slightly or if the coefficients of hole capture by acceptors are considerably larger than those for electrons [8, 12]), and the free electrons occupy the states at the conduction band bottom ($I_{ca}(h\nu) \sim \rho_h(\varepsilon_{ai})\Delta\varphi_h(\varepsilon_{ai}) \sim \rho_h(\varepsilon_{ai})$, where $h\nu = E_g - \varepsilon_{ai}$). Then, by radiative recombination of free electrons at the levels of the acceptor impurity band, we should expect the appearance of a broad luminescence band with an emission peak at $h\nu_{m2} \cong E_g - \varepsilon_a$ and a half-width w_h on the order of the broadening of ionization energy of acceptor levels. The structure of this band is caused by the free-electron transitions to the individual acceptor levels ε_{ai} (the overall spectrum represents an integral of individual luminescence lines caused by transitions $\varepsilon \longrightarrow \varepsilon_{ai}$); i.e., the low-temperature values of I_{ca} will represent the distribution of the density of states in the acceptor impurity band (obviously, $I_{ca}(h\nu) \sim \rho_h(\varepsilon_{ai})$, if $\Delta\varphi_h \neq f(\varepsilon_{ai})$).

As the temperature increases, one should expect the following changes in the PL spectrum. First, we should observe a shift of the peak position (according to the law $h\nu_{im} = E_g - \varepsilon_{ai} + 0.5kT$) and a broadening (according to the law $w_{i1} = 1.8kT$) of each radiation line, caused by an increase in the free-electron kinetic energy, i.e., by transitions of free electrons of various energies to a given acceptor level ε_{ai}. Then, due to features indicated above, the emission spectrum observed at a certain temperature is the sum of elementary spectra caused by transitions of free electrons to an individual level ε_{ai} within the impurity band. Second, a shift of the PL spectrum to lower energies and a decrease in its half-width occur. The latter effect is associated with the localized states in the acceptor band gradual filling with electrons (obviously, the states located near the valence band top are primarily filled, since, undoubtedly, $\Delta\varphi_h(\varepsilon_{ai}) \sim \exp(\varepsilon_{ai}/kT)$); i.e., the hole concentration at these states decreases steadily (this process results in the thermal quenching of the PL induced by acceptors [12]). This effect clearly manifests itself at moderate temperatures ($\Delta\varphi_h = f(\varepsilon_{ai})$ at $kT \leq w_h$). It almost disappears at sufficiently high temperatures ($kT \gg w_h$), when the majority of acceptor states are approximately equally filled by holes ($\Delta\varphi_h \neq f(\varepsilon_{ai})$). In particular, as follows from relation (4), a shift of the radiation peak caused by this effect is given by $\Delta h\nu_m = -w_h^2/(8\ln 2)kT \cong -0.18 w_h^2/kT$.

2.3. Comparison of Models 1 and 2

As one should expect, these models yield significantly differing PL spectra at low temperatures. However, at reasonably high temperatures ($w_1 \cong 1.8kT \gg w_h$), they should result in approximately similar shapes of the spectra ($h\nu_{m1} \approx h\nu_{m2}$, and $w_1 \approx w_2$).

3. THE METHOD OF STUDYING AND CHARACTERIZING THE SI UNDOPED GaAs CRYSTALS

Studies were carried out on typical photoconductors, i.e., SI undoped GaAs crystals (which had a dark conductivity $\sigma \longrightarrow 0$ at $T \leq 200$ K). The dominant deep-level impurities in them are antisite defects *EL2*, the total concentration of which is $N_{EL2} = 1.2 \times 10^{16}$ cm^{-3}, including a concentration in the positive-charge state of $N^+_{EL2} = 3 \times 10^{15}$ cm^{-3}. The easily ionized shallow-level acceptors are carbon atoms (their concentration is $N_C \cong 5 \times 10^{15}$ cm^{-3}); these represent the main compensating impurity in these crystals. In thermal equilibrium, they were completely filled with electrons; i.e., they were in a negatively charged state. The holes at these acceptors appear only under illumination (the probability of filling the carbon atom with a hole is $\Delta\varphi_h$). In addition, these crystals also contain a relatively low concentration N_d of background shallow-level donors (their concentration is $N_d \cong 2 \times 10^{15}$ cm^{-3}). In thermal equilibrium, they were completely filled with holes; i.e., they were in the positively charged state. Electrons appear at donors only under illumination. Illumination did not result in a noticeable change of ionized acceptor and donor concentrations (in particular, $\Delta\varphi_h \ll 1$ for the L used).

The luminescence excited by a strongly absorbed radiation of a He–Ne laser was studied (the photon energy was 1.96 eV, and the absorption coefficient was 2.5×10^4 cm^{-1}). The PL spectra were analyzed using an MDR-23 spectrometer with a resolution no worse than 0.3 meV at temperatures from 4.8 to 77 K and illumination intensities L from 10^{17} up to 10^{19} photon/(cm^2 s). The luminescence spectra presented below are induced by transitions of free electrons to the carbon atoms and are obtained by extracting them from the edge PL spectra [12, 13]. The observed pattern of temperature variations of the carbon band shape under study (peak position $h\nu_m$ and half-width w) in fact (within the accuracy of variances in the values of $h\nu_m$ (±0.5 meV) and w (±0.5 meV)) were independent of L (see below); therefore, we will present the data obtained for L = 10^{18} photon/(cm^2 s). Gallium arsenide was nondegenerate for the values of L and T used in this study; i.e., we can use relations (1)–(4) given above to explain the shape of the PL carbon band observed in GaAs as well as the dependences of its peak position and half-width on temperature and excitation intensity.

The luminescence-band intensity I_{ca} (obviously, $I_{ca} \sim \Delta n N_C \Delta\varphi_h$; experimentally, we have $I_{ca} \sim \Delta p \sim L$ at low T and $I_{ca} \sim \Delta n \Delta p \sim L^2$ at high T [12]) varied with temperature according to the law (Fig. 1)

$$I_{ca} = \frac{aL^2}{bL + Q_+ \exp(-\varepsilon_a/kT)}, \qquad (5)$$

where $a \neq f(T, L)$, $b = 10^{-6}$ s/cm, $L = 10^{18}$ photon/(cm^2 s), Q_+ ($Q_+ \sim T^{3/2}$) is the effective density of states in the

valence band, and $\varepsilon_a = 26$ meV (factor L^2 for the coefficient a is written on the basis of the dependences I_{ca} on L observed at low and high T).

The changes in $I_{ca} = f(1/T)$ were mainly associated with corresponding changes in the probability of the occupation of carbon atoms by holes ($I_{ca} \sim \Delta\varphi_h$, since $\Delta n \neq f(T)$), i.e., with the thermally stimulated lowering of the carbon acceptor level occupancy by holes. It follows from this that, in the crystals studied, the probability of the occupation of carbon atoms by holes is defined by the relation (Fig. 1)

$$\frac{\Delta\varphi_h}{\Delta\varphi_h(0)} = \frac{bL}{bL + Q_+\exp(-\varepsilon_a/kT)}, \quad (6)$$

where $\Delta\varphi_h(0)$ is the value of $\Delta\varphi_h$ at $T \longrightarrow 0$ K ($\Delta\varphi_h(0) \ll 1$, see above), $b = 10^{-6}$ s/cm, $L = 10^{18}$ photon/(cm^2 s), and $\varepsilon_a = 26$ meV. We note that $\Delta\varphi_h \neq f(L, T)$ at low temperatures ($Q_+\exp(-\varepsilon_a/kT) \ll bL$) and almost exponentially (according to the law $\Delta\varphi_h \sim LT^{3/2}\exp(26\text{ meV}/kT)$) decreases at high temperatures ($Q_+\exp(-\varepsilon_a/kT) \ll bL$).

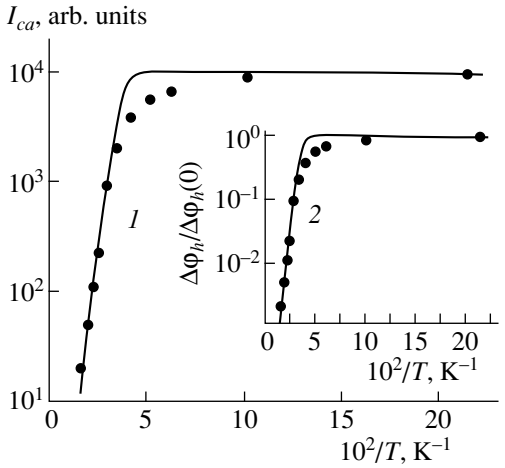

Fig. 1. (*1*) Intensity dependence of the PL band induced by recombination of free electrons at the carbon atoms and (*2*) the relative probability of them being filled by holes on temperature in SI undoped GaAs crystals. Points are for the experiment, solid lines are theoretical curves $I_{ca} = f(1/T)$ and $\Delta\varphi_h/\Delta\varphi_h(0) = f(1/T)$ plotted according to relations (5) and (6), respectively (for parameters of the curves, see the text).

4. BAND SHAPE OF LUMINESCENCE INDUCED BY RADIATIVE RECOMBINATION OF FREE ELECTRONS AT SHALLOW-LEVEL ACCEPTORS (CARBON ATOMS) IN SI UNDOPED GaAs CRYSTALS (EXPERIMENT)

4.1. Results

The PL spectra measured at various temperatures in SI GaAs crystals are shown in Fig. 2; these spectra are induced by free electron transitions at the carbon atoms occupied by holes. As can be seen, at a low temperature ($T = 4.8$ K), the PL spectrum can be approximately described by a Gaussian curve with the emission peak position $h\nu_m = 1.493$ eV and a half-width $w = 3.4$ meV:

$$I_{ca}(h\nu) = I_{ca}(h\nu_m)\exp\left[-(4\ln 2)\frac{(h\nu - h\nu_m)^2}{w^2}\right]. \quad (7)$$

As the temperature increases, the PL spectrum shape changes, and a nonmonotonic shift of the radiation peak position (first, to higher and then to lower energies), as well as a nonmonotonic increase of its half-width, are observed.

The above inference follows also from temperature dependences of the peak position and PL carbon band half-width studied (see Fig. 3).

The half-width and the position of the peak for the luminescence carbon band in relation to the excitation intensity are given in Fig. 4 at low and high temperatures (in the regions of $I_{ca} \neq f(1/T)$ and $I_{ca} = f(1/T)$, see Fig. 3). As can be seen, the values of $h\nu_m$ and w (as well as the shape of the PL band itself) are in fact independent of L.

The data obtained by us and also by other authors [1, 3, 13] on the dependences of low-temperature ($T = 1.8$–4.8 K) values of $h\nu_m$ and w for the luminescent carbon band as functions of the carbon atom concentration N_C and shallow-level background donors N_d are shown in Fig. 5.[1] As can be seen, $h\nu_m$ is independent of N_C and N_d, and the larger N_C and N_d are, the larger w is.

4.2. Discussion of the Results

4.2.1. Analysis according to model 1. The PL spectra calculated according to relation (1) for various temperatures are shown in Fig. 2; these spectra are related to the radiative recombination of free electrons at isolated carbon atoms (when calculating the theoretical dependences, the values of $E_g = f(T)$ were determined from the data reported in [14]). As can be seen, a difference between experimental and theoretical shapes of PL spectra caused by electronic transitions $e \longrightarrow C^0_{As}$ is observed. This difference is considerably large at low temperatures ($T \leq 25$ K). However, at a high temperature ($T \geq 35$ K), this difference is much less.

Theoretical (calculated according to relations (2) and (3)) dependences of $h\nu_m$ and w for transitions $e \longrightarrow C^0_{As}$ on temperature are shown in Fig. 3. As can be seen, in an entire temperature range, satisfactory agreement between experimental and theoretical dependences for

[1] In Ref. [3], the values w at 7 K ($w \cong 1.2$ meV $\cong 2kT$) and 10 K ($w \cong 1.6$ meV $\cong 2kT$) are reported. Their values are close to those theoretically predicted. Therefore, the values of w extrapolated to 4.8 K ($w \cong 0.8$ meV $\cong 1.8kT$) are shown in Fig. 5.

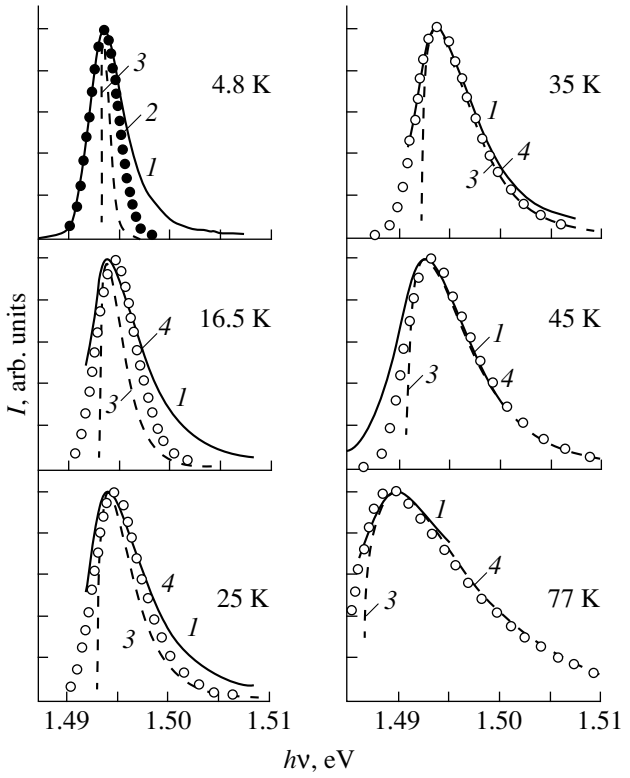

Fig. 2. PL bands appearing due to free-electron transitions to the neutral carbon atoms at various temperatures in SI undoped GaAs crystals. Circles *1* correspond to the experiment, *2* is a Gaussian curve plotted according to relation (7), and *3* and *4* are theoretical curves calculated according to relations (1) and (4), respectively (for parameters of the curves, see the text).

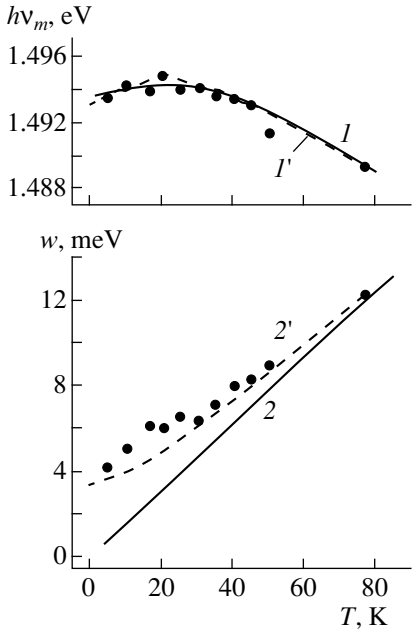

Fig. 3. Temperature dependences of $h\nu_m$ and w for the PL carbon band in SI undoped GaAs crystals. Points correspond to the experiment, solid and dashed lines *1*, *1*', *2*, and *2*' represent theoretical dependences of $h\nu_m(T)$ and $w(T)$ plotted according to relations (2), (4), (3), and (4), respectively (for parameters of the curves, see the text).

$h\nu_m = f(T)$ is observed. At the same time, the shape of dependences $w = f(T)$ differs from the theoretical ones and is close to those occurring at high temperatures.

Experimental dependences of $h\nu_m$ and w on L (see Fig. 4) are basically consistent with the theoretical ones (see relations (2) and (3)).

The expected theoretical dependences (based on the simplest model 1) of $h\nu_m$ and w for the PL band studied on the carbon concentration and background donors are shown in Fig. 5. As can be seen, the values of $h\nu_m$ are close to the theoretical ones (see relation (2)) in the range of values N_C and N_d. However, the values of w are close to theoretical (defined by relation (3)) only in weakly doped crystals (Fig. 5). In highly doped SI GaAs crystals (N_C and $N_d \cong 10^{15}$–10^{16} cm^{-3}), the magnitudes of w are considerably larger (Fig. 5).

4.2.2. Analysis according to model 2. It can be seen from the data given above, theoretical model 1 cannot explain the PL spectrum shape in SI GaAs crystals at low temperatures; for this spectrum caused by radiative recombination of free electrons on carbon atoms, a considerable difference between experimental and theoretical PL spectra, in particular, its significant broadening is observed. Only at moderate and high temperatures, does the PL spectrum shape observed experimentally satisfactorily agree with the theoretical one (as the temperature increases, the shape of the PL band considered approaches that expected theoretically). In relation to the aforesaid, one should carry out an analysis according to theoretical model 2.

Obviously, in order to explain the experimental data (in particular, a significant broadening of PL carbon spectra at low temperatures), we should assume that the carbon atoms are not isolated in the SI GaAs crystals under study. Then, a probable explanation of the PL carbon band broadening at low temperatures, as well as of its shape variation with temperature (this mechanism is confirmed by dependence $w = f(N_C, N_d)$, is observed experimentally, i.e., by a significant broadening of the PL band under study in the SI GaAs crystals, see Fig. 5).

Due to a relatively high mean concentration of carbon atoms and significant concentrations of easily ionized and deep-level donors in SI undoped GaAs crystals, a structural disorder is quite probable in the form of significant fluctuations of concentrations of negatively charged acceptors N_C^- and positively charged shallow-level N_d^+ and deep-level N_{EL2}^+ donors, which gives rise to the accumulation of randomly arranged and closely spaced charged acceptors and donors. This results in a significant force interaction of carbon atoms

with each other and with shallow- and deep-level donors; i.e., impurity potential fluctuations appear (as follows from the value w_h given below, the rms depth of the potential well is $\gamma \cong 1.5$ meV). The consequence of the effect of electric-field fluctuations on the neutral carbon atoms (these are the atoms, at which the radiative recombination of free electrons takes place) is the appearance of a wide range of ionization energies of carbon atoms ε_{ai} (a significant concentration-related broadening of the energy spectrum of the levels produced by atoms, i.e., the formation of the acceptor impurity band) (see Subsection 2.2).[2] It is very likely that the filling of any levels in this band, as follows from the dependence $\Delta\varphi_h = f(1/T)$ observed experimentally, is defined by the relation

$$\frac{\Delta\varphi_h(\varepsilon_{ai})}{\Delta\varphi_h(0, \varepsilon_{ai})} = \frac{bL}{bL + Q_+ \exp(-\varepsilon_{ai}/kT)}, \qquad (8)$$

where $\Delta\varphi_h(0, \varepsilon_{ai})$ is the value of $\Delta\varphi_h(\varepsilon_{ai})$ at $T \longrightarrow 0$ K ($\Delta\varphi_h(0, \varepsilon_{ai}) \ll 1$, see above); obviously, $\Delta\varphi_h \neq f(\varepsilon_{ai})$ at low temperatures ($Q_+\exp(-\varepsilon_{ai}/kT) \ll bL$) and decreases exponentially according to the law $\Delta\varphi_h(\varepsilon_{ai}) \sim \exp(\varepsilon_{ai}/kT)$ at high temperatures ($Q_+\exp(-\varepsilon_{ai}/kT) \ll bL$).

The density of acceptor levels in the impurity band of SI GaAs crystals, as follows from what was considered in Subsection 2.2 and from the shape (see relation (7)) of low-temperature PL spectrum observed (for $\Delta\varphi_h \neq f(\varepsilon_{ai})$, see relation (8)), is described by the following Gaussian curve:

$$\rho_h = \rho_{h\max} \exp\left[-(4\ln 2)\frac{(\varepsilon_{ai} - \varepsilon_a)^2}{w_h^2}\right]. \qquad (9)$$

Here, $\varepsilon_a = 26$ meV and $w_h = 3.4$ meV is the half-width of the spectrum of the density of states in the impurity acceptor band (undoubtedly, $w_h = (8\ln 2)^{1/2}\gamma$, see [8]).

The above naturally corresponds to a significant increase in the half-width of the luminescence band induced by transitions $e \longrightarrow C^0_{As}$; i.e., w turns out to be of the order of the spreading of the carbon-atom ionization energies $\varepsilon_{a\max} - \varepsilon_{a\min} \cong 4$ meV (see Subsection 2.2).

Undoubtedly, a temperature broadening of the luminescence band considered is associated mainly with the corresponding transformations of the electron energy distribution in the conduction band (electrons occupy higher energy states the higher the temperature is). The broadening itself is somewhat less than expected, since simultaneously with the temperature increase (at not very high temperatures), a relatively small narrowing of the PL spectrum occurs owing to a reduction in filling the shallowest states by holes in the acceptor impurity band (see Subsection 2.2).[3] Obviously, at high temperatures ($T > w_h/1.8k$), the emission spectrum broadening can far exceed the initial (observed at low T) half-width of the luminescence carbon band ($w_1 \cong 1.8kT \gg w_h$). Therefore, at high temperatures ($T \geq 35$ K), the shape of

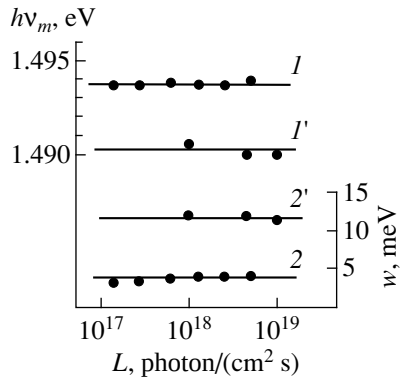

Fig. 4. Dependences of $h\nu_m$ (*1*, *1*') and w (*2*, *2*') for the PL carbon band on the excitation intensity at T = (*1*, *2*) 4.8 and (*1*', *2*') 77 K.

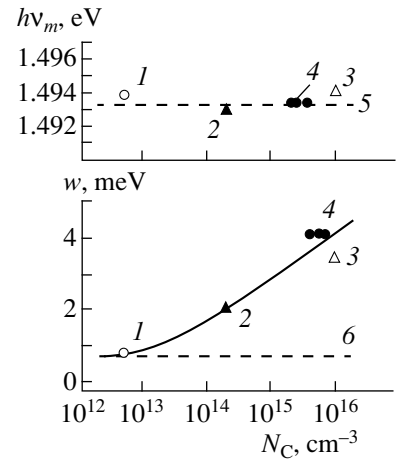

Fig. 5. Peak position and half-width of the PL band induced by carbon in SI undoped GaAs crystals with various concentrations of acceptors (carbon atoms) and donors at T = (*3*) 1.8, (*1*) 4.2, and (*2*, *4*) 4.8 K. $N_d \cong 10N_C$ (*1*, *2*); $N_d + N_{EL2} \cong 3N_C$ (*3*, *4*). *1*, *2*, and *3* correspond to the data reported in [1], [3], and [13], respectively; points *4* represent the data of this study. Dashed lines *5* and *6* are theoretical curves plotted according to relations (2) and (3), respectively (for parameters of the curves, see the text).

[2] Concentrations of charged acceptors and donors are approximately equal (obviously, $N_C^- \cong N_d^+ + N_{EL2}^+$) in the crystals under study. Consequently, an acceptor resides near each of the donors. However, due to their random arrangement, the distance between them (i.e., the force fields produced by them) substantially differs at various points of the crystal. Then, the broadening of carbon levels is associated with the fact that the latter are in force fields of various magnitudes.

[3] As can be seen from relation (8), an increase in L widens the domain of $\Delta\varphi_h$ independence on T. An evident consequence of this fact is the shift of the onset of the PL spectrum narrowing to higher temperatures.

the carbon spectrum will be almost completely caused by the temperature broadening ($w_2 \cong w_1 \gg w_h$ (Figs. 2, 3)).

One should also expect the coincidence of experimental and theoretical (for transitions $e \longrightarrow C^0_{As}$) dependences $h\nu_m = f(T)$. This is associated with the peak of the density of states in the acceptor impurity band being at the energy of $\varepsilon \cong \varepsilon_a$ [4, 8]. Therefore, the position of the PL carbon-band peak is defined by a relation similar to (2) irrespective of whether the radiation is caused by the isolated or interacting (resulting in the impurity band formation) carbon atoms.

The aforementioned independence of the PL spectrum shape ($h\nu_m$ and w values) of L, i.e., of Δp (in experiments, $\Delta p \sim L$), is associated with the fact that, in the crystals studied, filling of the electronic states in the impurity band is completely independent of L at low temperatures ($\Delta\varphi_h \neq f(T)$), and at high temperatures ($\Delta\varphi_h = f(T)$) varies similarly with L (see relation (8)).[4]

The explanations presented are confirmed by the comparison of measured and theoretical (plotted according to relation (4) using numerical simulations) PL carbon spectrum shapes at various temperatures. This comparison is illustrated in Figs. 4 and 5 (when calculating theoretical curves, the values of $\Delta\varphi_h$ and ρ_h were determined from relations (8) and (9), where $L = 10^{18}$ photon/(cm^2 s)). As can be seen, a qualitative agreement of the experimental and theoretical (according to model 2) shapes of the PL carbon band under consideration and temperature changes of its peak position and half-width were observed. A comparatively slight difference between experimental and theoretical shapes of the PL spectrum is associated mainly with the employment of a rather crude theoretical model for describing the radiative transitions of free electrons to the holes in the acceptor impurity band. In particular, we neglected the distortion of conduction and valence band edges by the fluctuating impurity potential as well as ignoring a possible dependence of the probability of free-electron transition to the split carbon levels on ε, ε_{ai}, etc. [8, 15, 16].

CONCLUSION

The substantial difference between the shape of the PL band observed in SI undoped GaAs crystals at low temperatures and induced by free-electron transitions to the acceptor levels introduced by carbon and the theoretically expected shape is associated with the concentration broadening of these levels, and the coincidence of these shapes at high temperatures is related to an increase in the mean energy of free electrons. A theoretical model proposed for radiative transitions of free electrons to the carbon impurity band satisfactorily explains the temperature variations of the shape of the PL band under consideration, in particular, variations of its peak position and its half-width. The above is important for understanding the physics of electronic processes in intermetallic semiconductors.

[4] One should note that if, with an increase in L, i.e., in Δp, a temperature domain of values $\Delta\varphi_h = f(T)$ transforms into the domain $\Delta\varphi_h \neq f(T)$ (see relation (8)), the increase in Δp will result in the shift of $h\nu_m$ by the value $\Delta h\nu_m \cong -0.18\, w_h^2/kT$ (see above).

REFERENCES

1. M. Ozeki, K. Nakai, K. Dazai, and O. Ryuzan, Jpn. J. Appl. Phys. **13**, 1121 (1974).
2. D. J. Ashen, P. J. Dean, D. T. J. Hurle, and J. B. Mullin, J. Phys. Chem. Solids **36**, 1041 (1975).
3. T. Kamiya and E. Wagner, J. Appl. Phys. **48**, 1928 (1977).
4. A. P. Levanyuk and V. V. Osipov, Usp. Fiz. Nauk **133**, 427 (1981) [Sov. Phys. Usp. **24**, 187 (1981)].
5. L. Pavesi and M. J. Guzzi, J. Appl. Phys. **75**, 4779 (1994).
6. A. M. Stoneham, Rev. Mod. Phys. **41**, 82 (1969).
7. A. A. Kal'fa and Sh. M. Kogan, Fiz. Tekh. Poluprovodn. (Leningrad) **6**, 2175 (1972) [Sov. Phys. Semicond. **6**, 1839 (1972)].
8. A. P. Levanyuk and V. V. Osipov, Fiz. Tekh. Poluprovodn. (Leningrad) **7**, 1575 (1973) [Sov. Phys. Semicond. **7**, 1050 (1973)].
9. B. I. Shklovskiĭ and A. L. Éfros, *Electronic Properties of Doped Semiconductors* (Nauka, Moscow, 1979; Springer, New York, 1984).
10. V. L. Bonch-Bruevich and S. G. Kalashnikov, *Physics of Semiconductors* (Nauka, Moscow, 1990).
11. J. D. Dow, D. L. Smith, and F. L. Lederman, Phys. Rev. B **8**, 4612 (1973).
12. K. D. Glinchuk, N. M. Litovchenko, A. V. Prokhorovich, and O. N. Stril'chuk, Optoélektron. Poluprovodn. Tekh. **34**, 42 (1999).
13. M. Maciaszek, D. W. Rogers, and R. P. Bult, Can. J. Phys. **67**, 384 (1989).
14. E. Grilli, M. Guzzi, and L. Pavesi, Phys. Rev. B **45**, 1638 (1992).
15. V. V. Osipov, T. I. Soboleva, and M. G. Foĭgel', Fiz. Tekh. Poluprovodn. (Leningrad) **11**, 1277 (1977) [Sov. Phys. Semicond. **11**, 752 (1977)].
16. V. V. Osipov, T. I. Soboleva, and M. G. Foĭgel', Fiz. Tekh. Poluprovodn. (Leningrad) **13**, 542 (1979) [Sov. Phys. Semicond. **13**, 319 (1979)].

Translated by T. Galkina

Semiconductors, Vol. 35, No. 4, 2001, pp. 391–393. Translated from Fizika i Tekhnika Poluprovodnikov, Vol. 35, No. 4, 2001, pp. 403–405.

ELECTRONIC AND OPTICAL PROPERTIES OF SEMICONDUCTORS

Relaxation Features of the Dielectric Response of $Cd_{1-x}Zn_xTe$ Crystals Grown from the Melt

I. A. Klimenko*, V. K. Komar', V. P. Migal'*, and D. P. Nalivaĭko****

** Kharkov Institute of Aviation, Zhukovsky State Aerospace University, Kharkov, 61070 Ukraine*

*** Institute of Single Crystals, National Academy of Sciences of Ukraine, Kharkov, 61001 Ukraine*

Submitted August 14, 2000; accepted for publication August 16, 2000

Abstract—It is shown that the low-frequency dielectric response of $Cd_{1-x}Zn_xTe$ crystals grown from the melt is controlled by macroscopic growth defects and their elastic and electric fields. An interconsistent realignment of these fields under the action of external forces changes the dielectric response, which reflects features of the large-scale potential-relief distortions. © *2001 MAIK "Nauka/Interperiodica".*

An appropriate combination of good transport properties of nonequilibrium charge carriers and high resistivity of $Cd_{1-x}Zn_xTe$ (CZT) crystals places them among the most promising materials for detecting ionizing radiation at room temperature. However, CZT crystals, being intermediate between semiconductors and insulators, are characterized by a variety of growth defects due to substantially nonequilibrium growth conditions. Therefore, the study and quality control of these crystals should be carried out by methods conventional for both semiconductors [1] and insulators [2]. This study is aimed at revealing the CZT dielectric response features caused by the interaction between elastic and electric fields induced by a variety of growth defects in piezoelectric crystals.

We studied $Cd_{1-x}Zn_xTe$ ($x = 0.1$–0.2) crystals grown by vertical crystallization from the melt under inert gas pressure. The above composition range is characterized by an optimum combination of high resistivity and transport properties of nonequilibrium carriers, necessary for radiation detection. Diverse growth defects induce a microrelief at the surface of a chemically polished crystal, visualized by the shadow method. Residual stresses of growth defects in the samples studied were revealed by examining the photoelasticity. Indium–gallium or gold contacts were formed at opposite faces of samples of $11 \times 11 \times 2$ mm and $5 \times 5 \times 2$ mm in size. The sample dielectric parameters ε' and ε'' were measured by the capacitance technique in the range of 10^2–10^7 Hz. To study the temperature dependences of the real ε' and imaginary ε'' parts of the complex dielectric constant ε^*, we mounted the samples in a thermostat whose temperature varied from 290 to 440 K with a constant rate of 0.5 K/min.

Photoelasticity and "dark" studies showed that most of the samples are characterized by a complex nonuniform distribution of growth defects over the crystal. Block boundaries, inclusions, as well as separate twin and slip bands were observed in these samples. Such defects induce large-scale elastic and electric fields in piezoelectric crystals.

A relaxation-type dispersion region was revealed in the frequency dependences $\varepsilon'(\omega)$ and $\varepsilon''(\omega)$ measured when samples were irradiated with photons within the photosensitivity range. An analysis of these dependences in the complex plane (using the Cole–Cole diagrams) showed that this region had a continuous distribution of relaxation times, characterized by a shortening of the most probable relaxation time as photoexcitation intensity increases. In this case, the value of variance and the most probable relaxation time are characteristic parameters of the sample. Similar dependences were observed by us previously in $ZnS_{1-x}Se_x$ crystals. As was shown in [3], these dependences reflect the features of the large-scale potential relief (LPR). We note that the frequency dependences of ε' and ε'' are independent of wavelength, while their spectral dependences are similar at low-intensity excitations.

The relaxation property of the CZT dielectric response during photoexcitation manifests itself in different spectral dependences of the low-frequency dielectric constant $\varepsilon'(\lambda)$ and the dielectric loss factor $\varepsilon''(\lambda)$. These dependences plotted as diagrams in the complex plane $\varepsilon^*(\lambda)$ allow the effect of elastic fields of growth defects on the photodielectric response to be assessed [4]. For example, the diagrams $\varepsilon^*(\lambda)$ of CZT samples with various densities of growth defects basically differ. The most optically uniform samples are characterized by rectilinear-segment diagrams $\varepsilon^*(\lambda)$ (see Fig. 1, curve *1*) differing only in their slopes. The diagrams $\varepsilon^*(\lambda)$ of the samples containing individual growth defects consist of arc-shaped portions of various curvatures (Fig. 1, curve *2*). It was established that the number of arcs, their distinctness, and the diagram area correlate clearly with the density of two-dimensional structural growth defects causing residual stresses of the second kind. We note that the diagrams

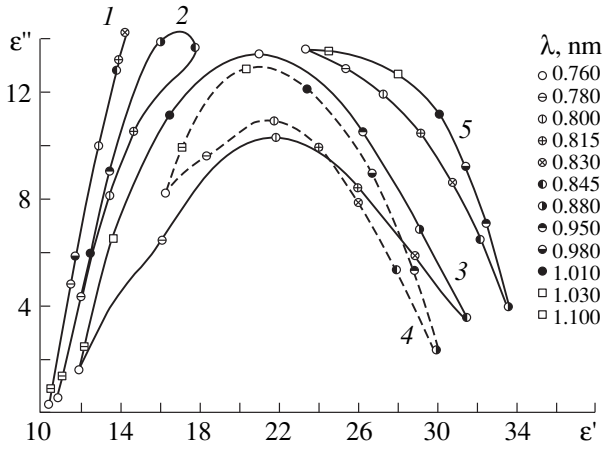

Fig. 1. The Cole–Cole diagrams with ε*(λ) as a parameter for $Cd_{1-x}Zn_xTe$ samples differing in growth defect densities, measured at $f = 10^3$ Hz and $T = 293$ K; wavelengths λ correspond to various symbols as is indicated in this figure.

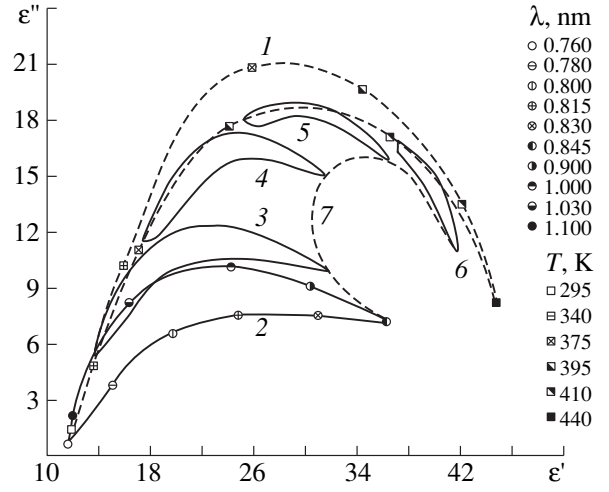

Fig. 2. The Cole–Cole diagrams ε*(*T*) (curves *1*, *7*; dashed lines) and ε*(λ) (curves *2*–*6*) for $Cd_{1-x}Zn_xTe$ samples at $f = 10^3$ Hz; wavelengths λ and temperatures *T* correspond to various symbols as is indicated in the figure.

ε*(λ) are specific for each crystal. The diagrams ε*(λ) of CZT crystals with an increased density of growth defects point to complex relaxation processes during photoexcitation. First, these diagrams exhibit regions where $d\varepsilon''/d\varepsilon' < 0$ (see Fig. 1, curves *3*–*5*). Second, the value of ε" near the inherent maximum is smaller than the "dark" level of ε" in the samples experiencing significant dielectric losses when in the dark (Fig. 1, curves *4*, *5*). Furthermore, the value of ε" under illumination is smaller than the starting one for some unilluminated samples in the entire photosensitivity range; i.e., negative photodielectric losses are observed (Fig. 1, curve *5*).

Such a photodielectric response property is obviously related to modification of the LPR when filled by nonequilibrium carriers. This process is controlled by

(i) the potential-fluctuation amplitude and scale controlled by the type and density of growth defects,

(ii) the correlation between elastic and electric fields induced by growth defects, and

(iii) a crystal electric state that varies as the nonequilibrium carrier concentration increases.

It is evident that the type and density of dominant growth defects have a significant effect on the counteraction of the elastic and electric subsystems in such a piezoelectric crystal to the extent of changing its state (according to a piezoelectric analogue of the Lenz law). Hence, features of the low-frequency dielectric response are closely related to internal fields, which in turn have a substantial impact on the transport, accumulation, and recombination of nonequilibrium charge carriers. In our opinion, features of the dielectric response reflect the growth conditions, adaptation to which just causes interrelation between superimposed fields of growth defects.

Therefore, a change in the ε" increment sign under illumination, observed in some crystals, is obviously explained by relating their dielectric response to two competing processes during photoexcitation. One process can smoothly transform into another as the internal-field screening by nonequilibrium carriers becomes more pronounced and the boundary conditions in the crystal are changed. Therefore, it may be expected that the dielectric response should also be similar as the temperature increases when the level of residual stresses lowers and the internal-field screening becomes more pronounced. Initially, the crystal dielectric losses grow nonlinearly on heating and, when a certain temperature specific to each sample is attained, ε" starts to decrease; i.e., the dependence ε"(*T*) has a maximum. We note that the steepest increase in ε' is observed in the vicinity of the peak. It is remarkable that the dependences ε'(*T*) and ε"(*T*) measured after heating the sample somewhat differ from those measured after cooling, which indicates that the dielectric response depends on the thermal history. The heating–cooling diagrams ε*(*T*) based on the dependences ε'(*T*) and ε"(*T*) for the most inhomogeneous samples exhibit arc-shaped portions with $(d\varepsilon''/d\varepsilon') < 0$ and > 0 (Fig. 2, curve *1*) which, by analogy with arc-shaped portions of diagrams ε*(λ), are indicative of the relaxation property of the dielectric response. We also note that the temperature increase for samples whose dielectric loss under illumination is lower than that in the dark for the entire photosensitivity range also decreases ε". This gives grounds to argue that the starting values of ε' and ε" measured at a dispersion-range frequency integrally reflect a crystal-growth thermoelastic history leading to the LPR.

Variations in the diagrams ε*(λ) obtained on heating the samples are regular (see Fig. 2, curves *2*–*6*). This

manifests itself in changes in the ε' and ε" increments under illumination, in the behavior of the latter increment, and in the curvature and length of arc-shaped segments. For example, at a sample temperature exceeding the value corresponding to the maximum of ε"(*T*), illumination reduces the dielectric loss factor in the entire photosensitivity range. As was shown above, such photodielectric response behavior was observed in some samples at room temperature. It is remarkable that, if starting dielectric parameters are increased by illumination, the diagram ε*(*T*) contains a portion of dielectric constant decrease, smoothly transforming into a portion of dielectric loss decrease (see curve *7*). These data confirm the dominant effect of elastic fields of growth defects on LPR formation. Therefore, distributions of elastic and electric fields in the crystal are similar. This is also confirmed by the fact that the effect of background illumination on the diagrams ε*(λ) is similar to the effect of sample heating. The background illumination augments the starting values of ε' and ε" and affects significantly the ε*(λ) portions near photosensitivity-range edges. Furthermore, as the illumination intensity increases, the value of ε" may become smaller than the starting one within the entire photosensitivity range.

The fact that the relaxation property of the photodielectric response of some CZT crystals can be substantially changed by additional background illumination or by temperature variation indicates that electric and elastic fields of some growth defects are self-consistently realigned. This affects the distribution of relaxation times, which manifests itself in changes in arc-shaped portions of the diagrams ε*(λ). It may be assumed that the dielectric loss decrease under illumination near the inherent maximum, observed in some crystals, is caused by the growth of individual barriers during the LPR rearrangement. These barriers hinder the through-current flows and simultaneously promote polarization. This is confirmed by studies on the photodielectric response of optically uniform samples with blocking contacts. The constructed diagram ε*(λ) is similar to curve *1* in Fig. 2.

Thus, individual features inherent in the dielectric response of some CZT crystals are closely related to a diversity of macroscopic growth defects and their elastic and electric fields. The interconsistent realignment of these fields caused by an external impact changes the dielectric response feature and affects the transport properties of these crystals.

REFERENCES

1. V. Komar, A. Gektin, D. Nalivaiko, *et al.*, in *Proceedings of the 11th International Workshop on Room Temperature Semiconductor X- and Gamma-ray Detectors and Associated Electronics, Vienna, 1999*, p. 8.
2. I. A. Klimenko, V. K. Komar, V. P. Migal, and D. P. Nalivaiko, Func. Mater. **7** (1), 1113 (2000).
3. V. P. Migal', A. L. Rvachev, and O. N. Chugaĭ, Fiz. Tekh. Poluprovodn. (Leningrad) **19** (8), 1517 (1985) [Sov. Phys. Semicond. **19**, 935 (1985)].
4. Yu. A. Zagoruĭko, V. K. Komar', V. P. Migal', and O. N. Chugaĭ, Fiz. Tekh. Poluprovodn. (St. Petersburg) **29** (6), 1065 (1995) [Semiconductors **29**, 552 (1995)].

Translated by A. Kazantsev

Semiconductors, Vol. 35, No. 4, 2001, pp. 394–397. Translated from Fizika i Tekhnika Poluprovodnikov, Vol. 35, No. 4, 2001, pp. 406–409.

ELECTRONIC AND OPTICAL PROPERTIES OF SEMICONDUCTORS

Semiempirical Model of Carrier Mobility in Silicon Carbide for Analyzing Its Dependence on Temperature and Doping Level

T. T. Mnatsakanov*, L. I. Pomortseva, and S. N. Yurkov

All-Russia Institute of Electrical Engineering, Moscow, 111250 Russia

** e-mail: mnatt@vei.ru*

Submitted August 21, 2000; accepted for publication September 7, 2000

Abstract—Experimental data on electron and hole mobility in three silicon carbide polytypes, 4*H*-SiC, 6*H*-SiC, and 3*C*-SiC, are analyzed. A semiempirical model is proposed for describing the dependence of the majority carrier mobility on temperature and doping level. The model describes well the accumulated body of experimental data and can be applied to model characteristics of multilayer silicon carbide structures. © *2001 MAIK "Nauka/Interperiodica".*

1. Silicon carbide (SiC) is one of the most promising materials for modern power electronics [1]. It has been used to create high-power rectifier diodes [2, 3], photo- [4] and Schottky diodes [5], and various types of thyristors [6, 7] and transistors [8, 9]. Further progress in the development and optimization of SiC devices is impossible without the numerical modeling of its structural characteristics [10, 11]. The experience of a wide application of numerical methods to calculate silicon structural characteristics indicates that the effectiveness of modeling is, to a significant extent, determined by the adequacy of the approximations used to describe the main electrical parameters of a material. For silicon, such approximations have been proposed and are well known [12]. However, for SiC we have the opposite situation, in particular, for such an important parameter of the material as carrier mobility. Experimental data on the dependence of mobility on temperature and doping level have been reported [13–22] for various SiC polytypes. However, no attempts have been made yet to analyze the accumulated data from a common standpoint. Therefore, the aim of this study was to derive relations and select parameters allowing a unified description of how the mobility depends on temperature and doping level in silicon carbide.

2. Experimental data characterizing the dependence of the mobility of majority carriers on the impurity concentration at $T = 300$ K are well described for practically all semiconductor materials studied by the known relation proposed in [23]

$$\mu_i = \mu_i^{\min} + \frac{\mu_i^{\max} - \mu_i^{\min}}{1 + \left(\frac{N}{N_{ig}}\right)^{\gamma_i}}, \quad (1)$$

where $i = n, p$; the parameters $\mu_i^{\max}$, $\mu_i^{\min}$, N_{ig}, and γ_i depend on the type of semiconductor material; and N is the dopant concentration.

Our analysis of the experimental data reported in [13, 14, 16, 20] showed that silicon carbide is no exception to this rule. It was found that in the three most frequently used silicon carbide polytypes 4*H*-SiC, 6*H*-SiC, and 3*C*-SiC, the parameters $\mu_i^{\max}$, $\mu_i^{\min}$, N_{ig}, and γ_i have the values listed in the table.

Figures 1 and 2 present experimental Hall mobilities of electrons and holes in 4*H*-SiC and 6*H*-SiC as a function of the doping level [16] and Hall mobilities calcu-

Table

Type of carriers	Polytype	$\mu_i^{\max}$, $cm^2 V^{-1} s^{-1}$	$\mu_i^{\min}$, $cm^2 V^{-1} s^{-1}$	N_{ig}, cm^{-3}	γ_i
Electrons	4*H*-SiC	880	30	2×10^{17}	0.67
	6*H*-SiC	400	25	10^{18}	0.8
	3*C*-SiC	800	25	3×10^{17}	0.87
Holes	4*H*-SiC	117	33	10^{19}	0.5
	6*H*-SiC	95	25	5×10^{18}	0.4

1063-7826/01/3504-0394$21.00

lated using formula (1) from data on the Hall factor [20] and the calculation parameters listed in the table.

The temperature dependence of mobility can be introduced into the model under consideration for the following reasons. At low doping level and sufficiently high temperature, scattering by phonons is the main mechanism of carrier scattering. In relation (1), we take

$$\mu_i^{\max} = \mu_{iL}. \tag{2}$$

Writing down the temperature dependence of mobility in the form

$$\mu_L(T) = \mu_L(T_0)\left(\frac{T}{T_0}\right)^{-\alpha},$$

we have from (2)

$$\mu_i^{\max}(T) = \mu_i^{\max}(T_0)\left(\frac{T}{T_0}\right)^{-\alpha_i}, \tag{3}$$

where $T_0 = 300$ K.

The contribution from carrier scattering by charged impurities can be obtained by subtracting from (1) the contribution associated with scattering by phonons, in accordance with Matthiessen's rule:

$$\mu_{iI} = \mu_i^{\max}\left[\frac{\mu_i^{\max}}{\mu_i^{\max} - \mu_i^{\min}}\frac{1 + \left(\frac{N}{N_{ig}}\right)^{\gamma_i}}{\left(\frac{N}{N_{ig}}\right)^{\gamma_i}} - 1\right]. \tag{4}$$

From (2) and (4), it readily follows that

$$\frac{\mu_i^{\max} - \mu_i^{\min}}{1 + \left(\frac{N}{N_{ig}}\right)^{\gamma_i}}\left(\frac{N}{N_{ig}}\right)^{\gamma_i} = \frac{\mu_{iL}}{1 + \frac{\mu_{iI}}{\mu_{iL}}}. \tag{5}$$

Substituting (5) into (1) and taking into account that [12]

$$\mu_L(T) = \mu_L(T_0)\left(\frac{T}{T_0}\right)^{-\alpha}$$

and

$$\mu_I(T) = \mu_I(T_0)\left(\frac{T}{T_0}\right)^{\beta},$$

we bring relation (1) to the form

$$\mu_i(N, T) = \mu_i^{\max}(T_0)\frac{B_i(N)\left(\frac{T}{T_0}\right)^{\beta_i}}{1 + B_i(N)\left(\frac{T}{T_0}\right)^{\alpha_i + \beta_i}}, \tag{6}$$

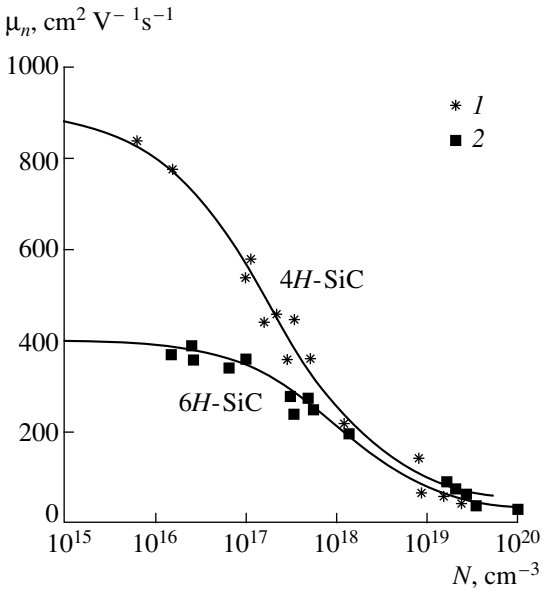

Fig. 1. Hall mobility of electrons vs. doping level at T = 300 K. (*1*) Experimental data for 4*H*-SiC from [16] and (*2*) the same for 6*H*-SiC; solid lines represent calculation by formula (1) with account of the data on the Hall factor from [20].

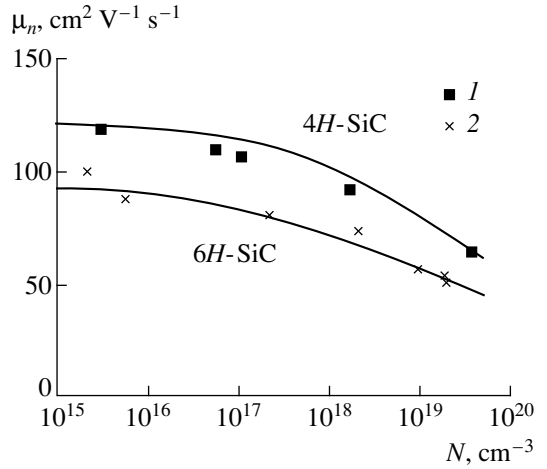

Fig. 2. Hall mobility of holes vs. doping level at T = 300 K. Experimental data (*1*, *2*) and solid lines are the same as in Fig. 1.

where

$$B_i(N) = \left[\left(\frac{\mu_i^{\max}}{\mu_i^{\max} - \mu_i^{\min}}\right)\frac{\left[1 + \left(\frac{N}{N_{ig}}\right)^{\gamma_i}\right]}{\left(\frac{N}{N_{ig}}\right)^{\gamma_i}} - 1\right]\Bigg|_{T = T_0} \tag{7}$$

and $T_0 = 300$ K.

3. Relations (6) and (7) correctly describe the temperature dependence of mobility in the limits of light

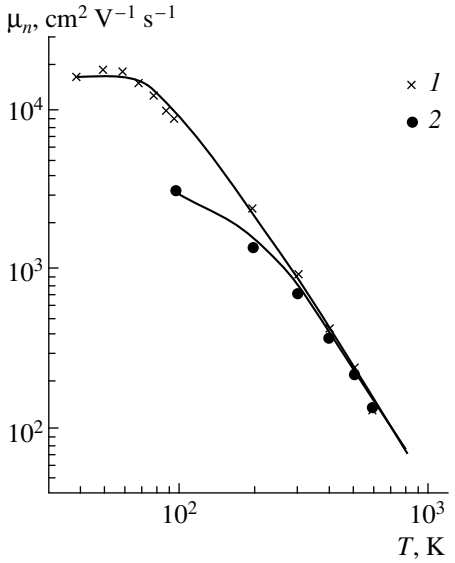

Fig. 3. Hall mobility of electrons vs. temperature. Donor concentration N_d: (*1*) 5×10^{14} and (*2*) 4×10^{16} cm^{-3}; solid lines—calculation by formulas (6) and (7) with account of the data on the Hall factor from [20].

and heavy doping in a qualitative sense. At a fixed doping level, relation (6) describes the experimentally observed nonmonotonic temperature dependence of mobility, with the dependence of the extremum point $T = T_m$ at which $d\mu/dT = 0$ on the doping level, and with other parameters represented as

$$T_{mi} = T_0\left[\frac{\beta_i}{\alpha_i}\frac{1}{B_i(N)}\right]^{\frac{1}{\alpha_i+\beta_i}}. \qquad (8)$$

Comparison of relations (6)–(8) with the available published data provides the opportunity to determine the effective values of the parameters appearing in these formulas. Figure 3 presents temperature dependences of the Hall mobility of electrons in the 4*H*-SiC samples [15, 16]. The slope of the experimental curves at high temperatures ($T \geq 500$ K) gives $a_n = 2.6$ for electrons. The value $T_{mn} \approx 50$ K for curve *1* in Fig. 1, corresponding to a donor concentration $N = N_d = 5 \times 10^{14}$ cm^{-3} according to a calculation by formula (1), gives $\beta_n \simeq 0.5$. The results obtained in calculating the dependence $\mu_n(T)$ in a wide temperature range for two doping levels by means of relations (1) and (6) are represented in Fig. 3 by solid lines.

Using the experimental data on the 6*H*-SiC polytype reported in [16–19, 22], we obtain the effective values of the parameters for 6*H*-SiC: $\alpha_n = 2.1$, $\beta_n = 0.7$, and $\alpha_p = 2.0$.

Processing data for the 3*C*-SiC polytype [13, 14], we get the values $\alpha_n = 2.5$, $\beta_n = 0.3$, and $\alpha_p = 2.2$ for 3*C*-SiC.

4. The values of the parameters α_i and β_i differ from those calculated theoretically in terms of the simple band structure of the semiconductor in [24]. However, the same pattern is observed in other semiconducting materials, e.g., in germanium ($\alpha_n = 1.66$, $\alpha_p = 2.33$), silicon ($\alpha_n = 2.42$, $\alpha_p = 2.2$), and gallium arsenide ($\alpha_n = 1.0$, $\alpha_p = 2.1$).

Among the reasons for this discrepancy can be named, first, a contribution from other scattering mechanisms which may vary widely between different materials and, second, the difference of the real band structure of the semiconductor from the simple band structure used in [24]. Revealing these reasons in any particular material requires additional, possibly prolonged, consideration. Under these conditions, the proposed relations (1) and (6)–(8) may be helpful in describing and modeling characteristics of multilayer structures based on silicon carbide.

ACKNOWLEDGMENTS

The authors are grateful to M.E. Levinshteĭn and P.A. Ivanov for their helpful participation in discussions and for critical comments.

This study was supported by the Russian Foundation for Basic Research.

REFERENCES

1. T. P. Chow, V. Khemka, J. Fedison, *et al.*, Solid-State Electron. **44**, 277 (2000).
2. Y. Sugawara, K. Asano, R. Singh, and J. W. Palmour, in *Abstracts of International Conference on SiC and Related Materials*, *ICSCRM 1999*, Pres. 170.
3. A. Flasser, M. Chezzo, N. Krishnamurthy, *et al.*, Solid-State Electron. **44**, 317 (2000).
4. F. Yang, J. H. Zhao, and G. N. Olsen, Solid-State Electron. **44**, 341 (2000).
5. K. J. Schoen, J. M. Woodall, J. A. Cooper, and M. R. Malloch, IEEE Trans. Electron Devices **45**, 1595 (1998).
6. N. V. Dyakonova, P. A. Ivanov, V. A. Koslov, *et al.*, IEEE Trans. Electron Devices **46**, 2188 (1999).
7. B. Li, L. Cao, and J. H. Zhao, IEEE Electron Device Lett. **20**, 219 (1999).
8. J. Spitz, M. R. Melloch, J. A. Cooper, and M. A. Capano, Mater. Sci. Forum **264–268**, 1005 (1999).
9. R. Schörner, P. Friedrichs, D. Peters, and D. Stephani, IEEE Electron Device Lett. **20**, 241 (1999).
10. J. Wang and B. W. Williams, Semicond. Sci. Technol. **13**, 806 (1998).
11. A. Elford and P. A. Mawby, Microelectron. J. **30**, 524 (1999).
12. S. Selberherr, *Analysis and Simulation of Semiconductor Devices* (Springer-Verlag, New York, 1984).
13. M. Yamanaka, H. Daimon, E. Sakuma, *et al.*, J. Appl. Phys. **61**, 599 (1987).
14. M. Shinohara, M. Yamanaka, H. Daimon, *et al.*, Jpn. J. Appl. Phys. **27**, L433 (1988).

15. W. J. Choyke and G. Pensl, Mater. Res. Bull., No. 25 (1997).
16. W. J. Schaffer, H. S. Kong, G. N. Nagley, and J. W. Palmour, Inst. Phys. Conf. Ser. **137**, 155 (1994).
17. R. Mickevicius and J. H. Zhao, J. Appl. Phys. **83**, 3161 (1998).
18. G. D. Chen, J. Y. Lin, and H. X. Jaing, Appl. Phys. Lett. **68**, 1341 (1996).
19. D. L. Barrett and R. B. Campbell, J. Appl. Phys. **38**, 53 (1967).
20. G. Rutsch, R. P. Devaty, W. J. Choyke, *et al.*, J. Appl. Phys. **84**, 2062 (1998).
21. T. Kinoshita, M. Schadt, K. M. Itoh, *et al.*, in *Abstracts of International Conference on SiC, III-Nitrides and Related Materials, Stockholm, 1997*, p. 631.
22. H. J. van Daal, W. F. Knippenberg, and J. D. Wasscher, J. Phys. Chem. Solids **24**, 109 (1963).
23. D. M. Caughey and R. E. Thomas, Proc. IEEE **55**, 2192 (1967).
24. V. L. Bonch-Bruevich and S. G. Kalashnikov, *Physics of Semiconductors* (Nauka, Moscow, 1977).

Translated by M. Tagirdzhanov

Semiconductors, Vol. 35, No. 4, 2001, pp. 398–404. Translated from Fizika i Tekhnika Poluprovodnikov, Vol. 35, No. 4, 2001, pp. 410–416.

ELECTRONIC AND OPTICAL PROPERTIES OF SEMICONDUCTORS

Dipole Moments of Ligands and Stark Splitting of Levels of Rare-Earth Ions

M. M. Chumachkova and A. B. Roĭtsin†

Institute of Semiconductor Physics, National Academy of Sciences of Ukraine, pr. Nauki 45, Kiev, 03028 Ukraine

Submitted July 18, 2000; accepted for publication September 11, 2000

Abstract—A model for describing polarization and relaxation of ligand ions around impurity defects in crystals is proposed and tested. This approach is based on the introduction of effective electric dipole moments, which are considered to be fundamental parameters of crystals and are determined from experimental data on the energy-level structure of an impurity ion. Calculations performed for rare-earth ions show that their energy spectra depend strongly on the effective electric dipole moments of host-crystal ions surrounding the impurity ions. Parameters of the theory are found. The results of the calculations are consistent with the available experimental data. The possibility of using the considered approach in studies of impurity defects in various crystals (semiconductors and insulators) is discussed. © *2001 MAIK "Nauka/Interperiodica".*

1. INTRODUCTION: FORMULATION OF THE PROBLEM

1.1. The calculation of energy-level structures of impurity ions in crystals and of the rates of transitions between ion levels is one of the major problems in the theoretical studies of defects [1], which is related to the strong influence of impurity ions on physical properties of materials and, consequently, their widespread practical use. Impurity ions are also of theoretical interest as model systems for describing complex many-electron structures of defects in solids. Among impurity ions, rare-earth (RE) ions stand out owing to their specific properties [2–4]. These ions are used mainly due to their optical properties (for example, see [5]). Of RE ions, ions with a small number of electrons (holes) in the *f* shell hold a particular position of importance. Although these ions are also many-electron systems with complex energy-level structures, they are easier to describe. Therefore, these ions can serve as model systems when studying the influence of the crystal environment on RE ions. Pr^{3+}, having two electrons in the *f* shell, is among such ions. In this study, we considered precisely the Pr^{3+} ion.

Various methods are used to calculate the energy-level structures of impurity ions [6, 7]: the linear combination of atomic orbitals (molecular orbitals); the crystal-field theory, the X–α method of scattered waves, various semiempirical techniques, and other approaches that are combinations or modifications of the above-listed methods. As yet, a good agreement between theory and experiment has seldom been achieved, because the problem is complex and laborious (due to the consideration of many-atom, many-electron, and many-level systems; the relaxation and polarization of atoms near a defect; and the presence of various compensators and complexes), and numerous approximations are used even in calculations from first principles. Therefore, simpler methods that require a minimum number of theoretical parameters and, at the same time, describe adequately major types of interactions in the structure of defects in crystals deserve attention. One such approach used in this study was proposed and tested by Klimov *et al.* [8, 9] and Chumachkova *et al.* [10]. In particular, they demonstrated the possibility of describing the energy-level structure of an impurity ion with a certain electronic configuration within a rather simple wave-function approximation.

1.2. When a foreign atom is incorporated into a crystal, a local distortion (relaxation) of the lattice takes place, which results in lattice expansion (compression) near the defect as well as in the polarization of ligands surrounding the impurity ion, which gives rise to electric dipole moments on the ligands. To describe adequately local physical properties, one should take into account these effects. In connection with this, a number of publications were devoted to studying this problem and, in particular, to determining new equilibrium positions as well as the character and degree of polarization of ions around a defect by minimizing the crystal bonding energy. Mixed alkali-halide crystals [11], alkaline-earth oxides [12] and halides [13–16], and semiconductors [17, 18] were considered; various impurity ions, including RE ions, were examined. At the same time, a number of authors (e.g., [13]) point to a discrepancy between estimates of ion displacements obtained by different researchers for the same materials. Moreover,

† Deceased.

there is a disagreement not only between quantitative results but also between qualitative data (on the direction of the displacement of ligands surrounding an impurity ion). All these factors underline the complexity of the problem.

1.3. In this context, as an alternative to direct calculations, it seems profitable to consider an inverse problem of some kind, i.e., to study the dependence of the energy-level structure of an impurity ion on the preset mutual arrangement of lattice ions and the character and degree of their polarization and then to find parameters corresponding to these effects from a comparison between theoretical and experimental data. These parameters should be considered as fundamental characteristics of a given crystal. It is important to set the aforementioned parameters and determine energy terms dependent on these parameters in the framework of the same concept. In this study, we attempted such a consideration. We found that, within a certain approximation, the terms related to displacements and polarizations of ions can be combined by introducing an effective electric dipole moment as a parameter. This allowed us to halve the number of parameters of the theory.

2. SUBJECTS OF INVESTIGATION

2.1. Pr^{3+} was chosen as an impurity ion, a kind of probe, for two reasons. First, as noted above, this ion is of methodical interest. Second, recent intensive studies of this ion have revealed its dramatic influence on the physical properties of crystals. This offers considerable possibilities for its practical use. Let us consider some of them. Crystals containing a high concentration of Pr^{3+} can be used as media with high gain and, therefore, are feasible for the fabrication of miniature surface lasers and microlasers. Doping phosphors with Pr^{3+} favors the accumulation of a light sum and the buildup or decay of luminescence induced by other activators. Incorporation of Pr^{3+} promotes the formation of an active medium for multifrequency lasers operating in the visible region of the spectrum. Recently, new possibilities of using Pr^{3+} for light generation have been found; in particular, a high-power praseodymium laser was devised [19]. Crystals activated with Pr can be used as phosphors, ultraviolet-to-visible converters, and high-power sources of modulated radiation. An amplifier with a high output power was designed based on Pr-activated fluoride fiber.

Nonoptical properties of Pr^{3+} that differ substantially from those of other RE ions are also of considerable interest. First of all, it should be noted that Pr^{3+} ions suppress superconductivity in high-temperature superconductors and have a dramatic effect on the critical temperature T_c: T_c decreases as the Pr^{3+} concentration increases. Pr^{3+} ions exhibit anomalous magnetic and other properties. There is a correlation between their anomalous properties and features of the suppression of superconductivity. Pr^{3+} ions show unusual transport properties, which are responsible for the metal–insulator transition and the dimensional effect characteristic of Pr^{3+}. Extensive studies of the properties of this promising ion are still in progress [4, 20].

2.2. RE ions are usually in a low-symmetry coordination, which is related to the low symmetry of numerous crystals as well as to the presence of compensators near the impurity ions. However, 3-coordinated ions (so-called centers with nonlocal charge compensation [15, 16, 21–23]) are not uncommon. In this case, a simpler system of energy levels arises, which facilitates the study of the effects of various factors responsible for the character and magnitude of splitting of free-ion terms. Therefore, in this study, we consider a cubic crystal containing 3-coordinated Pr^{3+} ions and perform calculations for alkaline-earth halides containing impurity ions substituting the metal ions. The choice of this group of crystals, fluorides, in particular, for primary consideration is also governed by the fact that they are often used as model objects in studies of impurity ions in semiconductors and insulators [22] and are widely used in laser technology [5]. These crystals are also of theoretical interest, since they are compounds with a high ionicity [24] to which the crystal-field theory and the point-charge model are best applicable [7, 25, 26].

3. STARTING EXPRESSIONS

3.1. According to the group theory, 13 terms of a free Pr^{3+} ion are generally split into 40 levels, E_i, by a cubic-symmetry crystal field. The E_i levels were calculated in the context of the crystal-field theory [7, 27]. An operator of the energy of the interaction between an ion and the crystal electric field, V, was chosen as a perturbation operator, and corrections to the atomic energy levels, ΔE_i, were determined in the framework of the first-order perturbation theory. By using the theory of symmetry [28], these corrections were expressed in terms of the minimum number of matrix elements of the potential V based on many-electron atomic functions. In turn, these matrix elements were expressed in terms of three diagonal matrix elements $V_{m,m}$ of the potential V based on one-electron functions (m is the quantum number of the orbital moment). Finally, the matrix elements $V_{m,m}$ specified in a unified system of coordinates were expressed as linear combinations of matrix elements of the potential of an isolated ligand, V^k, specified in the frame of reference in which the origin of the coordinates coincided with the center of the impurity ion and the z axis was directed toward the kth ligand [29]. The resulting expressions for all corrections ΔE_i were represented as linear combinations of the matrix elements $V^k_{m,m'}$ of the potential V^k. Coefficients entering into these combinations are numbers and angles defining the direction toward the kth ion. For a given coordination shell, the matrix elements $V^k_{m,m'}$

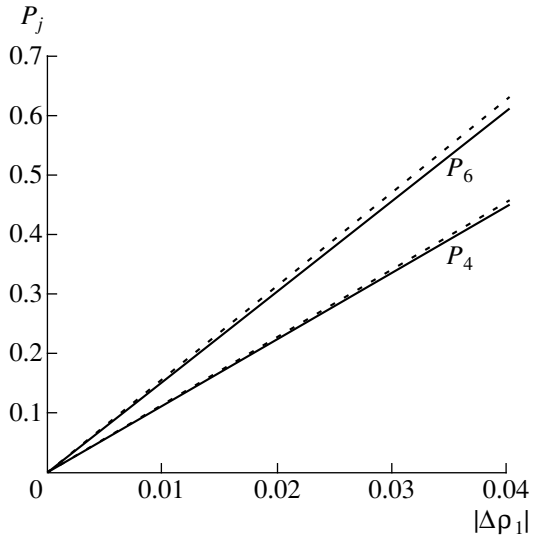

Fig. 1. P_j versus $|\Delta\rho_1|$ for the most important values of α: 2.4 (solid curves) and 2.6 (dotted curves).

are the same and depend solely on the distance to the kth ion, R_k. The expressions obtained are general in form and are independent of the form of the potentials V and V^k.

3.2. In calculations, a radial function of the form [10]

$$R_{4f} = \frac{2}{3\sqrt{35}}\alpha^{9/2}r^3\exp(-\alpha r), \qquad (1)$$

was chosen as a starting one-electron wave function (α is the parameter of the Slater orbital), and the point-charge (dipole) approximation was used for the potential V. In this case, the matrix elements $V_{m,m'}$ are computed in an analytical form, so that all corrections ΔE_i are expressed explicitly in terms of parameters γ, q_k, α, and R_k, where γ is the parameter characterizing ionicity ($\gamma = 1$ for purely ionic crystals), and q_k is the charge (or charges, depending on the model) on the kth ligand (in units of the electron charge $|e|$). Upon performing the calculation, we obtain the following equation for ΔE_i (in atomic units, au):

$$\Delta E_i = \gamma\alpha\sum_k q_k\left[-2F_0(x_k) + \frac{t_i}{44}f_4^kF_4(x_k) + \frac{25}{1716}l_if_6^kF_6(x_k)\right]. \qquad (2)$$

Here,

$$x_k = \alpha R_k;\quad f_4^k = 35n_k^4 - 30n_k^2 + 3;$$
$$f_6^k = 231n_k^6 - 315n_k^4 + 105n_k^2 - 5;$$

$n_k = \cos\vartheta_k$, where ϑ_k is the polar angle defining the direction from the impurity ion (origin of coordinates) toward the kth ligand ion; and $F_n(x)$ are the direct and inverse polynomials in x in combination with $\exp(-2x)$ [8]. The coefficients t_i and l_i are constants characterizing a given level. For example, the fundamental term of free ion ($^3H_4$) is a cubic crystal field split into four levels: E, T_1, A_1, and T_2 (commonly accepted designations of irreducible representations). In this case, for the value $33t_i/2$, we obtain –2, –7, –14, and 13, respectively. Similarly, for $825l_i/68$, we obtain 16, 1, –20, and –5, respectively. The summation over the lattice (over the vector k) generally implies a summation over the ligands as well as over charges on a ligand.

4. EFFECTIVE ELECTRIC DIPOLE MOMENT

4.1. The local distortion of the lattice was taken into account by varying R_k near its equilibrium value, R_k^0, corresponding to the perfect lattice. Setting $R_k = h\rho_k$, where h is the lattice constant (10.32 au for CaF_2 [30]), we obtain

$$x_k = u\rho_k,\quad \rho_k = \rho_k^0 + \Delta\rho_k,\quad u = h\alpha.$$

Since the lattice near impurity ions may be compressed or expanded, the parameter $\Delta\rho_k$ is varied from –0.03 to +0.03 for all coordination shells. This range encompasses all fixed ion displacements calculated previously but is considerably less than the interionic distance in the undistorted lattice.

For small values of $\Delta\rho_k$, the functions of $\Delta\rho_k$ can be expanded in terms of this small parameter. Correct to a term linear in $\Delta\rho_k$, we can write

$$F_j(u\rho_k) = F_j(u\rho_k^0) + F_j'(u\rho_k^0)\Delta\rho_k. \qquad (3)$$

Expressions for F_j' are given in the appendix. The possibility of using expression (3) depends on the contribution of the second term at various values of $\Delta\rho_k$. Figure 1 shows the ratio $P_j = uF_j'\Delta\rho_1/F_j$ plotted as a function of $|\Delta\rho_1|$ for $j = 4$ and 6. The dependence for $j = 0$ is of little interest, since the corresponding term in Eq. (2) leads only to equal shifts of all levels. For more distant coordination shells ($k > 1$), the validity of expression (3) will be even stronger, because the quantity P_j decreases as ρ_k^0 increases. We can set, to a high accuracy, $P_j = \tau_j\Delta\rho_k/\rho_k^0$, where $\tau_4 = 5$, and $\tau_6 = 7$, so that P_j is halved even for $k = 3$ as an example. The validity of expression (3) can also be demonstrated by substituting this expression into formula (2) and comparing the obtained approximate results with the exact ones (without expansion in terms of $\Delta\rho_k$). Appropriate calculations of the energies E, T_1, A_1, and T_2 for the most important values of α (from 2.4 to 2.8) show that the greatest devia-

tion from the exact data is 14% for $\Delta\rho = +0.03$ and 8% for $\Delta\rho = -0.03$.[1] The greatest and smallest departures were obtained for the highest level (E) and the level A_1 (about 4%), respectively. To obtain these results, we performed the summation over k in formula (2) in two ways: immediately over coordination shells and (as verification) over cubes by the fractional-charge method [32], with 14 positive and 8 negative charges contained in each cube.

4.2. The polarization of the kth ligand was taken into account by introducing a dipole [7, 29] aligned along the (impurity ion)–ligand line. The center of the dipole was taken to be at a distance $h\rho_k$ from the impurity ion, i.e., at the position of the ligand displaced owing to relaxation. Then, based on expression (2) and an expansion of a formula of type (3), we can write

$$S_k\{F_j[u(\rho_k^0 + \Delta\rho_k + \delta_k/2)] - F_j[u(\rho_k^0 + \Delta\rho_k - \delta_k/2)]\} \approx uS_k\delta_k F_j'(u\rho_k^0), \quad (4)$$

where $h\delta_k$ is the distance between induced point charges of the dipole ($\pm S_k$). When obtaining Eq. (4), we neglected terms on the order of $\delta_k\Delta\rho_k$ and of higher orders of smallness. Combining formula (3) and Eq. (4), we obtain $\Delta E_i = \Delta E_{i0} + \Delta E_{i1}$, where ΔE_{i0} is given by expression (2) at equilibrium positions of ligands x_k^0 and their charges without regard for polarization, and

$$\Delta E_{i1} = \gamma\alpha u\sum_k d_k\left[-2F_0'(x_k^0) + \frac{t_i}{44}f_4^k F_4'(x_k^0) + \frac{25}{1716}l_i f_6^k F_6'(x_k^0)\right],$$

where

$$d_k = q_k\Delta\rho_k + S_k\delta_k. \quad (5)$$

Expression (5) defines the effective electric dipole moment of the kth ligand (in atomic units). The effective electric dipole moment is the sum of the moments of two dipoles: the dipole arising from polarization ($S_k\delta_k$) and the dipole resulting from the displacement of an ion from its equilibrium position ($q_k\Delta\rho_k$). To describe electrical effects related to paramagnetic resonance, Roĭtsin [33] developed a relation for the effective electric dipole moment, which is similar to expression (5). A similar expression was derived by Ivanenko and Malkin [16], who calculated local distortion and polarization of the crystal lattice around impurities. From the expression for ΔE_{i1}, we can see that the effects of polarization and deformation of a ligand in the kth shell are controlled by a common parameter d_k. Therefore, we can study the energy-level structure of impurity ions depending on the parameter d_k and determine this parameter experimentally.

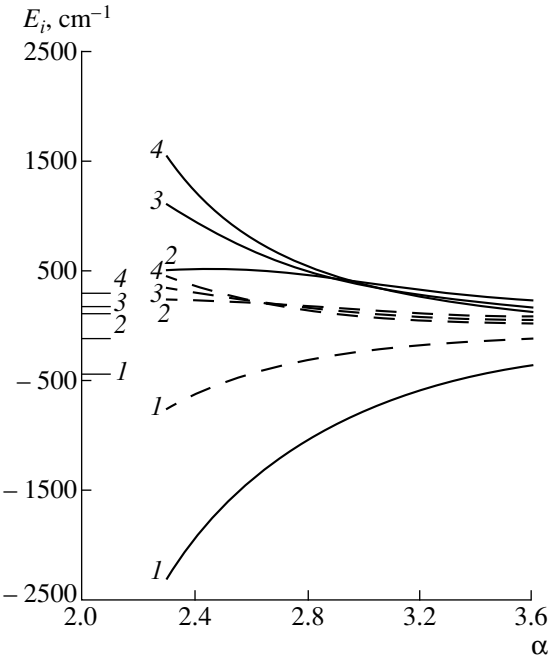

Fig. 2. Dependences of the energy levels (*1*) T_2, (*2*) A_1, (*3*) T_1, and (*4*) E on the parameter α calculated for $d_1 = 0.04$ (solid curves) and –0.04 (dashed curves) and $\gamma = 1$ ($d_k = 0$, if $k \neq 1$). In this and other figures, experimental values are shown on the vertical axis by straight-line segments.

5. CALCULATION OF ENERGY-LEVEL STRUCTURE

5.1. Klimov *et al.* [8] calculated impurity-ion terms with the use of only ΔE_{i0}. They demonstrated that satisfactory agreement between theory and experiment cannot be obtained for any of the values of α. However, we will demonstrate in what follows that the theory is consistent with the experiment if ΔE_{i1} is taken into account. To be brief, we present here calculated dependences of the energy-level structure on various parameters, including the effective electric dipole moment, only for the fundamental term $^3H_4$ of the ion in the crystal (i.e., for the levels E, T_1, A_1, and T_2).

Figure 2 shows dependences of the energy levels on the parameter α calculated for several limiting values of d_1. These values were preset tentatively on the basis of Fig. 1, the first term of expression (5), and the fact that the ligand charge is $|q_k| \leq 2$. The values of E_i corresponding to other values of d_1 fall between the limiting curves. In particular, $E_i(\alpha)$ curves calculated for $d_1 = 0$ run approximately midway between the curves calculated for $d_1 = 0.04$ and –0.04. One can see from Fig. 2 that, for small values of α for which the $E_i(\alpha)$ curves for

[1] The exact data were obtained previously [31] and were confirmed in this study.

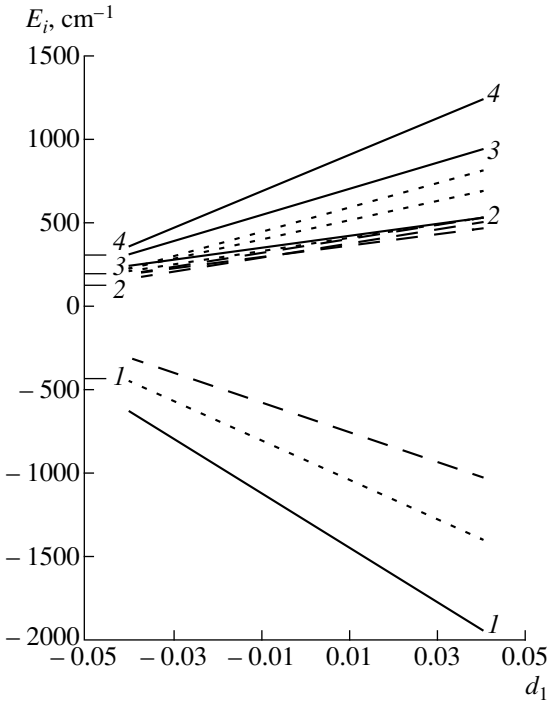

Fig. 3. Dependences of the energy levels on the parameter d_1 calculated at $\gamma = 1$ and $\alpha = 2.4$ (solid curves), 2.6 (dotted curves), and 2.8 (dashed curves); $d_k = 0$, if $k \neq 1$. Designations of the curves are the same as in Fig. 2.

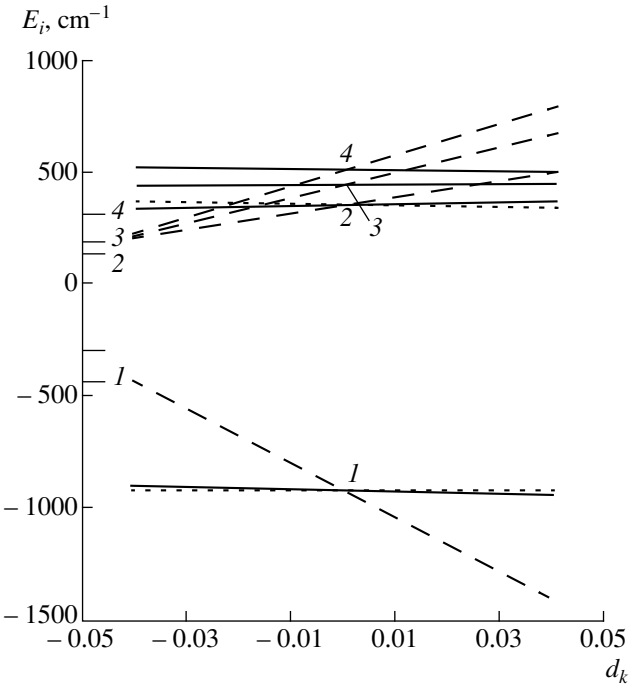

Fig. 4. Dependences of the energy levels on the parameter d_k calculated at $\gamma = 1$, $\alpha = 2.6$, and $k = 2$ (solid curves), 3 (dotted curves), and 1 (dashed curves); $d_j = 0$, if $j \neq k$. Designations of the curves are the same as in Fig. 2.

the levels E, T_1, and A_1 do not intersect and the relative positions of these levels are consistent with the experimental data [15, 34], an agreement between theory and experiment cannot be obtained for any values of α if $d_k = 0$. Although, in this case, the distances between the terms E, T_1, and A_1 are close to the experimental values in the range of α from 2.4 to 2.8, the distance from this group of terms to the term T_2 is about twice as large as the experimental value. However, the agreement between the theory and experiment is improved if $d_1 < 0$.

Figure 3 shows dependences of the energy levels on the effective electric dipole moment, and Fig. 4 illustrates the contribution of other coordination shells. It follows from Figs. 3 and 4 that the first coordination sphere makes a major contribution; for $k = 2$, 3, or 4, the levels virtually merge together. Relaxation and polarization of atoms also affect the intersection point of the curves, α_c. Figure 5 illustrates this effect with regard to the contribution of each coordination shell. All the above results of calculations were obtained for $\gamma = 1$, i.e., for purely ionic compounds. However, even for fluorides that are crystals with the highest ionicity, the effective charge of fluorine is only 0.8 [24]. With allowance made for this fact, the agreement between the theory and experiment was further improved (see Fig. 6).

As the analyses showed, the energy-level structure is controlled mainly by displacements and polarizations of ions in the first coordination sphere. Taking this into account, we obtained optimal values of the parameters d_1 and α which ensure the best fit to the experimental data for $\gamma = 0.8$. These values were found to be $(d_1)_{op} = -(0.018 \pm 0.002)$ and $\alpha_{op} = 2.60 \pm 0.02$. They can be regarded as fundamental parameters of the given extrinsic crystal. The theoretical predictions were compared with the experimental data for all three distances from the terms E, T_1, and A_1 to the term T_2. It should be emphasized that the choice of d_1 depends on the value of the parameter α: the greater α is, the smaller d_1 is.

6. DISCUSSION AND CONCLUSIONS

6.1. As follows from the above consideration, in order to describe adequately the experimental data, the impurity-ion theory should account for polarization and relaxation of the ligand ions surrounding an impurity ion. The effective electric dipole moment accounting for both effects can be considered as a unified parameter of the theory. This parameter is determined experimentally and serves as a fundamental characteristic of a given extrinsic crystal. In this regard, the present investigation can be considered as a generalization of our previous study [31], in which we considered only the role played by the relaxation of nearest neighbors of an impurity ion.

6.2. The experimental value $\alpha_{op} = 2.6$ was found to be smaller than the value $\alpha = 4.83$ obtained by approx-

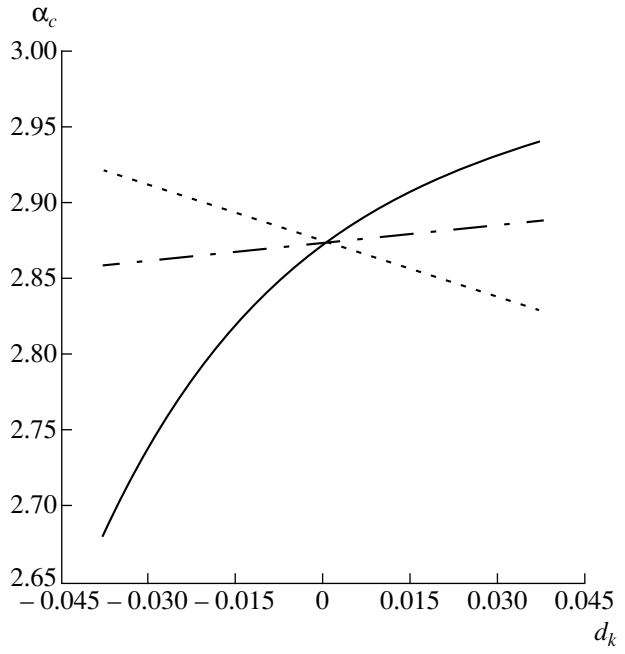

Fig. 5. Dependences of the parameter α_c on d_k calculated at $\gamma = 1$ and $k = 1$ (solid curve), 2 (dotted curve), and 3 (dot-and-dash curve); $d_j = 0$, if $j \neq k$.

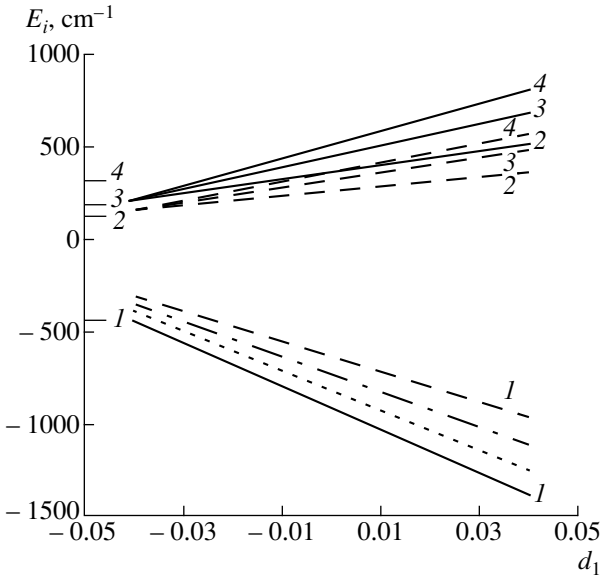

Fig. 6. Dependences of the energy levels on the parameter d_1 calculated at $\gamma = 1$ (solid curves), 0.9 (dotted curves), 0.8 (dot-and-dash curves), and 0.7 (dashed curves); $d_k = 0$, if $k \neq 1$. For the levels *2*, *3*, and *4*, only dependences calculated at $\gamma = 1$ and 0.7 and $\alpha = 2.6$ are shown, since these levels are closely spaced. Designations of the curves are the same as in Fig. 2.

imating the exact starting wave function of a free Pr^{3+} ion [35, 36] with expression (1) [10]. This discrepancy, the so-called nephelauxetic shift [1, 2, 7], is attributed to the influence of ligands on impurity ions. Therefore, the considered approach allows us to estimate the nephelauxetic shift based on the data on the other fundamental parameter of an extrinsic crystal, α_{op}.

6.3. The results of the calculations indicate that, for the class of crystals under consideration, the first coordination sphere makes the largest contribution to the energy-level structure of impurity ions. It should be noted that, in any case, the small distance from an impurity ion to its nearest neighbors is not a sufficient condition for the first coordination sphere to play a crucial role in the formation of the energy-level structure of the impurity ion. In some cases, the second coordination shell determines even the relative positions of the terms, as in some semiconductors (for example, see [29]).

6.4. From the results obtained, we also may conclude that the considered approach can be extended to other impurity ions and halides as well as to extrinsic alkaline-earth oxides with RE impurities. This approach may be advantageous for describing the properties of deep-level centers in semiconductors [6, 26], since, in many cases, including a series of covalent crystals, the crystal-field theory can be applied (e.g., in a dipole-ligand model or a model taking into account a spatial distribution of electron clouds at ligands). In semiconductors, RE ions can act as impurity ions.[2] Taking into account the relative simplicity of the method, we believe that it will find a wide application in the interpretation of experimental data for extrinsic semiconductors and insulators, in particular, in studies of their optical properties.

APPENDIX

Derivatives $F_i' = dF_i/dx$ are given by

$$F_0'(x) = -\frac{1}{x^2} + \frac{2x^6}{315}e^{-2x}f(x),$$

$$F_4'(x) = -\frac{7425}{2x^6} + \frac{2}{35}e^{-2x}[g(x) + 19x^4 + 92x^3 + 825x^2 f(x)/2],$$

$$F_6'(x) = 143\left\{-\frac{6615}{4x^8} + \frac{2}{15}e^{-2x}\left[\frac{g(x)}{231} + \frac{7x^4}{66} + \frac{7x^3}{11} + \frac{7}{2}x^2 + \frac{35}{2}x + \frac{315}{4}f(x)\right]\right\},$$

[2] For example, see [37] and other papers in the same issue of the journal that contains the Proceedings of the Workshop on Rare-Earth Impurities in Semiconductors and Low-Dimensional Semiconductor Structures.

$$f(x) = 1 + \frac{4}{x} + \frac{14}{x^2} + \frac{42}{x^3} + \frac{105}{x^5} + \frac{315}{x^6} + \frac{315}{x^7} + \frac{315}{2x^8},$$

$$g(x) = x^5(x+4).$$

REFERENCES

1. N. A. Kulagin and D. T. Sviridov, *Methods for Computing the Electron Structures of Free and Impurity Ions* (Nauka, Moscow, 1986).
2. E. F. Kustov, G. A. Bondurkin, É. N. Murav'ev, and V. P. Orlovskiĭ, *Electron Spectra of Rare-Earth Element Compounds* (Nauka, Moscow, 1981).
3. B. Z. Malkin, *Spectroscopy of Solids Containing Rare Earth Ions*, Ed. by A. A. Kaplyanskii and R. M. Macfarlane (Elsevier, Amsterdam, 1987), B.V., No. 4, p. 15.
4. A. A. Kornienko, Author's Abstract of Doctoral Dissertation (Inst. Molek. Atom. Fiz. Akad. Nauk Belarusi, Minsk, 1997).
5. A. A. Kaminskiĭ and B. M. Antipenko, *Multilevel Functional Diagram of Crystalline Lasers* (Nauka, Moscow, 1989).
6. A. B. Roĭtsin, Fiz. Tekh. Poluprovodn. (Leningrad) **8**, 3 (1974) [Sov. Phys. Semicond. **8**, 1 (1974)].
7. I. V. Bersuker, *Electron Structure and Properties of Coordination Compounds* (Khimiya, Leningrad, 1986).
8. A. A. Klimov, A. B. Roĭtsin, M. M. Chumachkova, and L. V. Artamonov, Ukr. Fiz. Zh. **38**, 4583 (1993).
9. A. A. Klimov, A. B. Roĭtsin, M. M. Chumachkova, and L. V. Artamonov, Fiz. Tverd. Tela (St. Petersburg) **37**, 225 (1995) [Phys. Solid State **37**, 120 (1995)].
10. M. M. Chumachkova, A. O. Klimov, O. B. Roĭtsin, and L. V. Artamonov, Ukr. Fiz. Zh. **40**, 866 (1995).
11. B. G. Dick and T. P. Das, Phys. Rev. **127**, 1053 (1962).
12. T. P. Das, Phys. Rev. A **140**, 1957 (1965).
13. C. Fainstein, M. Tovar, and C. Ramos, Phys. Rev. B **25**, 3039 (1982).
14. M. Tovar, C. Ramos, and C. Fainstein, Phys. Rev. B **28**, 4813 (1983).
15. M. P. Davydova and A. L. Stolov, Fiz. Tverd. Tela (Leningrad) **17**, 329 (1975) [Sov. Phys. Solid State **17**, 203 (1975)].
16. Z. I. Ivanenko and B. Z. Malkin, Fiz. Tverd. Tela (Leningrad) **11**, 1859 (1969) [Sov. Phys. Solid State **11**, 1498 (1969)].
17. M. Schefler, J. P. Vigneron, and G. B. Bachelet, Phys. Rev. B **31**, 6541 (1985).
18. F. Bechstedt and W. A. Harrison, Phys. Rev. B **39**, 5041 (1989).
19. A. A. Kaminskiĭ, N. I. Zhavoronkov, and V. P. Mikhaĭlov, Dokl. Akad. Nauk **329**, 578 (1993) [Phys. Dokl. **38**, 156 (1993)].
20. S. G. Nedél'ko, M. Diab, L. M. Limarenko, *et al.*, Ukr. Fiz. Zh. **42**, 415 (1997).
21. I. B. Aĭzenberg, B. Z. Malkin, and A. L. Stolov, Fiz. Tverd. Tela (Leningrad) **13**, 2566 (1971) [Sov. Phys. Solid State **13**, 2155 (1972)].
22. A. A. Kaplyanskiĭ and A. I. Ryskin, in *Spectroscopy of Crystals*, Ed. by A. A. Kaplyanskiĭ (Nauka, Leningrad, 1983), p. 5.
23. C. D. Cleven, S. H. Lee, and J. C. Wright, Phys. Rev. B **44**, 23 (1991).
24. K. Lesniak, Acta Phys. Pol. A **75**, 169 (1989).
25. W. F. Krupke, Phys. Rev. **145**, 325 (1966).
26. R. Boyn, Phys. Status Solidi B **148**, 11 (1988).
27. N. V. Eremin, in *Spectroscopy of Crystals*, Ed. by A. A. Kaplyanskiĭ (Nauka, Leningrad, 1989), p. 30.
28. A. B. Roĭtsin, *Some Applications of Symmetry Theory in Radiospectroscopy* (Naukova Dumka, Kiev, 1973).
29. A. B. Roĭtsin and L. A. Firshteĭn, Teor. Éksp. Khim. **2**, 747 (1966).
30. *Basic Properties of Inorganic Fluorides. Handbook*, Ed. by N. P. Galkin (Atomizdat, Moscow, 1976).
31. M. M. Chumachkova and A. B. Roĭtsin, Fiz. Tverd. Tela (St. Petersburg) **41**, 1194 (1999) [Phys. Solid State **41**, 1088 (1999)].
32. C. Kittel, *Introduction to Solid State Physics* (Wiley, New York, 1976; Nauka, Moscow, 1978).
33. A. B. Roĭtsin, Ukr. Fiz. Zh. **13**, 609 (1968).
34. B. M. Tissue and J. C. Wright, Phys. Rev. B **36**, 9781 (1987).
35. K. N. R. Taylor and M. Darby, *Physics of Rare-Earth Solids* (Chapman and Hall, London, 1972; Mir, Moscow, 1974).
36. N. V. Starostin and G. A. Sizova, in *Spectroscopy of Crystals*, Ed. by A. A. Kaplyanskiĭ (Nauka, Moscow, 1985), p. 70.
37. B. P. Zakharchenya, Fiz. Tekh. Poluprovodn. (St. Petersburg) **33**, 641 (1999) [Semiconductors **33**, 595 (1999)].

Translated by N. Izyumskaya

Semiconductors, Vol. 35, No. 4, 2001, pp. 405–408. Translated from Fizika i Tekhnika Poluprovodnikov, Vol. 35, No. 4, 2001, pp. 417–420.

ELECTRONIC AND OPTICAL PROPERTIES OF SEMICONDUCTORS

Mechanisms of Incorporation of an Antimony Impurity into Cadmium Telluride Crystals

E. S. Nikonyuk*, Z. I. Zakharuk, V. L. Shlyakhovyĭ*, P. M. Fochuk**, and A. I. Rarenko****

** Rivne State Technical University, Rivne, 33028 Ukraine*

*** Chernovtsy State University, Chernovtsy, 58012 Ukraine*

e-mail: microel@chdu.cv.ua

Submitted July 31, 2000; accepted for publication September 14, 2000

Abstract—The results of electrical studies of CdTe crystals grown by the Bridgman–Stockbarger method and doped with Sb impurity to concentrations of 10^{17}–3×10^{19} cm^{-3} were considered. An analysis of the temperature dependences of the Hall coefficient, the charge-carrier mobility, and photoconductivity under the intrinsic-absorption excitation for various portions of the ingots made it possible to conclude that Sb_{Te} and Sb_{Cd} centers and $Sb_{Te}Sb_{Cd}$ associations are introduced upon doping CdTe crystals with Sb impurity. The hole conduction in the doped crystals is controlled by A_3 (Sb_{Te}) acceptors whose concentration is no higher than 5×10^{16} cm^{-3} and is much lower than the actual Sb concentration. The ionization energy of the A_3 acceptors is 0.28 ± 0.01 eV. Under nonequilibrium conditions, these acceptors act as attachment centers for holes (at high temperatures) and as slow-rate recombination centers for electrons (at low temperatures). © *2001 MAIK "Nauka/Interperiodica".*

Cadmium telluride semiconductor crystals have useful optical and electrical parameters which can be intentionally varied in a wide range by doping with appropriate impurities; because of this, these crystals are used in a number of electronic devices.

As a rule, the impurities of the Group V elements (P and As) are shallow-level acceptors in CdTe crystals [1] and thus ensure the comparatively high electrical conductivity of this material. At the same time, it is known that doping of CdTe crystals with Sb impurity makes it possible to obtain a semi-insulating material [2] in which conductivity is controlled by deep-level acceptors with the levels distributed in energy. However, the latter refers only to samples with a high concentration of Sb in the solid phase (at a level of $C_{Sb} \approx 10^{19}$ cm^{-3}); at the same time, the properties of CdTe with a lower Sb concentration are unexplored. In this paper, we consider the results of measuring the electrical characteristics of CdTe:Sb crystals grown by the Bridgman–Stockbarger method and doped by introducing a Sb impurity (with concentrations of $C_0 = 10^{17}$–3×10^{19} cm^{-3}) into the melt. The actual Sb concentration C_{Sb} was assessed from the known values of the segregation factor, which is equal to $k = 4 \times 10^{-2}$ for $C_0 \le 10^{18}$ cm^{-3} and decreases with increasing C_0 for $C_0 > 10^{18}$ cm^{-3} [3].

As a rule, undoped CdTe crystals grown under similar conditions had *p*-type conductivity controlled by shallow-level A_1 acceptors with a level at E_v + (0.025–0.050) eV and by deep-level A_2 acceptors with a level at E_v + (0.11–0.15) eV. Light doping with Sb ($C_0 = 10^{17}$ cm^{-3}) did not result in a significant variation in the parameters of the crystals. However, the effect of doping became pronounced beginning with an antimony concentration of $C_0 = 5 \times 10^{17}$ cm^{-3}. Thus, the temperature dependence of the Hall coefficient R_H in the samples with various concentrations of Sb impurity (Fig. 1) indicates that *p*-type conductivity is controlled by acceptors with deeper levels, $E_v + (0.28 \pm 0.01)$ eV, irrespective of C_{Sb} in a wide antimony-concentration range of 2×10^{16}–5×10^{18} cm^{-3}. It is only in some of the samples, which were not represented in Fig. 1, that the above acceptors were completely compensated and the deeper levels at E_v + (0.40–0.45) eV manifested themselves.

In the samples studied, the lowest actual concentration of Sb was $C_{Sb} = 2 \times 10^{16}$ cm^{-3} and the highest was $C_{Sb} = 10^{19}$ cm^{-3}. It is impossible to establish a correlation between C_0 and C_{Sb}, on the one hand, and the hole concentration, on the other hand, taking into consideration the data shown in Fig. 1, the more so as a markedly nonuniform distribution of the charge-carrier concentration along the ingot axis is observed.

Rapid thermal treatment [4] at 700°C not only did not induce the conductivity-type conversion but, on the contrary, shifted the equilibrium Fermi level to the valence-band top (Fig. 1, curve *8*). The same effect resulted from prolonged annealing at 400°C (Fig. 1, curve *7*). In both cases, the conductivity was invariably controlled by acceptors with a level at E_v + 0.28 eV. Furthermore, these acceptors manifest themselves even in lightly doped samples ($C_{Sb} = 2 \times 10^{16}$ cm^{-3}) after

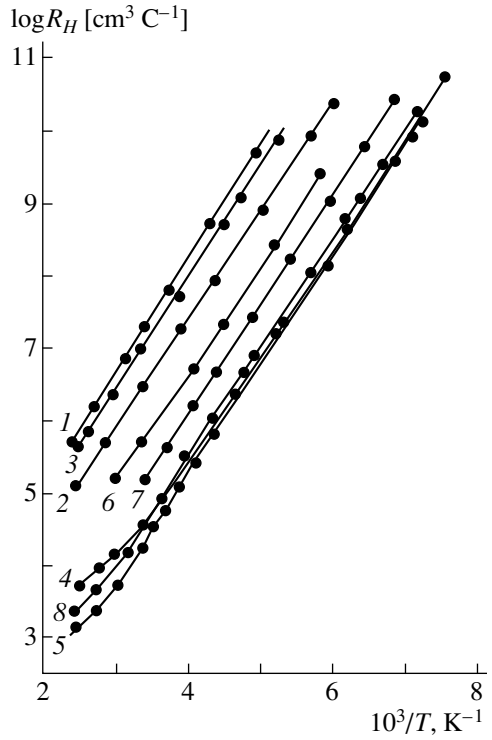

Fig. 1. Temperature dependences of the Hall coefficient for the CdTe:Sb samples with C_0 = (*1*) 5×10^{17}, (*2*) 1×10^{18}, (*3*) 2×10^{18}, (*4*) 3×10^{18}, and (*5*) 3×10^{19} cm^{-3}; curve *6* is for the sample with $C_0 = 10^{17}$ cm^{-3} subjected to a field-assisted doping with Ag; curve *7* corresponds to a sample that had $C_0 = 1 \times 10^{18}$ cm^{-3} and was annealed for 12 h at 400°C; and curve *8* is for a sample that had $C_0 = 2 \times 10^{18}$ cm^{-3} and was annealed for 60 s at 700°C.

low-temperature compensation [5] by field-assisted doping (Fig. 1, curve *6*).

It follows from the aforesaid that the above acceptors (we refer to them arbitrarily as A_3 acceptors) are formed in CdTe crystals owing to doping with Sb and, apparently, constitute the Sb atoms residing in Te sublattice sites (Sb_{Te}). However, doping with Sb is not reduced to the introduction of A_3 acceptors as indicated by the following factors. As a rule, the Fermi level is below the level E_v + 0.20 eV in undoped *p*-CdTe crystals. In the CdTe:Sb crystals, the Fermi level is above E_v + 0.28 eV. Consequently, additional compensating donors with a concentration exceeding [Sb_{Te}] are introduced along with the Sb_{Te} acceptors. At the same time, the calculated concentration of Sb impurity is much higher than the A_3 acceptor concentration. For example, in samples 4 and 5 (curves *4*, *5* in Fig. 1), the A_3 acceptor concentration determined from the Hall effect measurements was found to be equal to 4×10^{16} cm^{-3} for $C_{Sb} = 8 \times 10^{16}$ and 4×10^{17} cm^{-3}, respectively. Furthermore, an analysis of the temperature dependence of the hole mobility in a number of doped samples indicates that the concentration of scattering ionized centers is much higher than 2[A_3] and, at the same time, is lower than C_{Sb}, especially in heavily doped crystals. Thus, we should assume that the doping impurity is involved in the formation of compensating donors and is incorporated in the lattice as Sb_{Cd}. Since the strong inequality $[A_3] \ll C_{Sb}$ is valid and a pronounced electron conductivity is not observed (one exception being a semi-insulating material obtained by zone leveling where, however, *n*-type conduction is weakly pronounced and ceases to exist even at annealing temperatures of T_a = 100–150°C), the conclusion that the concentration of Sb_{Cd} donors in an isolated state is comparable to the concentration of the A_3 acceptors (i.e., $[Sb_{Te}] \approx [Sb_{Cd}] \ll C_{Sb}$) suggests itself. Consequently, the majority of impurity atoms are in a bound and electrically inactive state and form associations such as $Sb_{Te}Sb_{Cd}$. The mass balance equation may be then written as

$$C_{Sb} = [Sb_{Te}] + [Sb_{Cd}] + [(Sb_{Te}Sb_{Cd})], \qquad (1)$$

and the electroneutrality equation, as

$$[Sb'_{Te}] = [A'_1 + A'_2] = p + [Sb^{\bullet}_{Cd}] + [Cd^{\bullet}_i]. \qquad (2)$$

The presence of the term $[Cd^{\bullet}_i]$ corresponding to the concentration of interstitial cadmium in Eq. (2) is necessary due to the observation of the field-assisted purification effect in all the doped samples at T_a = 100–150°C; this effect consists in an increase in the hole concentration as a result of the extended exposure of the samples to an electric field (E = 3–15 V/cm), which is related to the drift of mobile donors (apparently, Cd_i) [5]. In our opinion, it is unlikely that Sb_{Cd} ions can perform the role of the above mobile ions in CdTe:Sb crystals.

We believe that the suggested model is corroborated by the results of room-temperature measurements of the edge-absorption spectra, which are indicative of a marked narrowing of the band gap [2]. Our experiments with heavily doped samples ($C_{Sb} \gg 10^{17}$ cm^{-3}) supported this conclusion and, in addition, made it possible to detect an absorption band corresponding to the $A_3 \longrightarrow E_c$ transitions; analysis of this band yielded a value of no larger than 5×10^{16} cm^{-3} for the A_3-acceptor concentration, which is in good agreement with the results of electrical measurements. On the other hand, the $Sb_{Te}Sb_{Cd}$ associations in various coordination shells ensure a wide quasi-continuous spectrum of levels in the range from E_v to E_v + 0.28 eV. It is these levels that form a broad absorption band merging with the fundamental absorption band, which is perceived as a narrowing of the band gap.

We studied the temperature dependence of photoconductivity σ_{ph} under the intrinsic-absorption excitation of highly compensated photosensitive samples with the Fermi level at $E_F \geq E_v$ + 0.35 eV. Figure 2

shows the temperature dependences of the total electrical conductivity $\sigma = \sigma_0 + \sigma_{ph}$ (σ_0 being the dark equilibrium conductivity) for various excitation levels. It was found that holes are involved in photoconductivity at temperatures of $T > 140$–180 K (depending on the excitation level); this photoconductivity is thermally activated and is related to the capture of holes by the attachment centers with a level at $E_v + 0.27$ eV (A_3). At $T <$ 140–180 K, hole-related photoconductivity becomes electron-related (Fig. 3), and temperature-related quenching of the photoconductivity is observed. The temperature of the sign reversal for the Hall coefficient R_H decreases with an increasing degree of compensation of the A_3 acceptors and a decreasing excitation level.

The temperature-related quenching of the electron photoconductivity can be easily explained in a model of two recombination channels for electrons: a rapid-recombination channel r and a slow-recombination channel s [6]. In order to analyze the lower boundary of the temperature-related quenching of photoconductivity, we use the formula [7]

$$\log n_1 = \log\frac{N_v S_{pr}}{S_{nr}} - 0.43\frac{E_{vr}}{k_0 T_1} \qquad (3)$$

where the electron concentration $n_1 = \sigma_{ph}/e\mu_n$ and the temperature T_1 correspond to the above boundary for different excitation levels; μ_n is the electron mobility; S_{pr} and S_{nr} are the cross sections for the capture of holes and electrons by the r centers; and $E_{vr} = E_r - E_v$ is the ionization energy for the r centers. As a result, we obtain the value $E_r = E_v + 0.28$ eV for the r-center energy level. Thus, the A_3 acceptors perform the role of r centers. The same formula (3) makes it possible to estimate the asymmetry of the cross sections for hole and electron capture by the above centers at $S_{pr}/S_{nr} \geq 2 \times 10^5$. This result is easily understandable because holes are captured by negatively charged centers, whereas electrons are captured by neutral centers. The role of the s centers may be performed by compensating deep-level donors (for example, by the Sb_{Cd} defects).

In order to analyze the upper boundary (with the corresponding electron concentration n_2 and the temperature T_2) for the range of the temperature-related photoconductivity quenching, we use the formula [6]

$$\log n_2 = \log\left(\frac{g_s}{g_r}\frac{N_v S_{pr}}{S_{ns}}\right) - 0.43\frac{E_{vr}}{k_0 T_2}, \qquad (4)$$

where g_s and g_r are the fractions of the charge-carrier fluxes through the s and r centers, respectively. Assuming that $g_s/g_r \approx 1 = \text{const}$, we obtain a value for the cross section of electron capture by the s centers (S_{ns}) which is at least two orders of magnitude larger than the electron-capture cross section for the r centers (S_{nr}); at the same time, we find the same value for E_{vr} as obtained

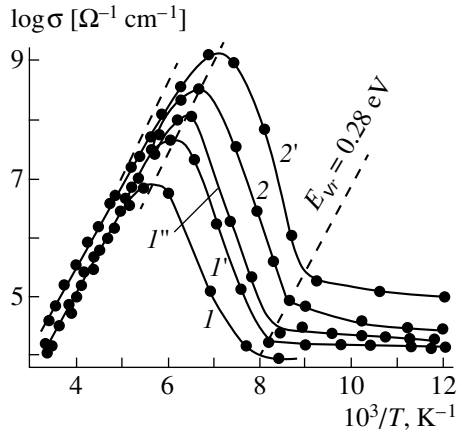

Fig. 2. Temperature dependences of total electrical conductivity for two CdTe:Sb samples with $C_0 = (1, 1', 1'') 1 \times 10^{18}$ and $(2, 2') 2 \times 10^{18}$ cm^{-3}. The fundamental absorption excitation was used. The excitation level increased in the sequences of $1 \longrightarrow 1' \longrightarrow 1''$ and $2 \longrightarrow 2'$.

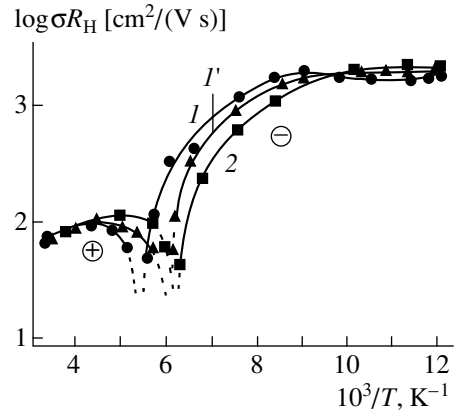

Fig. 3. Temperature dependences of the product σR_H for CdTe:Sb samples subjected to the fundamental absorption excitation (enumeration of the curves corresponds to that in Fig. 2).

using formula (3). All this supports the use of the two-center model for recombination of nonequilibrium charge carriers and suggests that, under nonequilibrium conditions, the A_3 acceptors (Sb_{Te}) perform the role of slow-recombination centers for electrons at low temperatures and hole-attachment centers at high temperatures.

Thus, on the basis of the above results, we may conclude that Sb_{Te} and Sb_{Cd} centers and $Sb_{Te}Sb_{Cd}$ associations are formed in CdTe crystals as a result of doping with Sb. The hole conductivity in the doped crystals is controlled by A_3 acceptors (Sb_{Te}) whose concentration is no higher than 5×10^{16} cm^{-3} and is much lower

than C_{Sb}. The ionization energy for A_3 acceptors is 0.28 ± 0.01 eV. Under nonequilibrium conditions, these acceptors perform the role of hole attachment centers (at high temperatures) and slow-recombination centers for electrons (at low temperatures).

REFERENCES

1. E. Molva, J. L. Pautrat, K. Saminadayar, *et al.*, Phys. Rev. B **30** (6), 3344 (1984).
2. Y. Iwamura, S. Yamamori, H. Negishi, and M. Moriyama, Jpn. J. Appl. Phys. **24** (3), 361 (1985).
3. P. M. Fochuk, O. É. Panchuk, and D. P. Belotskiĭ, Izv. Akad. Nauk SSSR, Neorg. Mater. **3**, 504 (1986).
4. E. S. Nikonyuk, V. L. Shlyakhovyĭ, M. A. Kovalets, *et al.*, Neorg. Mater. **28** (12), 2294 (1992).
5. V. P. Zayachkivskiĭ, N. V. Koshchanovskiĭ, and N. I. Kuchma, Available from TsNII "Élektronika," No. R-3326 (1981).
6. V. E. Lashkarev, A. V. Lyubchenko, and M. K. Sheĭnkman, *Nonequilibrium Processes in Photoconductors* (Naukova Dumka, Kiev, 1981).
7. R. H. Bube, *Photoconductivity of Solids* (Wiley, New York, 1960; Inostrannaya Literatura, Moscow, 1962).

Translated by A. Spitsyn

Semiconductors, Vol. 35, No. 4, 2001, pp. 409–414. Translated from Fizika i Tekhnika Poluprovodnikov, Vol. 35, No. 4, 2001, pp. 421–426.

ELECTRONIC AND OPTICAL PROPERTIES OF SEMICONDUCTORS

A Study of the Electrical and Optical Properties of Si Delta-Doped GaAs Layers Grown by MBE on a (111)A GaAs Surface Misoriented toward the [2$\bar{1}\bar{1}$] Direction

G. B. Galiev, V. G. Mokerov*, É. R. Lyapin, V. V. Saraĭkin, and Yu. V. Khabarov

Institute of Radio Engineering and Electronics, Russian Academy of Sciences, ul. Mokhovaya 11, Moscow, 103907 Russia

** e-mail: mok@beam.mail.cplire.ru*

Submitted October 2, 2000; accepted for publication October 23, 2000

Abstract—Electrical and photoluminescence studies of MBE-grown Si delta-doped GaAs structures at a varied partial pressure ratio $P_{As}/P_{Ga} = \gamma$ on substrates with (111)Ga orientation and misoriented toward the [2$\bar{1}\bar{1}$] direction have been performed. Hall effect measurements demonstrated that the conduction type changes from *p* to *n* on raising the As pressure (i.e., γ). The observed changes in the photoluminescence spectra are interpreted in terms of a kinetic approach based on different dangling bond densities on terraces and steps of the vicinal surface appearing on [2$\bar{1}\bar{1}$] substrates misoriented toward the [2$\bar{1}\bar{1}$] direction. © *2001 MAIK "Nauka/Interperiodica".*

1. INTRODUCTION

Obtaining high-perfection epilayers is a relevant task as regards both the investigation of their fundamental properties and device applications. Misorientation of GaAs substrates from the (111)Ga orientation toward the [$\bar{2}$11] direction by 1° to 4° gives, according to [1], a vicinal surface constituted by terraces with (111)Ga and steps with (111)As planes and, toward the [2$\bar{1}\bar{1}$] direction, terraces with (111)Ga and steps with (100) planes [2]. Lee *et al.* [1] fabricated heterostructures with a high uniformity and steps of up to ~30 monolayers deep by metalloorganic vapor phase epitaxy. In the authors' opinion, this growth technology can be used to fabricate structures with quantum wells. However, no data on the properties of doped epilayers were reported.

The interest in the properties of epilayers grown on (111)Ga GaAs substrates is also due to the fact that silicon, in this case, shows clearly pronounced amphoteric properties. With GaAs having a (100) orientation, silicon mainly occupies sites of the Ga sublattice, forming *n*-type epilayers, whereas in the case of (111)Ga orientation, both compensated and *p*- or *n*-type epilayers can be grown depending on the growth temperature (T_s) and ratio γ of arsenic and gallium fluxes ($\gamma = P_{As}/P_{Ga}$), where P_{As} and P_{Ga} are the partial pressures of As and Ga vapors in the epilayer growth zone in the molecular beam epitaxy (MBE) machine [2–7]. The use of δ-doping with silicon can give delta layers and, possibly, also *n*- and *p*-type quantum wires.

It is noteworthy that the properties of delta-doped *n*-type (with silicon) and *p*-type (with beryllium) epilayers grown on (100) GaAs substrates have been studied in sufficient detail [8–15]. In [15], mention was made of the fundamental difference between the photoluminescence (PL) spectra of *n*- and *p*-type delta-doped layers on (100) GaAs and difficulties in locating and studying the PL spectra of single *n*-type δ-layers. This is due to the repulsive action of the potential of the delta layer on minority carriers and the resulting nearly zero probability of recombination involving electrons localized in the potential well [11].

However, there have been no reports in the literature concerning investigations of Si delta-doped layers grown on GaAs substrates with (111)Ga orientation or those misoriented, in which Si delta layers on both *n*- and *p*-types can be obtained depending on the As to Ga flux ratio.

This paper presents the results obtained in studying the electrical properties and PL spectra of Si delta-doped epilayers MBE-grown at varied γ on (111)Ga GaAs substrates misoriented toward the [2$\bar{1}\bar{1}$] direction.

1063-7826/01/3504-0409$21.00 © 2001 MAIK "Nauka/Interperiodica"

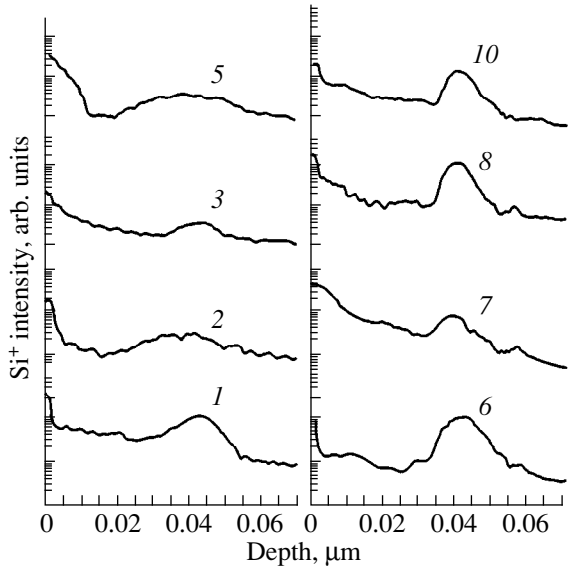

Fig. 1. SIMS depth profiles of silicon concentration $N_{Si}(x)$. The numbers on the curves correspond to sample numbers in the table.

2. GROWTH OF EPILAYERS AND INVESTIGATION TECHNIQUES

The samples under study were grown on a TsNA-24 MBE machine (Ryazan', Russia). Semi-insulating GaAs substrates with (111)Ga orientation misoriented toward the $[2\bar{1}\bar{1}]$ direction by $\alpha = 1°$, 1.5°, and 3° were used. Samples with these misorientation angles, a (111)Ga sample, and a sample on a (100) substrate were grown in the same run at a certain γ value. For this purpose, all these substrates were pasted with indium onto a molybdenum holder. The structures grown comprised an undoped buffer layer ~0.48 μm thick, a delta-layer of silicon, and a top undoped layer of thickness ~0.033 μm. The epitaxial growth was done at T_s = 600°C with the silicon source temperature set to ensure a conduction electron concentration of $n = 1 \times 10^{18}$ cm^{-3} and a time of delta-doping equal to 135 s in (100) GaAs layers. During the formation of the delta-layer, the growth was interrupted; i.e., the shutter of the molecular gallium source was closed. The conditions under which all the structures under study were fabricated are listed in the table. The carrier concentration and the type of conduction were determined by measuring the Hall coefficient. The PL spectra were taken at $T = 77$ K with the photon energies $\hbar\omega$ ranging from 1.3 to 1.55 eV. The PL was excited by an Ar^+ laser with a wavelength of $\lambda = 488$ nm and a radiation power density of up to 100 W/cm^2. Depth distributions of the silicon concentration $N_{Si}(x)$ were measured on a Cameca IMS-4F secondary-ion mass spectrometer with O_2^+ oxygen ions with an energy of $E_p = 5$ keV used as the primary beam. The raster area was 250×250 μm, and secondary silicon ions were collected from the central part of the raster (60×60 μm) at a mass resolution of 5000. Surface images of the samples under study were taken with a CamScan scanning electron microscope in the secondary electron mode at an accelerating voltage of 30 keV.

3. DISCUSSION OF RESULTS

The table illustrates layer growth conditions together with sheet concentrations n_s and mobilities μ measured at $T = 77$ and 300 K. It can be seen that samples grown on (111)Ga GaAs substrates (samples nos. 2–5) show *p*-type conduction at $\gamma = 18$ and are *n*-type at $\gamma = 63$. At the same time, structures grown on (100) GaAs (samples 1 and 6) have *n*-type conduction in both cases. Let us consider silicon profiles $N_{Si}(x)$ measured by secondary-ion mass spectrometry (SIMS) on the samples under study (Fig. 1). It can be seen that a high content of Si is observed in thin surface layers for all the samples. The reason for the presence of Si in

Table

Sample	Substrate orientation and misorientation angle α	Conduction type	Value of γ	Mobility μ, cm^2/(V s)		Sheet concentration n_s, cm^{-2}	
				$T = 300$ K	$T = 77$ K	$T = 300$ K	$T = 77$ K
1	(100)	*n*	18	601	1070	2×10^{12}	1.6×10^{12}
2	(111)A ±0.5°	*p*	18	54	53	6.3×10^{12}	4.8×10^{12}
3	(111)A 1°	*p*	18	43	50	1.0×10^{13}	6×10^{12}
4	(111)A 1.5°	*p*	18	49	205	6.2×10^{12}	7.3×10^{11}
5	(111)A 3°	*p*	18	60	145	4.9×10^{12}	1.3×10^{12}
6	(100)	*n*	63	305	1251	1.3×10^{13}	6×10^{12}
7	(111)A ±0.5°	*n*	63	129	1247	3.6×10^{12}	1.8×10^{11}
8	(111)A 1°	*n*	63	271	593	1.1×10^{12}	1.7×10^{11}
9	(111)A 1.5°	*n*	63	175	563	2.0×10^{12}	3.5×10^{11}
10	(111)A 3°	*n*	63	166	360	1.1×10^{12}	7×10^{11}

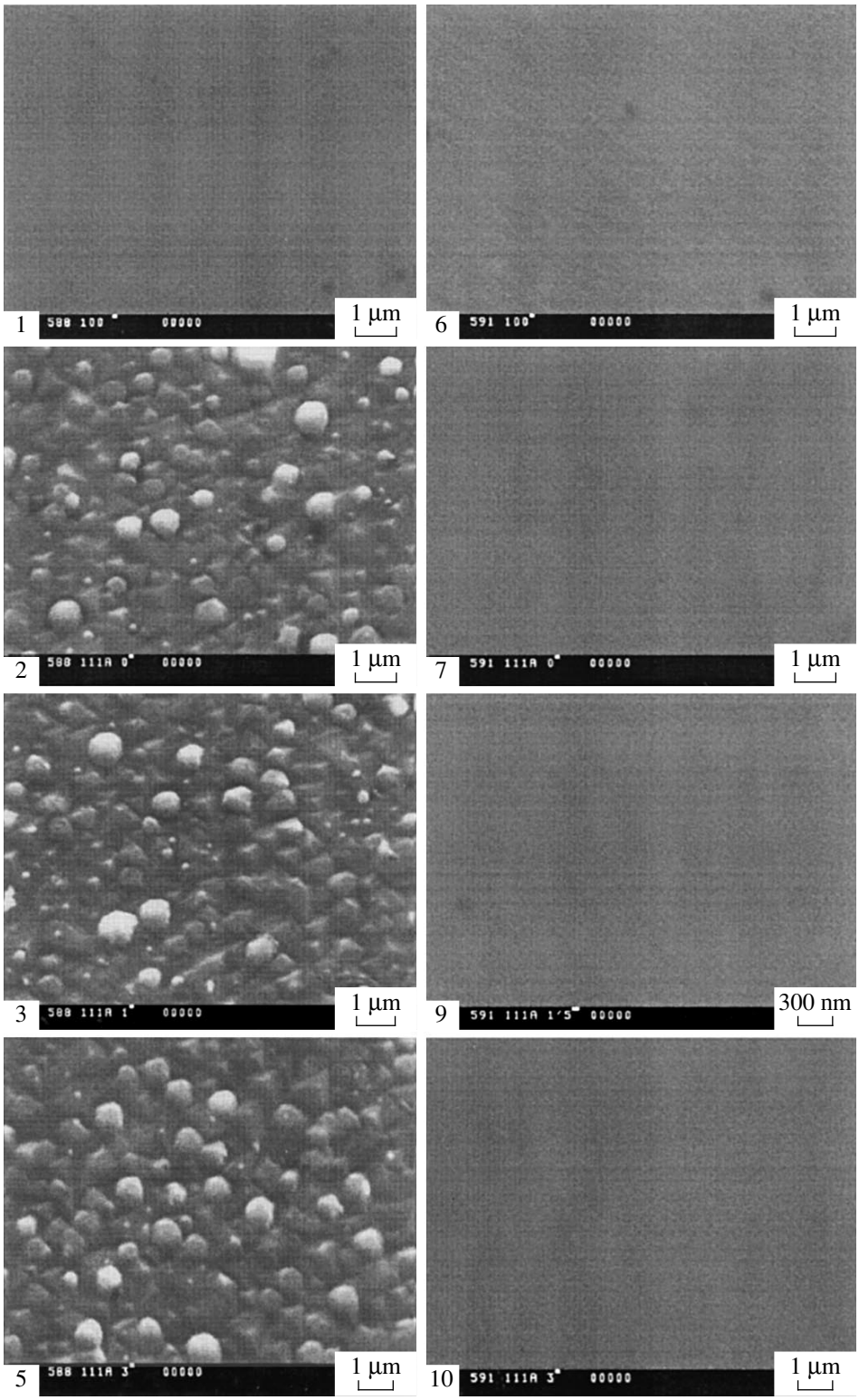

Fig. 2. Plan-view SEM images of the samples under study. The numbers at the micrographs correspond to sample numbers in the table.

GaAs structures containing Si-doped layers deep inside epilayers observed by SIMS was discussed in [16, 17] and will not be considered here.

As it can be seen from Fig. 1, $N_{Si}(x)$ SIMS profiles for the Si delta layer are strongly broadened for samples 2, 3, and 5 grown at $\gamma = 18$, and it is practically

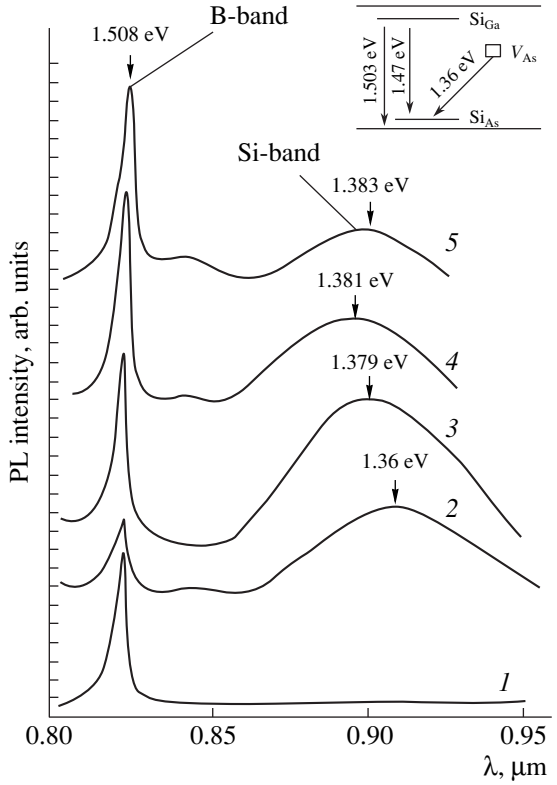

Fig. 3. PL spectra taken at T = 77 K from samples 1–5 grown at γ = 18 with Si delta-doped layers. The spectra are shifted with respect to one another along the ordinate. The insert shows the supposed band diagram for optical transitions.

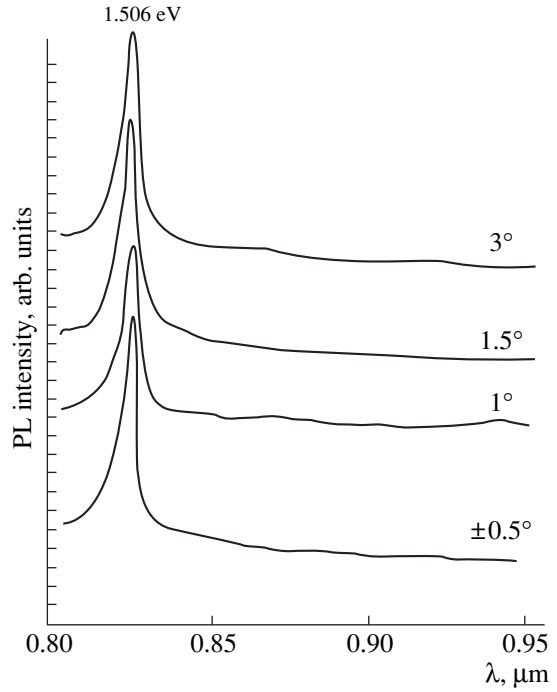

Fig. 4. PL spectra taken at T = 77 K from samples grown on (111)Ga substrates under the same conditions as samples 1–5, but without a Si delta layer. The spectra are shifted with respect to one another along the ordinate. The misorientation angles are indicated at the corresponding curves.

impossible to determine the full width at half-maximum (FWHM), Δ, of the delta layer. This is presumably due to the fact that the epitaxial films grown at small γ are more defective. It is noteworthy that similar behavior was observed in [2]. It is known that ion etching in SIMS makes the surface relief more developed, which, in turn, impairs the SIMS depth resolution. Figure 2 presents plan-view SEM images of the samples under study. As seen from Figs. 1 and 2, the samples with strongly broadened profiles are the most defective (samples 2, 3, and 5). Thus, the strong broadening of the Si delta-layer profiles for samples 2–4, shown in Fig. 1, is in all probability due to the surface morphology and surface relief development upon ion etching.

At the same time, the profiles of delta layers are not so strongly broadened for samples 1 and 7–11, although the egress of silicon toward the surface is still observed. The half-widths Δ are 120, 100, 123, 80, 71, and 63 Å for samples 1 and 6–10, respectively; i.e., they are close to the Δ values observed for the delta-doped layers by SIMS. That $\Delta_1 > \Delta_6$ (here the subscripts correspond to the sample numbers in the table) for the samples grown on (100) GaAs is presumably due to the fact that epitaxial growth at γ = 18 is not optimal as regards the surface morphology. It is noteworthy that, with the misorientation angle increasing from 0° to 3°, the Δ value, in particular, decreases: Δ_7 = 123 Å for α = 0°, whereas Δ_{10} = 63 Å for α = 3°. In our opinion, this is associated with the surface morphology of the epitaxial films improving as the misorientation angle increases. This, in turn, improves the depth resolution of the SIMS analysis and makes the Si delta layer less thick.

Let us now consider the PL measurements. Figure 3 shows the PL spectra taken from samples 1–5 at T = 77 K, with the insert presenting a diagram of optical transitions constructed for GaAs on the basis of the experimental data obtained in [4, 7, 9]. It can be seen that the PL spectra of all samples, except sample 1, contain two bands. One of these, lying at $\hbar\omega \approx 1.508$ eV and designated here as band B, corresponds to band-to-band radiative recombination (e–h). The second, broad band, peaked at $\hbar\omega \approx 1.36$–1.38 eV, is only observed for samples grown on (111)Ga substrates with varied α and a Si delta layer and is designated as a Si band (Fig. 3). Figure 4 presents PL spectra of samples grown under the same conditions on similar substrates [except (100) GaAs] but without a Si delta layer. It can be seen that there is no Si band in this case. This suggests that this band is associated with the Si delta layer. It should be noted that the PL spectra of single beryllium delta-doped layers grown on (100) GaAs substrates have no band at 1.36–1.38 eV, either. The features in the PL spectra of Be delta layers associated with transitions between the conduction band and acceptor levels related to Be atoms are observed at $\hbar\omega \approx 1.42$–1.49 eV [11, 12, 15]. The band at $\hbar\omega \approx 1.36$ eV in the PL spectra of the epilayers grown on (111)Ga substrates is com-

monly attributed to the recombination of electrons localized at As vacancies V_{As} with holes at the level of the Si acceptor at the As site Si_{As} [4, 7], i.e., to the V_{As}–Si_{As} transition. This PL band is also observed in silicon-doped epilayers grown on (100) GaAs substrates and annealed at $T > 600$°C [16] and films grown on (111)Ga, (211)Ga, and (311)Ga substrates at low As pressures [7, 18] or also annealed [18, 19].

Let us consider the behavior of a Si band with the misorientation angle α. As can be seen from Fig. 3, the peak of the Si band is shifted, with increasing α, to shorter wavelengths: from $\hbar\omega = 1.36$ eV for $\alpha = 0°$ to 1.383 eV for $\alpha = 3°$. This shift of the Si band with increasing α can be understood by considering the density of bonds on terraces and steps. Figure 5 shows schematically the positions of Ga and As atoms on the vicinal surface for a (111)Ga GaAs substrate misoriented toward the $[2\bar{1}\bar{1}]$ direction. It can be seen that the vicinal surface is characterized by different densities of dangling Ga bonds on terraces and steps; i.e., the conditions of the appearance of a V_{As} vacancy and occupation of As sites by silicon are different on the terraces and the steps. Let us assume that donor–acceptor (*D*–*A*) pairs are formed with the distance *r* between donors and acceptors exceeding the Bohr radius. Then, according to [20], the emission energy is determined for such a pair by the expression

$$\hbar\omega = E_g - (E_A + E_D) + \frac{e^2}{4\pi\varepsilon\varepsilon_0 r},$$

where E_g is the energy gap, E_A and E_D are the acceptor and donor levels, ε and ε_0 are the dielectric constant of GaAs and the permittivity of the vacuum, *e* is the electron charge, and *r* is the distance between a donor and an acceptor.

Thus, we have a correction $e^2/4\pi\varepsilon\varepsilon_0 r$ associated with the interaction within the *D*–*A* pair to the transition energy $E_g - (E_A + E_D) \approx 1.36$ eV. For the case in question, the *r* value is determined by the average distance between the donor and acceptor pairs for each terrace length L_{ter}. The L_{ter} values are 37.2, 18.6, 12.4, and 6.2 nm for $\alpha = 0.5°$, 1°, 1.5°, and 3°, respectively. The correction $e^2/4\pi\varepsilon\varepsilon_0 r$ equals ~0.0027 and 0.012 eV for, respectively, $r = 40$ and 10 nm; i.e., it grows with increasing misorientation angle α and is comparable with the observed shift of the Si band in the PL spectra in Fig. 3 to higher energies. Thus, the shift of the Si band with increasing α can be accounted for by changes in the distances of *D*–*A* pairs on the steps and terraces of the vicinal face.

Let us consider epilayers grown at large γ, i.e., at $\gamma \approx 63$. In this case, silicon-doped epilayers are known to exhibit *n*-type conduction. Figure 6 presents PL spectra for samples 6–10 grown at $\gamma = 63$. As can be seen from the table, these samples show *n*-type conduction. Figure 6 shows that the spectra of samples grown on (111)Ga substrates at various misorientation angles contain, in addition to the main band at $\hbar\omega \approx 1.508$ eV, a feature at $\hbar\omega \approx 1.47$–1.48 eV. For sample 7, this feature has the form of a shoulder at $\hbar\omega \approx 1.483$ eV, whereas, with increasing α (for samples 8–10), it becomes a more clearly defined band. The same band was observed in PL spectra for uniformly doped epilay-

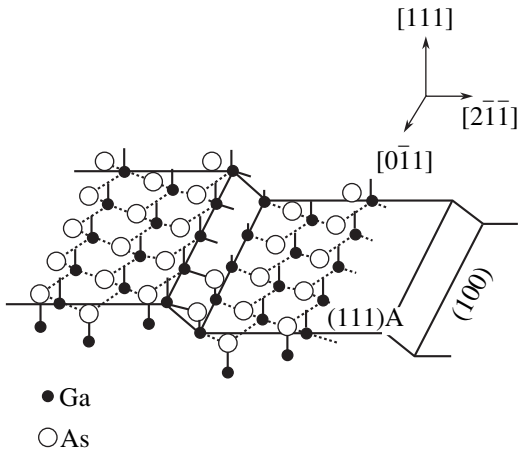

Fig. 5. Schematic arrangement of Ga and As atoms on the (111)Ga surface for substrate misorientation toward the $[2\bar{1}\bar{1}]$ direction.

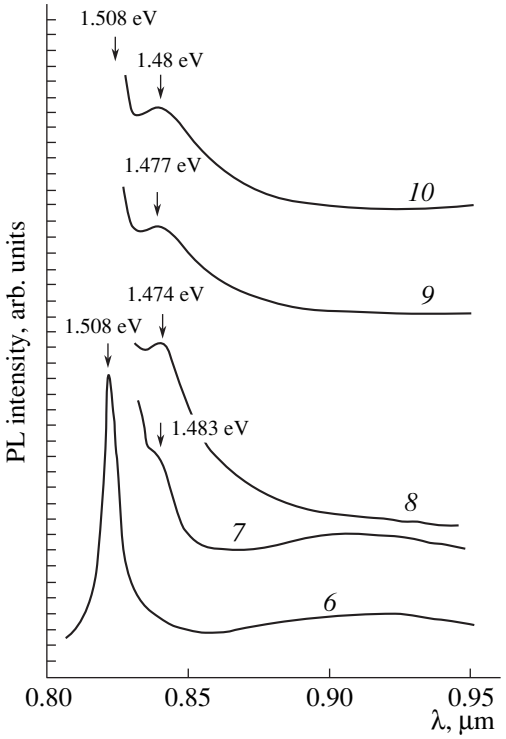

Fig. 6. PL spectra taken at $T = 77$ K from samples 6–10 grown at $\gamma = 63$ with Si delta-doped layers. The spectra are shifted with respect to one another along the ordinate. For samples 7–10, the main band at $\hbar\omega = 1.508$ eV is not shown because of the high intensity of the signal.

ers grown on (111)Ga GaAs substrates at large γ in [5]. In the same study, a shift of the main band from $\hbar\omega \approx 1.508$ to ≈ 1.525 eV was observed on changing γ from 16 to 70. In the present case of Si delta-doping, no such shift of the main band is observed. Moreover, in [5], the intensity of the band at $\hbar\omega \approx 1.48$ eV exceeds that of the main band. In our opinion, the band at $\hbar\omega \approx 1.47$ eV is associated with transitions between donor and acceptor states of silicon, i.e., Si_{Ga}–Si_{As}.

Thus, the investigations performed indicate that with only silicon used for doping, both *n*- and *p*-type delta-doped layers can be obtained on (111)Ga substrates. The PL spectra of samples grown on (111)Ga substrates and those misoriented from this plane toward the $[2\bar{1}\bar{1}]$ direction contain bands related to single delta layers of silicon. Analysis of the PL spectra demonstrated that at small γ, when a *p*-type delta-doped layer is formed, the band $\hbar\omega = 1.36$ eV is shifted to higher energies with an increasing misorientation angle. This shift is attributed to a change in the average distance between donors and acceptors in *D*–*A* pairs because of the increase in the terrace length with an increasing misorientation angle α.

ACKNOWLEDGMENTS

This study was supported by the interdisciplinary Scientific-Technological program "Physics of Solid-State Nanostructures" (project no. 99-2044).

REFERENCES

1. J. S. Lee, H. Isshiki, T. Sugano, and Y. Aoyagi, J. Cryst. Growth **173**, 27 (1997).
2. Y. Okano, M. Shigeta, H. Seto, *et al.*, Jpn. J. Appl. Phys. **29**, L1357 (1990).
3. W. I. Wang, E. E. Mendez, T. S. Kuan, and L. Esaki, Appl. Phys. Lett. **47**, 826 (1985).
4. F. Piazza, L. Pavesi, M. Henini, and D. Johnston, Semicond. Sci. Technol. **7**, 1504 (1992).
5. V. G. Mokerov, G. B. Galiev, Yu. V. Slepnev, and Yu. V. Khabarov, Fiz. Tekh. Poluprovodn. (St. Petersburg) **32**, 1320 (1998) [Semiconductors **32**, 1175 (1998)].
6. Y. Okano, H. Seto, H. Katahama, *et al.*, Jpn. J. Appl. Phys. **28**, L151 (1989).
7. L. Pavesi, M. Henini, and D. Johnston, Appl. Phys. Lett. **66**, 2846 (1995).
8. J. C. M. Hening, Y. A. R. R. Kessener, P. M. Koenraad, *et al.*, Semicond. Sci. Technol. **6**, 1079 (1991).
9. J. Wagner, A. Fischer, and K. Ploog, Phys. Rev. B **42**, 7280 (1990).
10. C. H. Perry, K. S. Lee, W. Zhou, *et al.*, Surf. Sci. **196**, 677 (1988).
11. A. M. Gilinsky, K. S. Zhuravlev, D. I. Lubyshev, *et al.*, Superlattices Microstruct. **10** (4), 399 (1991).
12. J. Wagner, A. Ruiz, and K. Ploog, Phys. Rev. B **43**, 12134 (1991).
13. R. Enderlein, G. M. Sipahi, L. M. R. Scolfaro, *et al.*, Mater. Sci. Eng. B **B35**, 396 (1995).
14. D. Richards, J. Wagner, H. Schneider, *et al.*, Phys. Rev. B **47**, 9629 (1993).
15. G. M. Sipahi, R. Enderlein, L. M. R. Scolfaro, *et al.*, Phys. Rev. B **57**, 9168 (1998).
16. L. Pavesi, N. H. Ky, J. D. Ganiere, *et al.*, J. Appl. Phys. **71**, 2225 (1992).
17. G. B. Galiev, V. É. Kaminskiĭ, V. G. Mokerov, *et al.*, Fiz. Tekh. Poluprovodn. (St. Petersburg) **34** (7), 769 (2000) [Semiconductors **34**, 741 (2000)].
18. J. Harrison, L. Pavesi, M. Henini, and D. Johnston, J. Appl. Phys. **75**, 3151 (1994).
19. H. Birey and J. Sites, J. Appl. Phys. **51**, 619 (1980).
20. L. Pavesi and M. Guzzi, J. Appl. Phys. **75**, 4779 (1994).

Translated by M. Tagirdzhanov

Semiconductors, Vol. 35, No. 4, 2001, pp. 415–418. Translated from Fizika i Tekhnika Poluprovodnikov, Vol. 35, No. 4, 2001, pp. 427–430.

SEMICONDUCTOR STRUCTURES, INTERFACES, AND SURFACES

The Use of the Amphoteric Nature of Impurity Silicon Atoms for Obtaining Planar *p–n* Junctions on GaAs (111)A Substrates by Molecular Beam Epitaxy

G. B. Galiev, V. É. Kaminskiĭ*, V. G. Mokerov, and L. É. Velikhovskiĭ

Institute of Radio Engineering and Electronics, Russian Academy of Sciences, Mokhovaya ul. 11, Moscow, 103907 Russia

** e-mail: kamin@mail.cplire.ru*

Submitted July 31, 2000; accepted for publication August 2, 2000

Abstract—Epilayers of the *n*- and *p*-type were grown. It is demonstrated that the surface relief of the *p*-type layers is inferior to that of *n*-type layers. However, in both cases, the photoluminescence spectra and charge carrier mobility have no considerable distinctions from these characteristics for single-crystal samples. Planar *p–n* junctions were obtained, and diodes were fabricated as well. Depending on the layer structure, the current–voltage characteristics for devices take a form typical of conventional or inverted diodes. © *2001 MAIK "Nauka/Interperiodica".*

1. INTRODUCTION

It is known that Si dopant can form both donor (with an energy of 6 meV) and acceptor (with an energy of 35 meV) levels in GaAs. Doping with Si allows one to introduce acceptor levels only during epitaxial growth on the GaAs(100) substrates irrespective of growth conditions. Accordingly, the epilayers always have an *n*-type conduction. At the same time, epitaxial growth on the (111)A substrates enables one to obtain epilayers of both conduction types [1–3]. This is accomplished by varying the growth conditions. It is known that molecular beam epitaxy (MBE) ensures a high controllability of epilayer growth conditions. The required conduction type of epilayer is attained by varying the ratio between As and Ga fluxes $\gamma = P_{As}/P_{Ga}$. Here, P_{As} and P_{Ga} are the partial pressures of As and Ga vapors in the growth zone, respectively. For $\gamma \le 20$ and $\gamma \ge 50$, the layers of the *p*- and *n*-type of conduction are grown, respectively. For intermediate values $20 \le \gamma \le 40$, partly or completely compensated layers are grown [2, 3].

Fabrication of the GaAs-based lateral *p–n* junctions using only the Si dopant has been reported. Thus, lateral *p–n* junctions with dimensions of ~10 μm were formed on the GaAs(100) substrates, but only in the grooves formed by photolithography and selective etching in the (110) direction [4]. In this case, the face (111)A is formed in the groove due to the choice of the selective etchant, and the *p*-type conduction region is formed in the groove by MBE. It was reported that the lateral submicron regions with *p–n* junctions in GaAs(111)A were formed using Si dopant [5, 6]. In this case, the equilateral triangular etched regions with (111)A, (411)A [5], and (311)A [6] faces were formed on the substrate surfaces using photolithography and selective etching. The *p*- and *n*-regions were formed on these faces by MBE. The extension of these regions was as small as ~10 μm. However, there are no available data on epitaxially grown GaAs films with planar *p–n* junctions doped only with Si.

In this study, the properties of epilayers of the *p*- and *n*-type of conduction grown on the (111)A substrates and diode characteristics of the films consisting of epilayers of both types of conduction are investigated.

2. EXPERIMENTAL

The samples investigated were grown by the MBE on (111)A-oriented semi-insulating substrates. For this purpose, four (111)A-oriented samples and two (100)-oriented samples were cemented to the Mo holder using In. The latter two samples were used as references for comparison of concentrations as well as the electron and hole mobilities in the epilayers. Subsequent to growth on the undoped ~0.5-μm-thick buffer layer, the ~0.5-μm-thick Si-doped layer was grown at $\gamma = 77$ and a growth temperature of 600°C, in which case the *n*-layer is formed according to [3]. After that, the growth was terminated, and two (111)A-oriented samples and one (100)-oriented sample were unglued. These samples were further used for the investigation of characteristics of the *n*-layer. Then, two new (111)A-oriented samples and one (100)-oriented sample were cemented to the holder, and the *p*-type epilayer ~0.45 μm thick was grown at $\gamma = 15$. Thus, as a result of two growth runs, we were able to grow samples containing both single *n*- and *p*-type layers (samples 1 and 2, respectively) as well as the sample with the *p–n* junc-

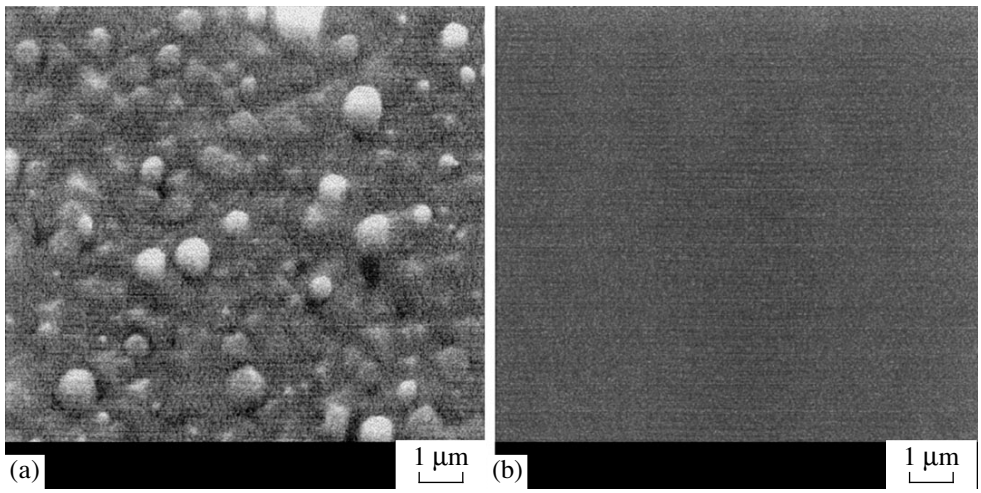

Fig. 1. Surfaces of the epilayers of (a) *p*- and (b) *n*-type of conduction. Images were obtained using a scanning electron microscope.

tion (sample 3). The concentration, carrier mobility, and conduction type were determined by the van der Pauw method. The photoluminescence (PL) spectra were measured at $T = 77$ K for the photon energy range from 1.3 to 1.7 eV. The excitation source was an Ar^+ laser with a wavelength of 514.5 nm and a radiation power density as high as 20 W/cm^2. Images of the sample surfaces were obtained using a Cam Scan scanning electron microscope in the secondary-electron detection mode at an accelerating voltage of 30 kV.

In order to measure current–voltage (*I–V*) characteristics of the *p–n* junctions (samples 3 and 4), the *p*-type cap layer was etched off from part of the sample. After that, Au/Ti nonrectifying contacts ~0.2 μm thick were deposited. The area of contacts was ~1 mm^2 and the distance between them was ~5 mm.

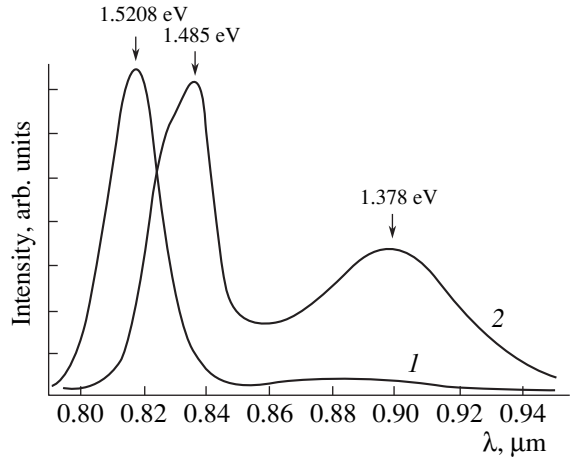

Fig. 2. Photoluminescence spectra for epilayers of (*1*) *n*- and (*2*) *p*-type conduction.

3. RESULTS AND DISCUSSION OF MEASUREMENTS OF ELECTRICAL CHARACTERISTICS FOR EPILAYERS

The images of the surface of the *n*- and *p*-type layer obtained using the scanning electron microscope are shown in Fig. 1. It can be seen that the *p*-type layer is characteristic of the developed surface relief. As a consequence, the crystalline perfection of this layer is poor, and, correspondingly, it contains a large number of defects. These defects play the role of traps and scattering centers for charge carriers. The high concentration of these defects has a pronounced effect on the electrical characteristics of the layers. Thus, the mobility was ~2000 cm^2/(V s) for sample 1 with an electron density of $\sim 6 \times 10^{17}$ cm^{-3}. At the same hole density, the mobility was ~100 cm^2/(V s) for sample 2. The mobilities measured were lower than those characteristic of the single-crystal samples grown on (100)-oriented substrates by a factor of 1.5 and 2, respectively.

The PL spectra for samples 1 and 2 are shown in Fig. 2. It can be seen that the energies corresponding to peaks of emission bands for band-to-band transitions are shifted to opposite sides in relation to the energy equal to the band gap $E_g = 1.507$ eV. Such behavior of the PL spectra is characteristic of heavily doped GaAs and was investigated in detail previously [7]. It is caused by the simultaneous effect of two factors, namely, the Burstein–Moss shift and narrowing of the band gap. The former factor is dominant in *n*-type materials, and the latter one is dominant in *p*-type materials. In addition, low-energy bands were observed in the PL spectra, which correspond [8] to optical transitions from the donor or acceptor to the As vacancy. The difference between peak energies for these bands is approximately equal to the energy difference between the donor and acceptor Si levels in GaAs.

4. CURRENT–VOLTAGE CHARACTERISTICS OF *p–n* JUNCTIONS

The *I–V* characteristics for diodes fabricated from samples 3 and 4 are shown in Figs. 3 and 4, respectively. Sample 3 has parameters of the layers for samples 1 and 2. Sample 4 differed from sample 3 by the introduction of an additional undoped layer d_i = 68 nm thick between the *p*- and *n*-layers, as well as by a lower doping level ($\sim 4.5 \times 10^{17}$ cm^{-3}). It can be seen from Figs. 3 and 4 that the *I–V* characteristics are practically asymmetrical and strongly deviate from ideal characteristics. Major reasons for this deviation of the *I–V* characteristics are known [9]. These are (i) generation and recombination of charge carriers in the depletion region, (ii) state-to-state tunneling of carriers in the band gap and between the bands, (iii) a high injection level, and (iv) the influence of the series resistance.

It is easy to deduce from the experimental *I–V* characteristics that the series resistance for both cases is about 3.3 kΩ. It is mainly determined by the resistivity of the *n*-layer, its thickness, and distance between nonrectifying contacts. Note that this value can be significantly decreased by increasing the *n*-layer thickness. It follows from the figures that the largest current density is no higher than 5 mA/cm^2 in our case; i.e., the measurements are carried out in conditions of a low injection level. Thus, the difference between the *I–V* characteristics is determined by the two first reasons mentioned.

For a forward bias and voltage $U > \varphi_T = kT/q$, the total current through the diode is defined by the relationship [9]

$$J_F = q\sqrt{\frac{D_p}{\tau_p}}\frac{n_i^2}{N_D}\exp\left(\frac{U}{\varphi_T}\right) + q\sigma v_T N_t \frac{W}{2}\exp\left(\frac{U}{2\varphi_T}\right), \quad (1)$$

where n_i is the intrinsic carrier density, σ is the capture cross section for the traps, N_t is the trap concentration, v_T is the thermal velocity, and W is the total width of the depletion region. For sample 3, the W value coincides with the total width of the depletion region for the *p–n* junction W_0. For sample 4, $W > W_0$ and, as can be easily demonstrated, is determinable from the relationship $W^2 = W_0^2 + d_i^2$. The first and second terms in relationship (1) are the diffusion and recombination currents, respectively. Under a reverse bias and $|U| > 3\varphi_T$, the total current can be expressed approximately as the sum of the diffusion current in the neutral region, the generation current in the depletion region, and the tunneling current:

$$J_R = q\sqrt{\frac{D_p}{\tau_p}}\frac{n_i^2}{N_D} + \frac{qn_iW}{\tau_e} + J_T. \quad (2)$$

For GaAs, the value of n_i is very small. In addition, it was demonstrated above that the epilayer surface relief for the (111)A orientation is characteristic of a high level of imperfection and, as a consequence, high N_t values. This was indirectly confirmed by the low-frequency hysteresis in the *I–V* characteristics. By virtue of these reasons, the generation–recombination constit-

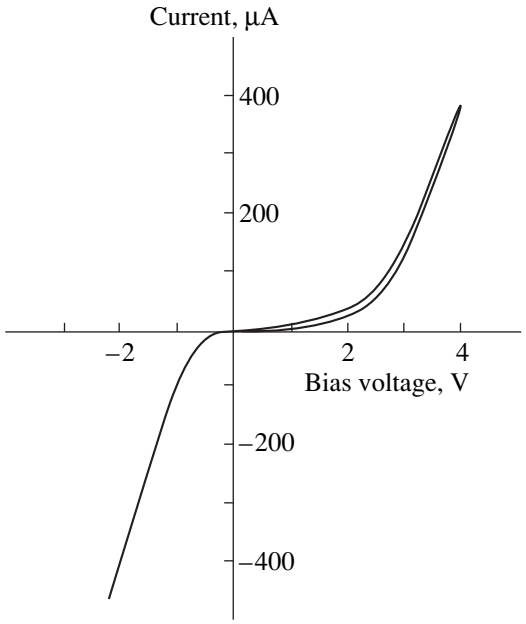

Fig. 3. Current–voltage characteristic for the diode with the structure of sample 3.

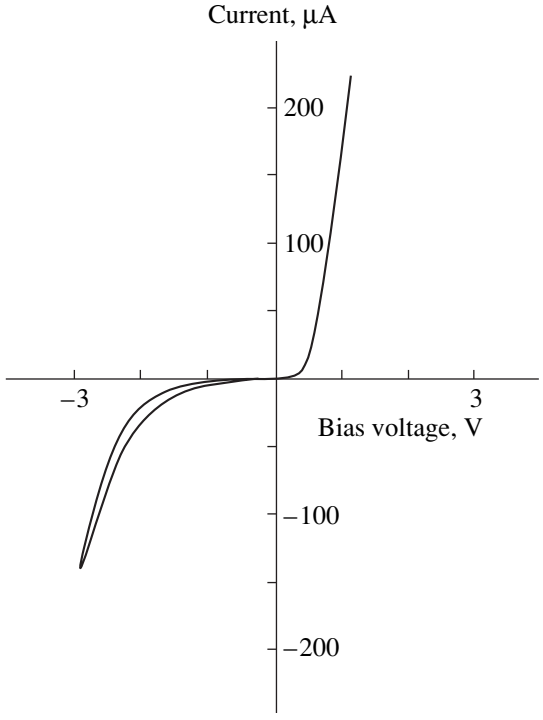

Fig. 4. Current–voltage characteristic for the diode with the structure of sample 4.

uent of the current is sufficiently larger than the diffusion one, with the latter depending quadratically on n_i. For the epilayers grown, the electron and hole densities are close to the effective density of states in the bands. As a consequence, the charge carriers are slightly degenerate. In these conditions, direct band-to-band tunneling becomes significant. It is known that the quantity J_T is given by

$$J_T \propto \exp\left(-\frac{\pi m^{1/2} E_g^{3/2} W}{2\sqrt{2}\hbar q \varphi_c}\right), \quad (3)$$

where φ_c is the contact potential difference, which is approximately equal to E_g/q in our case. It follows from expression (3) that J_T decreases rapidly with increasing W. The difference in the I–V characteristics for the samples is the consequence of this dependence of the tunneling current. For obtained concentrations in sample 3, $W_0 = 54$ nm. The tunneling current for the reverse bias exceeds the recombination current for the forward bias, and the I–V characteristic is typical of an inverted diode [9].

For sample 4, $W_0 = 62$ nm and $W = 93$ nm. The latter value is larger than W_0 for sample 3 by a factor of 1.7. It follows from expression (3) that J_T in expression (2) decreases exponentially by a factor of 10^{22}. At the same time, the recombination current magnitude in expression (1) increases linearly with increasing W. Thus, the tunneling current becomes significant at higher voltages (~1.5 V). The behavior of the I–V characteristics is therefore typical of conventional diodes. The results demonstrate that the diode characteristics can be controlled rather simply by introducing the undoped region.

5. CONCLUSION

We grew the epilayers of the *n*- and *p*-type of conduction on the GaAs (111)A substrates by molecular beam epitaxy and investigated their properties. The surface relief of the *n*-type epilayers is similar to that of the layers on the (100)-oriented substrates. At the same time, the surface relief of the *p*-type layers indicates that there is a large number of imperfections. However, electrical properties of epilayers are close to those of single-crystal samples with the same doping level. We also obtained planar *p*–*n* junctions and fabricated the diodes. Depending on the structure of the layers, the I–V characteristics of the devices are typical of the conventional or inverted diodes.

ACKNOWLEDGMENTS

We thank Yu. V. Khabarov for measurements of the PL spectra.

This work was supported by the Interdisciplinary Scientific and Technological Program of Russian Federation “Physics of Solid-State Nanostructures,” project no. 97-1093/4.

REFERENCES

1. Y. Okano, H. Seto, H. Katahama, *et al.*, Jpn. J. Appl. Phys. **28**, L151 (1989).
2. F. Piazza, L. Pavesi, M. Henin, and D. Johnston, Semicond. Sci. Technol. **7**, 1504 (1992).
3. V. G. Mokerov, G. B. Galiev, Yu. V. Slepnev, and Yu. V. Khabarov, Fiz. Tekh. Poluprovodn. (St. Petersburg) **32**, 1320 (1998) [Semiconductors **32**, 1175 (1998)].
4. D. L. Miller, Appl. Phys. Lett. **47**, 1309 (1985).
5. M. Fujii, T. Takebe, T. Yamamoto, *et al.*, Superlattices Microstruct. **12**, 167 (1992).
6. K. Fujita, H. Ohnishi, M. Hirai, *et al.*, Solid-State Electron. **40**, 663 (1996).
7. G. Borghs, K. Bhattacharyya, K. Deneffe, *et al.*, J. Appl. Phys. **66**, 4381 (1989).
8. L. Pavesi and M. Guzzi, J. Appl. Phys. **75**, 4779 (1994).
9. S. Sze, in *Physics of Semiconductor Devices* (Wiley, New York, 1981; Mir, Moscow, 1984), Vols. 1, 2.

Translated by N. Korovin

Semiconductors, Vol. 35, No. 4, 2001, pp. 419–423. Translated from Fizika i Tekhnika Poluprovodnikov, Vol. 35, No. 4, 2001, pp. 431–435.

SEMICONDUCTOR STRUCTURES, INTERFACES, AND SURFACES

Structural, Luminescent, and Transport Properties of Hybrid AlAsSb/InAs/Cd(Mg)Se Heterostructures Grown by Molecular Beam Epitaxy

V. A. Solov'ev*, I. V. Sedova, A. A. Toropov, Ya. V. Terent'ev, S. V. Sorokin, B. Ya. Mel'tser, S. V. Ivanov, and P. S. Kop'ev

Ioffe Physicotechnical Institute, Russian Academy of Sciences, Politekhnicheskaya ul. 26, St. Petersburg, 194021 Russia

** e-mail: vasol@beam.ioffe.rssi.ru*

Submitted September 13, 2000; accepted for publication September 14, 2000

Abstract—The fabrication of new hybrid AlAsSb/InAs/Cd(Mg)Se heterostructures by molecular beam epitaxy and investigation of their structural, luminescent, and transport properties are reported for the first time. These structures show intense luminescence both in the infrared and in the visible regions of the spectrum. This factor, taken together with structural data, indicates a heterointerface of high quality between the III–V and II–VI layers. A theoretical estimate is made of the relative positions of energy bands in the proposed hybrid structures, indicating that the InAs/CdSe interface is a type-II heterojunction, whereas the InAs/$Cd_{0.85}Mg_{0.15}Se$ interface is a type-I heterojunction with a large valence band offset $\Delta E_v \approx 1.6$ eV. The data obtained on the longitudinal electron transport at the InAs/Cd(Mg)Se heterointerface are in good agreement with the theoretical estimate.

1. INTRODUCTION

Among the known and widely used II–VI/III–V heteropairs characterized by nearly ideal lattice matching (e.g., ZnSe/GaAs [1] and CdTe/InSb [2]) the CdSe/InAs pair has received insufficient attention, even though the epilayer properties of cubic CdSe (with a zinc blende structure) grown by molecular beam epitaxy (MBE) on GaAs substrates are well understood [3]. Data on the structural and optical properties of bulk crystals of hexagonal CdMgSe have also been published [4]. It should be noted that the fabrication of heterostructures based on high quality Cd(Mg)Se/InAs heteropairs allows greater diversification in the design of hybrid structures containing a CdSe/InAs heterointerface in their active region; e.g., a two-dimensional (2D) channel with magnetic electron gas in the quantum wells (QWs) in an InAs layer confined on one side by a CdMnSe semimagnetic barrier can be obtained.

In this communication, we report for the first time on new hybrid heterostructures in the AlAsSb/InAs/Cd(Mg)Se system grown by MBE and study their structural, luminescent, and transport properties.

2. GROWTH OF HYBRID STRUCTURES

The hybrid structures studied comprised two parts: layers of III–V compounds, conventionally named the (III–V) part in what follows, and layers of II–VI compounds the (II–VI) part. They were grown successively in two separate MBE machines. The III–V part of the structures for optical measurements was grown on a Riber 32P machine at $T_s = 480$°C on p^+-InAs (100) substrates with hole concentration $p \approx 6 \times 10^{18}$ cm^{-3}. It comprised a 0.1-μm-thick Be-doped p^+ InAs buffer layer, a 20-nm-thick Si-doped p-AlGaAs barrier, and a 0.6-μm-thick nominally undoped InAs layer with electron concentration $n < 10^{17}$ cm^{-3}. On completion of growth, the substrate temperature was lowered to $T_s <$ 25°C and then the sample surface was covered, in the course of 1 h, with a layer of arsenic under an As_4 beam pressure of 8×10^{-6} Torr. This arsenic layer served as passivating coating protecting the structure surface from oxidation in air during sample transfer to the II–VI growth chamber (EP 1203 MBE machine). Before being used for II–VI growth, the passivated structures were stored in a special nitrogen-filled box for a week.

Layers of Cd(Mg)Se were grown with standard effusion cells providing molecular flows of Cd, Mg, and Se [5, 6]. The surface layer of arsenic was removed prior to II–VI growth by annealing the structure at $T_s <$ 480°C. The sample surface was monitored in all growth stages by reflection high-energy electron diffraction (RHEED). Before the growth of II–VI layers, a (4×2) surface reconstruction was observed, corresponding to an In-stabilized surface. However, for some samples

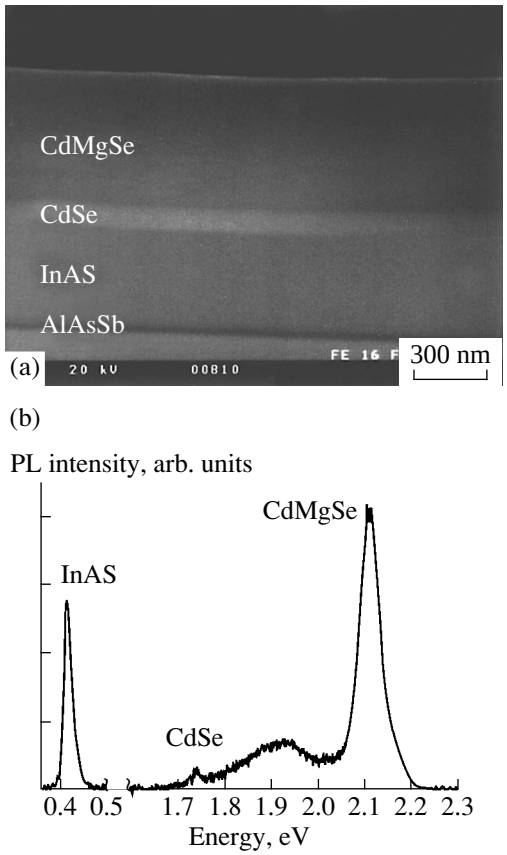

Fig. 1. Cross-sectional SEM image of an undoped AlAsSb/InAs/CdSe/CdMgSe structure (a) and its PL spectrum at 77 K (b).

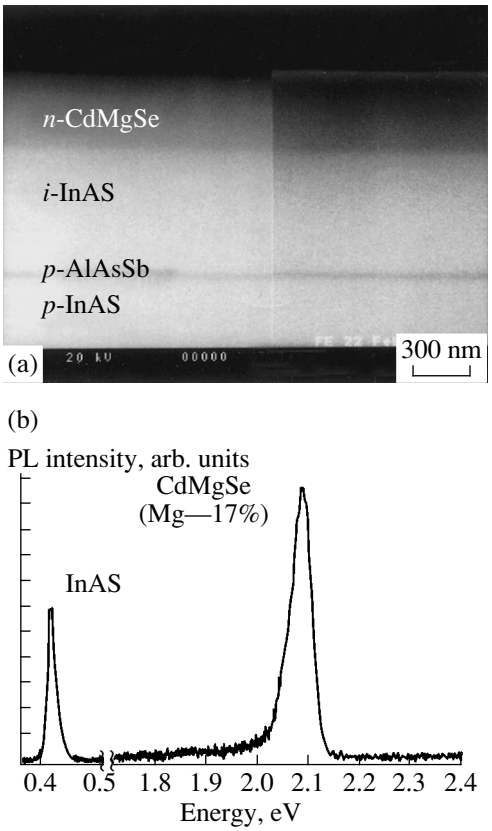

Fig. 2. Cross-sectional SEM image of a diode *p–i–n* *p*-InAs/*p*-AlAsSb/*i*-InAs/*n*-CdMgSe/*n*-CdSe structure (a) and its PL spectrum at 77 K (b).

with a thinner arsenic layer evaporating at a lower temperature (T_s = 460°C), a (2 × 4) surface reconstruction was observed at the initial instant of time, corresponding to an As-stabilized surface which, on being kept at the same temperature, gradually transformed into (4 × 2) via an intermediate reconstruction (4 × 4).

The growth of the (II–VI) part was started by placing the structure surface under a Cd flux for 5 s. Further, a thin (~10 nm) CdSe (or CdMgSe) buffer layer was grown in the epitaxy regime with an enhanced migration of atoms [7] at T_s = 200°C, with no stage of 3D growth revealed by RHEED. After that, the substrate temperature was raised to T_s = 280°C and the remaining (II–VI) part of the structure was grown in the MBE regime with beam pressure ratio Se/Cd ≈ 3. In doing so, a clear (2 × 1) diffraction pattern was observed, corresponding to a Se-enriched surface (the beam pressure ratio Se/Cd = 2 approximately corresponds to an effective II/VI flux ratio of 1 : 1). A $ZnCl_2$ source was used to obtain *n*-Cd(Mg)Se layers.

Two samples (A and B) intended for optical measurements had identical (III–V) parts and different layers in the (II–VI) part. Sample A comprised two intentionally undoped layers: a CdSe layer, 83 nm thick, and a CdMgSe layer of thickness 0.56 μm. The (II–VI) part of sample B consisted of a 50-nm-thick undoped CdMgSe layer and two chlorine-doped layers: a 0.3-μm-thick *n*-CdMgSe layer and a thin (10 nm) upper *n*-CdSe layer. The electron concentration in these doped layers was, according to capacitance–voltage data, $n \approx 4 \times 10^{17}$ cm^{-3}. Thus, sample B was a diode structure with a *p–n* junction at the AlAsSb/InAs interface. Cross-sectional SEM micrographs of samples A and B are presented in Figs. 1a and 2a, respectively.

To study transport characteristics, two more samples (C and D) were grown on semi-insulating GaAs (100) substrates. Both the samples were fabricated as conventional structures with a 2D electron gas on the basis of AlGaSb/InAs heterostructures with a quantum well (QW), i.e., an InAs layer 15 nm thick [8]; however, in the given case the growth was interrupted immediately after the QW was obtained, and, then, the structures were overgrown similarly to samples A and B but with different Cd(Mg)Se layers in the II–VI chamber. In the case of sample C, an undoped CdSe layer 15 nm thick was deposited first, followed by 10-nm-thick undoped and 50-nm-thick chlorine-doped CdMgSe

layers, and, finally, by an upper *n*-CdSe layer 10 nm thick. In the case of sample D, no CdSe layer was deposited onto InAs and the heterostructure was a modulation-doped AlGaSb/InAs/CdMgSe QW, in contrast to sample C, an AlGaSb/InAs/CdSe/CdMgSe heterostructure containing an InAs/CdSe heterointerface. Based on the calibration of the level of chlorine doping, performed for sample B, it was assumed that the electron concentration in the chlorine-doped layers was $n \sim 10^{18}$ cm^{-3}.

3. STRUCTURAL AND OPTICAL MEASUREMENTS

To assess the quality of separate layers constituting the hybrid structures, photoluminescence (PL) investigations were performed in a wide spectral range covering both the infrared and the visible part of the spectrum. The PL was measured with single-grating monochromators and various kinds of excitation sources for different spectral ranges. The PL in the (III–V) part of the structure, emitting in the infrared part of spectrum, was excited with an InGaAs laser diode operating in continuous wave (CW) mode at a wavelength of λ = 950 nm. The light intensity on the sample surface was 2 W/cm^2. The PL signal was recorded with a lead sulfide photodetector with thermoelectric cooling. The PL in the visible range from the Cd(Mg)Se layer was excited by a He–Cd laser (λ = 325 nm), also operating in the CW mode.

The PL spectrum of sample A, taken at 77 K, is presented in Fig. 1b. It can be seen that the spectrum shows three comparatively narrow peaks at 0.41, 1.737, and 2.111 eV, correlating well with the lines of band-edge luminescence in InAs, CdSe, and CdMgSe, respectively. In addition, the spectrum contains one more, rather broad peak at around 1.9 eV, which is presumably due to donor–acceptor recombination in the CdMgSe layer, typical of wide-bandgap II–VI compounds [9]. An estimate of the relative content of Mg in the $Cd_{1-x}Mg_xSe$ layer in an approximation of the linear dependence of the energy gap on the composition of the solid solution gives $x \approx 0.15$. A close value $x \approx 0.17$ was calculated from X-ray diffraction analysis data (Fig. 3), with the CdMgSe layer considered to be completely elastically strained (this solid solution is lattice-matched to InAs at $x \approx 0.1$). Despite the absence of relaxation and the intense luminescence from this structure, TEM studies demonstrated the presence of a rather high (~10^7 cm^{-2}) density of stacking faults arising at the InAs/CdSe heterointerface (Fig. 4). In our opinion, the high density of stacking faults is due to the fact that the growth of the (II–VI) part of the structure started, as mentioned above, on a surface enriched in indium. This, in turn, was due to the formation of a relatively thick passivating layer of arsenic, whose complete removal before the growth of the (II–VI) part required rather high annealing temperatures. It is assumed that optimization of the passivation and subsequent annealing will allow the growth of the (II–VI) part on the As-stabilized surface, which should lead to a lower density of stacking faults at the InAs/Cd(Mg)Se interface, as in the case of GaAs/ZnSe [10].

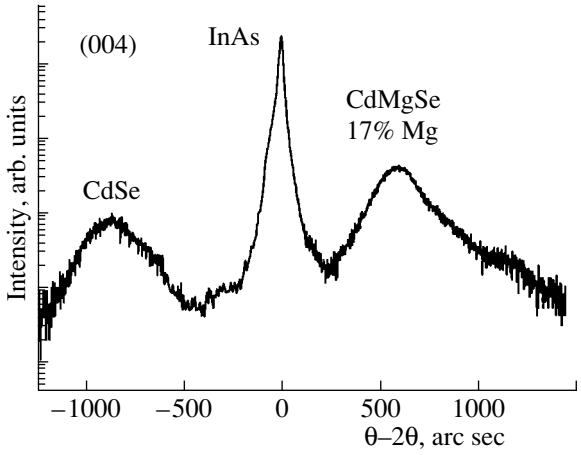

Fig. 3. Double-crystal X-ray rocking curve measured at (004) InAs reflection for an AlAsSb/InAs/CdSe/CdMgSe structure.

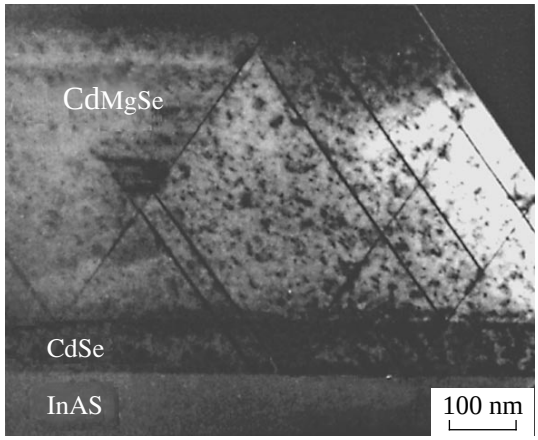

Fig. 4. Cross-sectional TEM image of the AlAsSb/InAs/CdSe/CdMgSe structure.

The PL spectrum of sample B, in contrast to sample A, only shows two narrow peaks corresponding to band-to-band transitions in InAs and CdMgSe (Fig. 2b). It should be noted that high-intensity electroluminescence was also observed in sample B both at 77 K and at room temperature. The electroluminescence spectrum contained only the InAs emission line, with the intensity decreasing only seven- to tenfold on elevating the temperature from 77 to 300 K.

The results presented of the structural and optical investigations confirm the high quality of the InAs/Cd(Mg)Se heterointerface, but fail to provide

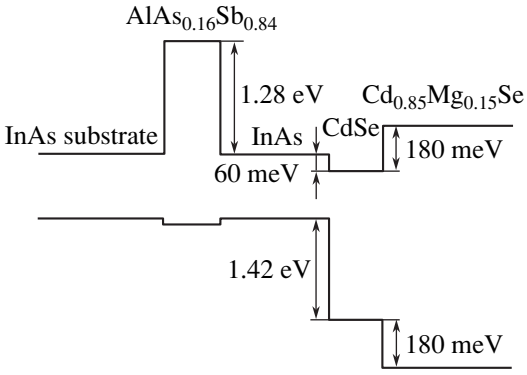

Fig. 5. Energy band diagram for a InAs/AlAsSb/InAs/CdSe/CdMgSe heterostructure.

exhaustive information about the relative position of energy bands. To theoretically evaluate the band offset at the InAs/CdSe interface, we used the known values for the heteropairs CdSe/ZnSe, ZnSe/GaAs, and GaAs/InAs and also Van de Walle's model-solid theory [11] to account for the effect of elastic strain on the band structure. The calculation we performed demonstrated that the InAs/CdSe interface is a type-II heterojunction, with InAs forming a potential barrier $\Delta E_c \approx$ 60 meV for electrons at the CdSe conduction band bottom and the heavy hole valence band offset at this interface $\Delta E_v \approx 1.42$ eV (Fig. 5). The opposite situation would be expected for the InAs/CdMgSe interface when there is a sufficiently high Mg content in the solid solution. For the structures under study, the difference between the energy gaps of CdSe and CdMgSe is, according to PL data (Figs. 1b and 2b), ~360 meV. It would be expected that at least half this value is accounted for by the conduction band offset. Thus, the InAs/$Cd_{0.85}Mg_{0.15}Se$ heterointerface is a type-I heterojunction with a conduction band offset of $\Delta E_c \approx$ 120 meV and a higher valence band offset of $\Delta E_v \approx$ 1.6 eV. It should be noted that, owing to such a large valence band offset, the InAs/CdMgSe heterojunction can be used in designing laser heterostructures emitting in the medium IR range (2–5 μm) as an effective barrier for holes, hindering their leakage from the active InAs region of a device.

To verify theoretical estimates, Hall effect measurements were performed on samples C and D. Sample C, containing an InAs/CdSe heterointerface, demonstrated relatively low electron mobility: $\mu_e =$ 800 cm^2/(V s) at $T = 300$ K and $\mu_e = 500$ cm^2/(V s) at $T = 77$ K. These values are close to the electron mobilities in bulk hexagonal *n*-CdSe, which suggests the absence of an electron channel in the InAs layer as a result of electron accumulation in the CdSe QW [12]. By contrast, much higher electron mobilities were obtained in sample D: $\mu_e = 2700$ cm^2/(V s) at $T = 300$ K and $\mu_e = 2200$ cm^2/(V s) at $T = 77$ K. Such high values cannot be accounted for only by the conduction in the CdSe layer, which indicates that electrons in InAs at the InAs/CdMgSe heterointerface are involved in conduction. The mobilities obtained for the 2D electron gas in InAs are much smaller than those commonly observed in AlGaSb/InAs/AlGaSb structures with QWs (>150000 cm^2/(V s) at 77 K). Such a significant difference is presumably due to the appearance of a high density of defects at the InAs/AlGaSb heterointerface through the relaxation of elastic strains in the InAs/CdMgSe part of the structure, lattice-mismatched with respect to the GaSb buffer layer. To make the mobility of the 2D electron gas higher, the GaSb buffer layer must contain ~6 mol % arsenic to become lattice-matched to InAs.

4. CONCLUSION

Hybrid AlAsSb/InAs/Cd(Mg)Se heterostructures were fabricated for the first time by successive growth in two separate MBE machines. These structures show high-intensity luminescence both under optical excitation and with current pumping, confirming the existence of effective energy barriers for the carriers. Investigations based on RHEED, X-ray diffraction analysis, transmission electron microscopy, and photoluminescence and electroluminescence methods indicate a relatively high quality of the interface between the III–V and II–VI layers. The data obtained on the longitudinal electron transport at the InAs/Cd(Mg)Se heterointerface are in good agreement with a theoretical estimate of the mutual positions on energy bands in the proposed hybrid structures. The estimate shows that the InAs/CdSe interface is a type-II heterojunction, whereas the InAs/$Cd_{0.85}Mg_{0.15}Se$ heterointerface is a type-I heterojunction with large valence band offset $\Delta E_v \approx 1.6$ eV.

Structures of this kind seem to be exceedingly effective in optoelectronic applications and in basic research into electron transport at the III–V/II–VI heterointerface.

ACKNOWLEDGMENTS

We thank K.D. Moiseev for the electroluminescence measurements.

This study was supported by the Russian Foundation for Basic Research (project nos. 98-02-18211, 99-02-17097, 00-02-17022), Program of the Ministry of Science "Physics of Solid-State Nanostructures" (grant nos. 1035 and 2014), and the Air Force Lab EOARD (contract no. F61775-99-WE-016). The efforts to grow the II–VI compounds were supported by the Volkswagen Foundation and INTAS (grant no. 97-31907).

REFERENCES

1. R. M. Park and N. M. Salansky, Appl. Phys. Lett. **44**, 249 (1984).
2. R. F. C. Farrow, J. Vac. Sci. Technol. **19**, 150 (1981).
3. N. Samarth, H. Luo, J. K. Furdyna, *et al.*, Appl. Phys. Lett. **54**, 2680 (1989).
4. F. Firszt, S. Legowski, H. Meczynska, *et al.*, J. Cryst. Growth **184/185**, 1053 (1998).
5. S. V. Ivanov, S. V. Sorokin, P. S. Kop'ev, *et al.*, J. Cryst. Growth **159**, 16 (1996).
6. S. V. Ivanov, S. V. Sorokin, I. L. Krestnikov, *et al.*, J. Cryst. Growth **184/185**, 70 (1998).
7. S. V. Sorokin, A. A. Toropov, T. V. Shubina, *et al.*, J. Cryst. Growth **201/202**, 461 (1999).
8. Yu. Vasilyev, S. Suchalkin, K. von Klitzing, *et al.*, Phys. Rev. B **60** (15), 10636 (1999).
9. J. Qui, J. M. DePuydt, H. Cheng, and M. A. Haase, Appl. Phys. Lett. **59**, 2992 (1991).
10. M. A. Haase, J. Qiu, J. M. DePuydt, and H. Cheng, Appl. Phys. Lett. **59**, 1272 (1991).
11. C. G. van de Walle, Phys. Rev. B **39**, 1871 (1989).
12. *Chemical Encyclopedia*, Ed. by I. L. Knunyants (Sov. Éntsiklopediya, Moscow, 1990), Vol. 2.

Translated by M. Tagirdzhanov

Semiconductors, Vol. 35, No. 4, 2001, pp. 424–426. Translated from Fizika i Tekhnika Poluprovodnikov, Vol. 35, No. 4, 2001, pp. 436–438.

SEMICONDUCTOR STRUCTURES, INTERFACES, AND SURFACES

Interface States and Capacitance–Voltage Characteristics of *n*-SnO_2:Ni/*p*-Si Heterostructures under Gas-Adsorption Conditions

R. B. Vasil'ev*, A. M. Gas'kov, M. N. Rumyantseva, L. I. Ryabova, and B. A. Akimov

Moscow State University, Vorob'evy gory, Moscow, 119899 Russia

** e-mail: mila@mig.phys.msu.su*

Submitted September 14, 2000; accepted for publication September 25, 2000

Abstract—The *n*-SnO_2:Ni/*p*-Si heterostructures were synthesized with a mean size of 6–8 nm of crystallites in the tin dioxide layer. The capacitance–voltage characteristics of these structures were measured in dry air and under adsorption of NO_2 and C_2H_5OH molecules. The variation of a reference-signal frequency within 0.5–20 kHz made it possible to separate out the contribution of heterointerface states to the structure capacitance. Adsorption of NO_2 molecules was shown to reduce the density of the heterointerface states, while adsorption of ethanol molecules resulted in its increase. © *2001 MAIK "Nauka/Interperiodica".*

The heterointerface states control to a large extent the properties of heterostructures of both diode and tunneling types. The presence of additional charges at an interface leads, in particular, to the appearance of an additional contribution to the capacitance of structures [1]. In contrast to the capacitance of the heterojunction itself determined in terms of the Anderson model, the additional capacitance associated with the heterointerface-state recharging depends on a reference-signal frequency f if the characteristic times of centers interface-state recharging $\tau \geq 1/2\pi f$. The possibility of modifying the heterointerface in the course of gas adsorption may be used to develop new approaches to solving gas-monitoring problems [2].

In this study, we investigate how the capacitance–voltage (C–V) characteristics of *n*-SnO_2:Ni/*p*-Si heterostructures in dry air and in a gaseous mixture containing NO_2 and C_2H_5OH molecules depend on a variation in the reference-signal frequency f from 0.5 to 20 kHz at room temperature. The reference-signal amplitude was below 1 mV and the bias amplitude V varied within $-3\ \text{V} < V < 3\ \text{V}$. The SnO_2 film was deposited by aerosol pyrolysis. As a substrate, we used a *p*-Si single crystal oriented along the ⟨100⟩ axis with a resistivity of 10 Ω cm. The thickness of the SnO_2:Ni layers amounted to 0.8–1.0 μm, and the mean size of the nanocrystallites was 6–8 nm. The porous structure of the layers is caused by the segregation of nanocrystalline grains in agglomerates of 0.05–0.10 μm in size. Thus, a SnO_2:Ni layer, as one of the forming elements of the heterojunction, serves simultaneously as a permeable membrane for gas molecules, which enables them to diffuse towards the heterointerface. The Ni-impurity content in the SnO_2 layer amounts to 0.8 at. %. The Au and Al ohmic contacts were deposited onto the SnO_2 and Si layers, respectively, by vacuum evaporation. The gold-contact area was ~0.07 cm^2 (less than 10% of the film area available for gas adsorption). The synthesis and the methods of structure investigations were described in more detail previously [3–5].

The C–V characteristics of heterostructures in dry air are shown in Fig. 1. An increase in the reference-sig-

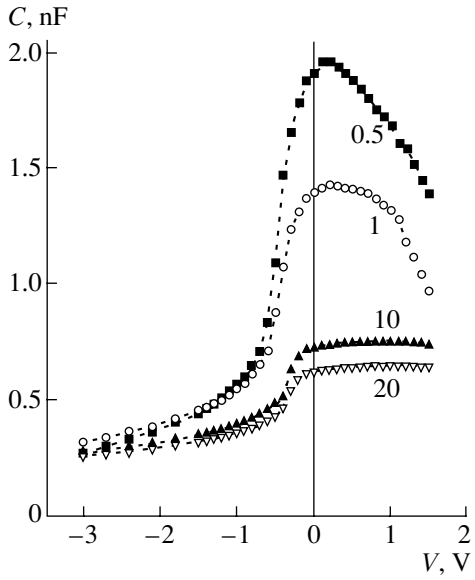

Fig. 1. Capacitance–voltage characteristics of the *n*-SnO_2:Ni/*p*-Si heterostructure in dry air. The numbers at the curves are the reference-signal frequencies expressed in kHz.

1063-7826/01/3504-0424$21.00 © 2001 MAIK "Nauka/Interperiodica"

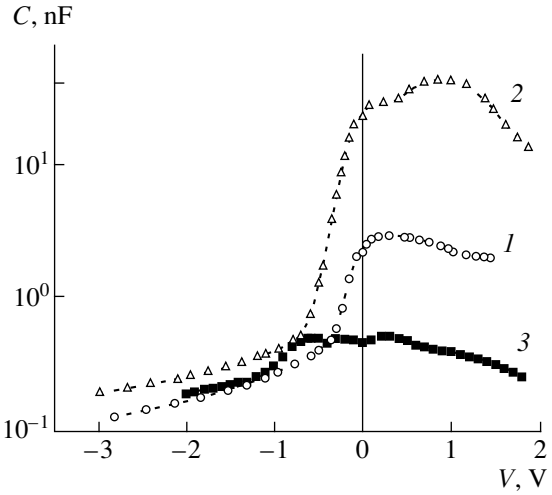

Fig. 2. Capacitance–voltage characteristics of the n-SnO_2:Ni/p-Si heterostructure in (*1*) dry air, (*2*) N_2 + 10^4 ppm C_2H_5OH, and (*3*) N_2 + 10^3 ppm NO_2.

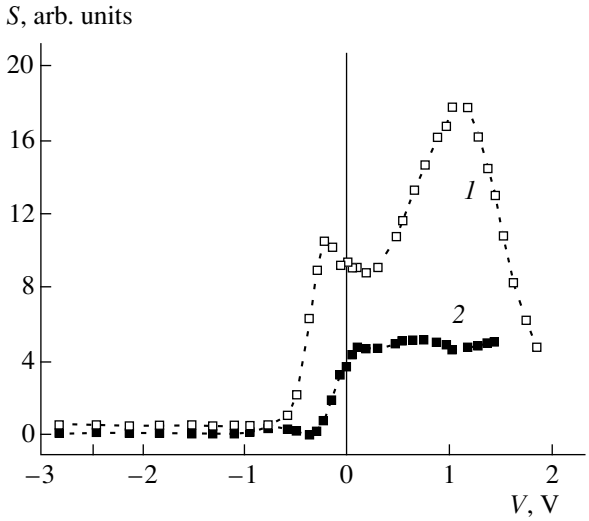

Fig. 3. Sensitivity S of the n-SnO_2:Ni/p-Si heterostructures to (*1*) C_2H_5OH and (*2*) NO_2 as a function of a bias V.

nal frequency leads to a significant reduction in capacitance C, which is indicative of the presence of a contribution from heterointerfaces. Under gas-adsorption conditions, the C–V characteristics are considerably modified. In Fig. 2, we show the heterostructure C–V characteristics measured for a reference-signal frequency of 1 kHz in air (curve *1*) and in gaseous mixtures of 10^4 ppm C_2H_5OH + N_2 (curve *2*) and 10^3 ppm NO_2 + N_2 (curve *3*). It can be seen from Fig. 2 that adsorbed C_2H_5OH and NO_2 molecules have opposite effects. The ethanol adsorption induces an additional increase in capacitance; at the same time, the NO_2 adsorption leads to a decrease in C, with the absolute value of capacitance being close to those obtained in air for higher f. This indicates that the concentration of heterointerfaces responsible for the frequency-dependent contribution to the capacitance decreases in this case.

The sensitivity of SnO_2 nanocrystalline films to gas is known to be mainly controlled by oxygen hemisorbed on the surface and at grain boundaries in the O_2^- state. The acceptor energy level corresponding to these oxygen states is located at higher energies than the surface acceptor level of an adsorbed NO_2 molecule [6]. We may assume that the NO_2 adsorption leads to recharging of the corresponding oxygen states and stimulates oxygen desorption. At the same time, the NO_2 molecules themselves are unlikely to initiate any additional charges at the heterointerface, which make a marked contribution to capacitance. It is not inconceivable that the recharging time is too large for these states compared to $1/2\pi f$. A reduction in density of heterointerfaces is indirectly evidenced also by the character of modifications in the current–voltage (I–V) characteristics of the structures under the effect of gas adsorption. It should be noted that, in the n-SnO_2:Ni/p-Si structures (compared to structures where the tin dioxide layer was either undoped or Cu- or Pd-doped [5]), the most significant decrease in the forward current was observed under conditions of NO_2 adsorption. Furthermore, only in the n-SnO_2:Ni/p-Si structures did the reverse current also decrease considerably. Nonlinearity of the I–V characteristic became less pronounced; in this case, the reverse current somewhat exceeded the forward one. As we have noted in [5], the behavior of the I–V characteristic of the n-SnO_2:Ni/p-Si heterostructures under gas adsorption is mainly dependent on the tunneling processes; it is the heterointerfaces that play an important role in the above processes. Thus, it seems logical to relate an abrupt increase in the resistance of the n-SnO_2:Ni/p-Si structure (accompanied by a reduction in the capacitance under the NO_2 adsorption) directly to a decrease in the density of heterointerfaces, which, on the one hand, form a channel for the tunneling current and, on the other hand, are responsible for the frequency-dependent contribution to the capacitance of these structures.

Contrary to this, the ethanol-molecule adsorption enhances the density of heterointerfaces. The growth of the forward tunneling current in the presence of C_2H_5OH molecules confirms this assumption [5]. It is difficult to determine unambiguously whether or not this increase in the heterointerface density is associated with an increase in the concentration of hemisorbed oxygen or with the origination of additional states induced by the ethanol-molecule dissociation. However, a modification in the C–V-characteristic shape is

noteworthy. Along with a peak near the zero bias, an additional peak of C shifted into the region of positive values of V appears. The appearance of this peak is more clearly pronounced for the field dependence of sensitivity $S = (C_1 - C_2)/C_2$, $C_1 > C_2$, where C_i are heterostructure capacitances in air and in a gas mixture (Fig. 3). The dependences obtained show that, when using the heterostructures investigated as gas sensors, it is necessary to choose bias voltages corresponding to the highest sensitivity of the structure.

ACKNOWLEDGMENTS

This study was supported in part by the Russian Foundation for Basic Research, project nos. 00-03-32083a and 98-03-32843a.

REFERENCES

1. J. P. Donnelly and A. G. Milnes, IEEE Trans. Electron Devices **ED-14**, 63 (1967).
2. J. N. Zemel, E. Keramati, C. W. Spivak, and A. D. D'Amico, Sens. Actuators B **1**, 427 (1981).
3. M. N. Rumyantseva, A. M. Gaskov, L. I. Ryabova, *et al.*, Mater. Sci. Eng. **41**, 333 (1996).
4. B. A. Akimov, A. M. Gas'kov, M. Labeau, *et al.*, Fiz. Tekh. Poluprovodn. (St. Petersburg) **33**, 205 (1999) [Semiconductors **33**, 175 (1999)].
5. R. B. Vasil'ev, A. M. Gas'kov, M. N. Rumyantseva, *et al.*, Fiz. Tekh. Poluprovodn. (St. Petersburg) **34**, 993 (2000) [Semiconductors **34**, 955 (2000)].
6. J. A. Agapito and J. P. Santos, Sens. Actuators B **31**, 93 (1996).

Translated by V. Bukhanov

Semiconductors, Vol. 35, No. 4, 2001, pp. 427–432. Translated from Fizika i Tekhnika Poluprovodnikov, Vol. 35, No. 4, 2001, pp. 439–444.

SEMICONDUCTOR STRUCTURES, INTERFACES, AND SURFACES

The Transition Layer in TiB_2–GaAs and Au–TiB_2–GaAs Schottky Contacts

E. F. Venger, R. V. Konakova, O. B. Okhrimenko, S. Yu. Sapko, L. V. Shekhovtsov*, and V. N. Ivanov

Institute of Semiconductor Physics, National Academy of Sciences of Ukraine, Kiev, 03028 Ukraine

**e-mail: k208@photon.kiev.ua*

Submitted July 18, 2000; accepted for publication September 26, 2000

Abstract—Spectral characteristics of the transverse bulk photovoltage in the TiB_2–GaAs and Au–TiB_2–GaAs Schottky contacts for starting samples (unannealed) and samples annealed at 400, 600, and 800°C were measured. The concentration of the dopant for the *n*-GaAs substrate was 10^{16} cm^{-3}. It was found that the transition layer is formed in the TiB_2–GaAs structures owing to the diffusion of boron atoms into the GaAs substrate. Thermal annealing leads to an increase in the doping level of the layer. For the Au–TiB_2–GaAs structure, the transition layer is formed, with the doping level of this layer being weakly affected by thermal annealing. The spectral position of the bulk-photovoltage peaks indicates that the tails of the density of states are formed in the band gap of the semiconductor transition layer owing to an increase in the dopant concentration to 10^{17}–10^{18} cm^{-3}. © *2001 MAIK "Nauka/Interperiodica".*

1. In recent years, numerous publications were devoted to borides of refractory metals (see, for example, review [1]). These materials are of interest because of their application as the contacts for semiconductor microelectronic devices, with the high electrical conductivity of these contacts accompanied by chemical and thermal stability [2–4].

Numerous investigations of boride compounds, which are used or supposed to be used as thermally stable contacts in the metal–semiconductor heterosystem, were devoted mainly to their structural properties [5–7]. In order to investigate these materials, Schottky contacts were formed via deposition of the films in various growth modes on various substrates, including GaAs.

For parameters of the Schottky diodes, in addition to the diffusion barrier height, the structural and electrical uniformity of the contact over the area is important. For current flow through the contact, the electrical resistance of both the metal (or metal-like) contact and the heterojunction (HJ) region at the interface are of great importance.

The photoelectric methods are important for investigation of the uniformity of electrical characteristics for Schottky contacts. These methods are sensitive to the nonuniformity of the potential barrier at the metal–semiconductor interface, as well as to electrical resistivity of the semiconductor crystal and charge carrier lifetime.

The structural methods of investigation yield extensive data on the parameters of the crystal lattice and near-interface regions, the structure of the metal film itself, and the distribution of the interstitial atoms and phases close to the contact. These data allow one to make indirect conclusions on the electrical properties of the contact, since the subsystem of free electrons of the crystal is not considered. However, the photogeneration of nonequilibrium charge carriers in conditions of weak excitation when carrier concentration is much lower than the dark concentration of majority carriers ($\Delta n \ll n_0$) leads to the appearance of diffusion–drift current–flow processes in semiconductor structures. This allows one to assess the electrical properties of objects under investigation.

Previously, discovery of the bulk photoeffect allowed one to be hopeful of its application for investigating the inhomogeneities of semiconductor crystals [8, 9]. However, the development of the growth technology of homogeneous semiconductor crystals put the capabilities of this method significantly behind.

A different situation is characteristic of semiconductor microelectronic heterostructures. First, they always contain several layers with differing physical characteristics. Second, their linear dimensions are comparable with macrononuniformities in electrical properties of these layers and with diffusion length of nonequilibrium charge carriers. In addition, the formation of transition regions between the layers introduces distortions into the current-flow mechanism in such a device structure. Consequently, the investigations of photovoltage spectral characteristics for multilayer (or just for two-layer) structures can give information about inhomogeneities, their spatial extension, and the band structure of semiconductor layers. It is noteworthy that recently published data confirm the necessity

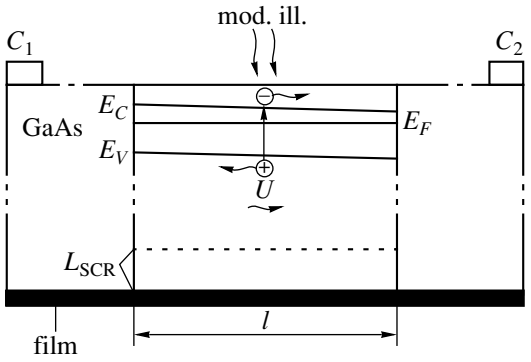

Fig. 1. The geometry of experiments with measurement of the transverse bulk photovoltage. Notation: mod. ill. stands for monochromatic modulated radiation; film denotes the TiB_2 or Au–TiB_2 film; E_C, E_V, and E_F are the conduction band bottom, valence band top, and Fermi level of the GaAs substrate, respectively; L_{SCR} is the space charge region of the Schottky contact; l is the length of the illuminated part of the sample; U is the bulk photovoltage generated by the modulated light; and C_1 and C_2 denote the measuring contacts.

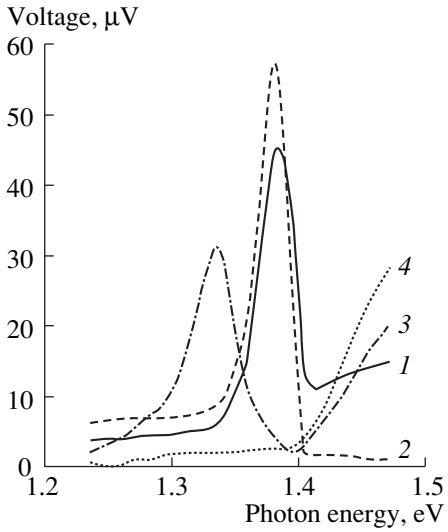

Fig. 2. Spectral characteristics of the transverse photovoltage for the TiB_2–GaAs samples measured under illumination from the substrate side: (*1*) starting (unannealed) sample; (*2*), (*3*), and (*4*) samples annealed at T = 400, 600, and 800°C, respectively.

of taking into account the nonuniformity of impurity distribution over the interface of a semiconductor structure [10, 11].

This paper is devoted to the investigation of the spectral characteristics of the transverse bulk–gradient photovoltage for the TiB_2–GaAs and Au–TiB_2–GaAs structures. It was demonstrated previously that the specific features of the photovoltage spectral characteristics for a semiconductor heterostructure [12, 13] contain information about uniformity of the regions adjoining the heterointerface.

2. The objects investigated were *n*-type epilayers grown on the Te-doped n^+-GaAs substrate. The layer thickness was ~2 μm and the density of charge carriers was 10^{16} cm^{-3} without illumination. The GaAs substrate was 200 μm thick. A TiB_2 film 500 Å thick was deposited on this structure from the epilayer side using magnetron sputtering.

The metal film in the Au–TiB_2–GaAs structures consisted of two layers, namely, the TiB_2 and Au films, each of which was 500 Å thick. The samples of starting structures and structures annealed for 1 min at temperatures T = 400, 600, and 800°C were investigated. Thus, the structures investigated were the TiB_2–GaAs and Au–TiB_2–GaAs Schottky contacts. The samples used for measurements were 10–12 mm in length and width. The length of the illuminated part of the sample was l = 5 mm, and the width was 2 mm.

The geometry of experiments is shown in Fig. 1. The gradient of the dark resistivity (doping), which gave rise to photovoltage, is conventionally shown by the slope of the conduction-band bottom E_C and the valence-band top E_V for the GaAs crystal. The photovoltage amplitude U was measured between the C_1 and C_2 contacts, normally to the gradient of the nonequilibrium-carrier concentration.

The C_1 and C_2 measuring contacts were formed on the edges of the GaAs substrate at a distance of 2–3 mm from the boundary of the illuminated part of the sample. Photovoltage was generated by exposing the samples to monochromatic light from both the GaAs substrate side and from the TiB_2 or Au–TiB_2 sides. The light was modulated at a frequency of 537 Hz. The incident light intensity was kept constant at the level of $N = 8 \times 10^{14}$ photon/(cm^2 s) over the entire spectral range under investigation. The aperture spectral width for the MDR-24 monochromator was 0.0026 μm.

The procedure also allows one to direct the unmodulated monochromatic light on the part of the sample irradiated with monochromatic modulated light, as well as to vary the illumination intensity and wavelength. Investigations were carried out at T = 300 K.

3. Spectral characteristics of the transverse photovoltage that were measured on illumination of the sample from the GaAs substrate side are shown in Fig. 2. Curve *1* corresponds to the starting (unannealed) sample, and curves *2–4* refer to the samples annealed at 400, 600, and 800°C, respectively. It can be seen from Fig. 2 that the photovoltage peak is observed in the spectral characteristics. The peak shifts to longer wavelengths as the annealing temperature increases. The photovoltage amplitude varied insignificantly. The peaks for curves *1–3* are positioned beyond the GaAs absorption edge, i.e., at photon energies lower than the GaAs band gap. Curve *4*, which corresponds to the sample annealed at T = 800°C, is an exception. In this

case, the amplitude decreases gradually in the GaAs fundamental adsorption region and further to the wavelength $\lambda = 0.92$ μm ($h\nu = 1.35$ eV), the photovoltage peak being absent.

It should be noted that the ratio between the photovoltage amplitudes in the vicinity of the peak and in the intrinsic absorption region for GaAs varied in the spectral characteristics shown with variation of the annealing temperature for the sample (Fig. 2, curves *1–3*).

Spectral characteristics of the transverse photovoltage that were measured for the same samples on their illumination from the TiB_2 film side (Fig. 3) also have their own specific features. It should be noted that the photovoltage amplitudes (see curves *1–3*) in the intrinsic absorption region for GaAs are normalized to an identical magnitude for convenience of comparison to each other. The falloff portion of curve *2* (annealing temperature of 400°C) is shifted to longer wavelengths practically in parallel with curve *1* (starting sample). At the same time, the falloff of curve *3* (annealing temperature of 600°C) is more gently sloped compared to curves *1* and *2*. All curves have tails that are extended to longer wavelengths. For the samples annealed at $T =$ 800°C (curve *4*), the shape of the spectral characteristic differs significantly from curves *1–3* (Fig. 3). After a small falloff in the vicinity of the intrinsic absorption edge for GaAs, the photovoltage peak in the vicinity of $\lambda = 0.915$ μm ($h\nu = 1.358$ eV) is observed, whose amplitude significantly exceeds the photovoltage value in the intrinsic absorption region for GaAs ($\lambda \lesssim 0.88$ μm, $h\nu \gtrsim 1.41$ eV). At the same time, the photovoltage amplitude of curves *1–3* is practically constant in this wavelength region. It is noteworthy that the photovoltage amplitude of curve *4* in Fig. 3 is diminished by a factor of two compared to the experimental photovoltage values for convenience of representation.

4. Specific features of the spectral characteristics of the transverse photovoltage measured for the TiB_2–GaAs Schottky contact allowed us to suggest the HJ model.

First of all, the spectral position of the peaks in the curves obtained on illumination of the samples from the GaAs side (Fig. 2) allows us to suggest the existence of a transition layer between the substrate and the TiB_2 film. The transition layer is formed during the stage of deposition of the TiB_2 film on the GaAs substrate. This follows from the existence of the photovoltage peak positioned beyond the GaAs absorption edge in the spectral characteristics, which corresponds to the starting sample (curve *1* in Fig. 2). At annealing temperature $T =$ 400°C, the peak begins to broaden and shift to lower photon energies. An increase in temperature to 600°C leads to further peak shifts to the longer wavelength $\lambda = 0.93$ μm ($h\nu = 1.33$ eV), and the peak completely disappears at $T =$ 800°C. Curve *4* ($T =$ 800°C) features a gently sloping edge (Fig. 2). This behavior indicates that the transition layer broadens with increasing temperature, and the layer nonuniformity

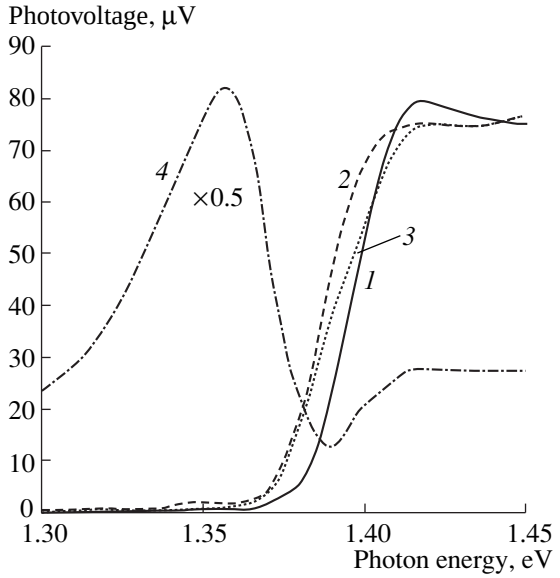

Fig. 3. Spectral characteristics of the transverse photovoltage for the TiB_2–GaAs samples measured under illumination from the TiB_2 film side. Curves *1–4* demonstrate the data for the same samples as in Fig. 2.

increases due to the mixing of chemical compounds of the TiB_2 film and GaAs. A decrease in the peak height with an increase in the annealing temperature and peak disappearance at $T =$ 800°C points to an increase in the recombination rate of electron–hole pairs in the transition-layer region. This is related to an increase in imperfection of the layer, a decrease in the band bending at the TiB_2–GaAs contact, and an accompanying natural increase in the recombination flux to the interface. An increase in the photovoltage amplitude in the fundamental absorption region for GaAs was also observed experimentally with an increase in the annealing temperature (Fig. 2). This points to a change in the ratio between the recombination rates at the interface and in the GaAs bulk. However, no regular relation was observed between these parameters and the annealing temperature.

The shape of the photovoltage spectral characteristics that were measured under excitation from the TiB_2 film side (Fig. 3) can also be described by the model of the TiB_2–GaAs HJ with the transition layer. The falloff portion of the photovoltage spectral characteristics for the starting sample (Fig. 3, curve *1*) lies in the range of photon energies lower than the GaAs band gap. After annealing at $T =$ 400°C (curve *2*), this portion shifts to lower photon energies, i.e., to the long-wavelength spectral region. This shift in the spectral characteristic can be related to an increase in the thickness of the transition semiconductor layer with a simultaneous increase in its doping level. The falloff, which is more gradual and extended to the long-wavelength region of the spectral characteristic at an annealing temperature

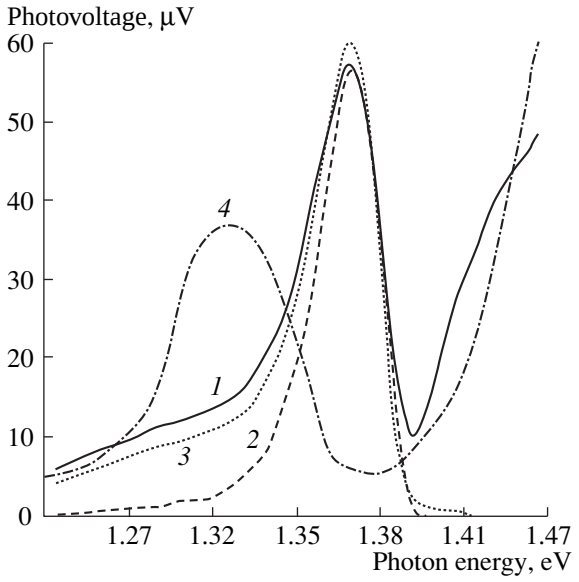

Fig. 4. Spectral characteristics of the transverse photovoltage for the Au–TiB_2–GaAs samples measured under illumination from the substrate side: (*1*) starting (unannealed) sample; (*2*), (*3*), and (*4*) samples annealed at T = 400, 600, and 800°C, respectively.

of 600°C (curve *3*), points to an increase in the transition layer thickness. The photovoltage spectral characteristic for the samples annealed at T = 800°C (curve *4*) differs from curves *1–3*. In the vicinity of $\lambda = 0.92$ μm ($h\nu = 1.35$ eV), a photovoltage peak appears whose amplitude exceeds the photovoltage amplitude in the fundamental absorption region for GaAs. This is apparently related to the formation of the extended nonuniform transition layer at this annealing temperature. In the vicinity of the wavelength $\lambda = 0.88$ μm ($h\nu$ = 1.41 eV), which corresponds to the GaAs absorption edge, the photovoltage amplitude decreases.

The shape of curves *1–3* (Fig. 3) in the range λ = 0.84–0.87 μm is of great importance. Here, the photovoltage amplitude for each particular curve is practically constant for the following reason. The light-absorption coefficient for GaAs at wavelengths λ = 0.84–0.87 μm varies from 10^4 to 10^3 cm^{-1} [14], which corresponds to an effective absorption depth of $\gtrsim 1$ μm. According to published data, the band bending for the TiB_2–GaAs Schottky contact is in the range of 0.7–0.8 eV [15]. The width of the space charge region (SCR) is $L_{SCR} = 0.3$ μm, which is smaller than the effective light-absorption depth for GaAs. For this reason, the influence of recombination in the SCR on the photovoltage amplitude is slight compared to that of the bulk recombination. The transition layer contribution to the photovoltage in the wavelength range of 0.84–0.87 μm is also undetectable (Fig. 2). Its influence on the spectral characteristics manifests itself at wavelengths $\lambda > 0.87$ μm ($h\nu < 1.42$ eV) only. Here, the fundamental absorption for GaAs is reduced and the relative contribution of the photovoltage, which is formed in the transition layer, correspondingly increases.

5. Spectral characteristics of the transverse photovoltage, which were measured for the Au–TiB_2–GaAs structure on illumination of the samples from the GaAs side, are shown in Fig. 4. Curve *1* corresponds to starting (unannealed) samples, and curves *2–4* correspond to the samples annealed at T = 400, 600, and 800°C, respectively. A clearly defined peak was observed in curves *1–3* in the vicinity of $\lambda = 0.9$ μm ($h\nu = 1.38$ eV). At T = 800°C (curve *4*), this peak is shifted to λ = 0.925 μm ($h\nu = 1.34$ eV) and its height decreases. Compared to the TiB_2–GaAs structure (Fig. 2), two clearly defined special features are observed in the spectral characteristics. First, photovoltage peaks in the spectral characteristics of the starting sample and the samples annealed at T = 400 and 600°C are located in the vicinity of the same wavelength $\lambda = 0.9$ μm. Second, the peak is shifted to the longer wavelengths.

Spectral characteristics of the Au–TiB_2–GaAs structure that were measured on illumination from the Au–TiB_2 film side are shown in Fig. 5. Their shape resembles analogous characteristics for the TiB_2–GaAs structure. However, no absorption edge shift is observed for the unannealed sample or samples annealed at T = 400 and 600°C (curves *1–3*). Annealing at T = 800°C changes the spectral characteristics. In contrast to curves *1–3* (Fig. 3), no flat portion was observed in the spectral characteristic for the wavelength range of 0.84–0.87 μm on illumination from the Au–TiB_2 film side (Fig. 5, curve *4*). A peak of small height is observed in the vicinity of $\lambda = 0.91$ μm. The photovoltage amplitude, which corresponds to curve *4* in Fig. 4, is increased by a factor of four compared to the experimental data.

6. When comparing the spectral characteristics of the transverse photovoltage, which were measured for the TiB_2–GaAs samples (Fig. 2) and Au–TiB_2–GaAs samples (Fig. 4), the following distinctions should be noted. First, as it was mentioned above, the photovoltage peak for the starting Au–TiB_2–GaAs sample is shifted to the longer wavelengths compared to the peak in the spectral characteristic for an analogous sample of the TiB_2–GaAs structure. Second, the peak shift and broadening for the Au–TiB_2–GaAs structures occurs at a higher annealing temperature (Figs. 3, 4).

Spectral characteristics for the Au–TiB_2–GaAs structures, which were measured on illumination from the Au–TiB_2 film side (Fig. 5), also resemble analogous curves obtained for the TiB_2–GaAs structures (Fig. 3). However, the absorption edge shift with an increase in annealing temperature is apparently not observed.

It follows from the analysis of the spectral characteristics of the transverse photovoltage that a transition layer also exists in the Au–TiB_2–GaAs structures. This

is also confirmed by the photovoltage peak shift to the longer wavelengths.

Nonuniformity of the band bending, which is usually observed for Schottky contacts [16], does not affect the characteristics of the photovoltage measured. This follows from the fact that no variations were experimentally observed in spectral characteristics of the sample exposed to additional unmodulated illumination, although this should lead to a decrease in both the initial band bending and its relative nonuniformity along the interface.

It is also of interest that the photovoltage spectral characteristics that were measured on illumination of the samples from the side of the TiB_2 and Au–TiB_2 films have no specific features at a large light absorption coefficient $\alpha = 4 \times 10^4$ cm^{-1} ($\lambda = 0.64$ μm, $h\nu = 1.94$ eV), in which case the nonequilibrium-carrier generation occurs at the interface of the structures under investigation (Figs. 3, 5). This indicates that the interface formed between the metal and semiconductor is not destroyed at annealing temperatures of 400 and 600°C, and the recombination rate for nonequilibrium charge carriers does not vary in this region.

7. It follows from the above results and their analysis that the structures investigated consist of the TiB_2 or Au–TiB_2 film, a transition layer, and the GaAs layer.

The transition layer is a layer of certain thickness in which the distinctions from the starting material in doping level and recombination parameters are clearly observed.

This transition layer may be not only a semiconductor with the doping level [17, 18] and conductivity type [2] changed, but also a solid solution with the band gap increased [13] or decreased in relation to the starting material (GaAs). The variation in the conditions of the current flow through the contact is primarily determined by the changed concentration of equilibrium carriers and recombination parameters for the transition region, as well as by the degree of uniformity of the carrier distribution for this region.

The generation of photovoltage was experimentally observed for TiB_2–GaAs structures at a photon energy lower than the GaAs band gap (Figs. 2, 3). This is possible if the tails of the density of states that manifest themselves in doped semiconductors exist in the conduction and valence bands [19]. An increase in the GaAs doping level to 10^{17}–10^{18} cm^{-3} leads to the absorption band shift to the longer wavelengths [20]. We may assume that the transition layer comprises the boron-doped region adjoining the interface between the TiB_2 film and GaAs. Boron is the acceptor impurity in GaAs, and the transition layer can be of the *p*-type conduction depending on the B concentration [2].

The photovoltage generation in the TiB_2–GaAs structure on absorption of photons with energies lower than the GaAs band gap demonstrates that the transition layer, which is much thinner compared to the Debye screening length ($L_D = 400$ Å at $n = 10^{16}$ cm^{-3}),

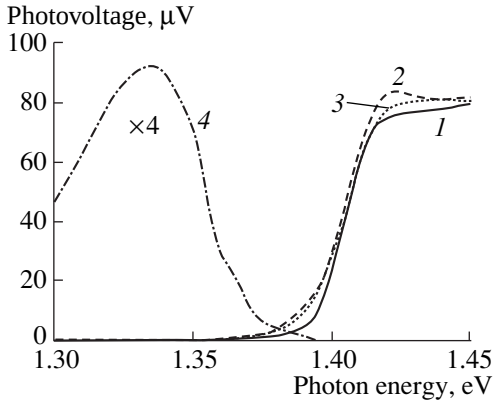

Fig. 5. Spectral characteristics of the transverse photovoltage for the Au–TiB_2–GaAs samples measured under illumination from the Au–TiB_2 film side. Curves *1–4* demonstrate the data for the same samples as in Fig. 4.

forms already during the stage of formation of this structure. Thermal annealing leads to an increase in both the thickness and doping level of the transition layer.

For the Au–TiB_2–GaAs structure, Au atoms diffuse into the GaAs near-contact region during the structure formation. Gold is also an acceptor impurity [21] which can compensate the starting doping impurity in GaAs. The energies of photovoltage peaks in Fig. 3 (curves *1–3*) indicate that a decrease in the band gap due to the appearance of the tails in the density of states corresponds to Au concentration in the transition region of 10^{17}–10^{18} cm^{-3}.

Diffusion of B atoms and impurity gettering in the near-contact region of the GaAs lattice occurs against the background of the extended transition layer, which is already formed by Au atoms during the formation of the structure. For the Au–GaAs structure, this layer is several hundred angströms thick [18, 22]. It is clear that the existence of the TiB_2 film should impede the diffusion of Au atoms into the GaAs lattice. However, the peak in the spectral characteristics for the Au–TiB_2–GaAs structures does not shift after annealing at T = 400 and 600°C (Fig. 2, curves *1–3*) compared to the peak for the unannealed sample. This points to the formation of the Au-doped layer, which is tolerant to annealing. For this reason, annealing at T = 400 and 600°C only slightly affects the doping level of the transition region. Accordingly, no changes in position of the peaks in curves *1–3* (Fig. 4) of the photovoltage spectral characteristics are observed. The variation in the photovoltage peak position is observed only at T = 800°C (Fig. 4, curve *4*), which reflects an increase in the doping level of the transition region.

It is noteworthy that the layer formed by Au atoms is naturally absent in the TiB_2–GaAs structures. The formation of the transition region is due to doping with B atoms. For this reason, the variation in the level of the

transition-layer doping with B atoms during annealing leads to the steady shift of the peak to longer wavelengths (Fig. 2, curves *1–3*) up to the point of disappearance.

Investigations of luminescence for the TiB_2–GaAs and TiN–GaAs structures demonstrated the existence of the transition layer. It is the authors' opinion that the layer comprises a solid solution with the band gap increased in reference to GaAs [13].

This discrepancy with the results given above can be related to a highly nonequilibrium technology of fabrication of the Schottky contacts investigated. For this reason, the variation in the technological conditions and subsequent annealing leads to the formation of transition layers of different nature.

8. The above experimental results allowed us to make the following conclusions.

The specific features of the spectral characteristics of the transverse bulk photovoltage point to the appearance of the B-doped semiconductor transition layer at the interface of the TiB_2–GaAs Schottky contacts during their formation.

The transition layer in the Au–TiB_2–GaAs structure is formed primarily due to doping with Au atoms.

Due to the formation of the stable Au-doped transition layer in the Au–TiB_2–GaAs structure, the change of the layer doping level and thickness as a result of thermal annealing occurs at higher temperatures compared to the TiB_2–GaAs structure.

An increase in the doping level of the transition layer up to 10^{17}–10^{18} cm^{-3} leads to the formation of tails in the density of states. Because of this, the electron–hole pairs in the semiconductor structures can be generated at the photon energy of the exciting light lower compared to the GaAs band gap.

The measurements of the spectral characteristics of the transverse bulk photovoltage allowed us to conclude that the mechanism of formation of the transition layer for Schottky contacts of different types during their thermal annealing is different.

ACKNOWLEDGMENTS

We thank I.B. Ermolovich and N.E. Korsunskaya for fruitful participation in discussions.

This study was supported by the Ukrainian State Foundation for Basic Research, grant no. 2.4/621.

REFERENCES

1. R. A. Andrievskiĭ, Usp. Khim. **66**, 57 (1977).
2. A. V. Galanikhin, B. V. Markin, and V. V. Chikun, Élektron. Tekh., Ser. SVCh Tekh. **4**, 38 (1994).
3. A. S. Dranenko and L. A. Dvorina, *Refractory Compounds in Microelectronics* (Inst. Probl. Materialoved., Kiev, 1996), p. 10.
4. V. B. Bessonov, V. N. Ivanov, A. S. Dranenko, V. Z. Skanun, and V. M. Yashnin, *Application of Traditional Film Materials and Development of New Ones* (Inst. Probl. Materialoved., Kiev, 1994), p. 65.
5. R. González, M. G. Barandika, D. Oña, *et al.*, Mater. Sci. Eng. A **216**, 185 (1996).
6. A. Hirose, M. Hasegawa, and K. F. Kobayashi, Mater. Sci. Eng. A **239–240**, 46 (1997).
7. I. Zergioti, M. Velegrakis, and G. N. Haidemenopoulos, Appl. Surf. Sci. **126**, 92 (1998).
8. J. Tauc, *Photo- and Thermoelectric Effects in Semiconductors* (Pergamon, Oxford, 1962; Inostrannaya Literatura, Moscow, 1962).
9. I. A. Baev and E. G. Valyashko, Fiz. Tverd. Tela (Leningrad) **7**, 2585 (1965) [Sov. Phys. Solid State **7**, 2093 (1965)].
10. S. I. Nesmelov, Izv. Vyssh. Uchebn. Zaved., Fiz., No. 3, 37 (1999).
11. V. V. Antipin, V. A. Godovitsyn, D. V. Gromov, *et al.*, Zarubezhn. Radioélektron., No. 1, 37 (1995).
12. L. V. Shekhovtsov, A. V. Sachenko, and Yu. M. Shvarts, Fiz. Tekh. Poluprovodn. (St. Petersburg) **29** (3), 566 (1995) [Semiconductors **29**, 293 (1995)].
13. E. F. Venger, V. V. Milenin, I. B. Ermolovich, *et al.*, Fiz. Tekh. Poluprovodn. (St. Petersburg) **33** (8), 948 (1999) [Semiconductors **33**, 865 (1999)].
14. M. D. Sturge, Phys. Rev. **127** (3), 768 (1962).
15. A. S. Dranenko, L. A. Dvorina, and V. M. Yashnik, *Refractory Compounds in Microelectronics* (Inst. Probl. Materialoved., Kiev, 1996), pp. 52–55.
16. V. B. Bondarenko, Yu. A. Kudinov, S. E. Ershov, and V. V. Korablev, Fiz. Tekh. Poluprovodn. (St. Petersburg) **32** (5), 554 (1998) [Semiconductors **32**, 495 (1998)].
17. A. N. Andronov, N. T. Bagraev, L. E. Klyachkin, and S. B. Robozerov, Fiz. Tekh. Poluprovodn. (St. Petersburg) **32** (2), 137 (1998) [Semiconductors **32**, 124 (1998)].
18. B. I. Bednyĭ, Fiz. Tekh. Poluprovodn. (St. Petersburg) **33** (11), 1350 (1999) [Semiconductors **33**, 1221 (1999)].
19. J. I. Pankove, *Optical Processes in Semiconductors* (Prentice-Hall, Englewood Cliffs, 1971; Mir, Moscow, 1973).
20. H. C. Casay, Jr., D. D. Sell, and K. W. Wecht, J. Appl. Phys. **46** (1), 250 (1975).
21. A. G. Milnes, *Deep Impurities in Semiconductors* (Wiley, New York, 1973; Mir, Moscow, 1977).
22. Z. Liliental-Weber, R. Gronsky, J. Washburn, *et al.*, J. Vac. Sci. Technol. B **4** (4), 912 (1986).

Translated by N. Korovin

Semiconductors, Vol. 35, No. 4, 2001, pp. 433–435. Translated from Fizika i Tekhnika Poluprovodnikov, Vol. 35, No. 4, 2001, pp. 445–447.

SEMICONDUCTOR STRUCTURES, INTERFACES, AND SURFACES

Hot-Hole Lateral Transport in a Two-Dimensional GaAs/$Al_{0.3}Ga_{0.7}As$ Structure

Yu. L. Ivanov, I. V. Elizarov, V. M. Ustinov, and A. E. Zhukov

Ioffe Physicotechnical Institute, Russian Academy of Sciences, Politekhnicheskaya ul. 26, St. Petersburg, 194021 Russia

Submitted October 5, 2000; accepted for publication October 6, 2000

Abstract—A narrow peak at the leading edge of the current pulse was found in samples of *p*-GaAs/$Al_{0.3}Ga_{0.7}As$ structures subjected to a high electric field. An analysis of the shape and height of the peak as a function of the electric field, as well as the field redistribution along the sample, allows us to conclude that domain instability exists under these conditions. It is also shown that the energy of holes heated in moderate electric fields can significantly exceed the optical phonon energy. *© 2001 MAIK "Nauka/Interperiodica".*

INTRODUCTION

The aim of studying the hot holes in 2D structures is to produce an inverse hole distribution. Recently, a number of publications have been devoted to this problem ([1, 2], for example) in which the possibility of generating far-infrared radiation is discussed. At the same time, problems of lateral transport of hot holes in 2D structures in connection with various effects such as the Gunn effect [1, 3] and the negative magnetoresistance of hot holes [3] are also discussed.

In this paper, we consider lateral transport of hot holes in the modulation-doped multiple-quantum-well GaAs/$Al_{0.3}Ga_{0.7}As$-based structures separated by impermeable barriers.

EXPERIMENTAL

The quantum wells (QWs) are 40, 20, and 17 nm in width, and the barrier width varies from 16 to 24 nm. Each structure consists of ten QWs doped with beryllium in the middle of the barrier (the layer has a thickness of 4 nm) to a concentration of 2×10^{18} cm^{-3}. Such a high level of doping causes the band edges to bend both in barriers and in QWs, and an actual band diagram is similar to the diagram shown in Fig. 1. In this case, at least one quantum level with an energy of 10 meV appears in "pockets" in the QWs. This level is occupied by holes, the degeneracy energy of which is approximately 6 meV. At the same time, QWs also appear in the barriers, and elementary calculations show that only one quantum level can exist in these QWs. Strip ohmic contacts to the samples 5×5 mm in size were formed by firing evaporated Au with 3% Zn as a doping impurity. These contacts provided linear current–voltage characteristics near the bias voltage $V \longrightarrow 0$. The distance between contacts in the [110] direction is 2 mm. Some probe measurements were performed on the samples in which the distance between contacts was 8 mm. An electric-field pulse with a 3 μs duration was applied to the samples. The leading-edge time of a pulse did not exceed 30 ns. Measurements were performed at sample temperatures of 4.2 and 77 K as well as in the temperature range of 77–200 K.

RESULTS

In fairly weak electric fields that induce heating, the current pulse shape replicates the voltage pulse shape, and, as the voltage increases, a narrow peak appears at a certain voltage at the leading edge of the current pulse. The height of this peak sublinearly increases with voltage. The other part of the current pulse a plateau also increases in magnitude with voltage but much more slowly. A typical picture of current kinetics with a peak is shown in Fig. 2a. It can be seen from Fig. 3 that the half-width of the peak decreases as voltage increases. Dependences of the currents at the peak and at the pulse plateau on an electric field are also shown in Fig. 3. For most of the samples, the current kinetics is similar to that shown in Fig. 2a. However, in many samples, current oscillations similar to oscillations in Fig. 2b are observed. As can be seen, the oscillation frequency increases as the electric field increases, though the effect is rather small. It should be noted that this phenomenon is more pronounced only at rather low temperatures when the thermal energy kT is much less than the energy gap between the lower quantum level and the $Al_{0.3}Ga_{0.7}As$ band edge. At room temperature, oscillations are not observed. This phenomenon is also not observed in quantum-confined structures

1063-7826/01/3504-0433$21.00 © 2001 MAIK "Nauka/Interperiodica"

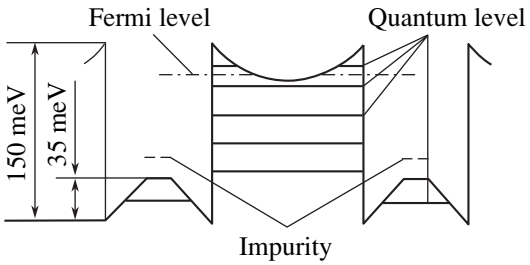

Fig. 1. Schematic representation of the band edge bending of the 20-nm width QW.

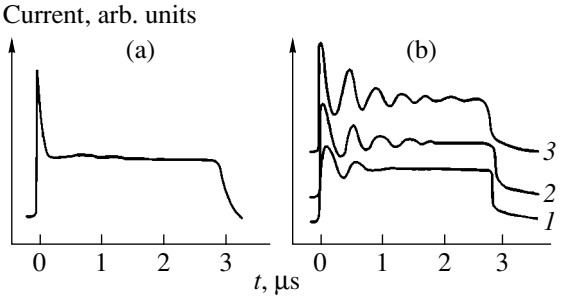

Fig. 2. (a) Shape of the current pulse in the sample of the 2-524 structure. Width of the QW is 17 nm, electric field E = 1 kV/cm, temperature T = 77 K, and the peak half-width is equal 125 ns. (b) Damped current oscillations in 4-353 sample subjected to electric fields with strengths of (*1*) 700, (*2*) 1000, and (*3*) 1500 V/cm.

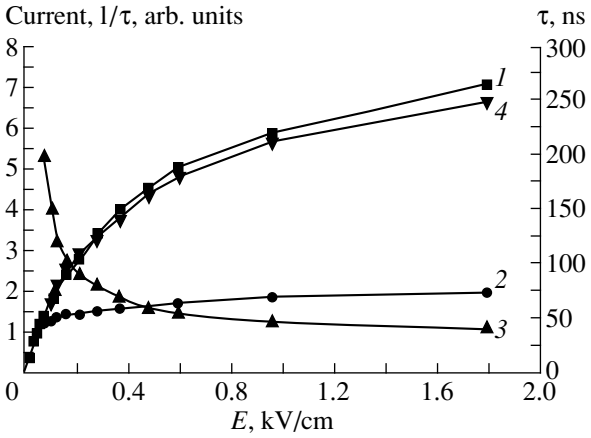

Fig. 3. The current dependence on electric field: (*1*) at the current peak and (*2*) at the plateau of the current pulse. Dependences of (*3*) the domain formation time and (*4*) the domain formation rate on the electric field for sample 2-524. The QW width is 17 nm, T = 4.2 K.

based on other materials (for example, in an $In_{0.14}Ga_{0.86}As/Al_{0.25}Ga_{0.75}As$ structure) in which the band offset is much larger than in the $GaAs/Al_{0.3}Ga_{0.7}As$ structure.

DISCUSSION

It is reasonable to explain the results obtained by the domain instability, which is characterized by the following features. A high electric field applied along the quantum-confined layers at low temperatures causes significant heating of holes whose mobility is high due to modulation doping of the structure. Hot holes located originally in the GaAs QWs can acquire an energy equal to the band edge energy of $Al_{0.3}Ga_{0.7}As$ and can diffuse into the QWs located in barriers where the hole mobility is significantly lower than in the GaAs QWs due to a strong impurity scattering. As a result, spatial separation of holes with high and low mobilities creates the necessary conditions for the Gunn effect to occur. Such a situation was discussed in [1] using as an example the InGaAs/GaAs structure, in which, however, the energy gap between the first quantum level of the InGaAs QW and the GaAs band edge is much less than in a $GaAs/Al_{0.3}Ga_{0.7}As$ system. As mobility decreases with increasing electric field, a high-field and low-mobility domain can appear, which will determine the sample current. In the course of domain formation, the current of the high-mobility holes in a homogeneous sample decreases, which manifests itself in a narrow peak at the leading edge of the current pulse. A single peak at the onset of the current pulse is indicative of the existence of a static domain. Nonuniform field distribution between the sample contacts measured by a probe is evidence that the domain exists. This nonuniformity arises simultaneously with the current peak. It turns out that this strong-field region is adjacent to the cathode. It should be noted that, in *p*-type samples, the location of a static domain near the cathode was previously observed in uniaxially stressed germanium [4]. Current oscillations are evidence that a mobile-domain exists. The small variation in the oscillation frequency is related to rather low differential conductivity in the leveling-off region of the peak current. It is easy to understand that the peak height characterizes the current of all free holes (corresponding to the concentration of doping impurity N_a) in the GaAs QWs when the electric field in the sample is homogeneous. The current pulse magnitude at the plateau is governed by the domain conduction and by its electric field. As the voltage applied to the sample increases, the domain increases in size, but its field changes only slightly. Due to this factor, the current increases insignificantly. In previous studies of hot holes in 2D structures [5], in which the time of the leading edge of the voltage pulse was much longer, the current peak at the leading edge was not observed. A rather small current increase with increasing electric field was explained by strong streaming in the case of scattering of hot holes by optical phonons.

Features of the temperature dependence of the currents at the peak and at the plateau (see Fig. 4) confirm the assumption that the high-field and low-mobility domain which determines the current through the sam-

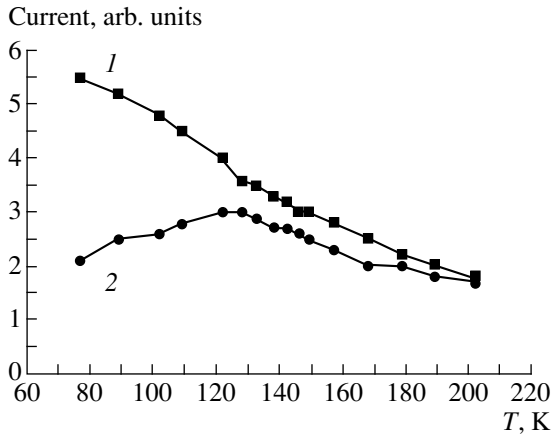

Fig. 4. The temperature dependences of (*1*) the peak current and (*2*) the plateau current for sample 2-524. Electric-field strength equals to 3 kV/cm.

ple is formed due to the transfer of hot holes from the GaAs QWs to the $Al_{0.3}Ga_{0.7}As$ barrier QWs. It is possible to explain a decrease in the peak current with temperature by a decrease in mobility of the high-mobility holes in the GaAs QWs due to scattering by acoustic phonons; at the same time, a certain increase in the plateau current at temperatures slightly higher than 77 K can be explained by an increase in the hole mobility in the domain in the case of impurity scattering.

The domain-formation time considered for the classical case can be approximately expressed, according to [6], as $\tau = 3.5/\mu_1 E_m$, where μ_1 is the charge-carrier mobility in the lower valley (electrons in the case of GaAs) and E_m is the electric field in a homogeneous sample. In other words, product $\mu_1 E_m$ is the carrier drift velocity in a homogeneous sample. In the case of a 2D *p*-$GaAs/Al_{0.3}Ga_{0.7}As$ structure, the hole drift velocity in a homogeneous sample and its dependence on the electric field are characterized by the current peak and by its dependence on the electric field. The rate of the domain formation should be proportional to the hole drift velocity. In fact, the electric field reciprocal value of the domain formation time displayed in Fig. 3 (curve *4*) is very similar to the dependence of the peak current on the electric field, i.e., on the drift velocity. This result again confirms the validity of the domain-instability model in the experiments described above.

CONCLUSION

The main results of this study are as follows:

(1) Static domain formation in *p*-$GaAs/Al_{0.3}Ga_{0.7}As$ structures makes the main contribution to current leveling-off in high electric fields. Optical phonon scattering yields a more gradual approach of the current–voltage characteristic to saturation in much higher electric fields.

(2) Due to heating of "2D holes" in moderately strong electric fields, their energy in the $GaAs/Al_{0.3}Ga_{0.7}As$ structure may be higher than doubled energy of an optical phonon for the majority of holes. Due to this factor, hole transfer to the QWs in barriers becomes probable.

ACKNOWLEDGMENTS

This study was supported by the Russian Foundation for Basic Research (project no. 98-02-18403) and by the Interdisciplinary Science and Technology Program "Physics of Solid-State Nanostructures" (project no. 97-1044).

REFERENCES

1. V. Ya. Aleshkin, A. A. Andronov, A. V. Antonov, *et al.*, Mater. Sci. Forum **297–298**, 261 (1999).
2. Yu. L. Ivanov, V. M. Ustinov, A. E. Zhukov, *et al.*, in *Proceedings of the International Conference on Nanostructure Physics and Technology, St. Petersburg, 1999*, p. 435.
3. Yu. L. Ivanov, G. V. Churakov, V. M. Ustinov, *et al.*, Solid-State Electron. **40**, 391 (1996).
4. I. V. Altukhov, M. S. Kagan, K. A. Korolev, and V. P. Sinis, Zh. Éksp. Teor. Fiz. **103**, 1829 (1993) [JETP **76**, 903 (1993)].
5. Yu. L. Ivanov, G. V. Churakov, V. M. Ustinov, and A. E. Zhukov, Fiz. Tekh. Poluprovodn. (St. Petersburg) **29** (9), 1702 (1995) [Semiconductors **29**, 887 (1995)].
6. M. E. Levinshteĭn, Yu. K. Pozhela, and M. S. Shur, *The Gunn Effect* (Sov. Radio, Moscow, 1975).

Translated by I. Kucherenko

Semiconductors, Vol. 35, No. 4, 2001, pp. 436–443. Translated from Fizika i Tekhnika Poluprovodnikov, Vol. 35, No. 4, 2001, pp. 448–455.

LOW-DIMENSIONAL SYSTEMS

Conductance of Quasi-Two-Dimensional Semiconductor Systems with Electrostatic Disorder in the Region of the Percolation Metal–Insulator Transition

B. A. Aronzon*, D. A. Bakaushin, A. S. Vedeneev**, A. B. Davydov*, E. Z. Meĭlikhov*, and N. K. Chumakov***

** Institute of Molecular Physics, Russian Research Center Kurchatov Institute, pl. Akademika Kurchatova 1, Moscow, 123182 Russia*

e-mail: davydov@imp.kial.ru

*** Institute of Radio Engineering and Electronics, Russian Academy of Sciences (Fryazino Branch), pl. Vvedenskogo 1, Fryazino, Moscow oblast, 141120 Russia*

Submitted July 10, 2000; accepted for publication October 2, 2000

Abstract—Special features of the percolation transition in quasi-two-dimensional (quasi-2D) electron systems (metal–nitride–oxide–semiconductor structures with *n*-type inversion channels) with a strong fluctuation potential (FP) and a gate length smaller than the correlation radius of a percolation cluster (in which case the structure conductance is controlled by isolated saddle-point regions of the FP) are considered. Experimentally measured dependences of the conductance on the field-electrode potential and the temperature are analyzed in the context of the Landauer–Büttiker formalism. Energy parameters of the FP saddle-point regions and effective density of electron states ($N_{ss} \propto m/\pi\hbar^2$) near the percolation level are determined from the experimental data. Consistency between the experimental results and the proposed statistical model of the formation of FP saddle-point regions in quasi-2D systems is demonstrated. It is shown that saddles transform into potential troughs extended in the direction of the percolation route as the percolation trough is approached. *© 2001 MAIK "Nauka/Interperiodica".*

Quasi-two-dimensional (quasi-2D) electron systems existing in metal–insulator–semiconductor structures [1], which are widely used both in applications as field-effect transistors (FETs) [2, 3] and in fundamental studies of the metal–insulator transition [4], are inherently disordered [5]. Due to the advances of modern technology, disorder effects are usually related to the presence of built-in charges located at impurities in the doped layers or at traps (defects) in the gate insulator, rather than to the structure nonuniforminty. Under different experimental conditions determined by the temperature and the potential of the field electrode (the gate), these effects show up in different ways and to a variable extent.

The statistical ensemble of built-in charges induces a chaotic potential relief and a fluctuation potential (FP) at the location of the quasi-2D electron channel [6]. When the fluctuation amplitude exceeds the typical energy of quasi-2D electrons, specific features in the electron transport are observed [7]. In modern FETs, the density of impurities amounts to ~10^{13} cm^{-2}. At these densities of chaotically arranged built-in charges, the FP amplitude may be as large as ~ 100 meV [6], and it is the FP that begins to control the electron transport in semiconductor systems important for microelectronics. This factor also makes the issue of the FP effect on conduction in quasi-2D systems near the percolation metal–insulator transition interesting from a fundamental point of view.

Spatial redistribution of quasi-2D electrons caused by the FP is accompanied by their localization in the wells of the chaotic potential relief [6] and results in a dramatic change in the nature of electron transport: under these conditions, percolation conduction takes place [7], which proceeds by electron transitions between the potential wells separated by the FP saddle points. These saddle-point regions, acting as ballistic quantum contacts between the wells [8], control the properties of quasi-2D systems even at relatively high temperatures. However, the view of the FP as smoothly varying [6] leads to the conclusion that the characteristic spatial scale (correlation radius [7]) of the percolation cluster is macroscopic.

A promising class of objects for investigating disorder effects in quasi-2D systems is represented by silicon metal–nitride–oxide–semiconductor (MNOS) structures [2] in which the FP is primarily determined by the charge state of traps in the region of the SiO_2–Si_3N_4 interface [9]. The density of the charged traps n_t can be varied in the range of 10^{11}–10^{13} cm^{-2} by controlled electron injection from silicon, which occurs at increased field-electrode voltages (~30 V) (see [2]). This enables one to study the electron transport in a wide range of FP amplitudes.

1063-7826/01/3504-0436$21.00 © 2001 MAIK "Nauka/Interperiodica"

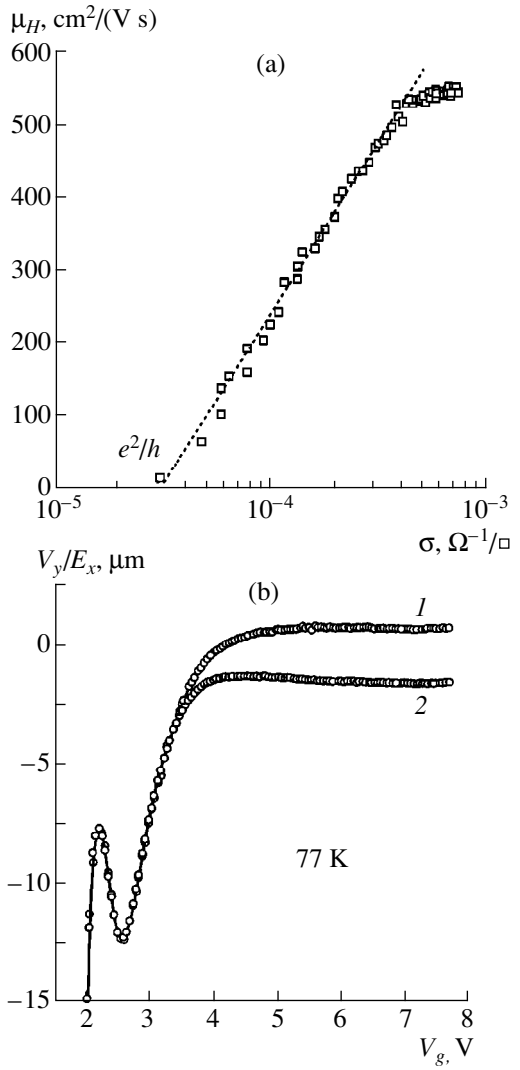

Fig. 1. (a) Hall mobility as a function of the channel conductivity at 77 K. (b) Dependence of V_y / E_x on V_g (here, E_x is the longitudinal electric field, and V_y is the voltage between the Hall probes). Curves *1* and *2*, recorded in a magnetic field of 1 T, correspond to the two opposite field directions; deviation between them at $V_g \geq 3.5$ V is due to the Hall effect for $\sigma(V_g) \geq e^2/h$. An increase in the asymmetry voltage between the Hall probes at $V_g \leq 3.5$ V is evidence of the transition to the percolation conduction mode with a typical scale for the cluster correlation radius $L_c \sim V_y/E_x$ [10, 11].

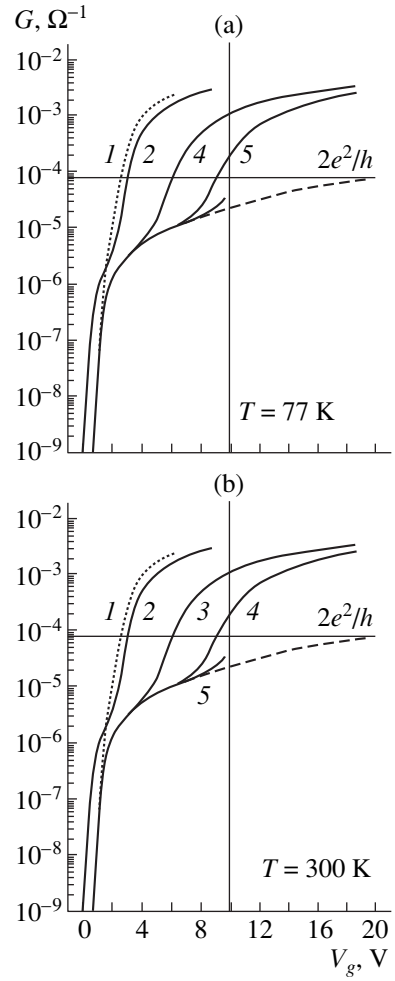

Fig. 2. Field-effect curves for the MNOS transistor structures with a "long" and a "short" channel (dotted and solid lines, respectively) at (a) 77 and (b) 300 K; $n_t \approx$ (*1*, *2*) 2.5×10^{12}, (*3*) 4.5×10^{12}, (*4*) 5.3×10^{12}, and (*5*) 6.5×10^{12} cm^{-2}. The conductance of a "long" transistor is adjusted to the geometry of a "short" one.

It was shown in recent studies [9–11] that the conductance G of Si-MNOS structures with an *n*-type inversion channel becomes percolation-controlled as the gate potential V_g is lowered. This is accompanied by the disappearance of the Hall effect as the channel conductivity falls below the threshold value, about e^2/h (see Fig. 1a). For low V_g, fluctuations of the voltage V_y between the Hall probes were observed (see Fig. 1b), which makes it possible to evaluate the characteristic cell size of the percolation cluster, or, in other words, its correlation radius L_c, by the method proposed in [10]; the value thus obtained approaches ~ 10 μm. The origin of these fluctuations is related to the electrical asymmetry between the Hall contacts, which exists (even for a pair of contacts whose locations are perfectly matched geometrically) due to the stochastic nature of the percolation cluster and results in the appearance of an asymmetry voltage on the order of $V_y \sim L_c E_x$, where E_x is the longitudinal electric field. The value of the asymmetry voltage depends on the specific form of the percolation cluster and varies when the latter is changed with varying V_g, which leads to fluctuations in V_y. This effect is described in [10, 11] and represents one of the incoherent mesoscopic phenomena [12, 13], which manifest themselves when the length scale characterizing the experimental conditions becomes comparable to L_c.

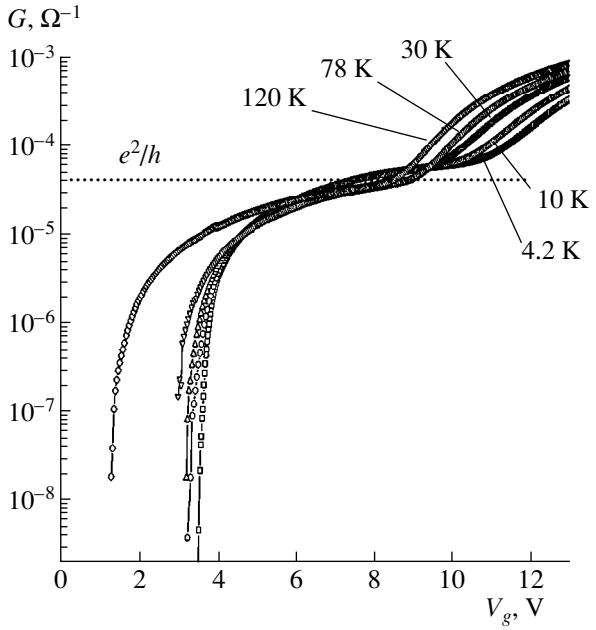

Fig. 3. Experimental field-effect curves for a short-channel MNOS structure in the temperature range of 4.2–120 K.

Here, we consider this effect only to obtain an estimate of the correlation radius.

Since the estimated value of the correlation radius is as large as ~ 10 μm, it is possible to fabricate Si-MNOS structures with the gate length $L \le L_c$, where mesoscopic effects can be observed. If, in addition, the gate width $W \gg L$, the conductance of such a FET structure is known to be controlled by individual percolation routes of anomalously low resistance, which shunt the source–drain gap (see [12, 13]). In turn, the conductance of these percolation routes is determined by the segments with the highest resistance, i.e., in our case, by isolated FP saddle-point regions across the sample [11]. It is possible that electron transport through these regions proceeds in the quantum ballistic mode. In this case, features typical of quantum quasi-one-dimensional (quasi-1D) systems are observed in the conductance. In other words, due to incoherent mesoscopic effects ($L < L_c$), a single quantum-sized region that controls the quantum nature of the conductance of the entire sample is self-selected. Mesoscopic features in the conductance of macroscopic samples, such as the appearance of quasi-plateau regions with typical values $G \sim 2e^2/h$ in the $G(V_g)$ curves, were observed experimentally at temperatures from 77 to 300 K in the following types of transistor structures with a short channel ($L < L_c$) [9]: Si-MNOS structures (L = 5 μm, W = 50 μm) (Fig. 2); GaAs metal–semiconductor FETs (L = 0.8 μm, W = 200 μm); GaAs–AlGaAs high electron mobility transistors with a thin (3 nm) spacer (L = 0.6 μm, W = 60 μm); etc.

In this paper, using Si-MNOS structures with an extremely high built-in charge density (limited by the breakdown voltage of the gate insulator [2]) as an example, we report the results of studying mesoscopic (in terms of [12], i.e., $L \le L_c \ll W$) quasi-2D systems under the conditions of a percolation metal–insulator transition. As in [9, 11], the structures have an *n*-type inversion channel of length 5 and width 50 μm and a gate insulator with SiO_2 and Si_3N_4 layer thicknesses of 2.5 and 35 nm, respectively. In an effort to investigate electron transport in disordered systems near the percolation threshold, the structure conductance G was measured as a function of the gate potential V_g at different temperatures from 4.2 to 300 K. Experimental details are reported in [9, 14].

Dependences of G on the gate potential V_g plotted in Fig. 3 reflect the formation of an inversion channel under conditions of strong disorder for a built-in charge density (which induces the FP) of $n_t \approx 1.6 \times 10^{13}$ cm^{-2}. For low gate potentials (V_g < 5 V), an exponential increase in G with both V_g and T is observed, which is typical of such systems when the Fermi level ε_f is below the percolation level [1, 5]. In the range of 5 V < V_g < 10 V, the dependence of G on V_g becomes weaker, and the quasi-plateau is observed. It should be noted that, at low temperatures ($T \le 20$ K), the conductance virtually is independent of temperature in the quasi-plateau region, which is evidence of the tunneling mechanism for electron transport. The behavior of the dependences $G(V_g, T)$ for V_g exceeding 10 V, which is the value corresponding to the isotherm crossing at $G \sim e^2/h$, is typical of the quasi-2D electron systems under the conditions of electron screening of the fluctuations [1].

Next, let us analyze, in the context of percolation transition [7] involving FP saddle-point regions [8], the main features in the dependence of G on V_g and T for the mesoscopic systems under consideration. In contrast to [8], finite tunneling transparency of saddle-point regions for the Fermi energies below the saddle-point level are taken into account. As previously [9, 11], we assume that the conductance of the structure (with $L \le L_c \ll W$) is controlled by the highest resistivity segment of the lowest resistivity percolation route, i.e., in our case, by a single saddle-point region of the FP. Following [15], we use the parabolic saddle point approximation for the electron potential energy in this region:

$$V(x, y) = V_s - \frac{m\omega_x^2 x^2}{2} + \frac{m\omega_y^2 y^2}{2}. \quad (1)$$

Here, V_s is the potential at the saddle point (which coincides with the classical percolation level); m is the charge carrier (electron) effective mass; and ω_x and ω_y are the parameters characterizing the potential curvature in the direction of electron motion and in the transverse direction, respectively.

At zero temperature, the transparency $t(\varepsilon_f)$ of the saddle-point region is given by the sum of the contributions $t_n(\varepsilon_f)$ from quasi-1D channels corresponding to the energies $V_s + \hbar\omega_y(n + 1/2)$ ($n = 0, 1, 2,\ldots$); i.e., we have

$$t_n(\varepsilon_f) = \left(1 + \exp\left(-2\pi\frac{\varepsilon_f - \hbar\omega_y(n + 1/2) - V_s}{\hbar\omega_x}\right)\right)^{-1}, \quad (2)$$

which results in the following dependence of the conductance on the Fermi energy:

$$G(\varepsilon_f) = \frac{2e^2}{h}t(\varepsilon_f) = \frac{2e^2}{h}\sum t_n(\varepsilon_f). \quad (3)$$

If $\hbar\omega_x/2\pi \ll \hbar\omega_y$ (e.g., in the case of $\hbar\omega_x \sim \hbar\omega_y$ and $\varepsilon_f - V_s \leq \hbar\omega_y/2$), only the first term ($n = 0$) in the sum can be retained:

$$G(\varepsilon_f) = \frac{2e^2}{h}t_0 = \frac{2e^2}{h}\left(1 + \exp\left(-2\pi\frac{\varepsilon_f - \hbar\omega_y/2) - V_s}{\hbar\omega_x}\right)\right)^{-1}. \quad (4)$$

Expressions (3) and (4) describe electron transport through an FP saddle-point region; in particular, they predict an exponential dependence $G(\varepsilon_f)$ for $\varepsilon_f - V_s < 0$. It can be seen that, for $\hbar\omega_x, \hbar\omega_y \gg kT$, the saddle-point conductance given by (3) and (4) (which determines the conductance of the entire structure) acquires quantum quasi-1D features. If $\varepsilon_f - V_s > 0$ and $\hbar\omega_x \ll \hbar\omega_y$, the function $G(\varepsilon_f)$ has a characteristic shape with steps at multiples of $2e^2/h$. In another situation of $\hbar\omega_x \approx \hbar\omega_y$, which is expected to be the case for the saddle-point regions of the FP considered (see below), the function $G(\varepsilon_f)$ has only inflection points (maxima and minima of the derivative $\partial G/\partial\varepsilon_f$) at values of G that are multiples of e^2/h (see Figs. 4, 5).

The saddle-point conductivity at finite temperatures is calculated following the formalism developed in [16]:

$$G(\varepsilon_f) = \frac{2e^2}{h}\int d\varepsilon(-\partial F/\partial\varepsilon)t(\varepsilon). \quad (5)$$

Here, F is the Fermi–Dirac distribution function.

The dependences $G(\varepsilon_f)$ calculated for finite temperatures in the case of symmetric parabolic saddle-shape potential ($\hbar\omega_x = \hbar\omega_y$) are plotted in Fig. 4. Temperature-independent points, where conductance equals $G_0(1/2 + n)$ (where $n = 0, 1,\ldots$), are evident in the curves. The derivative $\partial G/\partial\varepsilon_f(G)$ has maxima at these points. It can be seen that, for $kT \ll \hbar\omega_x/2\pi$, the conductance becomes virtually independent of the temperature.

Under the same conditions, the derivative $\partial G/\partial\varepsilon_f$ as a function of G and the temperature dependence of the reciprocal value of the derivative maximum at $G = e^2/h$ were calculated; the results are shown in Figs. 5a and

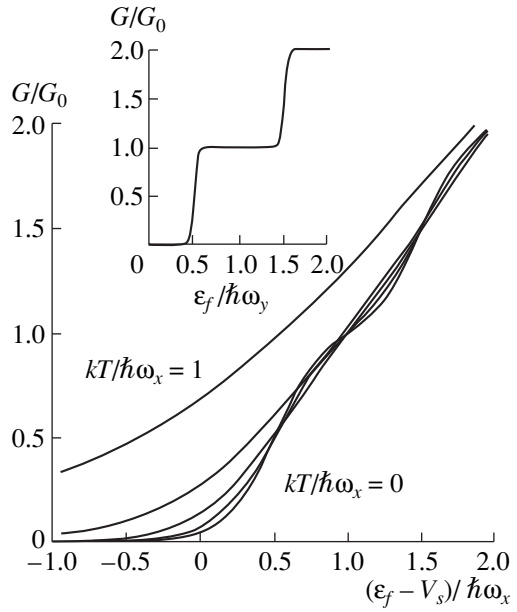

Fig. 4. Dependence of the conductance G of a parabolic saddle-point region (with $\omega_y = \omega_x$) normalized by the conductance quantum $G_0 = 2e^2/h$ on the Fermi energy ε_f, calculated for the temperatures $kT/\hbar\omega_x = 0$, 0.01, 0.02, 0.04, 0.1, 0.2, 0.4, and 1. Inset: $G(\varepsilon_f)$ for the case of $\hbar\omega_y \gg \hbar\omega_x \gg kT$.

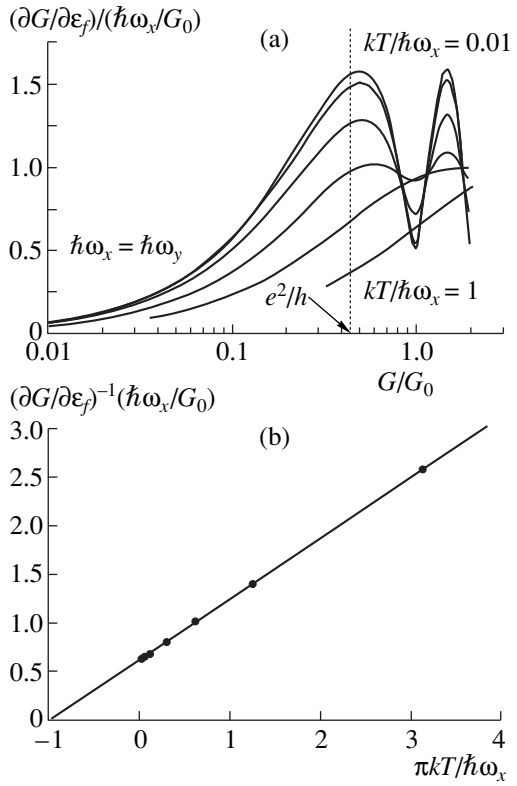

Fig. 5. (a) Derivative $\partial G/\partial\varepsilon_f$ of the conductance of a saddle-point region (with $\omega_x = \omega_y$) as a function of G for various temperatures ranging from 0 to $\hbar\omega_x$ and (b) temperature dependence of the quantity $(\partial G/\partial\varepsilon_f)^{-1}$ at the derivative maximum for $G = e^2/h$; $G_0 = 2e^2/h$.

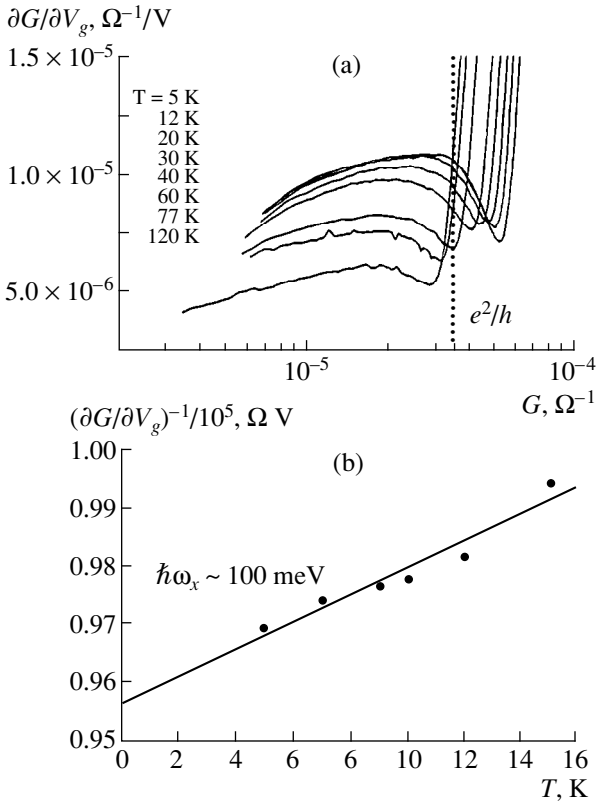

Fig. 6. Temperature characteristics of the derivative $\partial G/\partial V_g$ obtained from the data shown in Fig. 3.

5b, respectively. The calculations indicate that, for $0 \le kT/\hbar\omega_x \le 1$, the value of $(\partial G/\partial\varepsilon_f)^{-1}$ at $G = e^2/h$ depends linearly on the temperature and can be approximated by the following expression:

$$\frac{\partial G}{\partial \varepsilon_f} \approx \frac{e^2/h}{\hbar\omega_x/\pi + kT}. \tag{6}$$

In other words, if the line describing the dependence of $(\partial G/\partial\varepsilon_f)^{-1}$ on kT is extended to cross the abscissa axis, the length of the axis portion from the origin to the intersection point is equal to $\hbar\omega_x/\pi$. This makes it possible to obtain an estimate for $\hbar\omega_x$.

Expressions (5) and (6) can be used to predict the behavior of the experimentally measured curves $G(V_g)$, in particular, the existence of an extremum of the derivative $\partial G/\partial V_g$ at $G \approx e^2/h$ (see Fig. 6a). Indeed, an increment in the quasi-2D electron density ∂n_s at the semiconductor surface, resulting from an increase in the field-electrode potential ∂V_g, can be related to a change $\partial\varepsilon_f$ in the Fermi energy in the following way:

$$\partial n_s = C\partial V_g/e = N_{ss}\partial\varepsilon_f. \tag{7a}$$

Here, C is the gate-insulator capacitance and N_{ss} is the effective density of electron states near the semiconductor–insulator interface. Thus, it can be concluded from (6) and (7a) that the derivative $\partial G/\partial V_g(G)$ of the experimentally measured field-effect curves

$$\frac{\partial G}{\partial V_g} = \frac{\partial G}{\partial \varepsilon_f}\frac{C}{eN_{ss}}, \tag{7b}$$

should have an extremum in the vicinity of $G \sim e^2/h$ whose temperature dependence can be used to obtain an estimate for $\hbar\omega_x$ (see Fig. 6b). It should be taken into account that the value $G = e^2/h$ corresponds to a fixed position of the Fermi level (independent of temperature for $kT \ll \hbar\omega_x/2\pi$), determined from $\varepsilon_f - V_s = \hbar\omega_y/2$, which follows from (4) and can be seen in the curves in Fig. 4.

The derivatives $\partial G/\partial V_g$ of the experimentally measured $G(V_g)$ curves are plotted against G in Fig. 6a. As expected (cf. Figs. 5a and 6a), $\partial G/\partial V_g$ has an extremum in the vicinity of $G \approx e^2/h$. It is demonstrated below that the shift of the extremum to values of G smaller than e^2/h is caused, in particular, by the energy dependence of the density of fluctuation states and, more precisely, by an increase in N_{ss} with ε_f [6] (i.e., with G). According to (6) and (7b), at low temperatures, the value of $(\partial G/\partial V_g)^{-1}$ at $G = e^2/h$ depends linearly on the temperature (Fig. 6b). Extrapolating the temperature dependence of $(\partial G/\partial V_g)^{-1}$ to the intersection with the horizontal axis, the estimate we obtain is $\hbar\omega_x \approx 100$ meV.

Let us consider the factors that control the behavior of the experimentally obtained plots $\partial G/\partial V_g$ vs. G and their deviation from the calculated $\partial G/\partial\varepsilon_f$ dependences. These factors are the effective density N_{ss} of fluctuation electron states at the semiconductor–insulator interface in the percolation-transition region (which is inaccessible for investigation by classical spectroscopic techniques, i.e., by equilibrium C–V methods and relaxational ones, such as DLTS [17]) and the parameter $\hbar\omega_x$, which can vary with ε_f due to the deviation of the shape of the saddle-type potential from the parabolic one.

In the low-temperature region ($kT \ll \hbar\omega_x/2\pi$), the derivative $\partial G/\partial\varepsilon_f$ can be expressed, according to (4), as

$$\frac{\partial G}{\partial \varepsilon_f} = \frac{G[1 - G/(2e^2/h)]}{\hbar\omega_x/2\pi}, \tag{8}$$

which enables one to determine the dependence of $\partial G/\partial\varepsilon_f$ on G, once the dependence of $\hbar\omega_x$ on ε_f (or V_g) is known. Using Eq. (7b), one can compare the dependence of $\partial G/\partial\varepsilon_f$ obtained using Eq. (8) with the experimental data for $\partial G/\partial V_g$. Furthermore, the parameters N_{ss} and $\hbar\omega_x$ can be related to the experimentally measured quantities G and V_g by

$$N_{ss}\hbar\omega_x = -\frac{2\pi C}{e}\left(\frac{\partial \ln((2e^2/h)/G - 1)}{\partial V_g}\right)^{-1}. \tag{9}$$

In Fig. 7, the product $\hbar\omega_x N_{ss}$ (which stands on the left-hand side of (9)) normalized to the density of states in a 2D channel $D = 2m/\pi\hbar^2$ is plotted as a function of G. The displayed curves were obtained at 4.2 and 10 K; this is within the temperature range in which, as it was noted above (see Fig. 3), the conductance is virtually independent of the temperature for the gate voltages corresponding to the Fermi level above the classical percolation level (roughly, $\varepsilon_f > V_s$). The range of V_g where this condition is satisfied corresponds to the plateau region in the $G(V_g)$ curves, and it is this range that is of interest to us in this study. In Fig. 7, one can clearly see the range of V_g bounded from below, where experimental point arrangement is independent of the temperature; obviously, this range corresponds to $G \geq 0.05(2e^2/h)$. The latter estimate is consistent with those derived from (4). Analysis of the temperature dependence of $G(V_g)$ for smaller G will be the subject of a separate study to be carried out later.

The data represented in Fig. 7 indicate that under strong band bending (i.e., when the Fermi energy is considerably higher than the percolation level: $\varepsilon_f - V_s \sim \hbar\omega_y/2$ and $G \sim e^2/h$), the quantity $\hbar\omega_x N_{ss}/D$ is nearly constant, and its value agrees well with the estimate $\hbar\omega_x \approx 100$ meV, which is obtained from the experimental temperature dependence of the derivative $\partial G/\partial V_g$ (see Fig. 6b). This means that when the Fermi energy $\varepsilon_f - V_s \approx \hbar\omega_y/2$, the effective density N_{ss} of electron states is close to the value $D = 2m/\pi\hbar^2$. However, when G (i.e., ε_f) decreases (with decreasing V_g), the function $\hbar\omega_x N_{ss}/D$ drops sharply, which can be related to a decrease in both N_{ss} and $\hbar\omega_x$. It is known [6, 18] that from its value at $\varepsilon \gg V_s$ (which is about D), the density of fluctuation states falls off exponentially towards the middle of the semiconductor band gap. It is also known [18] that the density of states in 2D systems at the percolation level (i.e., for $\varepsilon_f = V_s$) is reduced by about a factor of two compared to its value for the case $\varepsilon_f - V_s \geq \hbar\omega_y/2$; i.e., it equals ~$D/2$. According to (4), the conductance is then equal to $G = (2e^2/h)\exp(-\pi\omega_y/\omega_x) \approx (2e^2/h)\exp(-\pi)$ for $\hbar\omega_y \approx \hbar\omega_x$. Meanwhile, it can be seen from the experimental data (Fig. 7) that in the range of G from $(2e^2/h)\exp(-\pi)$ to e^2/h, the function $\hbar\omega_x N_{ss}$ drops more steeply, almost by an order of magnitude; this is evidence that the parameter $\hbar\omega_x$ decreases sharply with decreasing Fermi energy in the range $V_s \leq \varepsilon_f \leq V_s + \hbar\omega_y/2$.

Such behavior of the parameter $\hbar\omega_x$ can be understood in the context of the following simple physical picture. Under high gate potentials corresponding to the condition $\varepsilon_f \approx \hbar\omega_y/2 + V_s$, the bottleneck region of the FP, which determines the system conductance, is shaped as a single saddle point with the parameters $\hbar\omega_y \approx \hbar\omega_x$. On the other hand, near the percolation level ($\varepsilon_f \leq V_s$), the potential relief profile has a markedly different shape: the bottleneck is formed by a set of saddle points connected in a series. Such a relief should actually be considered as a potential trough extended in the direction of electron motion, rather than a symmetric saddle point. This manifests itself in a decrease in the parameter $\hbar\omega_x$ from ~ 100 to ~ 20 meV (Fig. 7). Taking into account that in the V_g range corresponding to $(2e^2/h)\exp(-\pi) < G < e^2/h$ the conductance becomes temperature-independent at $T \ll T_m = \hbar\omega_x/2\pi$ and assuming that $\hbar\omega_x = 20$ meV, we obtain an estimate $T_m \approx 30$ K, which agrees with the experimental data.

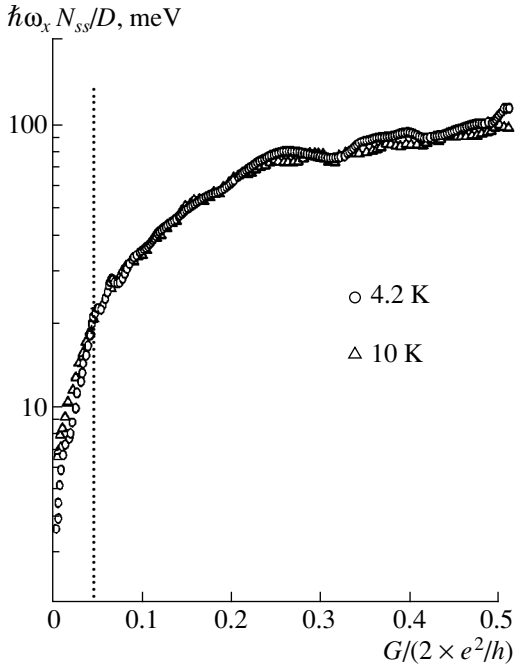

Fig. 7. Dependence of the parameter $\hbar\omega_x N_{ss}/D$ on G in the low-temperature region (4.2–10 K).

Analyzing the experimental curves $G(V_g)$, we can also obtain an estimate for the parameter $\hbar\omega_y$. For this purpose, let us use expressions (4) and (7a), which relate G and V_g to ε_f. It has already been noted above that the values of the Fermi energy determined by $\varepsilon_f - V_s = \hbar\omega_y/2$ and $\varepsilon_f - V_s = 0$ correspond, respectively, to the values of the conductance $G = e^2/h$ and $(2e^2/h)\exp(-\pi\omega_y/\omega_x) \approx (2e^2/h)\exp(-\pi)$ (for $\hbar\omega_y \approx \hbar\omega_x$). Consequently, the Fermi energy changes by $\delta\varepsilon_f = \hbar\omega_y/2$ as G varies in the indicated range. According to (7a), such change in the Fermi energy corresponds to a change in the gate potential $\delta V_g = \delta\varepsilon_f e\langle N_{ss}\rangle/C$, where $\langle N_{ss}\rangle$ is the density of electron states averaged over the energy range $0 \leq \varepsilon_f - V_s \leq \hbar\omega_y/2$. Thus, $\hbar\omega_y \approx C\delta V_g/e\langle N_{ss}\rangle$. Taking into account that, in this energy range, N_{ss} varies between $D/2$ and D [6, 18], which means that $D/2 \leq \langle N_{ss}\rangle \leq D$, we find that $2C\delta V_g/eD \leq \hbar\omega_y \leq 4C\delta V_g/eD$.

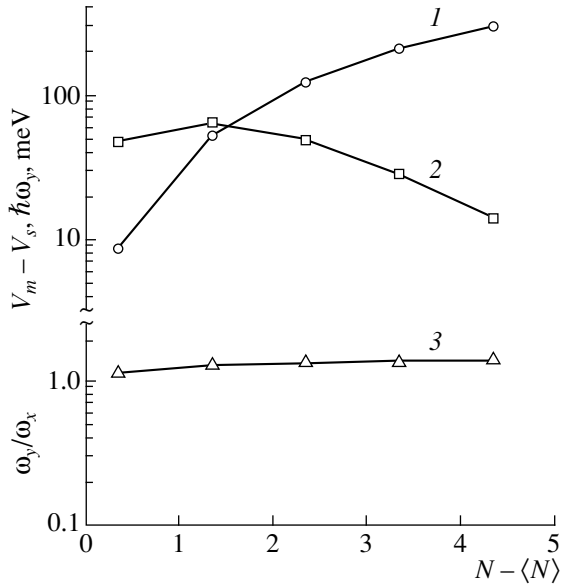

Fig. 8. (*1*) Relative height $V_m - V_s$ of the potential relief "hills," meV; (*2*) parameter $\hbar\omega_y$, meV; and (*3*) the ratio ω_y/ω_x as a function of the fluctuation $N - \langle N \rangle$ in the number of built-in charges on the area πs^2. The calculations were carried out for the spacer thickness $s = 2.5$ nm and $n_d = 1.6 \times 10^{13}$ cm^{-2} ($\langle N \rangle \approx 3$); the screening effect of the field electrode was disregarded.

Calculations relying on the low-temperature ($T \leq 10$ K) part of the data presented in Fig. 3 yield an estimate 70 meV $\leq \hbar\omega_y \leq$ 140 meV. Thus, in agreement with the assumption made above, for $\varepsilon_f - V_s \leq \hbar\omega_y/2$, the asymmetry of the FP saddle-point regions is small: $\hbar\omega_y \approx \hbar\omega_x \approx 100$ meV.

Next, let us consider the correspondence between the parameters $\hbar\omega_x$ and $\hbar\omega_y$ obtained from the experimental data analysis and a simple statistical model of the saddle-point region formation in the chaotic potential relief in quasi-2D systems. It follows from the properties of the FP correlator [6] that the spatial scale characterizing the channel local domains of uniform potential distribution is determined by the spacer thickness s (the distance between the quasi-2D electron channel and the plane of built-in charges). In the Si-MNOS structures under investigation, s is equal to the thickness of the SiO_2 layer ($s \approx 2.5$ nm). For the built-in charge density $n_t \approx 1.6 \times 10^{13}$ cm^{-2}, a local domain of area πs^2 contains, on average, $\langle N \rangle = \pi s^2 n_t \approx 3$ built-in charges. The deviation of the random number N of the built-in charges within this area from the mean value $\langle N \rangle$ results in the formation of chaotic-relief potential wells filled by electrons (for $N \leq \langle N \rangle$) and peaks (for $N \geq \langle N \rangle$); saddle points are formed between these peaks.

Obviously, the approximation of the parabolic saddle-point potential [12] used above is valid only under the condition that the energy spacing $V_m - V_s$ between the saddle point V_s and the nearby fluctuation peaks is considerably greater than the value of $\hbar\omega_y$. The height of the peaks $V_m \approx e^2(N - \langle N \rangle)/\kappa s$ (where κ is the permittivity in the region near the $Si–SiO_2$ interface [6]) increases with increasing N, while the average distance R between the peaks decreases due to the reduction in the probability $P(N)$ of strong fluctuations in the value of N: $R \approx 2s/P(N)^{1/2}$; evidently, this leads to a decrease in $\hbar\omega_y$ [15]. Thus, it can be expected that the condition $V_m - V_s \geq \hbar\omega_y$ begins to be satisfied from values for some $N \geq \langle N \rangle$ due to the statistical nature of the fluctuations.

Based upon these considerations, under the assumption of the Poisson probability distribution for the fluctuations of N, for $\langle N \rangle \approx 3$, we calculated the saddle-point potential between the two domains of size s and charge $e(N - \langle N \rangle)$ separated by a distance $R(N)$, the second derivatives of the potential with respect to coordinates x and y that determine the curvature parameters at the saddle point ($\hbar\omega_x$ and $\hbar\omega_y$), and the energy spacing $V_m - V_s$.

The calculation results, shown in Fig. 8, demonstrate that the condition $V_m - V_s \geq \hbar\omega_y$ is satisfied for quite reasonable values of N, their difference from the mean value $\langle N \rangle$ being within the standard deviation $\langle N \rangle^{1/2}$. The use of the symmetric saddle-point potential approximation ($\hbar\omega_y \approx \hbar\omega_x$) is also justified by these results (see Fig. 8, curve *3*). One can also see that the calculated values of $\hbar\omega_x$ and $\hbar\omega_y$ (the region of intersection between curves *1* and *2* in Fig. 8) agree with the experimentally derived estimates $\hbar\omega_y \approx \hbar\omega_x \approx$ 100 meV. This substantiates the basic possibility of observing quantum effects in the conductance of disordered semiconductor structures at sufficiently high temperatures determined by $kT < \{\hbar\omega_x/2\pi; (V_m - V_s - \hbar\omega_y/2)\}$. In the case under consideration, these are lower than room temperature (see Figs. 2, 3).

In conclusion, we note that the experimental results confirm unambiguously the tunneling nature of the conductance of short, highly disordered MNOS structures in the quasi-plateau region. Experimentally determined energy parameters characterizing the curvature in the saddle-point region that defines the conductance agree with the simulation results obtained in the context of a fluctuation potential statistical model.

ACKNOWLEDGMENTS

We are grateful to V.A. Volkov, V.A. Gergel', M.S. Kagan, V.A. Sablikov, and R.A. Suris for their participation in discussing the results.

This study was supported by the Russian Foundation for Basic Research (project nos. 98-02-16747, 99-02-16955), the Interdisciplinary Program "Physics of the Solid-State Nanostructures" (project nos. 99-1123, 97-1081), and the Federal Foundation for the Development of Electronics (project no. 040/99f).

REFERENCES

1. T. Ando, A. B. Fowler, and F. Stern, Rev. Mod. Phys. **54** (2), 437 (1982).
2. S. Sze, *Physics of Semiconductor Devices* (Wiley, New York, 1981; Mir, Moscow, 1984), Vol. 1.
3. M. Shur, *GaAs Devices and Circuits* (Plenum, New York, 1987; Mir, Moscow, 1991).
4. V. M. Pudalov, Pis'ma Zh. Éksp. Teor. Fiz. **66**, 168 (1997) [JETP Lett. **66**, 175 (1997)].
5. N. F. Mott and E. A. Davis, *Electronic Processes in Non-Crystalline Materials* (Clarendon Press, Oxford, 1979; Mir, Moscow, 1982).
6. V. A. Gergel' and R. A. Suris, Zh. Éksp. Teor. Fiz. **84**, 719 (1983) [Sov. Phys. JETP **57**, 415 (1983)].
7. B. I. Shklovskiĭ and A. L. Éfros, *Electronic Properties of Doped Semiconductors* (Nauka, Moscow, 1979; Springer-Verlag, New York, 1984).
8. Y. Meir, Phys. Rev. Lett. **83**, 3506 (1999).
9. B. A. Aronzon, D. A. Bakaushin, A. S. Vedeneev, *et al.*, Fiz. Tekh. Poluprovodn. (St. Petersburg) **31**, 1460 (1997) [Semiconductors **31**, 1261 (1997)].
10. B. A. Aronzon, A. S. Vedeneev, and V. V. Ryl'kov, Fiz. Tekh. Poluprovodn. (St. Petersburg) **31**, 648 (1997) [Semiconductors **31**, 551 (1997)].
11. B. A. Aronzon, D. A. Bakaushin, A. S. Vedeneev, *et al.*, Pis'ma Zh. Éksp. Teor. Fiz. **66**, 633 (1997) [JETP Lett. **66**, 668 (1997)].
12. A. I. Yakimov, N. P. Stepina, and A. V. Dvurechenskii, Phys. Low-Dimens. Struct. **6**, 75 (1994).
13. M. É. Raĭkh and I. M. Ruzin, Pis'ma Zh. Éksp. Teor. Fiz. **43**, 437 (1986) [JETP Lett. **43**, 562 (1986)].
14. A. S. Vedeneev, A. G. Gaĭvoronskiĭ, and A. G. Zhdan, Prib. Tekh. Éksp., No. 2, 246 (1992).
15. M. Buttiker, Phys. Rev. B **41**, 7906 (1990).
16. R. Landauer, Z. Phys. **68**, 217 (1987).
17. E. H. Nicollian and J. R. Brews, *MOS Physics and Technology* (Wiley, New York, 1982).
18. V. L. Bonch-Bruevich, I. P. Zvyagin, R. Kaĭper, A. G. Mironov, R. Enderlein, and B. Esser, *Electron Theory of Disordered Semiconductors* (Nauka, Moscow, 1981), p. 383.

Translated by M. Skorikov

Semiconductors, Vol. 35, No. 4, 2001, pp. 444–446. Translated from Fizika i Tekhnika Poluprovodnikov, Vol. 35, No. 4, 2001, pp. 456–459.

LOW-DIMENSIONAL SYSTEMS

Plasma Oscillations in Two-Dimensional Semiconductor Superstructures in the Presence of a High Electric Field

S. Yu. Glazov and S. V. Kryuchkov

Volgograd State University of Teacher Training, Volgograd, 400013 Russia

Submitted June 28, 2000; accepted for publication October 4, 2000

Abstract—The effect of a high constant electric field on plasma oscillations in the two-dimensional electron gas of a semiconductor with a superstructure was studied taking into account the Umklapp processes. A dispersion relation for the plasma-oscillation frequency $\omega(k)$ was derived for high temperatures ($\Delta \ll T$, where Δ is the conduction miniband width and T is the temperature in energy units). The plasmon frequency in a high electric field is shown to oscillate as the electric field strength and the wave number k vary. For arbitrary values of k, the spectrum is periodic with a period of $2\pi/d$. Numerical estimates show that the oscillations may manifest themselves at electric field strengths higher than 3×10^3 V/cm. © *2001 MAIK "Nauka/Interperiodica".*

Recently, interest in two-dimensional (2D) electronic structures in systems with periodic potential has been aroused. Fabrication of such 2D superlattices using electron-beam lithography and reactive ionic etching has been reported previously [1]. The Shubnikov–de Haas oscillations of 2D electrons residing in a 2D periodic potential with a period $d = 0.24$ μm were studied in [2]. A fabrication method for GaAlAs/GaAs-based 2D electronic structures has been proposed [3]. The energy spectrum in these structures can be described by the tight-binding approximation with good accuracy. The possibility of solitary electromagnetic wave propagation in 2D superstructures has been demonstrated in [4]. The possibility of plasma oscillations in the 2D electron gas in superstructures was investigated in [5]. It is also known that a sufficiently high constant electric field applied along one of the superstructure axes [6] markedly affects the electron spectrum, and the so-called Stark quantization occurs. In this context, it is interesting to study the effect of a high constant electric field on plasma oscillations in 2D superstructures and, in particular, on the wave-number dependence of the frequency of these oscillations.

Let us consider a 2D electron gas in a system with a periodic potential. A high constant electric field satisfying the condition $\Omega\tau \gg 1$ (where τ is the electron mean free time, $\Omega = eEd$ is the Stark frequency ($\hbar = 1$ hereafter), d is the superstructure period, and E is the electric-field strength) will be described by a time-dependent vector potential $\mathbf{A}(t) = \{-cEt, 0\}$ (the electric field being directed along the X axis). Thus, we use the Coulomb gauge for potentials. The electron dispersion law is the conduction miniband in the absence of an electric field and is described in the tight-binding approximation as

$$\varepsilon(\mathbf{p}) = \Delta - \frac{\Delta}{2}[\cos p_x d + \cos p_y d], \qquad (1)$$

where Δ is the conduction miniband half-width, and p_x and p_y are the electron quasi-momentum components in the superstructure plane.

In the self-consistent field approximation, the Hamiltonian of interacting electrons, with the Umklapp processes taken into account, can be written by analogy with the 3D electron gas [7] as

$$H = \sum_{\mathbf{p}} \varepsilon(\mathbf{p} - e\mathbf{E}t) a_{\mathbf{p}}^{+} a_{\mathbf{p}} + e\frac{1}{\sqrt{N_x N_y}} \times \sum_{\mathbf{p},\,\mathbf{k}} \sum_{n,\,m} U(\mathbf{k}, t) M(k_x) M(k_y) a_{\mathbf{p}-\mathbf{k}+\mathbf{g}}^{+} a_p, \qquad (2)$$

where $a_{\mathbf{p}}^{+}$ and $a_{\mathbf{p}}$ are creation and annihilation operators, respectively, for the electron with the quasi-momentum $\mathbf{p}$; N_x and N_y are the numbers of potential wells forming the superstructure along the x and y axes, respectively, where $\mathbf{g} = (n2\pi/d, m2\pi/d)$;

$$M(k_x) \int_0^{N_x d} \varphi^*(x)\varphi(x)\exp(-ik_x x)dx,$$
$$M(k_y) \int_0^{N_y d} \varphi^*(y)\varphi(y)\exp(-ik_y y)dy, \qquad (3)$$

$U(\mathbf{k}, t)$ is the self-consistent potential defined by the expression

$$U(\mathbf{k}, t) = \frac{2\pi e}{\chi k} \sum_{\mathbf{p}} \sum_{n,\,m} \langle a_{\mathbf{p}+\mathbf{k}+\mathbf{g}}^{+} a_{\mathbf{p}} \rangle M(-k_x) M(-k_y), \qquad (4)$$

and χ is the dielectric constant of the crystal lattice (the broken brackets indicate averaging over the density matrix corresponding to the Hamiltonian (2)). The

equation of motion in the random-phase approximation for the mean values $\langle a^+_{\mathbf{p}+\mathbf{k}+\mathbf{g}} a_{\mathbf{p}}\rangle$ is written as

$$\left\{\frac{\partial}{\partial t} + i[\varepsilon(\mathbf{p}+\mathbf{k}-e\mathbf{E}t) - \varepsilon(\mathbf{p}-e\mathbf{E}t)]\right\}\langle a^+_{\mathbf{p}+\mathbf{k}+\mathbf{g}} a_{\mathbf{p}}\rangle \tag{5}$$
$$= -ieU(\mathbf{k}+\mathbf{g}, t)M([\mathbf{k}+\mathbf{g}]_x)M([\mathbf{k}+\mathbf{g}]_y)(n_{\mathbf{p}+\mathbf{k}+\mathbf{g}} - n_{\mathbf{p}}),$$

where $n_{\mathbf{p}} = \langle a^+_{\mathbf{p}} a_{\mathbf{p}}\rangle$ are electron-level occupation numbers for the 2D electron gas. Inserting the solution of Eq. (5) into (4), we perform certain transformations and obtain the following expression for the Fourier component $U(\mathbf{k}, t)$:

$$\tilde{U}(\mathbf{k}, \omega) = \frac{2\pi e^2}{\chi k}\sum_p \sum_{n,m} M^*(k_x)M^*(k_y) \tag{6}$$
$$\times M([\mathbf{k}+\mathbf{g}]_x)M([\mathbf{k}+\mathbf{g}]_y)\Pi(\mathbf{k}, \omega)\tilde{U}(\mathbf{k}+\mathbf{g}, \omega).$$

Here,

$$\Pi(k, \omega) = \sum_p \sum_l J_l^2\left[\frac{\Delta}{\Omega}\sin\left(\frac{k_x d}{2}\right)\right] \tag{7}$$
$$\times \frac{n_{p+k} - n_p}{\varepsilon(p_y + k_y) - \varepsilon(p_y) - \omega + l\Omega}$$

is the polarization operator. The equation determining the dispersion law $\omega(\mathbf{k})$ follows from (6) and is written as

$$\frac{2\pi e^2}{\chi}\Pi(\mathbf{k}, \omega)S(\mathbf{k}) = 1, \tag{8}$$

where

$$S(\mathbf{k}) = \sum_{n,m} \frac{|M([\mathbf{k}+\mathbf{g}]_x)|^2 |M([\mathbf{k}+\mathbf{g}]_y)|^2}{\sqrt{(k_x+g_x)^2 + (k_y+g_y)^2}}. \tag{9}$$

From relations (7)–(9) it follows that the plasma frequency depends periodically on the wave vector with a period of $2\pi/d$. Therefore, we can restrict ourselves to considering the oscillation spectrum within the first Brillouin zone; i.e.,

$$-\pi/d < k_x < \pi/d, \quad -\pi/d < k_y < \pi/d. \tag{10}$$

The specific shape of the potential wells forming the superstructure must be known to calculate the factor $S(\mathbf{k})$. We consider the case when $\varphi(x) = \text{const}$ for $0 \le x \le d$ and $\varphi(x) = 0$ for $d < x < 0$. Hence, expression (9) becomes

$$S(k) = \frac{4}{d^4} \tag{11}$$
$$\times \sum_{n,m} \frac{(1-\cos k_x d)(1-\cos k_y d)}{(k_x+g_x)^2(k_y+g_y)^2\sqrt{(k_x+g_x)^2 + (k_y+g_y)^2}}.$$

The sum (11) cannot be expressed in terms of tabulated functions for arbitrary $\mathbf{k}$. For small $k(k_x, k_y \ll \pi/d)$, the function $S(\mathbf{k})$ varies as $1/|\mathbf{k}|$.

Let us now consider the nondegenerate electron gas for which

$$n(\mathbf{p}) \approx \exp[-\varepsilon(p_x, p_y)/T], \tag{12}$$

where T is the temperature in energy units. Calculation of the polarization operator is significantly simplified at high temperatures: $2\Delta \ll T$. Thus, we obtain

$$\Pi(\mathbf{k}, \omega) = -\frac{N_0}{T}\left(1 - \frac{1}{4\pi}\sum_l J_l^2(Z)\right. \tag{13}$$
$$\left.\times \int_{-\pi}^{\pi} \frac{\bar{\omega}\,dz}{\bar{\omega} - \sin(k_y d/2)\sin z}\right),$$

where N_0 is the surface density of the 2D electron gas, $\bar{\omega} = (\omega - l\Omega)/\Delta$, $Z = \frac{\Delta}{\Omega}\sin\left(\frac{k_x d}{2}\right)$, and $J_l(Z)$ is the Bessel function of the real argument. Integrating (13), we obtain the following expression for the polarization operator:

$$\Pi(\mathbf{k}, \omega) = -\frac{N_0}{T}\left[1 - \sum_n J_n^2(Z)\frac{\bar{\omega}}{\sqrt{\bar{\omega}^2 - \sin(k_y d/2)^2}}\right. \tag{14}$$
$$\left. - \frac{i}{4\pi}\sum_m J_m^2(Z)\frac{\bar{\omega}}{\sqrt{\sin((k_y d/2)^2 - \bar{\omega}^2)}}\right].$$

Here, summation over n and m is restricted by the inequalities

$$\begin{cases} n < \dfrac{\omega - \Delta|\sin(k_y d/2)|}{\Omega} \\ n > \dfrac{\omega + \Delta|\sin(k_y d/2)|}{\Omega} \end{cases}, \tag{15}$$
$$\frac{\omega - \Delta|\sin(k_y d/2)|}{\Omega} < m < \frac{\omega + \Delta|\sin(k_y d/2)|}{\Omega}.$$

We now consider the case of $\Omega \gg \Delta\sin(k_y d/2)$. Then, two different situations have to be distinguished.

(i) $\Omega \gg \omega$, $k_y d \ll 1$.

In this case, we may retain in (14) only the term with $n = 0$. In view of (8), the plasma frequency is then given by

$$\omega = V_m k_y \frac{F(k, \Omega)}{\sqrt{2F(k, \Omega) - 1}}, \tag{16}$$

where

$$F(k, \Omega) = 1 + q^2 J_0^2(Z)S(k)/2,$$

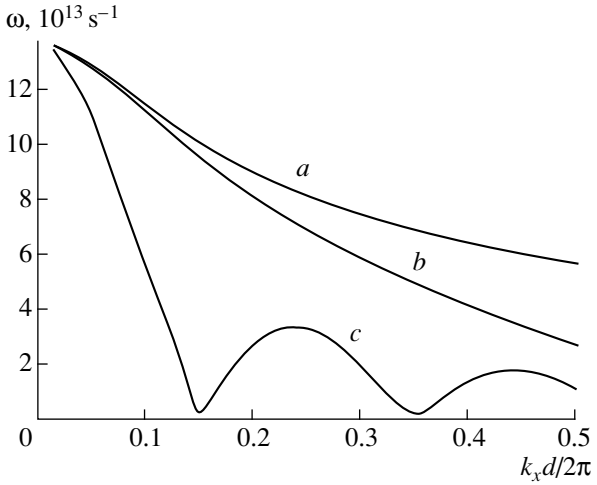

The $\omega(k_x)$ dependences for the concentration $N_0 = 10^{11}$ cm^{-2}, $d = 10^{-6}$ cm, $\Delta = 10^{-2}$ eV, $k_y \approx 10^4$ cm^{-1}, and the Δ/Ω parameter equal to (*a*) ≈0.1, (*b*) ≈1, and (*c*) ≈10.

$V_m = \Delta d/2$ is the characteristic velocity of electrons in the superstructure, and $q = (4\pi e^2 N_0/\chi T)^{1/2}$ is the reciprocal Debye radius.

An oscillatory field dependence of the plasma frequency at a high electric field follows from (16). A similar result was obtained for plasma oscillations in a 1D superlattice subjected to a high electric field [7]. In both cases, the oscillations stem from the geometrical resonance between the plasmon wavelength and the amplitude of the Stark oscillations of electrons in a high electric field. The $\omega(k_x)$ function calculated numerically with (11) and (16) is plotted in the figure.

If $k_x d \ll 1$, $k_y d \ll 1$, and $k_x = k_y$, the plasmon spectrum has a dispersion $\omega^2 \propto k$, which is characteristic of plasma waves in a 2D electron gas [8, 9].

(ii) $\Omega \gg \Delta$.

In this case, the Bessel function can be expanded in the Taylor series. In a zero-order approximation with respect to Z, for the plasma frequency, we have

$$\omega = \Delta\left|\sin\frac{k_y d}{2}\right|\frac{F(k)}{\sqrt{2F(k)-1}}, \qquad (17)$$

where $F(k) = 1 + q^2 S(k)/2$. There is no field dependence of ω in this case.

There is no Landau attenuation in the approximation $\Omega \gg \Delta\sin(k_y d/2)$ considered above. This attenuation is possible only if the plasma frequency ω satisfies the condition

$$m\Omega - \Delta\left|\sin\frac{k_y d}{2}\right| < \omega < m\Omega + \Delta\left|\sin\frac{k_y d}{2}\right|. \qquad (18)$$

In fact, the physical mechanism of the Landau attenuation is related to the absorption (emission) of a plasmon by a particle. The energy conservation law for this process is given by

$$\varepsilon_n(p_y) - \varepsilon_m(p_y \pm k_y) = \mp\omega, \qquad (19)$$

where the upper sign corresponds to the plasmon absorption. Substituting the electron energy spectrum in the presence of a high electric field

$$\varepsilon_n(p_y) = n\Omega - \Delta\cos(p_y d)/2$$

into (19), one can verify that Eq. (19) holds only if condition (18) is satisfied.

Let us make some numerical estimates. In order for the $\omega(k_x)$ oscillation dependence to be pronounced, as follows from (16), the Bessel function argument Z must be at least larger than $Z_0 \approx 2.41$ (the smallest root of the Bessel function). The first minimum in the figure is bound to be observed at $E = 3 \times 10^3$ V/cm under the condition that $\Delta = 10^{-2}$ eV and $k_x \approx 8 \times 10^4$ cm^{-1}.

REFERENCES

1. A. A. Bykov, G. M. Gusev, Z. D. Kvon, *et al.*, Pis'ma Zh. Éksp. Teor. Fiz. **53** (8), 407 (1991) [JETP Lett. **53**, 427 (1991)].
2. G. M. Gusev, Z. D. Kvon, V. B. Besman, *et al.*, Fiz. Tekh. Poluprovodn. (St. Petersburg) **26** (3), 539 (1992) [Sov. Phys. Semicond. **26**, 304 (1992)].
3. D. Ferry, L. Akers, and E. Greeneich, *Ultra-Large-Scale Integrated Microelectronics* (Prentice-Hall, Englewood Cliffs, 1988; Mir, Moscow. 1991).
4. S. V. Kryuchkov and A. I. Shapovalov, Fiz. Tverd. Tela (St. Petersburg) **39** (8), 1470 (1997) [Phys. Solid State **39**, 1305 (1997)].
5. S. Yu. Glazov and S. V. Kryuchkov, Fiz. Tekh. Poluprovodn. (St. Petersburg) **34** (7), 835 (2000) [Semiconductors **34**, 807 (2000)].
6. V. A. Yakovlev, Fiz. Tverd. Tela (Leningrad) **3** (7), 1983 (1961) [Sov. Phys. Solid State **3**, 1442 (1962)].
7. É. M. Épshteĭn, Fiz. Tverd. Tela (Leningrad) **21** (6), 1719 (1979) [Sov. Phys. Solid State **21**, 986 (1979)].
8. F. Stern, Phys. Rev. Lett. **18** (14), 546 (1967).
9. T. Ando, A. B. Fowler, and F. Stern, Rev. Mod. Phys. **54** (2), 437 (1982).

Translated by S. Ktitorov

Semiconductors, Vol. 35, No. 4, 2001, pp. 447–450. Translated from Fizika i Tekhnika Poluprovodnikov, Vol. 35, No. 4, 2001, pp. 460–463.

LOW-DIMENSIONAL SYSTEMS

Magnetic-Field-Induced Transitions between Minibands in GaAs/$Al_xGa_{1-x}As$ Superlattices

V. F. Sapega*[1], D. N. Mirlin*, T. Ruf, M. Cardona**, W. Winter**, and K. Eberl****

** Ioffe Physicotechnical Institute, Russian Academy of Sciences, Politekhnicheskaya ul. 26, St. Petersburg 194021, Russia*

[1] e-mail: sapega@dnm.ioffe.rssi.ru

*** Max-Planck-Institut für Festkörperforschung, D-70569 Stuttgart, Germany*

Submitted October 18, 2000; accepted for publication October 19, 2000

Abstract—The transition from closed to open electron orbits in a magnetic field has been studied by polarized hot electron photoluminescence (HEPL) in superlattices with varied widths of electron minibands. The dependence of the HEPL depolarization on the miniband width is observed. The strong depolarization occurring when the kinetic energy of electrons exceeds the energy gap between the minibands is interpreted in terms of a magnetic-field-induced transition between the electron minibands (magnetic breakdown). © *2001 MAIK "Nauka/Interperiodica".*

1. INTRODUCTION

Recombination of electrons with the wave vector $\mathbf{k} = (k_x, k_y, k_z)$ in III–V semiconductors gives rise to linearly polarized radiation [1–3]. The degree of linear polarization of photons with wave vector q_z, generated by the recombination of electrons with wave vector $\mathbf{k}$ and heavy holes, is

$$\rho_l = \frac{k_y^2 - k_x^2}{k_y^2 + k_x^2 + 2k_z^2}. \quad (1)$$

The degree of linear polarization of photons emitted in the z direction is defined by $\rho_l = (I_x - I_y)/(I_x + I_y)$, where I_x (I_y) is the intensity of luminescence with photon polarization $\mathbf{e}_{\text{lum}}$ lying along the x (y) axis. In an external magnetic field, the Lorentz force changes the direction of the electron wave vector, which, in accordance with relation (1), leads to depolarization of the hot electron photoluminescence (HEPL) [1]. In a bulk crystal, charge carriers move along cyclotron orbits in the plane perpendicular to the direction of the applied magnetic field, this motion being independent of the magnetic field orientation with respect to the crystal axes in the case of spherical symmetry. Such cyclotron motion causes HEPL depolarization only when the symmetry axis of the quasi-momentum distribution of photoexcited electrons does not coincide with the magnetic field direction. The character of carrier motion is strongly modified in crystals of lower dimensionality. In quantum wells (QWs), charge carriers still execute cyclotron motion when the magnetic field is perpendicular to the QW plane, but this motion is forbidden in the case of a magnetic field (in-plane) if the QW width is less than the magnetic length: $L_z \le l_B$, where L_z is the QW width and $l_B = (\hbar c/eB)^{1/2}$ is the magnetic length. Accordingly, the HEPL depolarization in a magnetic field is either observed (when the field is perpendicular to the QW plane) or not (in the case of an in-plane field) [4, 5]. In superlattices (SLs), the magnetic field affects the carrier motion both when the field direction coincides with the direction of the SL growth and when the field vector lies in the plane of the SL layers [5].

In this study, we analyzed the electron motion in a magnetic field in superlattices with broad electron minibands. In distinction to the case discussed in [5], the kinetic energy of electrons was able to significantly exceed the energy of the first forbidden band separating the first and the second electron minibands. This enabled a study of the magnetic-field-induced transition between the electron minibands.

2. EXPERIMENT

The experiments were performed using GaAs/$Al_xGa_{1-x}As$ superlattices with $x \approx 0.2$–1 doped with Be to ~10^{18} cm^{-3}. The QW and barrier widths were fixed at 40 and 6 Å, respectively. Hot electron photoluminescence was excited by a tunable Ti sapphire or (R6G) dye lasers pumped by an Ar-ion laser. Photoluminescence was detected with a SPEX 1404 double-grating monochromator equipped with a GaAs photomultiplier and photon counting system. The HEPL depolarization was studied in $B \le 14$ T magnetic fields with a Voigt (the in-plane magnetic field being perpendicular to the photon wave vector) or Faraday configuration (the magnetic field being aligned with the SL growth direction and the photon wave vector). The linear polarization was measured at the maximum of the

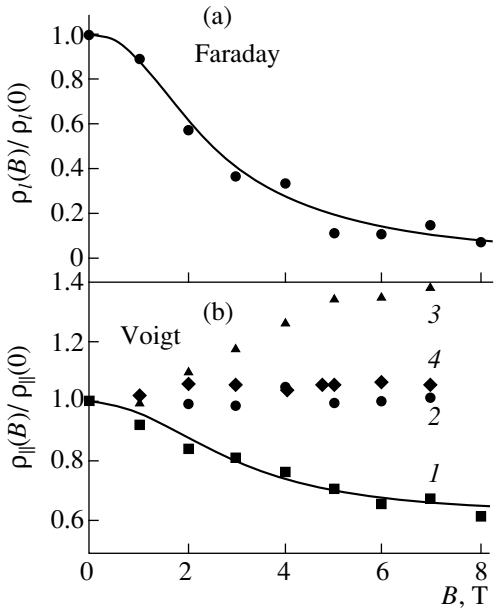

Fig. 1. Linear polarization ρ_l vs. the magnetic field at the maximum of the zero-phonon HEPL peak: (a) Faraday configuration for 40 Å/6 Å SL; solid line represents an approximation by a function of the type $\rho_l(B)/\rho_l(0) = [1 + (B/B_{1/2})^2]^{-1}$; (b) Voigt configuration for bulk GaAs (*1*), QWs (*2*), and narrow-miniband SL at kinetic energy of electrons $\varepsilon \sim \Delta_1$ (*3*) and $\varepsilon \sim 2\Delta_1$ (*4*).

zero-phonon HEPL peak [5] and its value was determined using the standard expression

$$\rho_l = \frac{I_\parallel - I_\perp}{I_\parallel + I_\perp}, \qquad (2)$$

where $I_\parallel$ and $I_\perp$ are the luminescence intensities with polarization being parallel ($\mathbf{e}_{\text{lum}} \parallel \mathbf{e}_{\text{ex}}$) for the former or perpendicular for the latter to that of the exciting light ($\mathbf{e}_{\text{lum}} \perp \mathbf{e}_{\text{ex}}$). In the Voigt configuration, two quantities were measured, $\rho_\parallel$ and $\rho_\perp$, with the electric vector of the exciting light parallel and perpendicular, respectively, to the magnetic field.

3. RESULTS AND DISCUSSION

Figure 1a presents the degree of linear polarization ρ_l vs. the magnetic field in the Faraday configuration for one of the SLs studied. Similar to the bulk sample [1], QWs [4], and SLs with narrow electron minibands [5], the degree of linear polarization also decreases in the magnetic field with the behavior of the depolarization curve $\rho_l(B)/\rho_l(0) = [1 + (B/B_{1/2})^2]^{-1}$ ($B_{1/2}$ is the field in which the polarization is reduced by half) being independent of the kinetic energy of electrons. In the Voigt configuration (Fig. 1b), the HEPL depolarization manifests itself in different ways in QWs, SLs, and in the bulk. The HEPL polarization in the bulk decreases with an increasing magnetic field, similar to the Faraday configuration (data set *1* in Fig. 1b); however, $\rho_\parallel(B)/\rho_\parallel(0) \longrightarrow 0.63$ for $B \longrightarrow \infty$. In this configuration, the magnetic field is aligned with the symmetry axis of the electron momentum distribution function and, therefore, the decrease in $\rho_\parallel(B)$ can only be understood after considering the valence band warping. In QWs with $L_z \approx 150$ Å, the magnetic field does not affect the HEPL polarization in experimentally obtainable magnetic fields (data set *2* in Fig. 1b). In SLs with narrow electron minibands (i.e., in SLs where the first electron miniband in the SL growth direction is narrower than the energy gap between the first and second minibands: $\Delta_1 < \Delta_G$), the effect of the magnetic field on the polarization depends on the kinetic energy of electrons. The degree of polarization markedly increases with the magnetic field (rather than decreasing, as occurs in the bulk) when the kinetic energy of electrons (ε) is lower than or equal to the first miniband width (Fig. 1b, data set *3*). The polarization depends on the field only slightly (Fig. 1b, data set *4*) when the kinetic energy of electrons lies within the first forbidden band separating the first and second allowed minibands of the SL.

For SLs with broad electron minibands ($\Delta_1 \geq \Delta_G$), the magnetic-field behavior of the polarization differs from that in the bulk and from SLs with narrow minibands. Figure 2 shows the linear polarization vs. the magnetic field in the Voigt configuration for an SL with the following miniband parameters (calculated in terms of model [6]): $\Delta_1 \approx 232$ eV, $\Delta_G \approx 77$ meV, and a distance between the bottoms of the first and the second minibands of $\Delta_1 + \Delta_G \approx 309$ meV. When the kinetic energy of electrons lies within the first miniband ($\varepsilon \lesssim \Delta_1$), the depolarization curve for this SL is similar to the curve obtained for bulk GaAs (compare data sets *1* in Figs. 1b, 2). When the electrons are excited to energies within the band gap ($\Delta_1 < \varepsilon < \Delta_1 + \Delta_G$), the effect of the magnetic field on the HEPL polarization is weak, which is similar to what happens in QWs or SLs with narrow minibands at energies exceeding the width of the first miniband (compare data sets *2* or *4* in Fig. 1b with data set *2* in Fig. 2). With the electron energy increasing further ($\varepsilon > \Delta_1 + \Delta_G$), i.e., at an energy exceeding the energy of the second miniband bottom, bends in the depolarization curves are observed (marked by arrows B_0^i in Fig. 2) with the corresponding magnetic field B_0^i decreasing with increasing kinetic energy of electrons.

Now we consider the reasons for the anomalous behavior of HEPL polarization in SLs with broad minibands. Hot electron photoluminescence polarization in narrow-miniband SLs was discussed in detail in [5]; it was shown that in the strong-coupling approximation, the electron motion in the Voigt configuration is described by the pendulum equation. In this model, the miniband quasi-momentum Q_z of electrons moving mainly in the direction of the SL growth (at $\varepsilon \lesssim \Delta_1$) is

transformed in the magnetic field into a lateral quasi-momentum $k_\perp$ [5]. At the same time, the field-aligned component of the lateral quasi-momentum $k_\parallel$ remains unchanged. If the magnetic field is aligned with the electric vector of the exciting light ($\mathbf{B} \parallel \mathbf{e}_{exc} \parallel x$), then k_y^2 in (1) can be replaced by $k_\perp^2$, and k_x^2, by $k_\parallel^2$ [see Eq. (1)]. In this case, the degree of HEPL polarization $\rho_\parallel$ increases (see Fig. 1b, data set *3*). If the luminescence is excited by light with polarization $\mathbf{B} \perp \mathbf{e}_{exc} \parallel x$, the replacement $k_x^2 = k_\perp^2$ and $k_y^2 = k_\parallel^2$ should be done in Eq. (1). Analysis of (1) shows that, in this case, the degree of polarization $\rho_\perp$ decreases with an increasing magnetic field [5] (this situation is not considered here).

In contrast to narrow-miniband SLs, $\rho_\parallel(B)$ decreases with an increasing magnetic field in SLs with broad minibands, as in the bulk case. This behavior of HEPL polarization in broad-miniband SLs at $\varepsilon < \Delta_1$ is presumably due to the tight-binding approximation not applicable to this case (as shown in [7]). Nevertheless, as for narrow-miniband SLs, the HEPL polarization is nearly unaffected by the magnetic field when the kinetic energy of photoexcited electrons falls within the forbidden band. In this situation, the electrons move along open orbits in **k**-space, and the change in the $k_\perp$ quasi-momentum component is small ($\Delta k_\perp \propto \sqrt{2m_c\Delta_1}$) compared with the total lateral quasi-momentum, and, therefore, the change in polarization is also small. In broad-miniband SLs, the situation changes fundamentally when the kinetic energy of electrons exceeds the energy of the bottom of the second electron miniband: $\varepsilon \gtrsim \Delta_1 + \Delta_G$. In this case, the electrons generated in the first miniband continue moving along open orbits and, therefore, the magnetic field cannot substantially affect the HEPL polarization ($\Delta k_\perp \ll k_\perp$). However, electrons can be thrown into the second miniband by inelastic scattering on polar optical phonons or via tunneling in the magnetic field. Evidently, the additional intersubband scattering on polar optical phonons cannot give rise to the bend in the depolarization curves (additional scattering can only increase the half-width of the depolarization curve). We suppose that the bend in the depolarization curves (B_0^i in Fig. 2) and its dependence on the kinetic energy of electrons are associated with the magnetic-field-induced transitions between electron subbands (known in the theory of metals as magnetic breakdown). As is shown in the theory of metals, a magnetic field can induce transitions of electrons between the electron subbands, which was manifested in the experiment as a variation of the period of the Shubnikov–de Haas oscillations (recently, magnetic breakdown has been observed in lateral semiconductor SLs [8, 9]). The transition from a cyclotron orbit of one band to a cyclotron orbit of another occurs when the distance δk between the orbits in **k**-space is small compared with the uncertainty of the electron wave vector. For metals, the tunneling of electrons with the wave vector lying on the Fermi surface occurs when $\delta k \sim l_B$. This condition can be written in an alternative form:

$$\hbar\omega_c \sim \frac{\Delta_{gap}^2}{E_F \sin 2\theta}, \qquad (3)$$

where ω_c is the cyclotron frequency, Δ_{gap} is the energy distance between two electron minibands in the tunneling region, E_F is the Fermi energy, and θ is the angle satisfying the Bragg scattering condition. Evidently, this condition is also applicable to SLs. To assess the possibility of magnetic breakdown in SLs, the Δ_{gap} in (3) should be replaced by Δ_G, the forbidden band separating the first and second electron minibands in the SL, and, instead of E_F, the kinetic energy of electrons in the first miniband should be used, which is in turn determined by the energy of an exciting photon. Therefore, the conditions allowing the observation of magnetic breakdown can be created by an appropriate choice of SL parameters and photon energy. Hence, a decrease in $\rho_\parallel$ would be expected in a magnetic field satisfying the breakdown condition. Indeed, due to the conditions of magnetic breakdown, the electrons with the quasi-

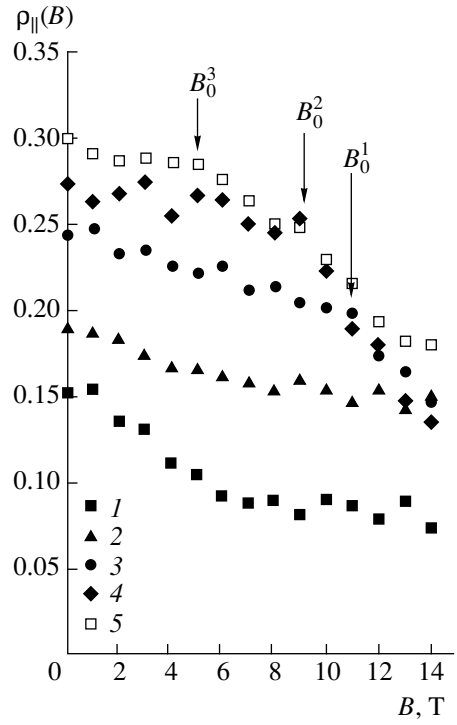

Fig. 2. Linear polarization $\rho_\parallel$ vs. the magnetic field at the maximum of the zero-phonon HEPL peak in the Voigt configuration for a broad-miniband SL at the kinetic energy of electrons ε = 102 (*1*), 243 (*2*), 293 (*3*), 321 (*4*), and 332 meV (*5*). Points *2* correspond to electrons with kinetic energy within the first forbidden band, and points *3*, to electrons with energy equal to the energy of the bottom of the second miniband.

momentum component k_y are scattered into the second miniband; consequently, their contribution to the distribution function decreases, thus depressing the polarization [see relation (1)]. Evidently, the characteristic magnetic field at which an abrupt change in polarization occurs depends, according to (3), on the kinetic energy of electrons in the first miniband. The probability of magnetic breakdown can be ascertained, in analogy with [10], by substituting the kinetic energy of electrons ε for E_F:

$$P = \exp\left(-\frac{\pi\Delta_G^2}{4\hbar\omega_c\varepsilon\sin(2\theta)}\right). \quad (4)$$

It is this general tendency that is observed in the experiment. In the experimentally accessible magnetic fields $B = 14$ T, $\Delta_G = 80$ meV, and when electrons in the first miniband have energy slightly exceeding the energy of the bottom of the second miniband, $\varepsilon \sim 310$ meV, expression (4) yields $P \approx 0.34$. With the kinetic energy of electrons increasing further, the probability P increases, and is manifested by the bend in the depolarization curves shifting to lower magnetic fields.

4. CONCLUSION

The depolarization of HEPL from SLs in a magnetic field has been studied. Anomalous behavior of the depolarization in the Voigt configuration is observed when the kinetic energy of electrons in the first miniband exceeds the energy of the bottom of the second miniband. This feature, manifesting itself as a bend in the depolarization curves, is accounted for by the effect of the magnetic-field-induced tunneling of electrons from the first to the second miniband (magnetic breakdown).

ACKNOWLEDGMENTS

The authors are grateful to V.I. Perel' for valuable discussions.

This study was supported by the Russian Foundation for Basic Research, project no. 99-02-18298. V.F. Sapega thanks Max-Planck Gesselshaft for financial support and the Max-Planck Institute for the experimental facilities provided.

REFERENCES

1. D. N. Mirlin, I. Ya. Karlik, L. P. Nikitin, *et al.*, Solid State Commun. **37**, 757 (1981).
2. B. P. Zakharchenya, D. N. Mirlin, V. I. Perel', and I. I. Reshina, Usp. Fiz. Nauk **136**, 459 (1982) [Sov. Phys. Usp. **25**, 143 (1982)].
3. M. A. Alekseev, I. Ya. Karlik, D. N. Mirlin, and V. F. Sapega, Fiz. Tekh. Poluprovodn. (Leningrad) **23**, 761 (1989) [Sov. Phys. Semicond. **23**, 479 (1989)].
4. P. S. Kop'ev, D. N. Mirlin, D. G. Polyakov, *et al.*, Fiz. Tekh. Poluprovodn. (Leningrad) **24**, 1200 (1990) [Sov. Phys. Semicond. **24**, 757 (1990)].
5. V. F. Sapega, V. I. Perel', A. Yu. Dobin, *et al.*, Phys. Rev. B **56**, 6871 (1997).
6. G. Bastard, Phys. Rev. B **25**, 7584 (1982).
7. V. F. Sapega, V. I. Perel', D. N. Mirlin, *et al.*, Phys. Status Solidi B **215**, 379 (1999).
8. M. Langenbuch, R. Henning, M. Suhrke, *et al.*, Physica E (Amsterdam) **6**, 565 (2000).
9. R. A. Deutschmann, A. Lorke, W. Wegscheider, *et al.*, Physica E (Amsterdam) **6**, 561 (2000).
10. P. Steda and A. H. MacDonald, Phys. Rev. B **41**, 11892 (1990).

Translated by D. Mashovets

Semiconductors, Vol. 35, No. 4, 2001, pp. 451–452. Translated from Fizika i Tekhnika Poluprovodnikov, Vol. 35, No. 4, 2001, pp. 464–466.

PHYSICS OF SEMICONDUCTORS DEVICES

The Effect of Pulsed Laser Annealing on the Parameters of $Cd_xHg_{1-x}Te$ Photoresistors

V. N. Ryzhkov*, M. I. Ibragimova, and N. S. Baryshev***

** GIPO Federal Scientific-Production Center, Kazan, 420075 Tatarstan, Russia*

*** Kazan Physicotechnical Institute, Kazan Scientific Center, Russian Academy of Sciences, Kazan, 420029 Tatarstan, Russia*

e-mail: ibragimova@dionis.kfti.knc.ru

Submitted July 26, 2000; accepted for publication September 14, 2000

Abstract—The effect of nanosecond-pulse radiation of a Nd laser (pulse duration $\tau = 10$ ns, wavelength $\lambda = 1.06$ μm) at 300 K on the parameters of $Cd_{0.19}Hg_{0.81}Te$ photoresistors was studied. At the optimal energy density $W = 0.2$–0.3 J/cm^2, the surface melts to yield a 0.04–0.52-μm-thick inversion layer with increasing sensitivity and detectivity of the photoresistors. At higher energy densities W, the parameters of the photoresistors deteriorate, and the dark resistance grows. © *2001 MAIK "Nauka/Interperiodica".*

Photoresistors based on $Cd_xHg_{1-x}Te$ solid solutions are widely used in both modern IR technology and scientific research. Various methods are known for surface treatment of the sensitive elements of these devices to improve their photoelectric parameters and characteristics. One of these techniques is the pulsed laser annealing (PLA).

The action of pulsed laser radiation on $Cd_xHg_{1-x}Te$ has been the subject of several studies, mainly concerned with the effect of radiation on the physicochemical properties of the modified layers. One of the important PLA parameters is the energy density W at which the surface layer melts. In [1–3], attempts were made to determine the $Cd_xHg_{1-x}Te$ melting threshold under the action of nanosecond pulses of ruby laser. The obtained data are contradictory, with the threshold W values ranging from 0.03 to 0.18 J/cm^2.

The aim of this study was to find the optimal regimes of annealing under the action of nanosecond pulses of Nd laser radiation that would improve the parameters of $Cd_xHg_{1-x}Te$ photoresistors. Numerical modeling of the process of pulsed laser irradiation was applied to determine the surface melting threshold and the thickness of the recrystallized layer.

The photoresistors were fabricated from *n*-type $Cd_xHg_{1-x}Te$ single crystals with $x = 0.19$, grown by the Bridgman technique. The annealing was done at 300 K with pulsed radiation of a Nd laser (wavelength $\lambda = 1.06$ μm, pulse duration $\tau = 10$ ns) through the entrance window of a vacuum cryostat in which the photosensitive elements were placed.

BaF_2 was used as the material for the entrance window. To prevent mercury evaporation in the course of PLA, the surface of the elements was protected with a ZnS film deposited by vacuum evaporation. The photoelectric characteristics were measured at 77 K.

Figure 1 presents spectral distributions of the photoresistor's sensitivity measured before (curve *1*) and after (curve *2*) annealing by radiation pulses with energy density $W = 0.3$ J/cm^2. A pronounced increase in sensitivity is observed in the short-wavelength part of the spectrum. At higher energy densities, the sensitivity decreases over the entire range of wavelengths $\lambda = 2$–14 μm.

Figure 2 presents the voltage sensitivity S of the photoresistor as a function of the PLA energy density. It can be seen that the maximum sensitivity is achieved at $W \approx 0.3$ J/cm^2. At higher W values, the sensitivity decreases. The dark resistance grows in the same range of energy densities ($W > 0.3$ J/cm^2).

The dependence of the detectivity (D^*) on the energy density is qualitatively similar to the $S(W)$ dependence; the maximum D^* value corresponds to

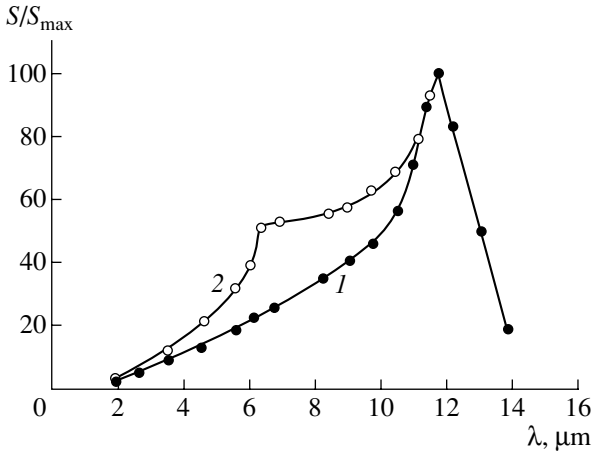

Fig. 1. Spectral distribution of the photoresistor sensitivity normalized to the maximum value (*1*) before and (*2*) after pulsed laser annealing at energy density $W = 0.3$ J/cm^2.

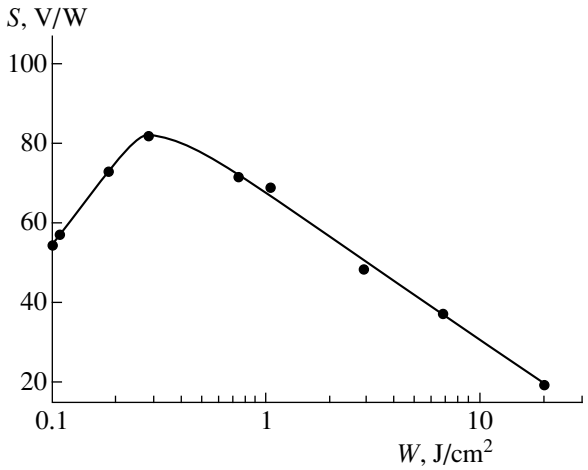

Fig. 2. Voltage sensitivity of photoresistor vs. energy density of pulsed laser annealing.

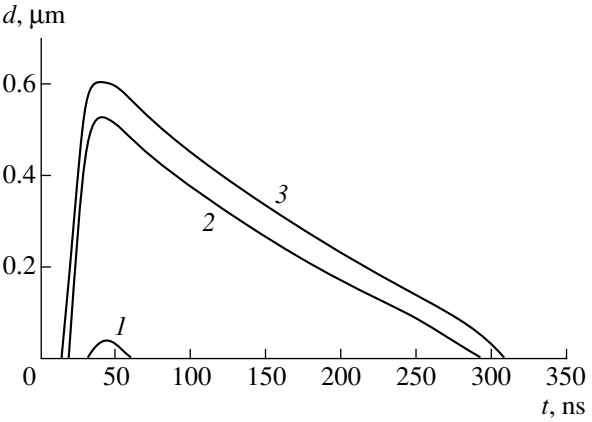

Fig. 3. Calculated time dependence of thickness of the $Cd_xHg_{1-x}Te$ layer recrystallized under the action of pulses with energy density W = (*1*) 0.19, (*2*) 0.3, and (*3*) 0.33 J/cm^2.

$W \approx 0.2$ J/cm^2, and the fast fall at $W > 1$ J/cm^2 is mainly due to the increasing amount of noise in the sensitive element.

To determine the optimal regimes of $Cd_xHg_{1-x}Te$ PLA, temperature fields were calculated numerically by a procedure described in [4]. Numerical calculations take into account all basic factors affecting the heating (including phase transitions) and furnish information about temperature profiles across the sample thickness and their evolution in time. Figure 3 presents the time dependences of the thickness d of the recrystallized $Cd_xHg_{1-x}Te$ layer upon exposure to laser radiation pulses with varied energy density. The performed thermal calculations indicate that, in the annealing of the surface of a photosensitive element by laser pulses, the surface layers start to melt at an energy density of ~0.16 J/cm^2. At an energy density of $W = 0.19$ J/cm^2, the thickness of the recrystallized layer is $d = 0.04$ μm, becoming as large as 0.52 μm at $W = 0.3$ J/cm^2.

Experimental and calculated data show that with the beginning of the surface melting the sensitivity and detectivity of the photoresistors grow. The rise in sensitivity in the short-wavelength part of the spectrum is due to a decrease in the rate of surface recombination and increase in the effective carrier lifetime. The latter may be due to the formation at the surface of an inversion layer hindering motion of photocarriers toward the surface and their recombination there. The growing effective lifetime leads to higher voltage sensitivity and detectivity. The rise in dark resistance on raising the PLA energy density to $W > 0.3$–0.5 J/cm^2 is most likely due to the increasing inversion layer thickness and its effect on the total resistance of the sample. At energy densities $W > 1$ J/cm^2, the resistance increases dramatically with the voltage sensitivity and detectivity markedly falling as a result of structural changes in the sample in the course of PLA.

Thus, the results indicate that irradiation of the photosensitive surface of photoresistors with nanosecond pulses of Nd laser radiation with energy density W = 0.2–0.3 J/cm^2 at a temperature of 300 K leads to melting of the photoresistor surface to give an inversion layer at the surface with thickness d = 0.04–0.52 μm. This layer makes the rate of surface recombination lower and the effective lifetime of photocarriers longer with the sensitivity and detectivity of a photoresistor becoming higher. Raising the PLA energy density further impairs the photoresistor parameters and leads to an increase in dark resistance.

REFERENCES

1. P. E. Mozol, V. V. Borsch, V. A. Gnatyuk, *et al.*, Semicond. Sci. Technol. **10**, 61 (1995).
2. M. M. Jevtic and M. J. Scepanovic, Appl. Phys. A: Solids Surf. **A53**, 332 (1991).
3. L. A. Golovan', P. K. Kashkarov, V. M. Lakeenkov, and V. Yu. Timoshenko, Fiz. Tekh. Poluprovodn. (St. Petersburg) **31**, 931 (1997) [Semiconductors **31**, 793 (1997)].
4. R. M. Bayazitov, M. I. Ibragimova, and I. B. Khaĭbullin, Available from VINITI No. 4716-81 (1981).

Translated by M. Tagirdzhanov

Semiconductors, Vol. 35, No. 4, 2001, pp. 453–458. Translated from Fizika i Tekhnika Poluprovodnikov, Vol. 35, No. 4, 2001, pp. 467–473.

PHYSICS OF SEMICONDUCTORS DEVICES

Photodiodes for a 1.5–4.8 μm Spectral Range Based on Type-II GaSb/InGaAsSb Heterostructures

N. D. Stoyanov, M. P. Mikhaĭlova, O. V. Andreĭchuk, K. D. Moiseev, I. A. Andreev, M. A. Afrailov, and Yu. P. Yakovlev

Ioffe Physicotechnical Institute, Russian Academy of Sciences, Politekhnicheskaya ul. 26, St. Petersburg, 194021 Russia

Submitted July 26, 2000; accepted for publication August 2, 2000

Abstract—Long-wavelength photodiodes based on LPE-grown type-II heterostructures in lattice-matched GaSb/InGaAsSb/GaInAsSb and GaSb/InGaAsSb/AlGaAsSb systems were fabricated and studied. Band energy diagram engineering for heterostructures with wide- and narrow-gap layers allows the photodiode parameters to be controlled by varying the conditions at heterointerfaces. Electrical and photoelectric characteristics and the dark current mechanisms in the heterostructures were investigated. The optimal photodiode structure was selected that consists of two type-II broken-gap heterojunctions and one *p*–*n*-junction in the narrow-gap active layer. Room-temperature detectivity $D_\lambda^* = 4.1 \times 10^8$ cm Hz$^{1/2}$/W at $\lambda = 4.7$ μm was obtained. Type-II heterostructures may help develop high-efficiency uncooled photodiodes for the 1.6–4.8 μm range for gas analysis, environmental monitoring, and also the diagnostics of combustion and explosion products. © *2001 MAIK "Nauka/Interperiodica".*

1. INTRODUCTION

In recent years, InAs–GaSb type-II heterojunctions have attracted attention as promising materials for optoelectronic devices (lasers and light-emitting diodes) operating in the $\lambda = 2$–5 μm spectral range [1–3] important for gas analysis, environmental monitoring, etc. This is due to the unusual band diagram of the heterojunctions with electrons and holes localized in self-consistent quantum wells on different sides of the heterointerface. The decisive role of the type-II heterointerface gives rise to a variety of new optical, photoelectric, and magnetotransport phenomena [4].

Previously, we described long-wavelength photodiodes based on multicomponent III–V solid solutions (InAsSb/InAs, InAs/InAsSbP) operating either under deep cooling [5] or at room temperature [6]. However, operation without cooling was limited by a number of design defects in these structures. Thus, a new alternative approach to the design of mid-IR range photodiodes operating at room temperature is necessary.

This paper presents a new approach to the creation of long-wavelength photodiodes based on type-II heterojunctions in the $In_{1-x}Ga_xAsSb/GaSb$ system. Previously, we showed [7] that $In_{1-x}Ga_xAsSb/GaSb$ heterojunctions with a narrow-gap solid solution containing more than 70% In ($x < 0.3$) are type-II broken-gap heterojunctions, with the conduction band of the narrow-gap semiconductor lying about $\Delta \approx 60$–100 meV higher in the energy than the valence band of the wide-gap semiconductor. The electron flow across the heterojunction gives rise to strong band bending on both sides of the junction and to a semimetallic channel for electrons and holes at the interface [8, 9].

The intense electroluminescence observed in type-II broken band-gap heterojunctions in the GaInAsSb/InAs system [10, 11] indicates the high efficiency of radiative recombination at a heterointerface of this kind. Furthermore, it has been shown theoretically [10] that non-radiative Auger recombination must be strongly suppressed at the type-II heterointerface [12].

It has also been established [7, 13] that the broken-gap heterojunction behaves as a Schottky diode in which the role of a metal is played by a wide bandgap (*P*–*p* structure) or a narrow band semiconductor (*N*–*n* structure). In this case, depending on the type of structure, the photoresponse spectrum lies in the range of absorption of either the narrow-gap, or the wide-gap semiconductor [7]. It has also been shown that the *P*-GaSb/*n*-InGaAsSb system demonstrates metallic conduction; i.e., it behaves as an ohmic contact [4, 14]. This feature, in particular, was used to reduce the series resistance of the structure.

The described properties of type-II heterojunctions allow the photoresponse wavelength and the photodiode structure parameters to be varied by changing the type of the band diagram and the conditions at the heterointerface. The results obtained indicate that type-II heterojunctions based on InAs–GaSb solid solutions show promise for creating high-efficiency photodiodes.

1063-7826/01/3504-0453$21.00 © 2001 MAIK "Nauka/Interperiodica"

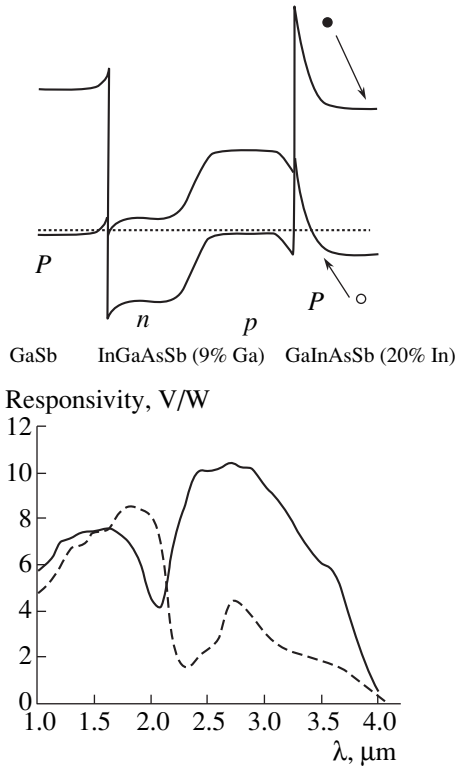

Fig. 1. Band diagram and photoresponse spectra of an *A*-type structure.

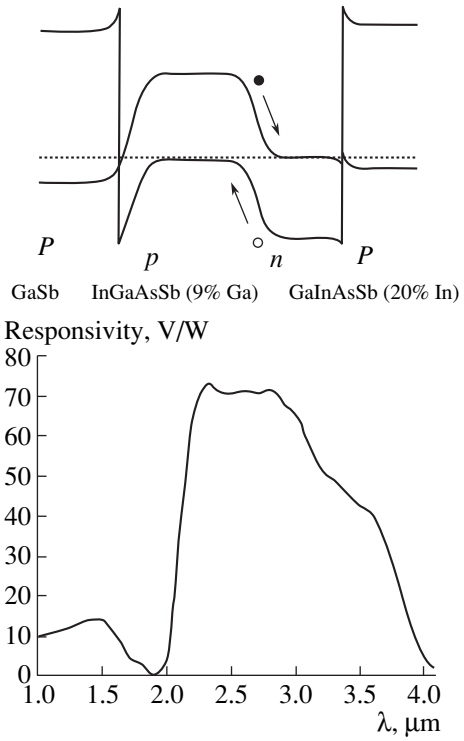

Fig. 2. Band diagram and photoresponse spectrum of a *B*-type structure.

2. EXPERIMENTAL

In order to choose the optimal photodiode structure, we have fabricated and studied three types of heterostructures based on isoperiodic quaternary solid solutions grown by liquid-phase epitaxy on GaSb substrates.

Structure *A* has a narrow-gap *n*–*p*-homojunction in the active region: *P*-GaSb/*n*-InGaAsSb/*p*-InGaAsSb/*P*-GaInAsSb; the In content in the narrow-gap InGaAsSb active layer varies within 3–2%, the Ga content in the wide-gap GaInAsSb "window" is 20%.

Structure *B* has a narrow-gap *p*–*n* homojunction in the active region: *P*-GaSb/*p*-InGaAsSb/*n*-InGaAsSb/*P*-GaInAsSb; the layer composition is the same as in structure *A*.

Structure *C* has a wider-gap AlGaAsSb window: *P*-GaSb/*P*-AlGaAsSb/*p*-InGaAsSb/*n*-InGaAsSb/*N*-AlGaAsSb; the In content in the narrow-gap InGaAsSb active layer is 9%, and the Al content in the wide-gap AlGaAsSb window is 34%.

Undoped (100) GaSb substrates with a hole concentration of $p = 5 \times 10^{16}$ cm^{-3} were used in all cases. High-quality mirror-surface $In_{1-x}Ga_xAs_{1-y}Sb_y$ epilayers with Ga content $0.03 < x < 0.12$ and Sb content $y = x + 0.12$ (the band gap was practically the same for all the compositions, $E_g \approx 0.26$ eV [7] within the range under study) were grown at 600°C from a growth solution in metallic In at a cooling rate of 0.6°C/min. The initial oversaturation was set to be within 5–8°C. As is known, the system of GaSb–InAs binary solutions is characterized by the unlimited solubility of GaSb-rich compounds in InAs-rich melts and is very sensitive to deviations from the phase equilibrium. Hence, in the given case, growth solutions with nonequilibrium composition of the liquid phase are saturated with Ga and Sb from the GaSb substrate. To resolve this problem and improve the quality of the interface, we introduced a wide-gap GaInAsSb solid solution with a high Ga content, which served as a buffer layer between the GaSb substrate and the narrow-gap InGaAsSb layer. It is worth noting that we deal with equilibrium epitaxial growth of materials with markedly different mechanical properties: the thermal expansion coefficient of GaSb is twice that of InAs. Therefore, the experimental lattice mismatches obtained at 300 K ($\Delta a/a \sim 3 \times 10^{-3}$) correspond to a zero mismatch between the InGaAsSb solid solution and the substrate at the temperature of epitaxy, which is confirmed by the presence of thickness oscillations in the X-ray diffraction spectra.

Structures *A* and *B* contained type-II broken-gap heterojunctions formed by an active narrow-gap layer and wide-gap materials (GaSb and GaInAsSb, respectively) (Figs. 1, 2). Structure *C* contained type-I heterojunctions between narrow-gap *n*- and *p*-InGaAsSb layers and a wide-gap AlGaAsSb capping layer (Fig. 3). In

all the structures, the *p*–*n*-homojunction was formed during the epitaxy of the narrow-gap $In_{1-x}Ga_xAsSb$. An undoped narrow-gap *n*-type layer had an electron concentration of 5×10^{16} cm^{-3}. To obtain *p*-type conduction, the quaternary solid solution was doped with Zn ($p = 1 \times 10^{17}$ cm^{-3}). In structures *A* and *B*, the wide-gap window was formed by a $Ga_xIn_{1-x}AsSb$ quaternary solid solution with a composition close to GaSb ($x = 0.8$, $E_g = 0.63$ eV). This layer was doped with Ge to obtain *p*-conduction ($p = 2 \times 10^{16}$ cm^{-3}). In the *C*-type structure, the narrow-gap $In_{1-x}Ga_xAsSb$ ($x = 0.03$–0.12) quaternary solid solution was confined on both sides by AlGaAsSb layers with 34% Al, whose band gap, $E_g = 1.1$ eV, was substantially higher than that of GaSb ($E_g = 0.71$ eV) or $Ga_{0.8}In_{0.2}AsSb$.

The electrical and photoelectric properties of the structures grown were studied on mesadiodes 300 μm in diameter fabricated by conventional photolithography. Ohmic contacts 50 μm in diameter were deposited by sputtering Au:Te and Au:Zn alloys onto *n*- and *p*-layers, respectively.

3. ANALYSIS OF RESULTS

We now discuss separately specific features of the spectral characteristics for structures *A*, *B*, and *C*. Band diagrams and photoresponse spectra of the heterostructures under study are presented in Figs. 1, 2, and 3.

In the *A*-type structure (*PnpP*), there is very strong band bending at the heterointerface *p*-$In_{1-x}Ga_xAsSb$ ($x = 0.03$–0.12)/*P*-$Ga_xIn_{1-x}AsSb$ ($x = 0.8$) (Fig. 1). Electron–hole pairs generated in the upper layer are effectively separated by the strong built-in electric field. Accordingly, the sensitivity in the $\lambda \approx 2$ μm range is comparable with, and in some cases exceeds, the sensitivity in the long-wavelength range.

In the *B*-type structure (*PpnP*), the band bending at the interface with the wide-gap layer (window) is negligible (Fig. 2). At compositions of the narrow-gap solid solution $x = 0.03$–0.12, the broken-gap *n*-$In_{1-x}Ga_xAsSb$/*P*-$Ga_{0.8}In_{0.2}AsSb$ heterojunction behaves as an ohmic contact [7]. Carriers are not separated at this interface and, therefore, the photosensitivity is close to zero at $\lambda < 2$ μm (Fig. 2). Effective photon absorption and carrier separation mainly occur in the narrow-gap layer at the *p*-InGaAsSb/*n*-InGaAsSb homojunction, with the spectral sensitivity lying in the long-wavelength part of the spectrum.

In the *C*-type structure (Fig. 3), the short-wavelength edge of the photoresponse spectrum is defined by the wide-gap AlGaAsSb window ($E_g = 1.1$ eV), with the long-wavelength threshold of sensitivity determined by the narrow-gap $In_{1-x}Ga_xAsSb$ layer ($E_g = 0.26$ eV). This type of structure allows fabrication of photodiodes with a very wide spectral range of sensitivity (0.9 to 4.8 μm at room temperature), which is important, e.g., for analyzing combustion and explosion products.

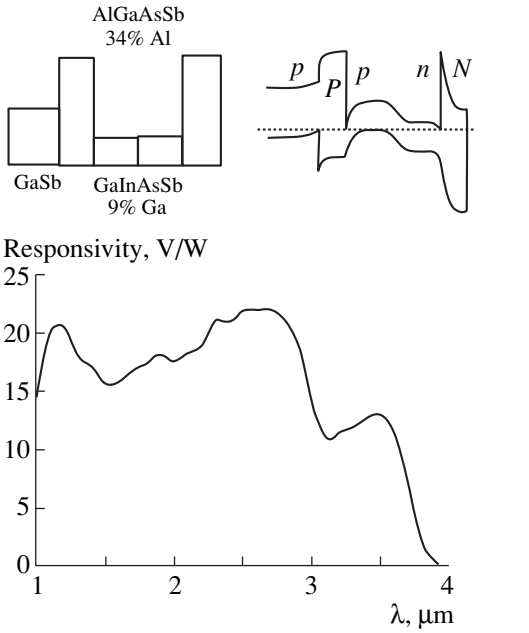

Fig. 3. Band diagram and photoresponse spectrum of a *C*-type structure.

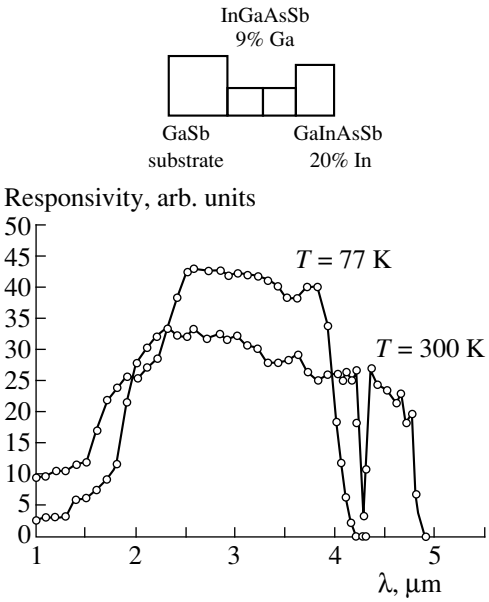

Fig. 4. Optimized photodiode structure and its photoresponse spectra at $T = 300$ and 77 K.

An analysis of the above data led us to conclude that the type *B* structure, with a narrow-gap *p*–*n*-homojunction in the active region (Fig. 4), is optimal as regards efficiency. Next, we optimized the parameters of this structure, which allowed us to fabricate photodiodes that work at room temperature.

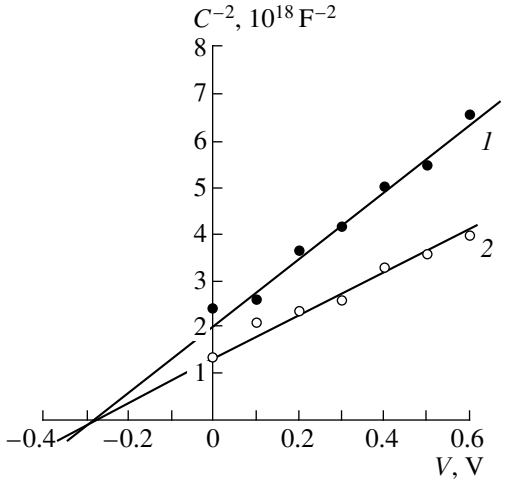

Fig. 5. Inverse square of capacitance vs. applied voltage for the optimized structure at T = 300 K.

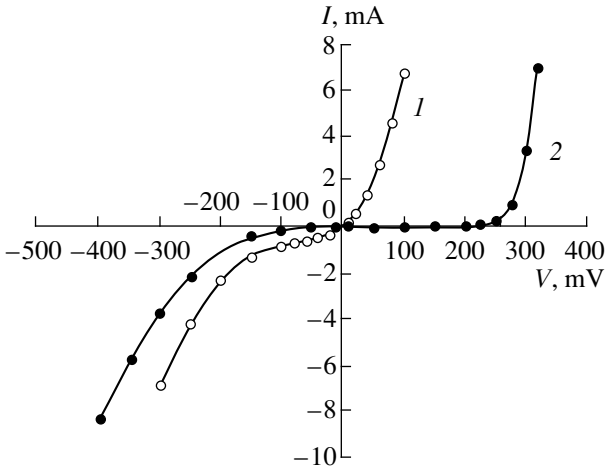

Fig. 6. *I–V* characteristics at T = 300 (*1*) and 77 K (*2*).

Figure 5 shows the capacitance–voltage characteristics $C(V)$ for the optimized structures taken at a temperature T = 300 K and frequency f = 1 MHz. At low reverse biases (V < 0.8 V), the characteristics are satisfactorily described by the dependence $C^{-2} \sim V$, typical of an abrupt junction. The contact potential difference V_D found from the linear dependence of C^{-2} on V (0.26 eV) coincides with the band gap of the narrow-gap $In_{0.91}Ga_{0.09}AsSb$ solid solution. Using the approximation of an asymmetric *p–n*-junction of area S, we determined the donor concentration N in the unintentionally doped *n*-region:

$$C = S\sqrt{\frac{q\varepsilon_0\varepsilon N}{2(V_D - V)}}, \quad N = \frac{C^2 2(V_D - V)}{S^2 q\varepsilon_0\varepsilon},$$

where ε_0 is the permittivity of free space and ε is the dielectric constant. The values obtained lie in the range $(1–3) \times 10^{17}$ cm^{-3}.

Figure 6 presents the current–voltage (*I–V*) characteristics of an optimized structure at T = 300 and 77 K. The structure comprises a sequence of three junctions: a broken-gap type-II heterojunction *P*-GaSb/*p*-$In_{0.91}Ga_{0.09}AsSb$, a homojunction in the narrow-gap $In_{0.91}Ga_{0.09}AsSb$ solid solution, and a broken-gap type-II heterojunction *n*-$In_{0.91}Ga_{0.09}AsSb$/*P*-$Ga_{0.80}In_{0.20}AsSb$.

As stated above, the third junction behaves as an ohmic contact that does not limit the current and, consequently, does not affect the *I–V* characteristic. Further, we discuss the processes related to the first two junctions.

3.1. Forward Bias

Forward-bias *I–V* characteristics of structure *B* are shown in Fig. 7 in log–log scale. The room temperature value of the ideality factor obtained from (*I–V*) characteristics n = 1.5 is intermediate between the values of this parameter for the diffusion (n = 1) and the generation-recombination currents (n = 2). Indeed, forward-biasing of the *p–n* junction lowers its barrier in the first place. The flow of holes from the *p*-region reaches the negative contact unimpeded, but electrons encounter a high barrier at the heterointerface and find themselves in a deep potential well. Some electrons and holes with high energy pass over the barriers at the heterointerface. However, the carrier recombination at the homojunction and at the heterointerface, with subsequent tunneling of carriers through it, makes a substantial contribution to the total current. At low temperatures, the tunneling processes become dominant, since passing over barriers becomes improbable. This is confirmed by the n values obtained (n = 7.3 and 3.4) for two linear portions of the logarithmic *I–V* characteristic at T = 77 K (Fig. 7).

3.2. Reverse Bias

Figure 8 presents reverse *I–V* characteristics for the type *B* structure in log–log scale at T = 300 and 77 K, and Fig. 9 shows the corresponding band diagrams of the two junctions under study, accounting for the applied reverse bias. At small reverse biases (<100 mV), the current depends on temperature dependence very strongly. The zero-bias resistance (measured at V = –10 mV) increases from R_0 = 70 Ω at T = 300 K to R_0 = 1.7 MΩ at T = 77 K. The ideality factor n, determined from the slope of the *I–V* characteristics in the logarithmic scale at T = 77 K and small reverse biases, is equal to n = 1.2 (Fig. 8) and indicates the predominantly diffusive nature of the current. That is, the current is governed by minority carriers being extracted from the *n*- and *p*-regions of the narrow-gap semiconductor. At room temperature, a quadratic dependence of the current on the bias is observed for small biases

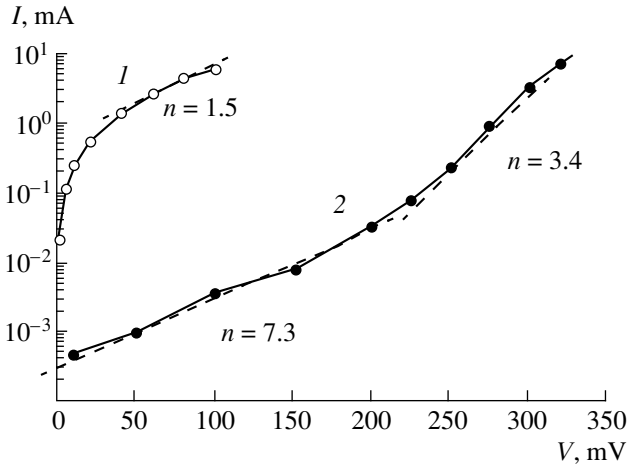

Fig. 7. Forward-bias *I–V* characteristics in log–log scale. T = 300 (*1*) and 77 K (*2*).

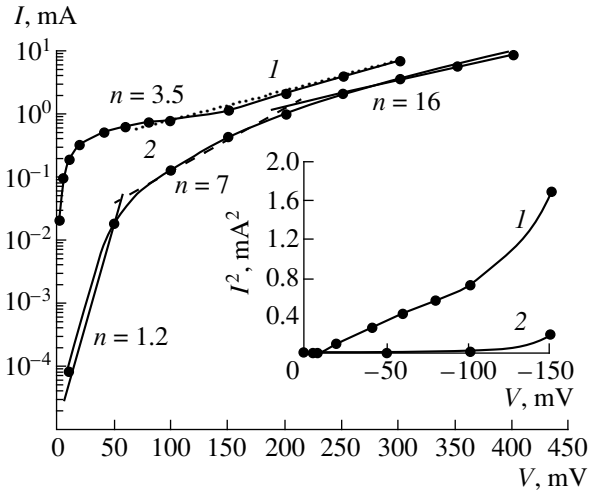

Fig. 8. Reverse-bias *I–V* characteristics in logarithmic and quadratic scales. T = 300 (*1*) and 77 K (*2*).

($V < 100$ mV) (Fig. 8), thus indicating the predominance of the generative character of the current. The generation and subsequent separation of carriers occur in the space-charge region of the *p–n* junction in the narrow-gap layer. The effective carrier lifetime τ_{eff} was determined from this portion of the *I–V* characteristic, using the known relation for the generation-recombination current [15]:

$$I_{GR} = \frac{qn_iWS}{\tau_{eff}},$$

where S is the *p–n* junction area, W is the width of the space-charge region (proportional to $V^{1/2}$), q is the electron charge, and n_i is the intrinsic carrier concentration at a given temperature. The values obtained are $\tau_{eff} \approx$ 6 ns. The effective carrier lifetime is a key factor in the detectivity of a photodetector operating at about room temperature in the photovoltaic mode. Therefore, further improvement of the photodiodes under study requires that the carrier lifetime should be made longer.

Estimations show that at room temperature with reverse biases over 100 mV, and also at low temperatures (T = 77–120 K), the tunneling mechanism of the current dominates (n = 7 and 16 at T = 77 K, n = 3.5 at T = 300 K) (Fig. 8). This is also confirmed by the weak temperature dependence of the current under reverse biases $V > 150$ mV. Apart from the tunneling through the reverse-biased *p–n* junction, one more mechanism may contribute to the total current. The reverse bias applied to the *p–n* junction lowers the energy barriers at the heterojunction, and the energy bands become partly unbent. It becomes possible for electrons to pass from the valence band of *P*-GaSb to the conduction band of *p*-InGaAsSb, from where they are drawn by the strong field of the *p–n* junction, pass into the *n*-region of the narrow-gap layer, and move further toward the positive contact.

Spectral characteristics of photodiodes based on optimized *B*-type structures are presented in Fig. 4. The long-wavelength threshold of sensitivity at 77 K lies at about λ_{th} = 4.0 μm, which corresponds to the optical gap of the narrow-gap $In_{0.91}Ga_{0.09}AsSb$ at this temperature, E_g = 0.31 eV; at 300 K, λ_{th} = 4.75 μm, which corresponds to E_g = 0.26 eV. The zero-bias resistance R_0 at 300 K is 60–80 Ω. This important parameter is only 2–3 times lower than the R_0 values typical of much shorter-wavelength InAs-based photodetectors (λ_{th} = 3.8 μm) [16].

We also estimated the noise characteristics of a *B*-type structure. Thermal noises predominated in the photovoltaic regime at room temperature. The calcu-

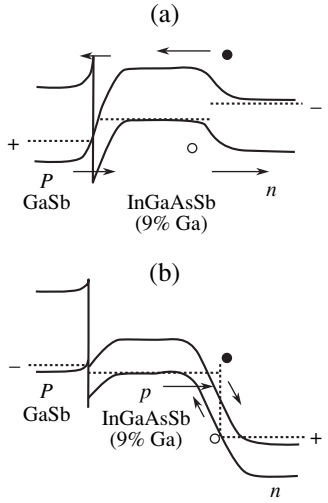

Fig. 9. Band diagrams of a *P*-GaSb/*p*-InGaAsSb/*n*-InGaAsSb heterostructure under forward (a) and reverse (b) biases.

lated thermal noise was about

$$\langle i_n \rangle = (4kT\Delta f/R_0)^{1/2} = 1.4 \times 10^{-11} \text{ A Hz}^{-1/2}.$$

Spectra of the current–light sensitivity of the photodiodes under study were directly recorded at $T = 300$ and 77 K using the radiation of a Globar. The room temperature sensitivity $R_\lambda = 0.21$ A/W was obtained at $\lambda = 4.7$ μm.

The threshold sensitivity, or the noise equivalent power (NEP) at $\lambda = 4.7$ μm, was estimated to be

$$\text{NEP} = \langle i_n \rangle / R_\lambda = 6.4 \times 10^{-11} \text{ W Hz}^{-1/2}.$$

Hence, the room temperature detectivity at $\lambda = 4.7$ μm is

$$D^*_\lambda = S^{1/2}/\text{NEP} = 4.1 \times 10^8 \text{ cm Hz}^{1/2}/\text{W}.$$

At 77 K, the zero-bias resistance R_0 was as high as 1.7 MΩ and the detectivity was $\lambda = 3.8$ μm,

$$D^*_\lambda = S^{1/2}/\text{NEP} = 4.4 \times 10^{10} \text{ cm Hz}^{1/2}/\text{W}.$$

These results suggest that thermoelectric cooling ($T = 250$ K) could raise the detectivity up to $D^*_\lambda = 2 \times 10^9$ cm Hz$^{1/2}$/W.

4. CONCLUSION

We presented the results obtained in designing and studying uncooled photodiodes for a $\lambda = 1.5$–4.8 μm spectral range based on type-II heterostructures in the GaInAsSb/GaSb system and employing wide-gap AlGaAsSb layers as a window. Advantages and specific features of the proposed photosensitive structures such as the presence of a wide-gap window, strong band bending at heterointerfaces, the use of a broken-gap heterojunction between the narrow-gap active region and the wide-gap window, and the unique properties of the *n*-$In_{0.91}Ga_{0.09}AsSb$/*p*-$Ga_{0.80}In_{0.20}AsSb$ ohmic contact allow the fabrication of photodiodes with a wide spectral range of sensitivity (0.9 to 4.8 μm) and a room temperature detectivity $D^*_\lambda = 4.1 \times 10^8$ cm Hz$^{1/2}$/W ($\lambda = 4.7$ μm). This value can be raised to $D^*_\lambda = 2 \times 10^9$ cm Hz$^{1/2}$/W ($\lambda = 4.5$ μm) through the application of thermoelectric cooling. Despite some technological problems, the quality of the layers grown can be improved further. This will make the carrier lifetime longer and, consequently, will improve the current–light sensitivity and the detectivity.

Photodiodes for the spectral range in question are promising sensors for analyzing important gases like carbon dioxide (CO_2), carbon monoxide (CO), and also combustion and explosion products. The photodiodes under study show a higher speed of response (up to 2 MHz), which exceeds, by nearly three orders of magnitude, the value for lead chalcogenide photoresistors currently used in portable instruments for this spectral range.

REFERENCES

1. A. N. Baranov, N. Bertu, Y. Cumminal, *et al.*, Appl. Phys. Lett. **71**, 735 (1997).
2. Y. R. Meyer, C. A. Hoffman, and F. Y. Bartoli, Appl. Phys. Lett. **67**, 757 (1995).
3. M. P. Mikhaĭlova, K. D. Moiseev, O. G. Ershov, and Yu. P. Yakovlev, Fiz. Tekh. Poluprovodn. (St. Petersburg) **30**, 399 (1996) [Semiconductors **30**, 223 (1996)].
4. M. P. Mikhailova and A. N. Titkov, Semicond. Sci. Technol. **9**, 1279 (1994).
5. M. P. Mikhaĭlova, N. M. Stus', S. V. Slobodchikov, *et al.*, Fiz. Tekh. Poluprovodn. (St. Petersburg) **30**, 1613 (1996) [Semiconductors **30**, 845 (1996)].
6. I. A. Andreev, M. A. Afrailov, A. N. Baranov, and M. P. Mikhaĭlova, Pis'ma Zh. Tekh. Fiz. **16** (4), 27 (1990) [Sov. Tech. Phys. Lett. **16**, 135 (1990)].
7. M. A. Afrailov, A. N. Baranov, A. P. Dmitriev, *et al.*, Fiz. Tekh. Poluprovodn. (Leningrad) **24**, 1397 (1990) [Sov. Phys. Semicond. **24**, 876 (1990)].
8. M. R. Singh, A. Shik, and W. Law, Physica E (Amsterdam) **11/12**, 49 (1997).
9. M. P. Mikhailova, T. I. Voronina, T. S. Lagunova, *et al.*, Superlattices Microstruct. **24** (1), 105 (1998).
10. M. P. Mikhailova, G. G. Zegrya, K. D. Moiseev, and Yu. P. Yakovlev, Solid-State Electron. **40**, 673 (1996).
11. N. L. Bazhenov, G. G. Zegrya, V. I. Ivanov-Omskiĭ, *et al.*, Fiz. Tekh. Poluprovodn. (St. Petersburg) **31**, 1316 (1997) [Semiconductors **31**, 1046 (1997)].
12. G. G. Zegrya and A. D. Andreev, Appl. Phys. Lett. **67**, 2681 (1995).
13. Y. Mao and A. Krier, J. Electron. Mater. **23**, 503 (1994).
14. I. A. Andreev, A. N. Baranov, M. P. Mikhaĭlova, *et al.*, Pis'ma Zh. Tekh. Fiz. **18** (17), 50 (1992) [Sov. Tech. Phys. Lett. **18**, 567 (1992)].
15. S. Sze, *Physics of Semiconductor Devices* (Wiley, New York, 1981; Mir, Moscow, 1984).
16. *Infrared Detectors. Catalog* (EG&G Inc., Optoelectronics Group, 1995).

Translated by D. Mashovets

Semiconductors, Vol. 35, No. 4, 2001, pp. 459–463. Translated from Fizika i Tekhnika Poluprovodnikov, Vol. 35, No. 4, 2001, pp. 474–478.

PHYSICS OF SEMICONDUCTORS DEVICES

Photoelectric Characteristics of Infrared Photodetectors with Blocked Hopping Conduction

D. G. Esaev* and S. P. Sinitsa

Institute of Semiconductor Physics, Siberian Division, Russian Academy of Sciences, pr. Akademika Lavrent'eva 13, Novosibirsk, 630090 Russia

** e-mail: esaev@thermo.isp.nsc.ru*

Submitted July 26, 2000; accepted for publication August 2, 2000

Abstract—It is shown that the current–voltage characteristics of Si:As-based structures that have blocked hopping conduction (blocked-impurity-band, or BIB, structures) and are subjected to infrared radiation in the photosensitivity range have two distinct portions. In the first portion, the photocurrent is controlled by an infrared-radiation flux and by an avalanche impurity-related breakdown. In the second portion, the photocurrent is controlled by merging of the depletion region with the contact N^{++} region. It is shown that the avalanche-multiplication mode can be used in focal multielement photodetector systems. The uniformity of photoelectric parameters over an array of elements in a system of focal multielement photodetectors operating in the avalanche-multiplication mode compares well with that observed in BIB arrays operating without avalanche multiplication. © *2001 MAIK "Nauka/Interperiodica".*

1. INTRODUCTION

Study of current–voltage (*I–V*) characteristics of the Si:Sb-based [1] and Si:B-based [2] structures with blocked hopping conduction [or the blocked-impurity-band (BIB) conduction] subjected to infrared (IR) radiation in the photosensitivity range have shown that the photocurrent dependence on the bias voltage had several characteristic portions. In the first portion, the photocurrent depends exponentially on the bias voltage and almost linearly on the IR irradiation intensity. Such behavior of the photocurrent was related [2] to the Pool–Frenkel effect, which enhances the hopping-conduction current in a high field [3]. In the subsequent portions, the photocurrent increases linearly and sublinearly with increasing bias V_b [2]. These portions were not observed by Huffman *et al.* [1]. As the bias V_b increases further, the current increases exponentially and much more steeply than in the first portion, which may be attributed to impurity-related impact ionization by electrons [1] and holes [2].

The results of similar studies of the Si:As-based BIB structures have apparently not been published, although these structures have been studied most often. At the same time, the knowledge of mechanisms controlling the photocurrent makes it possible to optimize the design of BIB structures intended for use in both focal arrays and photon counters.

When designing focal arrays intended for use in the far-IR region of the spectrum (12–28 μm) and based on Si:As BIB structures [4–6], superior values of photoelectric parameters and a high degree of their uniformity were obtained. Thus, for the best array consisting of 10×50 elements [4], the relative rms deviation is $\delta S/S = 1.52\%$ for the average current–power sensitivity of $S = 6.52$ A/W. The noise distribution over the array's elements is somewhat different. For a small noise factor (expressed in terms of the value of an rms fluctuating charge equivalent to $N_e = 130$ electrons) at the storage capacitor $C = 0.6$ pF, the variance amounts to $\delta N_e/N_e = 25\%$. For other arrays [4], nonuniformity of sensitivity was $\delta S/S \approx 4\%$. The current–power sensitivity reported elsewhere [4, 5] corresponded to the external quantum efficiency of $\eta < 1$.

At the same time, it is known [7] that in the Si:As-based BIB structures with an enhanced concentration of compensating acceptor impurity in the photosensitive layer (which enhances the contact-injection voltage), it is possible to detect individual IR photons by initiating an avalanche multiplication of electrons in the structure. As the latter takes place, the multiplication factor M may be as high as several tens of thousands. It is significant that the amplitudes of resulting pulses which arise upon detecting one, two, or three photons simultaneously are well resolved [7]. This result is indicative of the low level of noise that accompanies the emergence of an avalanche in a BIB structure.

This is also supported by measurements of the noise factor in a BIB photodetector [8]; two independent methods were used to show that avalanche multiplication in the range of $M = (1.0–1.8) \times 10^4$ was not accompanied by the appearance of additional noise [8]. The measured noise factor $K = \langle M^2 \rangle / \langle M \rangle^2$ amounted to $K \approx 1 \pm 0.05$.

The objective of this study was to identify the mechanisms which control the photocurrent in Si:As-based BIB structures in relation to the bias voltage and tem-

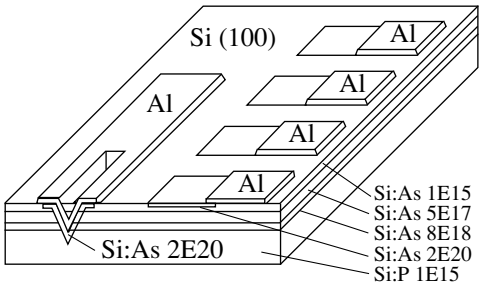

Fig. 1. Schematic representation of a linear BIB photodector array 1×64 in size.

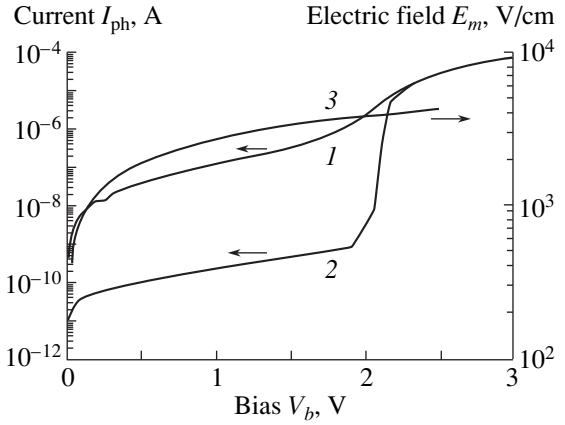

Fig. 2. (*1*, *2*) Photocurrent and (*3*) the highest electric field in the depletion region of a BIB structure. The measurements were performed at 10 K. The surface area of the structure was 190×290 μm^2. The flux of IR radiation was (*1*) 3×10^8 and (*2*) 4×10^{11} photon/(cm^2 s).

perature and to clarify whether it is feasible to use the mode of avalanche electron multiplication in multielement BIB-structure photodetector systems.

2. EXPERIMENTAL

Linear photodetector arrays containing 1×64 active elements were fabricated on the basis of epitaxial silicon structures described previously [9]. Schematic representation of an array is shown in Fig. 1. All the basic technological processes are consistent with planar silicon technology.

Contact to the buried N^{++} layer that was common to all elements was formed using anisotropic-etching technology [10] that made it possible to etch a V-shaped groove in silicon to a considerable depth. Subsequently, arsenic was implanted into the lateral surfaces of the groove. Arsenic was also implanted into the surface of the blocking layer to form the second contact to the BIB elements of the photodetector array. The contact formation was completed by the deposition and firing of aluminum onto the implanted surface.

We measured the photoelectric characteristics of individual BIB photodetectors using a system designed on the basis of a CF1104 helium cryostat produced by Oxford Instruments Ltd. The system made it possible to set and control the temperature at the operating table of the cryostat in the relevant temperature range of 4.2–25 K to an accuracy of 0.1 K. The vacuum in the cryostat corresponded to a pressure no higher than 10^{-5} Torr. In order to reduce the background flux incident on the photodetector, we installed two cold screens (with temperatures of 77 and 20 K) inside the vacuum chamber. The estimated background flux in the spectral sensitivity range of the photodetector was no larger than 10^{-10} W/cm^2. The samples were subjected to blackbody radiation. A chopper with a modulation frequency of 600 Hz and an optical filter with a passband of 15–25 μm were mounted between the blackbody radiator (with a temperature of 500 K) and the cryostat. In order to determine the photocurrent, we used a selective nanovoltmeter to measure the voltage drop across a 16-kΩ load resistor connected in series with a BIB element. The measured voltage was digitized using a 12-bit analog-to-digital converter and was fed to a personal computer. The voltage was swept using a sawtooth generator. The current–power sensitivity was determined from the measured photocurrent, and the calculated IR flux was governed the blackbody-radiator temperature and the optical channel characteristics. The setup was used to measure the photoelectric characteristics of individual elements illuminated from the planar side.

The second setup intended for measuring the photoelectric parameters of 1×64 linear photodetector arrays was based on a special helium Dewar vessel with a large inlet window 150 mm in diameter. Temperature in the cryogenic chamber containing a linear array and a built-in blackbody radiator with a temperature of 300 K was controlled by varying the distance between the chamber and the liquid-helium level. The background flux at the position of the BIB linear array did not exceed 10^{-10} W/cm^2.

In order to measure the linear array parameters, we designed and fabricated a cryogenic multiplexer based on 1×64 *p*-channel silicon transistors. The structure of the multiplexer's input cell and the diagrams of the control-voltage phases have been described previously [11]. For the input cell storage capacitance of $C = 2$ pF, the current noise of the multiplexer was $I_n = 4 \times 10^{-14}$ A in the bandwidth of 500 Hz. The sampling time for a single linear array cell was $\tau = 16$ μs. The signal-accumulation time (or the data acquisition time for the entire 1×64 linear array) was about 1 ms. The multiplexer crystal was positioned close to the photodetector array crystal. The corresponding contact pads were connected using ultrasonic bonding. The linear array was illuminated from the planar side.

3. RESULTS AND DISCUSSION

In Fig. 2, we show the typical *I–V* characteristics of individual BIB photodetectors under two levels of irradiation with unmodulated light. First of all, it should be noted that portions II and III typical of the dark *I–V* characteristics are not observed (see Fig. 1 in [9]). In a wide range of bias voltages (0–2 V), the voltage dependence of photocurrent resembles that of dark current in a N^{++}–N^{+}–N^{++} structure obtained from a BIB structure after the blocking layer had been etched off [12].

When a BIB structure is illuminated, the total current observed in a wide range of bias voltages (0–2 V) is in fact the photocurrent, because the dark current may be disregarded since it is small. An unilluminated BIB structure may be partitioned into a neutral region where there is no electric field and a region that includes both the blocking layer and the depletion layer (where there are no mobile holes) with a high electric field. When the structures are illuminated, the electron–hole pairs are generated both in the neutral region and in the depletion region, where the As concentration may be as high as $(3–5) \times 10^{17}$ cm^{-3}. As this takes place, an electric field $E_{ph} \cong \Phi_S W/\mu_p p_0 L$ (here, $p_0 = N_a \exp(-\varepsilon_3/kT)$ is the equilibrium hole concentration at the peak of the density of states in the impurity band) emerges to the linear approximation in the initially neutral region; this field increases as the bias voltage and the flux intensity Φ_S of the IR irradiation increase (Fig. 3).

For As-doped Si, the electron mobility μ_n [13] and lifetime τ_n [14] controlled by recombination at the As^+ centers are well known at temperatures close to that of liquid helium. It may be verified that the neutral portion of a BIB structure is not involved in initiation of the photocurrent. In fact, electrons drift over the distance of $l_n = \mu_n E_{ph} \tau_n$ during their lifetime τ_n. This distance is equal to a mere $l_n = 10^{-4}$ cm even in a field of $E_{ph} = 10$ V/cm (which corresponds to $V_b > 3$ V [15]) and is much smaller than the width of the quasi-neutral region in the structure. Consideration of electron trapping by neutral donors can only reduce the value of l_n. This means that electrons are not pulled out of the quasi-neutral region by the field and, by recombining with As^+, are involved in the formation of photocurrent.

The time of electron transit through the depletion layer is equal to $\tau_d \cong W/V_d = 10^{-10}$ s ($W = 10^{-3}$ cm and $V_d = 10^7$ cm/s), which is much smaller than the lifetime τ_n. Therefore, electrons leave the depletion region without recombination. The remaining "slow" holes form the electric field E_{ph}. This field is proportional to the illumination intensity and controls the photocurrent. Thus, the photocurrents in the blocking layer, quasi-neutral region, and depletion region are predominantly due to electron transport, hole transport, and combined electron and hole transport, respectively (see Fig. 3).

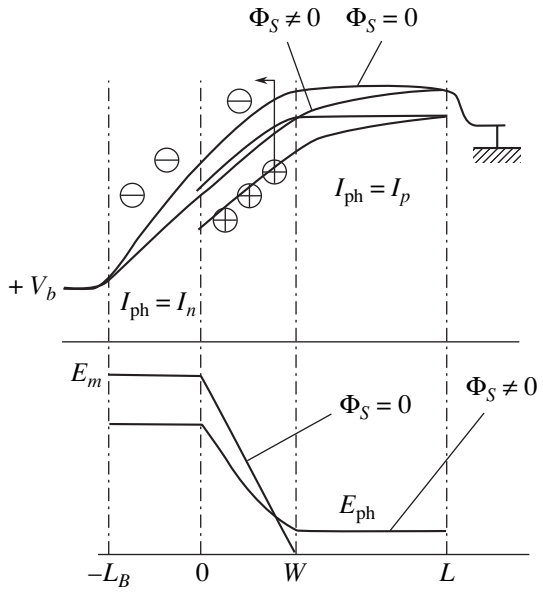

Fig. 3. Schematic representation of distributions of the potential and the electric field in an unilluminated ($\Phi_S = 0$) and an illuminated ($\Phi_S \neq 0$) BIB structure to the linear approximation in the current.

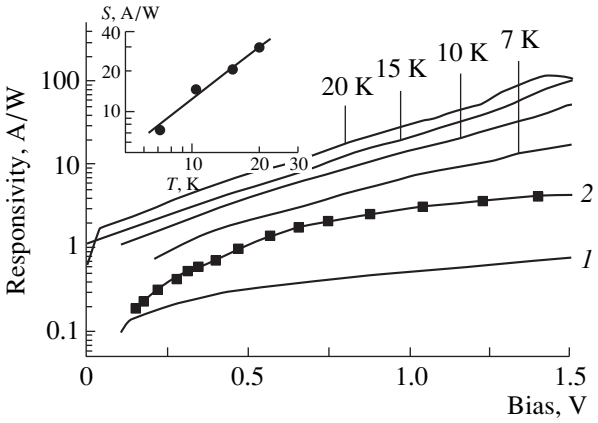

Fig. 4. Experimental dependences of the current–power sensitivity S on the bias voltage and temperature. The surface area of the structure was 650×650 μm^2. Curve *1* was calculated [17], and curve *2* corresponds to experimental data [6].

As the bias voltage V_b increases, the bias dependence of the photocurrent is initially controlled by the bias dependence of the depletion layer width $W(V_b)$ and, at a later stage, by a stronger field dependence of the impurity-related avalanche multiplication. As can be seen from Fig. 2, the magnitude of the highest electric field in the depletion region E_m rapidly approaches the value of the characteristic field for impact ionization of As atoms in Si $E_{av} \cong 7 \times 10^3$ V/cm [16]; this causes both the photocurrent to increase and the photo-

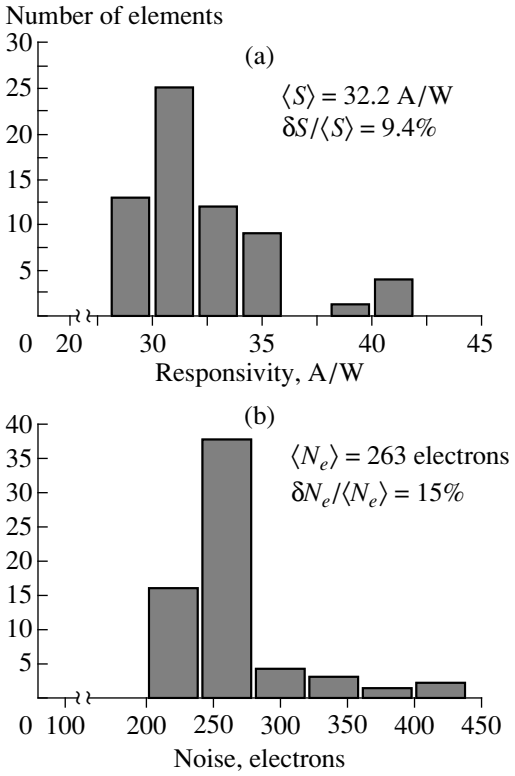

Fig. 5. Histograms representing the distributions of (a) current–power sensitivity S and (b) the noise charge N_e over the elements of a linear photodetector system 1×64 in size. The measurements were carried out at 10 K. The surface area of an element was 70×80 μm^2.

current dependence on bias to become stronger than it is in the expression $I_{ph} \approx q\Phi_S W(V_b)/L$. The second portion of the I–V characteristic for the illuminated sample is related to the punch-through of the depletion region and the contact N^{++} region and to an abrupt uncontrolled increase in the current and the noise level.

The results of measuring the current–power sensitivity S shown in Fig. 4 indicate that, beginning with a certain bias voltage (0.5–1.2 V, depending on temperature), the quantity S exceeds the value that corresponds to the external quantum efficiency of $\eta = 1$. It has been shown previously [17] that this is caused by avalanche multiplication of charge carriers in the depletion region. Our experiments demonstrate that the value of S in the voltage range corresponding to $\eta > 1$ depends not only on the bias voltage but also on temperature. The temperature dependence may be approximated by the power-law function $S \propto T^n$, where $n = 1.6 \pm 0.1$ (see the inset in Fig. 4). Such an increase in S with temperature may be attributed to a decrease in the cross section for electron recombination at a Coulomb center in the vicinity of $T \approx m^* v_s^2/k = 3$ K, where m^* is the effective electron mass and v_s is the velocity of sound in silicon [18]. Therein lies the difference between experimental dependence $S(T)$ and the dependence predicted by the theoretical model [17]; in the latter, the dependence of S on T is disregarded in the temperature range that corresponds to the operation of a BIB structure in background-limited mode (see Fig. 6 in [6]).

In Fig. 5, we show the bar-chart representations of sensitivity and noise charge distributions over the elements of a linear photodetector array combined with a multiplexer (a photodetector system). The mean value of the noise charge in the photodetector system is close the multiplexer's noise charge. This means that the photodetector system noise is primarily controlled by the multiplexer, even in the mode of "soft" avalanche multiplication under exposure to a luminous flux of $\Phi = 1.06 \times 10^{-11}$ W/element.

It can be seen that if the mean sensitivity of the elements is five times higher, its variance is close to the variance for $S \cong 6$ A/W [4, 5]. In other words, a changeover of the BIB elements in a linear array to the avalanche-multiplication mode with a small multiplication factor ($M < 10$) does not cause the sensitivity variance to increase.

Our results are in agreement with data reported previously [4, 5, 8] and supplement them by offering the prospect of designing multielement photodetector systems based on BIB structures that operate in an enhanced-detectivity mode due to the avalanche-multiplication effect. Thus, the studied linear arrays feature the detectivity of $D^* > 10^{14}$ cm Hz$^{1/2}$/W and the noise equivalent power of NEP $< 0.7 \times 10^{-16}$ W/Hz$^{1/2}$, which is superior to the corresponding values reported previously [4, 5].

CONCLUSION

(1) Study of Si:As-based BIB structures optimized for operation in focal linear arrays showed that the main mechanism responsible for the bias-voltage dependence of photocurrent consists in the avalanche breakdown of the impurity band.

(2) The avalanche breakdown of the impurity band in the above structures enhances the current–power sensitivity but does not cause the nonuniformity of this sensitivity over the array of photodectors to increase.

(3) It is shown that the current–power sensitivity of the Si:As-based BIB structures increases with temperature as $S \approx T^{1.6}$ in the range of 7–20 K.

(4) In the low-background situation (with the background flux being $<10^{-10}$ W/cm^2), the noise and detectivity of a Si:As-based linear-array photodetector system are controlled by the multiplexer.

REFERENCES

1. J. E. Huffman, A. G. Grouse, B. L. Hallek, *et al.*, J. Appl. Phys. **72**, 273 (1992).

2. B. A. Aronzon, D. Yu. Kovalev, A. M. Kozlov, *et al.*, Fiz. Tekh. Poluprovodn. (St. Petersburg) **32**, 192 (1998) [Semiconductors **32**, 174 (1998)].
3. D. I. Aladashvili, Z. A. Adamiya, K. G. Lavdovskiĭ, *et al.*, Fiz. Tekh. Poluprovodn. (Leningrad) **23**, 213 (1989) [Sov. Phys. Semicond. **23**, 132 (1989)].
4. S. B. Stetson, D. B. Reynolds, M. G. Stapelbroek, and R. L. Stermar, Proc. SPIE **686**, 48 (1986).
5. D. B. Reynolds, D. H. Seib, S. B. Stetson, *et al.*, IEEE Trans. Nucl. Sci. **36**, 857 (1989).
6. R. A. Noel, Proc. SPIE **1685**, 250 (1992).
7. M. D. Petroff, M. G. Stapelbroek, and W. A. Kleinhans, Appl. Phys. Lett. **51**, 406 (1987).
8. J. Kim, Y. Yamamoto, and H. H. Hogue, Appl. Phys. Lett. **70**, 2852 (1997).
9. D. G. Esaev, S. P. Sinitsa, and E. V. Chernyavskiĭ, Fiz. Tekh. Poluprovodn. (St. Petersburg) **33**, 614 (1999) [Semiconductors **33**, 574 (1999)].
10. Z. Yu. Gotra, *Technology of Microelectronic Devices* (Radio i Svyaz', Moscow, 1991).
11. A. A. Frantsuzov, N. V. Sapozhnikova, and G. N. Feofanov, Mikroélektronika **25**, 172 (1996).
12. D. G. Esaev, S. P. Sinitsa, and E. V. Chernyavskiĭ, Fiz. Tekh. Poluprovodn. (St. Petersburg) **33** (8), 1005 (1999) [Semiconductors **33**, 915 (1999)].
13. P. Norton, T. Braggius, and H. Lewinstein, Phys. Rev. B **8** (12), 563 (1973).
14. V. N. Abakumov, L. N. Kreshchuk, and I. N. Yassievich, Fiz. Tekh. Poluprovodn. (Leningrad) **12**, 264 (1978) [Sov. Phys. Semicond. **12**, 152 (1978)].
15. V. D. Shadrin, V. T. Coon, and I. K. Blokhin, J. Appl. Phys. **74**, 6972 (1993).
16. S. Sze, *Physics of Semiconductor Devices* (Wiley, New York, 1981; Mir, Moscow, 1984), Part 1.
17. F. Szmulowicz and F. L. Madarsz, J. Appl. Phys. **62**, 2533 (1987).
18. V. N. Abakumov, V. I. Perel', and I. N. Yassievich, Fiz. Tekh. Poluprovodn. (Leningrad) **12**, 3 (1978) [Sov. Phys. Semicond. **12**, 1 (1978)].

Translated by A. Spitsyn

Semiconductors, Vol. 35, No. 4, 2001, pp. 464–467. Translated from Fizika i Tekhnika Poluprovodnikov, Vol. 35, No. 4, 2001, pp. 479–481.

PHYSICS OF SEMICONDUCTORS DEVICES

Suppression of Current by Light in *p*-Si–n^+-ZnO–*n*-ZnO–Pd Diode Structures

S. V. Slobodchikov, Kh. M. Salikhov, E. V. Russu, and Yu. G. Malinin

Ioffe Physicotechnical Institute, Russian Academy of Sciences, Politekhnicheskaya ul. 26, St. Petersburg, 194021 Russia

Submitted August 30, 2000; accepted for publication September 5, 2000

Abstract—The mechanism of charge transport in an anisotype *p*-Si–n^+-ZnO–*n*-ZnO–Pd heterostructure with Schottky contact was studied. Photoelectric characteristics of this heterostructure were analyzed. The observed dependence $I \propto V^3$ is attributed to the double injection of charge carriers in the drift approximation. A suppression (decrease) of the forward current by irradiation with photons in the wavelength range of $\lambda = 0.7$–1.2 μm was observed. This effect is accounted for by special features of the trapping of photogenerated (excess) minority charge carriers (holes) and their recombination with thermally equilibrium electrons. © *2001 MAIK "Nauka/Interperiodica".*

Crystals and thin films of ZnO and ZnO-based diode structures have been the subject of numerous scientific and application-oriented studies. In particular, considerable advances have been made in the development of gas sensors, varistors, displays, and so on. We previously reported [1] the results of studying the electrical and photoelectric characteristics of an isotype *n*-ZnO–*n*-Si heterostructure, and possible practical applications of this heterostructure were outlined.

In this paper, we report the results of studying the mechanism of charge transport in an anisotype *p*-Si–n^+-ZnO–*n*-ZnO–Pd heterostructure with a Schottky contact; photoelectric properties of this heterostructure were also studied. It is noteworthy that both elements of this structure (*p*-Si–n^+-ZnO and ZnO–Pd) have been tested previously as a solar cell [2] and hydrogen detector [3], respectively.

The formation process of the structures included three consecutive stages. First, a conducting n^+-ZnO layer was formed on a *p*-Si substrate by organometallic deposition; zinc acetylacetonate $Zn(A_cA_c)_2$ was used as a source of Zn. The ZnO layer was deposited in a vertical reactor; the substrate temperature was maintained within 300–350°C. The supporting gas was Ar saturated with $Zn(A_cA_c)_2$ vapors and O. During n^+-ZnO layer deposition, the temperature of the $Zn(A_cA_c)_2$ source was 120°C; a flux of Ar mixed with O_2 in the proportion of $[Ar]/([Ar] + [O_2]) = 0.5$ was used. The n^+-ZnO layers were 0.15 μm thick; the electron concentration in these layers was $(5–8) \times 10^{19}$ cm^{-3}, and electron mobility was ~50 cm^2 V^{-1} s^{-1}. An *n*-ZnO layer 100–300 Å thick was then deposited using electron-beam evaporation of *n*-ZnO crystals ($\rho \simeq 10^2$ Ω cm). Finally, a Pd layer ~400 Å thick was deposited using vacuum evaporation. Figure 1a shows a schematic representation of the complete structure.

We measured the steady-state current–voltage (*I–V*) characteristics and photoelectric parameters of the structures using conventional instrumentation.

Figure 2 shows a typical dependence of forward current on the applied voltage (a positive voltage was applied to Pd) for one of the samples; the measurements were performed at $T = 300$ K. Two power-law

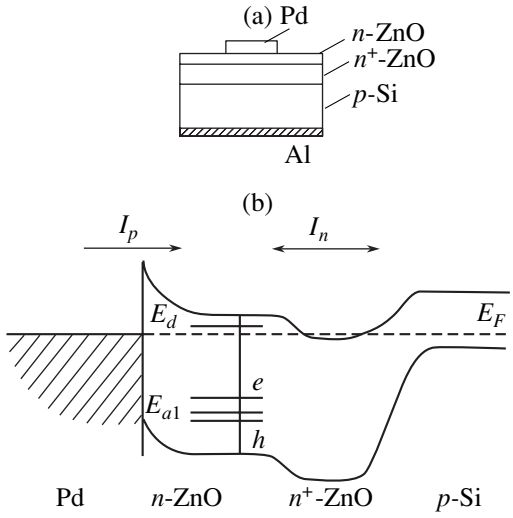

Fig. 1. (a) Schematic cross section and (b) presumed energy band diagram of a *p*-Si–n^+-ZnO–*n*-ZnO–Pd structure.

portions are observed in the *I–V* characteristic; in the first portion (for $V \le 0.2$ V), we have $I \propto V^{1.2–1.5}$ (depending on the sample), whereas in the second portion, $I \propto V^3$. Figure 3 shows the spectral photosensitivity of a structure in the wavelength region of $\lambda > 0.6$ μm. Two relatively narrow bands that peaked at $\lambda_{max} = 0.95$ and 2.65 μm are observed. The first of these bands is obviously related to the photovoltage value generated in the n^+-ZnO–*p*-Si heterojunction, whereas the second band with a lower intensity is governed by the *n*-ZnO–Pd Schottky barrier.

A distinctive feature of the charge-transport mechanism in the structure is its negative photosensitivity, i.e., the decrease in (a suppression of) the dark forward current I_d when the structure is exposed to illumination, with wavelengths of photons being in the range of 0.7–1.2 μm (see Fig. 4). The current-suppression curve is the inverted photosensitivity curve (see Fig. 3). Only positive photosensitivity is observed for reverse-biased structures.

The applied forward bias voltage is distributed over the three regions of the structure as

$$V = V_1 + V_2 + V_3, \quad (1)$$

where V_1 is the voltage at the Pd–*n*-ZnO Schottky barrier, V_2 is the voltage drop across the *n*-ZnO layer, and V_3 is the voltage at the n^+-ZnO–*p*-Si heterointerface. The existence of an extended region of cubic dependence of the current on the voltage suggests that the main fraction of the applied bias voltage drops across the *n*-ZnO layer; thus, we may assume that $V_2 \gg V_1$ and $V_2 > V_3$. The aforementioned power-law $I(V)$ dependence is characteristic of the mechanism of the charge-carrier double injection in the drift approximation. According to the theory, we have

$$I \approx \mu_n \mu_p \tau_p V^3 / L^5, \quad (2)$$

where L is the high-resistivity layer (*n*-ZnO) thickness, μ_n and μ_p are the electron and hole mobilities, and τ_p is the hole lifetime.

A crude estimation of τ_p using formula (2) for $\mu_p \ll 1$ cm^2 V^{-1} s$^{-1} \le \mu_n$ yields a very small value for τ_p, on the order of or smaller than 10^{-10} s. Electrons are injected into the *n*-ZnO layer from the n^+-ZnO side (see Fig. 1b), whereas holes are injected from the Pd side. As was shown previously [4], relationship (2) follows from the condition that the distribution of injected holes features a pronounced minimum. In the situation under consideration, this minimum is positioned closer to the Pd–*n*-ZnO heterointerface. Thus, the transit time of electrons

$$t_{tr} = \frac{L^2}{\mu_n V}$$

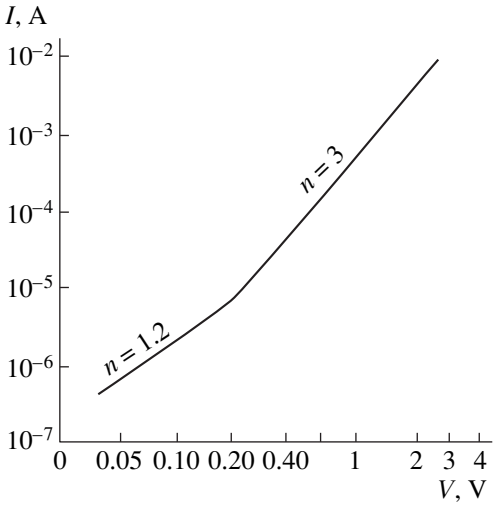

Fig. 2. The forward current–voltage characteristic of a *p*-Si–n^+-ZnO–*n*-ZnO–Pd structure.

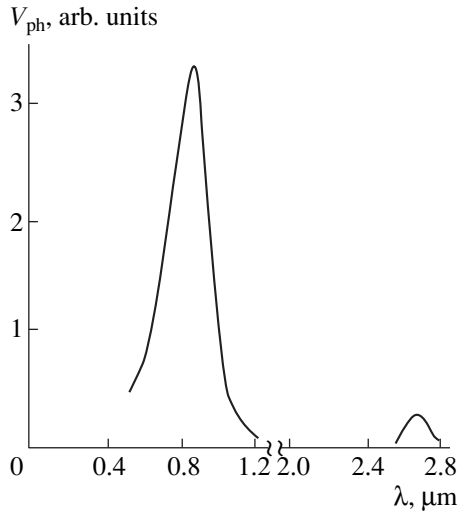

Fig. 3. Spectral photosensitivity of a *p*-Si–n^+-ZnO–*n*-ZnO–Pd structure.

amounts to 10^{-11}–10^{-12} s and corresponds to the conditions of the so-called dielectric relaxation, in which case $t_{tr} \ll \tau_M$ and $t_{tr} \ll \tau_p$, where τ_M is the Maxwell relaxation time. Under these conditions, the role of charge carriers in thermal equilibrium is unimportant, and the space charge is neutralized by injected electrons and holes. The effect of negative photosensitivity is not observed in this region. This effect is typical of the transition portion in the *I–V* characteristic for low injection levels. In our opinion, it is possible to explain the mechanism of the forward-current suppression by light in the structures studied on the basis of special features of the mechanism for the capture and recombina-

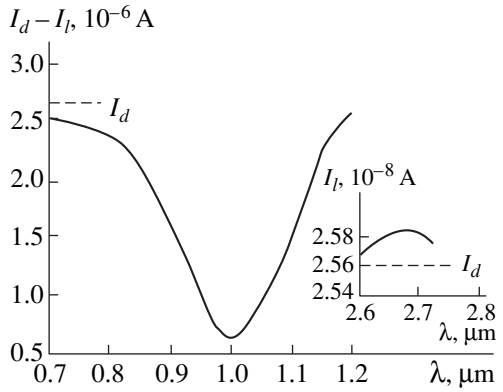

Fig. 4. Suppression of current by light ($I_d - I_l$) in a *p*-Si–n^+-ZnO–*n*-ZnO–Pd diode structure as a function of the illumination wavelength; here, I_d is the dark current and I_l is the current in illuminated structure. Positive photosensitivity observed under excitation with infrared radiation in the range of λ = 2.6–2.7 μm is shown in the inset.

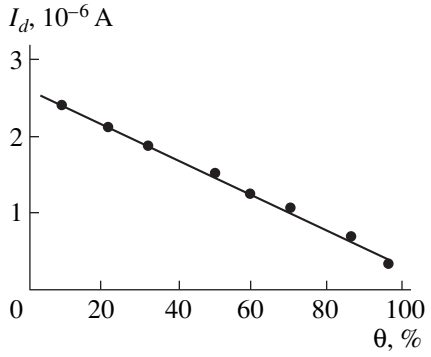

Fig. 5. Suppression of the dark current I_d as a function of the excitation-radiation intensity θ (λ = 0.98 μm).

tion of charge carriers in the *n*-ZnO layer. A similar effect (negative photoconductivity) was observed in Ge when minority charge carriers were excited to the impurity level [5]. In particular, the possible increase in the resistivity of semi-insulators under injection of minority charge carriers has been discussed previously [6].

In the case under consideration, we may assume that compensated acceptor levels E_{ai} were formed in the lower half of the band gap of the *n*-ZnO layer as a result of the technological process of forming the structure and, in particular, of the above layer (Fig. 1b). It is reasonable to assume that these levels should feature a large capture cross section for minority charge carriers (holes). It is possible that one of the E_{ai} levels has a larger concentration N_{a1} and is the most efficient in the course of recombination. The donor level E_d lies above the equilibrium Fermi level E_F, so that the ionization energy $E_d \gg kT$; i.e., the rate of thermal excitation of electrons to the conduction band is low [this rate is proportional to $\gamma m \exp(-E_d/kT)$, where m is the number of occupied centers]. Under excitation with light with the wavelength corresponding to the fundamental absorption in silicon, electron–hole pairs producing the photocurrent are generated at the heterojunction. As this takes place, the nonequilibrium electrons are thermalized in the n^+-ZnO layer, whereas holes (the minority charge carriers in *n*-ZnO) are captured by efficient E_{a1} recombination centers in this layer. For these centers, the recombination probability is proportional to the product of the electron capture coefficient γ_n by the concentration of thermally equilibrium charge carriers n, so that

$$\gamma_n n > \gamma_p P_v \exp\left(-\frac{E_g - E_{ai}}{kT}\right), \qquad (3)$$

where P_v is the effective density of states in the valence band and the coefficient of electron capture γ_n is larger than the coefficient of capture by the E_d centers. Under these conditions, the high rate of recombination of nonequilibrium photogenerated holes with thermal equilibrium electrons results in the suppression of the forward dark current. The magnitude of suppression defined as $I_d - I_l$ (I_d is the dark current and I_l is the current in the structure under illumination) depends on the concentration of nonequilibrium holes and increases with increasing illumination intensity (Fig. 5). The characteristic current-suppression curve (Fig. 4) is obviously related to variation in the coefficient of collection of the electron–hole pairs. Most probably, a high recombination rate at the n^+-ZnO–*p*-Si heterointerface markedly reduces the above coefficient; the same occurs in the long-wavelength region. In both cases, the flux of photogenerated holes to the E_{a1} levels is reduced correspondingly and the recombination rate is lowered, which results in the current-suppression curve that resembles the inverted spectral-photosensitivity curve. The narrow photoresponse band that peaked at λ_{max} = 2.65 μm can be accounted for by a high rate of surface recombination in the adjoining space-charge layer as well. We relate this band to the electron transit through the Schottky barrier from Pd to the *n*-ZnO layer. Only positive photosensitivity was observed for this band (see the inset in Fig. 4). This supports the assumption that the generation of minority charge carriers plays the determining role in the emergence of negative photosensitivity.

It should be noted that measurements of the current-suppression dependence on temperature have shown that this effect is observed at $T > 120$ K, with its magnitude increasing with temperature. Only positive photosensitivity is observed at $T < 120$ K. This indicates that the conditions for observing the suppression of current by light are limited. At low temperatures, the concentration of charge carriers in thermal equilibrium

decreases and the Fermi level changes its position with respect to the levels E_d and E_{a1}, which affects markedly the mechanisms of trapping and recombination and thus results in the disappearance of the current-suppression effect.

REFERENCES

1. S. V. Slobodchikov, Kh. M. Salikhov, and E. V. Russu, Fiz. Tekh. Poluprovodn. (St. Petersburg) **33**, 435 (1999) [Semiconductors **33**, 421 (1999)].
2. M. Shimizu, T. Horii, T. Shiosaki, and A. Kawabata, Thin Solid Films **96**, 149 (1982).
3. K. Ito, Surf. Sci. **86**, 345 (1979).
4. É. I. Adirovich, P. M. Karageorgiĭ-Alkalaev, and A. F. Leĭderman, *Double-Injection Currents in Semiconductors* (Sov. Radio, Moscow, 1978), Chap. 3, p. 115.
5. F. Stöckmann, Z. Phys. **143**, 348 (1955).
6. C. Popescu and H. K. Henisch, Phys. Rev. B **14** (2), 517 (1976).

Translated by A. Spitsyn

Semiconductors, Vol. 35, No. 4, 2001, pp. 468–473. Translated from Fizika i Tekhnika Poluprovodnikov, Vol. 35, No. 4, 2001, pp. 482–488.

PHYSICS OF SEMICONDUCTORS DEVICES

A Study of Deep Traps at the SiO_2/6*H*-SiC Interface Relying upon the Nonequilibrium Field Effect

P. A. Ivanov, T. P. Samsonova, V. N. Panteleev, and D. Yu. Polyakov

Ioffe Physicotechnical Institute, Russian Academy of Sciences, Politekhnicheskaya ul. 26, St. Petersburg, 194021 Russia

Submitted July 12, 2000; accepted for publication September 18, 2000

Abstract—The nonequilibrium field effect associated with deep surface states at the SiO_2/6*H*-SiC interface has been observed and studied in a 6*H*-SiC MOSFET of depletion–accumulation type. An analysis of the relaxation of channel conductance at elevated temperatures upon filling of the surface traps with nonequilibrium carriers has shown that the energy distribution of the surface traps has the form of a narrow Gaussian peak in the upper half of the 6*H*-SiC band gap, with a peak energy $E_C - E_{tm} = 1.19$ eV, peak width $\Delta E_t \approx 85$ meV, and electron capture cross section $\sigma_n \approx 10^{-14}$ cm^2. These surface states are believed to have the fundamental nature of "oxidation defects" similar to P_b centers in the SiO_2–Si system (of dangling silicon bonds). © *2001 MAIK "Nauka/Interperiodica".*

1. INTRODUCTION

So far, several types of MOSFETs have been created on the basis of silicon carbide [1–4]. However, these transistors are as yet inferior to SiC transistors with a *p*–*n* junction or Schottky barrier as regards the effective mobility of electrons in the channel, which is due to the influence of electron traps at the SiO_2/SiC interface [5].

Traps at the SiO_2/SiC interface have been extensively studied by analyzing the capacitance–voltage (*C*–*V*) characteristics of SiC-MOS capacitors (see, e.g., [6–8]). However, the majority of studies have been performed at room temperature, which gives no way of revealing deep states in such a wide-gap semiconductor as SiC (for example, deep states adversely affect the threshold voltage and the subthreshold transconductance of inversion-channel transistors).

In this paper, the nonequilibrium field effect at elevated temperatures in deep surface states at the SiO_2/6*H*-SiC interface was studied. Depletion–accumulation 6*H*-SiC MOSFETs with doped *n* channels served as the object of study. In these transistors (normally in on-state), variations in the trap filling at the oxide–semiconductor interface lead to changes in the thickness of the depletion region at the gate, and, consequently, to changes in the drain current. The surface state parameters, namely, their energy distribution in the 6*H*-SiC band gap and the electron capture cross section, have been determined from the kinetics of the channel conductance after nonequilibrium filling of surface traps with electrons. The data obtained are compared with the results of other studies, and the nature of the states revealed is discussed.

2. SAMPLES AND EXPERIMENT

Transistors (Fig. 1) were based on epitaxial 6*H*-SiC p^+–n–n^+ structures CVD-grown at the Industrial Microelectronics Center in Stockholm, Sweden. The device was fabricated according to the following standard processes: (i) reactive-ion etching of SiC in SF_6 plasma to form mesa structures and to make the channel between the source and the drain thinner; (ii) thermal oxidation of the SiC surface in a flow of humid oxygen to form the gate dielectric; (iii) thermal burning-in of nickel to obtain ohmic contacts to the source, drain, and p^+-substrate; and (iv) formation of a molybdenum MOS gate. The resulting discrete mesa-isolated transistor structures had the following parameters: the donor density in the channel was $N = 5 \times 10^{15}$ cm^{-3}; channel thickness, $d \approx 1.5$ μm; channel length, $L = 5$ μm; channel width, $Z = 0.56$ mm; mesa-structure area, $S = 0.35 \times 0.25$ mm^2; and thickness of the gate SiO_2 layer, $d_{ox} \approx 0.1$ nm.

The donor impurity concentration in the channel and the thickness of the channel's active region were chosen so that the density of donors per unit area (*Nd*) did not exceed 10^{12} cm^{-2}. This ensured that the drain current was highly sensitive to charge variations at the interface. In the structure under study, the drain current can be controlled by both the upper MOS gate and the lower p^+–n junction. The p^+–n junction can also be used to inject holes into the surface, where they recombine with nonequilibrium electrons captured by surface states.

The drain current relaxation curves were taken in the dark at several temperatures in the range 293–442 K, using an XY recorder. During the recording, a constant temperature was automatically maintained to within 0.1 K. The measurements were done in

the linear mode of transistor operation, which was ensured by applying a small voltage V_{DS} = 100 mV to the drain. In this case, the measured drain current is directly proportional to the channel G_{DS} conductance: $I = G_{DS}V_{DS}$.

3. EXPERIMENTAL RESULTS AND QUALITATIVE INTERPRETATION

Figure 2 presents current–voltage characteristics of the fabricated transistors, taken with an L2-56 curve tracer in the depletion regime (in single- and double-gate operation modes). These characteristics are typical of the depletion-type transistors: the drain current saturates well and is controlled by a negative voltage on the MOS gate or the p^+–n junction.

A study of the effect of the MOS-gate voltage pulses on the drain current demonstrated that the character of the channel conductance modulation depends substantially on the polarity of the applied pulse. Figure 3 demonstrates the modulation of the room-temperature conductance produced by negative and positive pulses of 5 V amplitude and 1 s duration. During the negative pulse, the conductance decreases from 2.1 mA/V to nearly zero, and its initial value is restored almost instantly after the pulse ends. During the positive pulse, the conductance slightly increases, but, after the pulse ends, the transistor is almost in the off-state (the conductance also falls nearly to zero, but is not restored during the experiment).

The initial conductance of the channel could be restored in three ways: (i) by illuminating the structure with visible light; (ii) by applying a positive voltage to the p^+–n junction; and, finally, (iii) by elevating the temperature (the respective drain current relaxation curves at different temperatures are represented by solid lines in Fig. 4). It can be seen that the characteristic time of the relaxation process decreases from several hundred to several seconds with the temperature increasing in a very narrow range from 391 to 442 K.

We ascribe the behavior of the drain current observed to the effect of deep surface states, partially filled in quasi-equilibrium conditions. With a negative voltage applied to the MOS gate, the electron charge of surface states becomes nonequilibrium (excess). In the dark, surface state filling can return to quasi-equilibrium via thermal excitation of electrons from the surface states; for deep levels, the characteristic time of this process at room temperature may be very long. After the pulse ends, the initial state is rapidly regained. Consequently, no substantial variation of the charge on surface states occurs under the action of the negative pulse.

When a positive voltage is applied to the MOS gate, electrons from the conduction band are quickly captured by the initially free surface states. This results in the positive potential of the MOS gate being screened: the applied voltage drops mainly across the insulator,

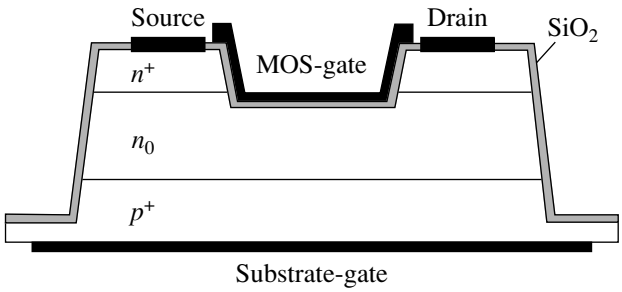

Fig. 1. Schematic cross section of 6*H*-SiC MOSFET with a buried *n*-doped channel and two opposite gates.

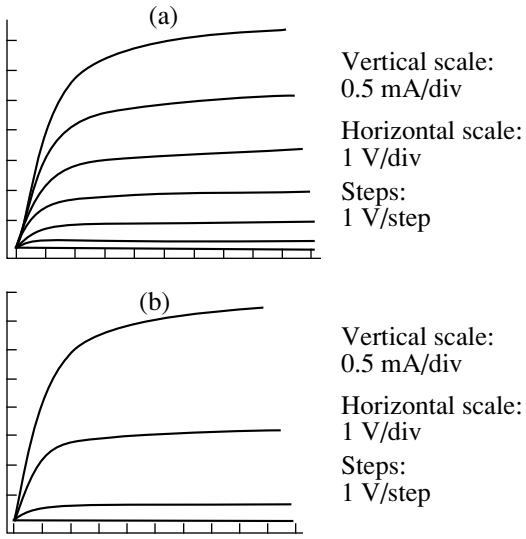

Fig. 2. Families of source–drain current–voltage characteristics of a 6*H*-SiC MOSFET, taken at room temperature in the channel depletion regime (common-source circuit): (a) single-gate regime (one gate grounded, negative bias on the second), (b) double-gate regime (the same negative bias on both gates). Upper curves correspond to a zero-biased gate. The gate bias is changed in 1-V increments.

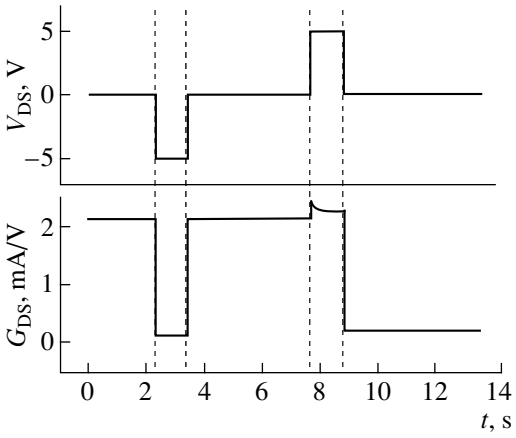

Fig.3. Modulation of the channel conductance by negative (– 5 V) and positive (+ 5 V) pulses on the gate. Room temperature.

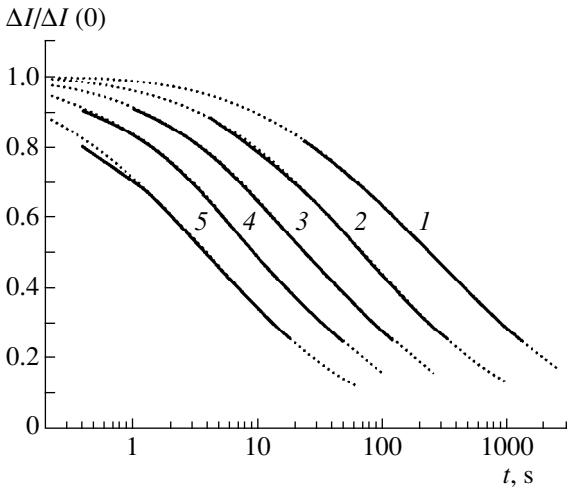

Fig. 4. Relaxation curves of the drain current after applying a positive (+5 V) pulse to the MOS gate. Temperature *T*: (*1*) 391, (*2*) 404, (*3*) 417, (*4*) 430, and (*5*) 442 K. Solid curves, experiment; dotted curves, approximation (for explanations, see the text).

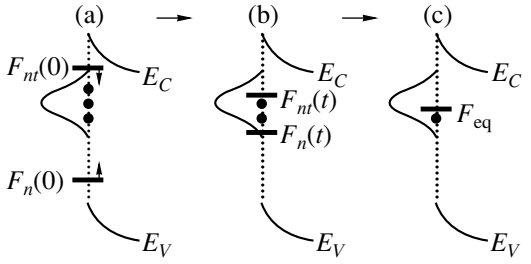

Fig. 5. Semiconductor band diagrams at several instants of time after applying a positive pulse to the MOS gate: (a) immediately after the pulse end ($t = 0$), (b) at an instant of time during the current relaxation, and (c) quasi-equilibrium state ($t = \infty$).

while the thickness of the depleted region at the gate and the drain current change only slightly. After the pulse ends, the negative charge of the trapped electrons becomes nonequilibrium. This "frozen" excess charge leads to nonequilibrium depletion in the semiconductor, which is responsible for the drop of the drain current after the end of the pulse. In this regime, the restoration of the quasi-equilibrium conductance by the methods described above can be explained in the context of (i) structure illumination by optical transitions of nonequilibrium electrons from the surface state levels to the conduction band; (ii) the positive bias of the p^+–n junction, attained by injecting holes from the p^+ region to the interface, where they recombine with nonequilibrium electrons in surface states; and (iii) a temperature increase from the thermal emission of nonequilibrium electrons from the surface state levels to the conduction band.

4. QUANTITATIVE MODEL OF CURRENT RELAXATION

Now we discuss the relaxation of the system after nonequilibrium filling of the surface states with electrons, i.e., after applying a positive bias pulse to the MOS gate. Figure 5 shows band diagrams of the semiconductor at different instants of time: (a) immediately after the end of the pulse ($t = 0$), (b) at a certain instant of time during the current relaxation, and (c) after the attainment of quasi-equilibrium ($t = \infty$). The diagrams in Figs. 5a and 5b reflect the nonequilibrium state of the system, with the Fermi quasi-levels for electrons in surface states (F_{nt}) and those in the conduction band (F_n) not coinciding and lying on opposite sides of the quasi-equilibrium Fermi level (F_{eq}).

Let us first relate the changes in the excess electron concentration in surface states, $\Delta n_t(t)$, and in the drain current, $\Delta I(t)$, with time.

During relaxation, a change in the charge of the surface states, ΔQ_t, is accompanied by changes in the charges on the metallic electrode, ΔQ_m, and in the space charge region (SCR), ΔQ_s. The relationship between these quantities is governed by the overall electroneutrality of the system:

$$\Delta Q_m(t) = -[\Delta Q_t(t) + \Delta Q_s(t)]. \quad (1)$$

In its turn, a change in the surface potential ($\Delta\psi_s$) is equal to the voltage drop across the insulator (ΔV_{ox}), the sign being reversed:

$$\Delta\psi_s(t) = -\Delta V_{ox}(t). \quad (2)$$

By definition, ΔV_{ox} is related to ΔQ_m by

$$\Delta V_{ox} = \frac{\Delta Q_m}{C_{ox}}, \quad (3)$$

where C_{ox} is the insulator capacitance per unit area. In turn, the quantity $\Delta\psi_s(t)$ can be expressed in terms of changes in the SCR thickness in the semiconductor, $\Delta h(t)$:

$$\delta\psi_s = -\frac{qN}{\varepsilon_s}\tilde{h}\Delta h, \quad \tilde{h}(t) = \frac{h(0) + h(t)}{2}, \quad (4)$$

where q is the absolute value of the electron charge, and ε_s is the dielectric constant of the semiconductor. Let us make use of some evident relations for charges in the surface states and in the SCR of the semiconductor:

$$\Delta Q_t = -q\Delta n_t, \quad \Delta Q_s = qN\Delta h. \quad (5)$$

Then the expression relating the change in the electron concentration in surface states to a change in the SCR thickness can be brought to the form

$$\Delta n_t(t) = N\Delta h(t)\left[1 + \frac{\tilde{h}(t)}{\tilde{d}_{ox}}\right], \quad \tilde{d}_{ox} = \frac{\varepsilon_s}{\varepsilon_{ox}}d_{ox}, \quad (6)$$

where ε_{ox} is the dielectric constant of the oxide layer. The quantity d_{ox} in (6) is called the length of surface

charge screening by a metallic electrode. Its meaning is well understood in the limiting case of a thick insulator. If $d_{ox} \gg h$, then the charge of the metallic electrode does not change during relaxation, with changes in the charge in the surface states and in the SCR being equal in absolute value (but having opposite signs). Conversely, the thinner the insulator, the stronger the screening of the surface charge by metal.

In the linear mode of transistor operation, the change in the drain current is proportional to that in the SCR thickness: $\Delta I(t) \propto -\Delta n(t)$. If $|\Delta h(t)| \ll h(0)$, the time dependence $\Delta I(t)$ coincides, within a constant factor, with the time dependence $\Delta h(t)$, so that

$$\frac{\Delta I(t)}{\Delta I(0)} \approx \frac{\Delta n_t(t)}{\Delta n_t(0)}. \tag{7}$$

Now we consider the kinetics of filling monoenergetic surface states after a departure from quasi-equilibrium. For a monopolar *n*-type semiconductor and its surface state levels in the upper half of the band gap, the carrier exchange between the traps and the valence band can be neglected. Furthermore, when initial excess filling of traps occurs at the start of the relaxation process, the capture of electrons from the conduction band is also negligible. Then the kinetic equation describing the thermal emission of electrons from the traps has the simplest form:

$$\begin{gathered} \frac{dn_t}{dt} = \sigma_n v n_1 n_t = \frac{n_t}{\tau_n}, \\ n_1 = N_C \exp\left(-\frac{E_C - E_t}{kT}\right), \quad (\tau_n)^{-1} = \sigma_n v n_1, \end{gathered} \tag{8}$$

where σ_n is the cross section of electron capture by surface traps, v is the thermal velocity of electrons, N_C is the effective density of states in the conduction band of the semiconductor, $E_C - E_t$ is the energy depth of the surface state levels in the band gap relative to the conduction band edge, and kT is the thermal energy.

The solution to (8) has the form

$$\frac{\Delta n_t(t)}{\Delta n_t(0)} = \exp\left(-\frac{t}{\tau_n}\right). \tag{9}$$

According to (7), the relaxation curve for the current in the linear transistor operation mode must obey the expression

$$\frac{\Delta I(t)}{\Delta I(0)} = \exp\left(-\frac{t}{\tau_n}\right). \tag{10}$$

It was found that in the case in question the time dependence of $\Delta I(t)/\Delta I(0)$ is not described by a simple exponent (10), being a superposition of exponents with different τ_n. The reason for this is that the surface states under study are distributed over a certain energy range. For a quasi-continuous energy distribution of surface states ($D_t(E)$ is the density of states as a function of energy), states lying in arbitrarily chosen intervals dE near the energy E are depleted in accordance with the law for the monoenergetic surface states (9), where τ_n grows exponentially with increasing level depth. In this case, the position of the Fermi quasi-level for electrons in surface states, $F_{nt}(t)$, can be determined for any instant of time $t > 0$ from the condition

$$\tau_n(F_{nt}) = t = (\sigma_n v N_C)^{-1} \exp\left(\frac{E_C - F_{nt}(t)}{kT}\right), \tag{11}$$

$$E_C - F_{nt}(t) = kT \ln(\sigma_n v N_C t). \tag{12}$$

Expression (12) shows that in the course of relaxation the quasi-level F_{nt} moves toward the midgap. It is assumed that at any given instant of time all the surface state levels lying above the Fermi quasi-level are free, and all those below the Fermi quasi-level are filled with electrons. Then the time variation of Δn_t is calculated to be

$$\Delta n_t(t) = \int_{F_{eq}}^{F_{nt}(t)} D_t(E) dE. \tag{13}$$

Further, we consider surface states with a Gaussian density distribution over energy:

$$D_t(E) = D_{tm} \exp\left[-\frac{(E - E_{tm})^2}{2(\Delta E_t)^2}\right]. \tag{14}$$

Also, we consider a situation when (i) the concentration of quasi-equilibrium electrons in surface states is much smaller than the total concentration of levels ($F_{eq} < E_{tm} - \Delta E_t$) and (ii) the initial concentration of nonequilibrium electrons in the surface states is close to the total concentration of levels ($F_{nt}(0) > E_{tm} + \Delta E_t$). In general, these conditions can be fulfilled by choosing the initial bias on the gate and the amplitude of the positive pulse.

Changing the variables, $X = (E - E_{tm})/\Delta E_t$, and taking into account relation (12), we obtain the relative change in the drain current with time in the form

$$\frac{\Delta I(t)}{\Delta I(0)} = \frac{\Delta n_t(t)}{\Delta n_t(0)} \approx \int_{-\infty}^{Z(t)} \frac{1}{\sqrt{2\pi}} \exp\left(-\frac{X^2}{2}\right) dX, \tag{15}$$

$$Z(t) = \frac{E_C - E_{tm} - kT \ln(\sigma_n v N_C t)}{\Delta E_t}. \tag{16}$$

Thus, at known surface state parameters ($E_C - E_{tm}$, ΔE_t, and σ_n), the time dependence of the drain current is described by the function defined by (15) and (16).

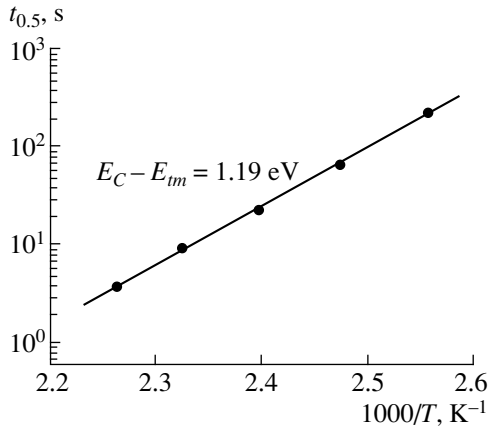

Fig. 6. $t_{0.5}$ vs. 1000/T (for explanations, see the text).

5. APPROXIMATION OF EXPERIMENTAL RESULTS

The inverse problem (determining the surface state parameters from a measured current relaxation curve) can be solved by approximating the experimental curve by the function obtained above (with three fitting parameters). As seen from (16), at a fixed temperature the quantities $E_C - E_{tm}$ and $kT\ln\sigma_n$ make additive contributions to the $Z(t)$ function, and, therefore, a numerical approximation of a single experimental curve cannot give a single-valued result for the parameters $E_C - E_{tm}$ and σ_n. Consequently, one of the parameters, namely, $E_C - E_{tm}$, was found using the results of temperature measurements.

In the situation under study, the Fermi quasi-level for electrons in surface states passes through the peak in energy distribution of surface states at the instant of time $t_{0.5}$, when $\Delta I(t)/\Delta I(0) = 0.5$: $F_{nt}(t_{0.5}) = E_{tm}$. According to (11), $t_{0.5}$ depends on temperature as follows:

$$t_{0.5} = (\tau_n)_{\max} = (\sigma_n v N_C)^{-1}\exp\left(\frac{E_C - E_{tm}}{kT}\right). \quad (17)$$

According to this formula, the energy depth of the density-of-states peak is found as the activation energy of the quantity $t_{0.5}$, measured at several temperatures. Other surface state parameters (ΔE_t and σ_n) were determined for each temperature by computer approximation of the experimental $\Delta I(t)/\Delta I(0)$ curves, but now with only two fitting parameters. For this case, the integral of the probability distribution, appearing in (15), was calculated using the known formula

$$\int_{-\infty}^{x}\frac{1}{\sqrt{2\pi}}\exp\left(-\frac{y^2}{2}\right)dy = 1 - \frac{1}{\sqrt{2\pi}}\exp\left(-\frac{x^2}{2}\right)(a_1 z + a_2 z^2 + \ldots + a_5 z^5), \quad (18)$$

where $z = 1/(1 + px)$, $p = 0.232$, $a_1 = 0.319$, $a_2 = -0.357$, $a_3 = 1.781$, $a_4 = -1.821$, $a_5 = 1.330$ (with a calculation error of no more than 7.5×10^{-8}).

Figure 6 presents the dependence of $t_{0.5}$ on $1/T$ plotted in semilogarithmic scale using the experimental data from Fig. 4. The slope of this straight line corresponds to the energy depth of the peak in the surface state distribution, $E_C - E_{tm}$ = 1.19 eV. The results of a computer approximation (using two adjustable parameters) of current relaxation curves at several temperatures are shown in Fig. 4 by dotted lines, and the adjustable parameters obtained for these temperatures are given in the table. In the calculations, the following room-temperature values of the thermal velocity and the effective density of states in the conduction band were taken: $v(T = 300\ \text{K}) = 2 \times 10^7$ cm/s and $N_C(T = 300\ \text{K}) = 10^{19}$ cm^{-3} (it is noteworthy that the deviation of the product vN_C introduces error only into the capture cross section σ_n).

As seen from Fig. 4 and the table, the discussed model describes the experimental data fairly well. The integral trap density can be evaluated on the basis of the transistor being nearly fully turned off when applying a +5 V pulse to the gate. This means that the integral density of states (N_t) must be higher than the sheet density of donors in the channel, i.e., $N_t > N_d \approx 7.5 \times 10^{11}$ cm^{-2}.

Thus, the surface traps responsible for the observed nonequilibrium field effect have an energy distribution in the form of a narrow Gaussian peak in the upper half of the 6*H*-SiC band gap. The integral density of traps is about 10^{12} cm^{-2}, the ionization energy in the distribution peak $E_C - E_{tm}$ = 1.19 eV, the peak broadening $\Delta E_t \approx$ 85 meV, and the electron capture cross section $\sigma_n \approx 10^{-14}$ cm^2.

Best-fit parameters ΔE_t and σ_n obtained by approximating current relaxation curves using a function described by (15) and (16)

Parameters	Temperature T, K				
	391	404	417	430	442
ΔE_t, meV	85	83	85	86	92
$10^{14}\,\sigma_n$, cm^2	2.8	2.8	2.6	2.2	2.3

6. DISCUSSION OF THE RESULTS

Deep surface states with parameters close to those listed above were detected in our previous studies using other experimental methods. Among these, a comparative analysis of the dark and light *C–V* characteristics of 6*H*-SiC(0001)C MOS capacitors at room temperature revealed the existence of states with an ionization energy exceeding 1 eV and integral density of no less than 10^{13} eV^{-1} [9]. The density-of-states peak at the energy $E_C - E_{tm} \approx 1.2$ eV, with an integral density of

about 10^{12} cm^{-1} has been revealed by analyzing the high-temperature (600 K) *C–V* characteristics of 6*H*-SiC(0001)Si MOS capacitors [10]. Moreover, similar states have been found on a "free" surface of SiC, not subjected to special oxidation. Studies of low-frequency noise in thin 4*H*-SiC films [11] have shown that the generation–recombination noise observed at elevated (550–700 K) temperatures is due to surface traps with ionization energy $E_C - E_t \approx 1.3$ eV, density $N_t = 1.5 \times 10^{12}$ cm^{-2}, and electron capture cross section $\sigma_n \approx 10^{-14}$ cm^2. It is worth noting that for 6*H*- and 4*H*-SiC the density-of-states peak lies about 0.3 eV above the midgap. The existence of these surface states provides a consistent explanation for the dependence of the height of the Schottky barrier formed on a SiC surface with a thin layer of natural oxide on the work function of a metal [12].

We believe that the states revealed are similar in nature to P_b centers in the SiO_2/Si system. These centers, making a major contribution to the density of surface states, are "oxidation defects"—silicon dangling bonds [13]. The centers are amphoteric and give rise to two density-of-states peaks in the silicon band gap. Acceptor states corresponding to electronic transitions 0/– lie in the upper half of the gap, and donor states corresponding to electronic transitions +/0, in the lower half. The difference between the detachment energies for the first and second electrons (the so-called "correlation energy") is about 0.6 eV. If we assume the existence of a symmetrical peak of surface states in the lower half of the SiC band gap, the "correlation energy" will also be about 0.6 eV. Finally, assuming that this energy is determined by the internal structure of a center, we suggest that the nature of deep surface states at the SiO_2/SiC interface is similar to P_b centers in the SiO_2/Si system. The integral density of states and the broadening of the density peak depends on the crystallographic orientation and the conditions of the SiC surface treatment: the density of states is lowest on the well-oxidized surface of (0001)Si orientation and highest on a free SiC surface with (0001)C orientation.

7. CONCLUSION

A nonequilibrium field effect associated with deep surface states has been found and studied in the SiO_2–*n*-6*H*-SiC system. The revealed states are "oxidation defects" similar to P_b centers in the SiO_2–Si system and characterized by the following parameters: ionization energy in the distribution peak of $E_C - E_{tm} = 1.19$ eV, peak broadening of $\Delta E_t \approx 85$ meV, and an electron capture cross section of $\sigma_n \approx 10^{-14}$ cm^2.

ACKNOWLEDGMENTS

The authors are grateful to A.O. Konstantinov, C. Harris, and S. Karlsson from the Industrial Microelectronics Center (Stockholm, Sweden) for the provision of epitaxial SiC structures.

REFERENCES

1. A. K. Agarwall, J. B. Casady, L. B. Rowland, *et al.*, IEEE Electron Device Lett. **18**, 586 (1997).
2. J. Spitz, M. R. Melloch, J. A. Cooper, Jr., and M. A. Capano, IEEE Electron Device Lett. **19**, 100 (1998).
3. J. N. Shenoy, J. A. Cooper, and M. R. Melloch, IEEE Electron Device Lett. **18**, 93 (1997).
4. R. Singh, S. H. Ryu, and J. W. Palmour, in *Abstracts of the International Conference on Silicon Carbide and Related Materials, ICSCRM'99, Sheraton Imperial Center, Research Triangle Park, 1999*, Abstract No. 345.
5. E. Arnold, N. Ramungul, T. P. Chow, and M. Ghesso, in *Silicon Carbide, III-Nitrides and Related Materials*, Ed. by G. Pensl, H. Morkoc, B. Monemar, and E. Janzen (Trans. Tech. Publications, Switzerland, 1998), Part 2, p. 1013.
6. P. A. Ivanov, A. O. Konstantinov, V. N. Panteleev, *et al.*, Fiz. Tekh. Poluprovodn. (St. Petersburg) **28**, 1172 (1994) [Semiconductors **28**, 668 (1994)].
7. P. Friedrichs, E. P. Burte, and R. Schorner, J. Appl. Phys. **79**, 7814 (1996).
8. J. A. Cooper, Jr., Phys. Status Solidi A **162**, 305 (1997).
9. P. A. Ivanov, V. N. Panteleev, T. P. Samsonova, *et al.*, Fiz. Tekh. Poluprovodn. (St. Petersburg) **27**, 1146 (1993) [Semiconductors **27**, 631 (1993)].
10. P. A. Ivanov, K. I. Ignat'ev, V. N. Panteleev, and T. P. Samsonova, Pis'ma Zh. Tekh. Fiz. **23** (20), 55 (1997) [Tech. Phys. Lett. **23**, 798 (1997)].
11. P. A. Ivanov, M. E. Levinshtein, J. W. Palmour, and S. L. Rumyantsev, Semicond. Sci. Technol. **15**, 164 (2000).
12. P. A. Ivanov and K. I. Ignat'ev, in *Silicon Carbide, III-Nitrides and Related Materials*, Ed. by G. Pensl, H. Morkoc, B. Monemar, and E. Janzen (Trans. Tech. Publications, Switzerland, 1998), Part 2, p. 809.
13. G. J. Geardi, E. H. Poindexter, and P. J. Caplan, Appl. Phys. Lett. **49**, 348 (1986).

Translated by D. Mashovets

Semiconductors, Vol. 35, No. 4, 2001, pp. 474–476. Translated from Fizika i Tekhnika Poluprovodnikov, Vol. 35, No. 4, 2001, pp. 489–491.

PHYSICS OF SEMICONDUCTORS DEVICES

Consideration of the "Island" Background Charge in Single-Electron Transistor Simulation

I. I. Abramov* and E. G. Novik

Belarussian State University of Information Science, Electronics, and Radio Engineering, ul. P. Brovka 6, Minsk, 220027 Belarus

** e-mail: device@micro.bsuir.edu.by; nanodev@bsuir.edu.by*

Submitted August 8, 2000; accepted for publication September 18, 2000

Abstract—Three approximations of the "island" background charge are described within the proposed 2D numerical model of the metal single-electron transistor. These approximations fit the experimental data well when calculating *I–V* characteristics of single-electron transistors according to the model developed in many cases. The validity of these approximations is exemplified by specific calculations of *I–V* characteristics.

INTRODUCTION

A topical line of research in nanoelectronics is the development and study of device structures based on the single-electron tunneling effect. Currently, much attention is being paid to single-electron transistors owing to the advantages of using these transistors in various devices including integrated circuits with a higher level of integration compared to the known ones [1, 2]. The study and development of single-electron transistors call for adequate models.

The best known models for calculating the electrical characteristics of single-electron transistors are those based on semiclassical approximation and the solution of the master equation [3], as well as on the Monte Carlo method [4]. These models allow one to calculate the device characteristics on the basis of its equivalent circuit, taking discrete tunneling events into account. To achieve a good fit to the experimental data, matching parameters are introduced in various models when simulating the device and structure characteristics. Such parameters in the above models include the tunneling junction resistance and capacitance, the gate capacitance, and the "island" background charge. A two-dimensional (2D) numerical model of the metal single-electron transistor was proposed in [5–7] within the semiclassical approximation, which allows the physical characteristics of the device to be calculated in relation to the structural design, technological, and physical parameters. This model is characterized by fewer matching parameters: these are the density of states in metal electrodes and the island background charge. In many cases, good agreement with experimental data can be achieved within the 2D numerical model neglecting the background charge, i.e., using a single matching parameter [5, 6].

In this paper, we describe three approximations for the island background charge within the proposed 2D numerical model and show their validity.

BACKGROUND CHARGE CONSIDERATION

In the known semiclassical models [3, 4], the background charge is treated as a certain constant $Q_0 = N_0' e$, where e is the elementary charge. In this case, the number of excess carriers on the island is given by

$$N' = N_t' + N_0', \tag{1}$$

where N_t' is the number of island carriers participating in tunneling, and N_0' can be a noninteger number to be fitted to the experimental data.

The model developed is based on the numerical solution to the 2D Poisson equation (the effect of a magnetic field on transistor operation is neglected); i.e., (see [5–7]) we have

$$\nabla\varepsilon\nabla\varphi(x, y) = -q_M, \tag{2}$$

where ε is the dielectric constant ($\varepsilon = \varepsilon_m$ in the conductive island region and $\varepsilon = \varepsilon_i$ in the insulator region); φ is the electrostatic potential; and q_M is the volume charge density including the density q_t of carriers directly involved in tunneling, as well as the background charge density q_0. A finite-difference approximation of the Poisson equation (2) was proposed in [6, 7] on the basis of the Tikhonov–Samarskiĭ integral interpolative approach combined with a number of assumptions. Thus, the averaged density of excess charges at the island, integrated over the area S of a cell

in a spatial discretization mesh is written as (see [7])

$$F = \iint_S q_M dS = \frac{N}{kL_{\text{char}}}, \quad (3)$$

where N is the number of excess carriers per spatial discretization cell of area S, k is a constant, and L_{char} is the island length in the carrier transport direction. As the data of [7] show, the most expedient numerical values of the coefficients k lie within the interval [1/6, 1/4].

Unfortunately, the background charge is in fact randomly distributed over the island. Therefore, it is generally virtually impossible to adequately describe it microscopically. Below, we show that this description is not needed, at least within the semiclassical approximation. We propose three approaches to account for the effect of the background charge in the 2D numerical model developed with consideration of a very small number of discrete charges composing the island background charge.

In the first approach, it is assumed that the background charge distribution is analogous to the distribution of a charge involved in tunneling. Then, formula (3) can be written as

$$F = \frac{N_t + N_0}{kL_{\text{char}}}, \quad (4)$$

where N_t and N_0 are the numbers of excess carriers involved in tunneling and controlling the background charge, respectively.

In contrast to the first approach, the second implies a uniform distribution of the background charge over the entire island area. In this case, the function F is written as

$$F = \frac{N_t + N_0 S/L_x L_y}{kL_{\text{char}}}, \quad (5)$$

where L_x and L_y are the island length and width, respectively, and N_0 is the total number of excess carriers of the island background charge.

However, one should consider the probability of background charge dependence on transistor operating conditions, in particular on the drain voltage. In this case, it is expedient to write the number N of excessive carriers as $N = k_f N_t$, where k_f is the coefficient accounting for the background charge and its dependence on the device operating conditions.

Hence, in the third approach, k_f is the matching parameter depending on the operating voltage. An analogous example of a matching parameter dependent on the operating conditions is the bipolar transistor gain. Thus, formula (3) in the third approach takes the form

$$F = \frac{k_f N_t}{kL_{\text{char}}}. \quad (6)$$

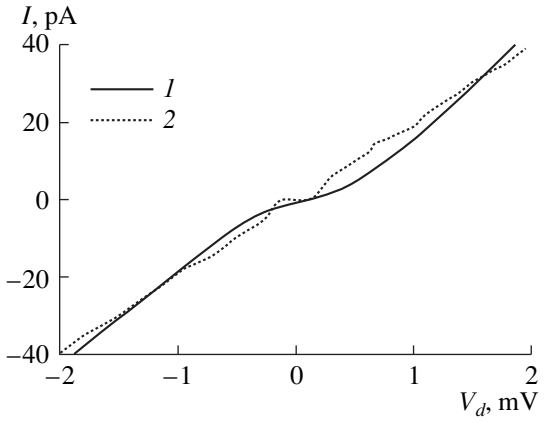

Fig. 1. *I–V* characteristics of the single-electron transistor based on Al/AlO_x/Al tunnel junctions: (*1*) experimental data of [8] and (*2*) data calculated in the context of the 2D numerical model.

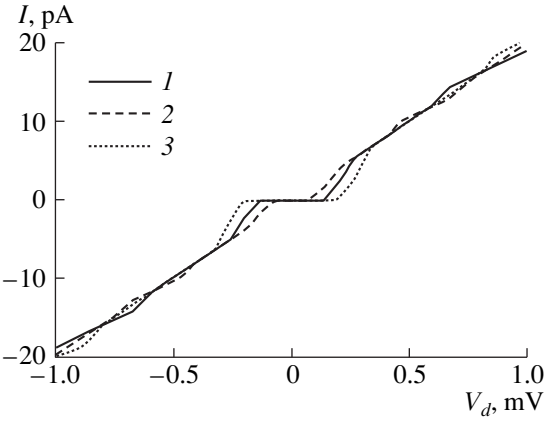

Fig. 2. *I–V* characteristics of the single-electron transistor based on Al/AlO_x/Al tunnel junctions for various island background charges (see text).

THE RESULTS OF SIMULATION

Choosing one of the above approaches to the island background charge, a good fit to the experimental data can be achieved in many cases when calculating the *I–V* characteristics of single-electron transistors according to the proposed 2D numerical model.

We consider several examples. Figure 1 shows the dependence of the current I on the drain voltage V_d, calculated using the 2D numerical model for a transistor based on Al/AlO_x/Al tunneling junctions at an operating temperature of 0.05 K (curve *2*) in comparison to the experimental data of [8] (curve *1*). We chose the third approach to the background charge approximation, which yields a satisfactory fit to the experimental data. The coefficient k_f accounting for the background charge is constant.

We also calculated *I–V* characteristics of the device with other background charges (see Fig. 2). Curves *2*

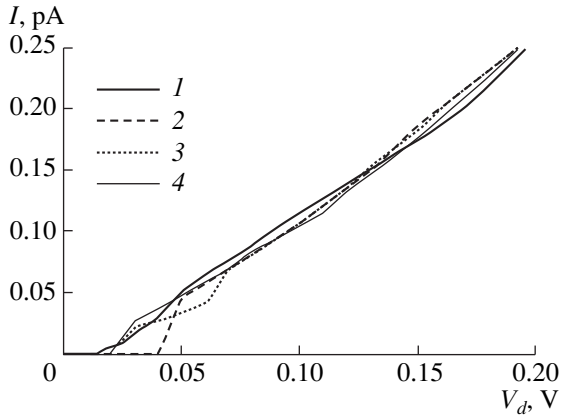

Fig. 3. *I–V* characteristics of the single-electron transistor based on Ti/TiO_x/Ti tunnel junctions: (*1*) experimental data of [9], (*2*) the data calculated neglecting the background charge, and (*3*, *4*) the data calculated according to the first (second) and third approaches to the background charge distribution, respectively.

and *3* correspond to the smallest and greatest chosen charges, respectively. It is evident that the background charge variation significantly affects the Coulomb blockade range (the drain voltage V_d range corresponds to the zero current) and affects the current only slightly. We note that the background charge in the known semiclassical model [1] also has a strong effect on this domain.

As mentioned above, one of the proposed approaches applied to the approximation of the background charge distribution allows a good fit to the experiment. In many cases, all three approaches can be employed, which yields almost the same *I–V* characteristics. As an example, Fig. 3 displays *I–V* characteristics for a transistor based on the Ti/TiO_x/Ti tunneling junctions corresponding to calculations by various approaches (curves *3*, *4*), as well as to a calculation neglecting the background charge (curve *2*), and in comparison to the experimental data of [9] (curve *1*). The data calculated by the first and second approaches coincide quite well and correspond to curve *3*. It is also evident from Fig. 3 that the characteristics calculated taking the background charge into account differ significantly only in the Coulomb blockade domain compared to the dependence constructed neglecting its impact.

CONCLUSION

To account for the island background charge, we propose three approximations yielding a good fit to the experiment. Their validity was demonstrated by calculating *I–V* characteristics of single-electron transistors.

ACKNOWLEDGMENTS

This study was supported in part by the State Programs “Low-Dimensional Systems” and “Nanoelectronics,” as well as by the Belarussian Foundation for Basic Research, project no. F99M-074.

REFERENCES

1. *Single Charge Tunneling: Coulomb Blockade Phenomena in Nanostructures*, Ed. by H. Grabert and M. H. Devoret (Plenum, New York, 1992), NATO ASI Ser., Ser. B **294** (1992).
2. I. I. Abramov and E. G. Novik, Fiz. Tekh. Poluprovodn. (St. Petersburg) **33** (11), 1388 (1999) [Semiconductors **33**, 1254 (1999)].
3. M. Amman and K. Mullen, J. Appl. Phys. **65**, 339 (1989).
4. R. H. Chen and K. K. Likharev, Appl. Phys. Lett. **72**, 61 (1998).
5. I. I. Abramov and E. G. Novik, Fiz. Tekh. Poluprovodn. (St. Petersburg) **34** (8), 1014 (2000) [Semiconductors **34**, 975 (2000)].
6. I. I. Abramov and E. G. Novik, Pis’ma Zh. Tekh. Fiz. **26** (16), 63 (2000) [Tech. Phys. Lett. **26**, 726 (2000)].
7. I. I. Abramov and E. G. Novik, *Numerical Simulation of Metal Single-Electron Transistors* (Bestprint, Minsk, 2000).
8. M. Götz, K. Blüthner, W. Krech, *et al.*, J. Appl. Phys. **78**, 5499 (1995).
9. K. Matsumoto, M. Ishii, K. Segawa, *et al.*, Appl. Phys. Lett. **68**, 34 (1996).

Translated by A. Kazantsev

Semiconductors, Vol. 35, No. 4, 2001, pp. 477–480. Translated from Fizika i Tekhnika Poluprovodnikov, Vol. 35, No. 4, 2001, pp. 492–494.

PHYSICS OF SEMICONDUCTORS DEVICES

The Effect of Dislocations Formed during Growth on the Structure and Photoluminescence of *i*–n^-–*n*–n^+-GaAs Epilayers and on the Related Microwave Transistors Parameters

M. P. Lisitsa, F. V. Motsnyĭ*, V. F. Motsnyĭ, and I. V. Prokopenko

Institute of Semiconductor Physics, National Academy of Sciences of Ukraine, pr. Nauki 45, Kiev, 03028 Ukraine

**e-mail: motsnyi@sun.semicond.kiev.ua*

Submitted September 15, 1999; accepted for publication September 26, 2000

Abstract—The structure of two types of GaAs *i*–n^-–*n*–n^+ epilayers on GaAs⟨100⟩ semi-insulating substrates was studied by electron microscopy. The low-temperature photoluminescence spectra were measured and their special features were analyzed. It is shown that the formation of dislocations during growth in such structures significantly affects the photoluminescence spectra and impairs the parameters of microwave field-effect transistors based on these structures. © *2001 MAIK "Nauka/Interperiodica"*.

1. INTRODUCTION

Ion-implanted and epitaxial GaAs structures are widely used in the fabrication of microwave Schottky gate field-effect transistors (SFETs). More stringent requirements for the enhanced yield of semiconductor devices, for an increase in their reliability, and for a reduction of their degradation are stimulating further studies of both the starting structures and the SFETs based on these structures.

The origin of the centers and mechanisms of radiative recombination in GaAs crystals implanted with silicon ions has been studied previously [1]. The effect of the growth method on the background concentration of carbon in GaAs films was studied by Tejayardi *et al.* [2]. The objective of this study was to gain insight into the effect of dislocations formed during growth on the photoluminescence (PL) of GaAs *i*–n^-–*n*–n^+ structures and on the parameters of microwave SFETs based on the above structures.

2. EXPERIMENTAL

We studied two types of *i*–n^-–*n*–n^+-GaAs structures that are used in conventional microwave SFETs. The structures were grown by molecular-beam epitaxy in a unified technological process.

The structures of the first type (sample 572) were obtained in the growth chamber under a pressure of $(1.3–1.9) \times 10^{-7}$ Pa, whereas the pressure was $(7.5–8.7) \times 10^{-8}$ Pa for the structures of the second type (sample 573). The structures of both types were formed by consecutive deposition of an undoped buffer n^- layer and also *n*- and n^+-GaAs active layers doped with Si to different concentrations onto high-quality semi-insulating *i*-GaAs⟨100⟩ substrates. The choice of Si as the dopant was prompted by the wide use of Si in *n*-GaAs technology.

The substrate temperature was maintained at 540 ± 20°C. The thicknesses of the substrate and of the n^-, *n*, and n^+ layers were 350, 1.0, 0.25, and 0.20 μm, respectively.

The concentration and mobility of electrons in the layers were determined from the capacitance–voltage characteristics and the measurements of the Hall coefficient by the van der Pauw method, respectively.

Photoluminescence (PL) was excited with an LG 106 M-1 argon laser with a photon energy of 2.41 eV and a power of 50 mW. The highest power density in the focused beam amounted to 5×10^{17} photon/(cm^2 s). The PL spectra were measured with the samples immersed in liquid helium and with the PL emission coming from the surface on which the luminous flux was incident; a setup based on a DFS-24 high-resolution (4.5 Å/mm) spectrometer was used.

Electron microscopy measurements were performed using a JSM-35 scanning electron microscope.

3. RESULTS AND DISCUSSION

Certain electrical characteristics of both types of the *i*–n^-–*n*–n^+-GaAs structures and the parameters of

1063-7826/01/3504-0477$21.00

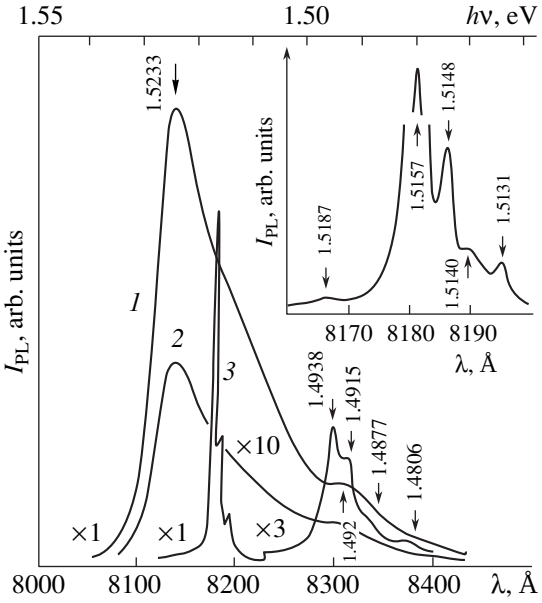

Fig. 1. The PL spectra of i–n^-–n–n^+-GaAs structures for conventional field-effect transistors with the Schottky gate: (*1*, *2*) the emission from different spots of sample batch 572 and (*3*) the same for sample batch 573. In the inset, the central portion of the PL spectrum for sample batch 573 (curve *3*) is shown. $T = 4.2$ K. The wavelength of the excitation radiation was 5145 Å. The characteristic energies $h\nu$ expressed in eV are indicated.

microwave SFETs based on these structures and measured at a characteristic frequency of 12 GHz are listed in the table. We draw attention to the fact that even a slight deterioration of vacuum in the growth chamber due to inleakage of atmospheric oxygen (a peak related to oxygen was detected in the mass spectrum of residual gases only when the wafers of the 572 series were grown) markedly affected the concentration and mobility of electrons in the n^+ and n layers of initial wafers. In turn, this significantly impairs the basic operating parameters of microwave SFETs, specifically, the noise temperature and the gain.

Typical PL spectra I_{PL} of the GaAs structures studied are shown in Fig. 1. As can be seen, these spectra differ significantly for the above two structures. Thus, the PL spectra of the samples of the first type, recorded from two different spots on the sample surface, are diffuse and consist of a broad featureless edge band that peaked at 1.523 eV with a steep short-wavelength wing and a gently sloping long-wavelength wing, with a low-intensity impurity band that peaked at 1.492 eV being superimposed on the latter. It is significant that the intensity of PL emission from these samples varies from one point on the surface to another, which is a clear manifestation of the nonuniformity of the samples.

The PL spectra of structures of the second type (see curve *3* and the inset in Fig. 1) consist of a number of narrow lines related to free excitons in the first excited state (1.5187 eV), to polaritons of the upper (1.5157 eV) and lower (1.5148 eV) branches, to excitons bound by neutral donors (D, X) (1.5140 eV), to the recombination of free holes at a neutral donor (D, h) (1.5131 eV), and to electron transitions either between the conduction band and acceptors (E_c–A) (1.4938 and 1.4877 eV) or in the donor–acceptor pairs (DAPs) (1.4915 and 1.4806 eV), in which the acceptors are carbon C^0_{As} and silicon Si^0_{As} in a state of $1S_{3/2}$ with the thermal-ionization energies of 26.5 and 35.1 meV, respectively [1, 3]. In addition, we note the following:

(i) The polaritonic channel of radiative recombination significantly dominates over all other channels.

(ii) The quantum yield of radiative recombination from the upper polaritonic branch is about three times higher than that from the lower branch.

(iii) The lines related to the excitons bound at the point structural defects (d, X) are absent in the PL spectra.

Some electrical characteristics of GaAs i–n^-–n–n^+ structures and the parameters of the Schottky-gate field-effect transistors fabricated on the basis of these structures

The wafer no.		572		573	
T, K		300	77	300	77
Electron concentration in the layers, cm^{-3}	n^+	4×10^{18}	–	3×10^{18}	–
	n	5×10^{17}	–	3×10^{17}	–
The electron mobility in the layers, $cm^2\,V^{-1}\,s^{-1}$	n^+	1600	1660	2045	2140
	n	3260	2980	4465	3595
The SFET parameters at a frequency of 12 GHz	Gain, dB	7–7.5	–	8.5–9	–
	The noise temperature, K	225–300	–	90–140	–

The PL spectra for samples of both types in the range of the E_c–A and DAP transitions include low-intensity lines of comparable intensities, which is indicative of an approximately equal content of C^0_{As} and Si^0_{As} atoms in each of the sample types. Consequently, these impurities cannot be the cause of lower electron mobilities in the n^+ and n layers in the wafers of the first type and also of the inferior operating parameters of microwave SFETs based on these layers.

Thus, all the aforesaid, together with the presence of the spectral line related to free excitons in a state of $n = 2$, is directly indicative of an insignificant concentration of various lattice defects in the series of the 573 samples studied and, consequently, of a high degree of structural perfection of these samples.

These inferences are consistent with the results of electron microscopy measurements shown in Fig. 2. In fact, samples of batch 572 have a block structure and include a number of small-angle crystallite boundaries over which various dislocations are located (including the misfit dislocations at the interface between the n^- layer and the substrate) and penetrate even further into the substrate (see Fig. 2a), whereas the samples of batch 573 are homogeneous and of high quality and have sharp i–n^- and n^-–n interfaces (see Fig. 2b). On the basis of the results obtained, we may conclude that the dislocations formed during growth significantly impair the quality of the i–n^-–n–n^+ GaAs structures and the parameters of microwave SFETs based on these structures and that PL is a reliable method for determining the structural quality of such samples.

The crystal lattice of GaAs i–n^-–n–n^+ structures distorts under the effect of growth-related dislocations; as a result, the band gap E_g widens and the edge-emission band shifts to higher energies by 3.8 meV. Such a situation has been observed previously [4] in the PL spectra of n-GaAs crystals subjected at 2 K to uniaxial pressure along the ⟨100⟩, ⟨110⟩, and ⟨111⟩ directions. A shift of the excitonic band to shorter wavelengths was observed; the magnitude of this shift depended markedly on the direction of the applied force. The largest shift of this band for the above pressure directions was ~3.2, ~8.2, and 11.0 meV under the applied pressures of 7.0×10^8, 1.1×10^9, and 1.4×10^9 Pa, respectively. This shift is approximately equal to, or exceeds by two to three times, the value obtained for the i–n^-–n–n^+ GaAs structures with growth-related dislocations. However, it is impossible to state the force direction or to estimate the pressure imposed on such samples.

The observed special features of polaritonic emission may be due to scattering of the low-branch polaritons at various imperfections of the crystal lattice with the subsequent transfer of these polaritons to the upper branch [5, 6].

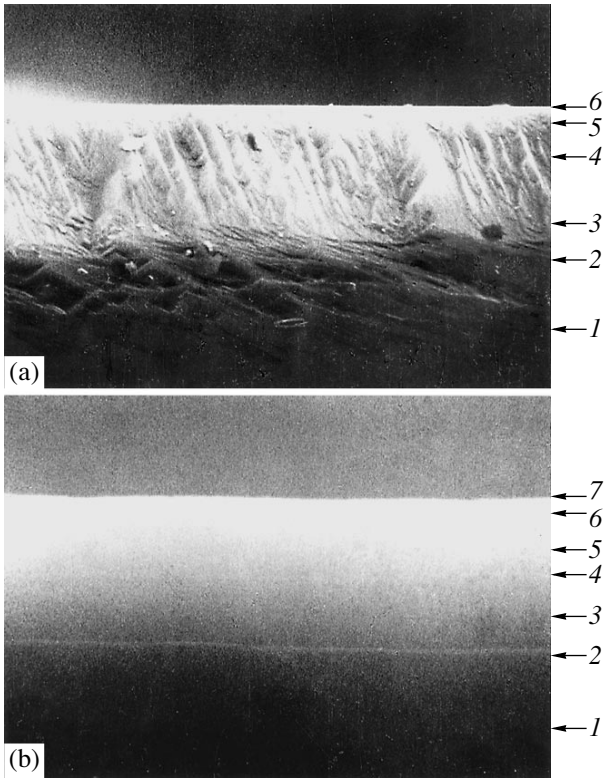

Fig. 2. The results of examining the GaAs i–n^-–n–n^+ structures using a JSM-35 scanning electron microscope. (a) Sample batch 572: (*1*) the substrate, (*2*) the interface between the n^- layer and the substrate, (*3*) the n^- layer, (*4*) the n layer, (*5*) the n^+ layer, and (*6*) the surface of the sample; (b) sample batch 573: (*1*) the substrate, (*2*) the interface between the n^- layer and the substrate, (*3*) the n^- layer, (*4*) the interface between the n^- and n layers, (*5*) the n layer, (*6*) the n^+ layer, and (*7*) the sample surface. The width of the scanned image is 11.3 μm.

4. CONCLUSION

(1) Leakage of atmospheric oxygen into the growth chamber during fabrication of i–n^-–n–n^+ GaAs structures by molecular-beam epitaxy is conducive to the formation of dislocations during growth.

(2) The growth-related dislocations significantly affect the PL spectra of i–n^-–n–n^+ GaAs structures and the concentration and mobility of electrons in the n^+ and n layers and also impair markedly the parameters of microwave SFETs (i.e., the noise temperature and the gain).

(3) Photoluminescence is a reliable method for assessing the quality of epitaxial i–n^-–n–n^+ GaAs structures.

ACKNOWLEDGMENTS

We thank E.P. Laurs for providing us with the samples and A.P. Ostryanitsa for performing electron microscopy studies.

This study was supported in part by the International Science Foundation under a program supporting education in the field of precise sciences (ISSP), grant no. ERI052023.

REFERENCES

1. F. V. Motsnyĭ, Author's Abstract of Doctoral Dissertation (Kiev, 1993).
2. O. Tejayadi, Y. L. Sun, J. Klem, *et al.*, Solid State Commun. **46**, 251 (1983).
3. V. G. Komarov, F. V. Motsnyi, V. F. Motsnyi, and O. S. Zinets, J. Phys. Stud. **2**, 555 (1998).
4. R. N. Bhargava and M. I. Nathan, Phys. Rev. **124**, 695 (1967).
5. V. I. Sugakov, Opt. Spektrosk. **26**, 732 (1969).
6. Yu. V. Kryuchenko and V. I. Sugakov, Phys. Status Solidi B **111**, 177 (1982).

Translated by A. Spitsyn

Semiconductors, Vol. 35, No. 4, 2001, pp. 481–484. Translated from Fizika i Tekhnika Poluprovodnikov, Vol. 35, No. 4, 2001, pp. 495–498.

PHYSICS OF SEMICONDUCTORS DEVICES

Radiation Hardness of SiC Ion Detectors under Relativistic Protons

A. M. Ivanov*, N. B. Strokan*, D. V. Davydov*, N. S. Savkina*, A. A. Lebedev*, Yu. T. Mironov, G. A. Ryabov**, and E. M. Ivanov****

**Ioffe Physicotechnical Institute, Russian Academy of Sciences, Politekhnicheskaya ul. 26, St. Petersburg, 194021 Russia*

e-mail: alexandrivanov@pop.ioffe.rssi.ru

*** Konstantinov Institute of Nuclear Physics, Russian Academy of Sciences, Gatchina, Leningrad oblast, 188350 Russia*

e-mail: riabov@mail.pnpi.spb.ru

Submitted October 19, 2000; accepted for publication October 23, 2000

Abstract—Schottky diodes based on 6*H*-SiC epitaxial films exposed to 1000 MeV protons at a dose of 3×10^{14} cm^{-2} have been studied by precision alpha spectrometry. Parameters of deep levels introduced by protons were determined by deep-level transient spectroscopy. The number of vacancies generated in proton tracks was found using TRIM software. The width of the space charge region and the hole diffusion length before and after irradiation were obtained by processing the alpha-spectrometry and capacitance measurements. Minor variations in the charge transport properties of epitaxial 6*H*-SiC detectors were observed. © *2001 MAIK "Nauka/Interperiodica".*

1. INTRODUCTION

Recently, considerable progress has been made in the fabrication of high-quality single-crystal SiC substrates and epitaxial films [1]. The interest of nuclear physicists in SiC as a material for hard radiation detectors [2] is due to the potentially high radiation hardness of SiC devices and the possibility of operating them at elevated temperatures [3].

Radiation hardness is important, in particular, when designing systems for detecting reaction products in key experiments of high-energy physics. Presently, experiments are being developed on CERN's Large Hadron Collider, where the detectors should be operational for at least ten years. In these experiments, the doses of detector irradiation by relativistic particles are within the limits 2×10^{14}–5×10^{15} cm^{-2}, depending on the detector position relative to the point of beam collision [4].

In these conditions, serious problems arise with highly technologically developed Si detectors even at doses of ~10^{14} cm^{-2}. First, the dissipated power increases dramatically (reverse currents and structure depletion voltages grow). Second, the efficiency of nonequilibrium charge transport falls, and, correspondingly, the signal amplitude decreases. In a review [4], the conclusion was made that a search for materials with higher radiation hardness is inevitable.

The effect of 8-MeV proton doses up to 2×10^{16} cm^{-2} on 6*H*-SiC has been studied in [5]. Under irradiation, the room-temperature free electron concentration in the layer decreases, while the total charge of ionized impurities $|N_D^+ - N_A^-|$ measured at the temperature T = 650 K increases. This means that under irradiation, deep centers (DCs) are formed in the upper half of the band gap, which capture the electrons from shallow donors. These DCs (for example, an R center with the ionization energy $E_c - E_t \approx 1.2$ eV) are ionized at high temperatures, but they do not contribute to $|N_D^+ - N_A^-|$ measured at 300 K, because at this temperature their recharging time is about two weeks.

In similar conditions, SiC p^+–n structures maintain their efficiency for detecting short-path ions after irradiation doses of up to 8×10^{15} cm^{-2} [6].

The goal of the present study was to analyze the radiation hardness of SiC Schottky diodes under irradiation conditions corresponding to those encountered when they are applied as detectors of relativistic particles. Data are presented concerning the change in the detector properties of diode structures upon irradiation with 1000 MeV protons. The dose was chosen to be ~3×10^{14} cm^{-2}, which is half an order of magnitude higher than the "critical" dose for silicon detectors.

2. EXPERIMENTAL

Schottky diodes, 600 μm in diameter, were used as detectors and were fabricated by magnetron sputtering of Ni onto the surface of 6*H*-SiC epitaxial films grown by vacuum sublimation epitaxy [2]. The film doping profile was inhomogeneous, with the carrier concentration varying from ~5×10^{14} cm^{-3} at the surface to 8×10^{15} cm^{-3} at a depth of ~7 μm. Such a distribution of

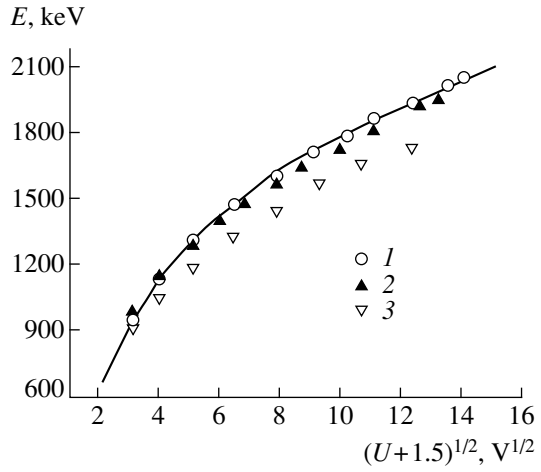

Fig. 1. Energy released by an alpha-particle in the sensitive region of the structure vs. reverse bias for three as-grown samples. Sample no.: (*1*) 56, (*2*) 36, and (*3*) 25.

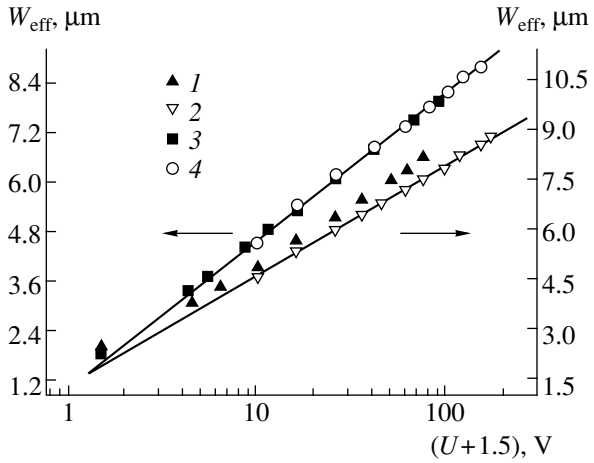

Fig. 2. Effective width of the sensitive region of the structure vs. reverse bias. Sample no.: (*1, 2*) 36 and (*3, 4*) 56. (*2, 4*) As-grown samples and (*1, 3*) those after proton irradiation with a dose of 2.7×10^{14} cm^{-2}.

$(N_D^+ - N_A^-)$ creates a "pulling field" in the space-charge region, thus increasing the effective diffusion length of carriers [7].

Samples were irradiated with a 1000-MeV proton beam extracted from the synchrocyclotron at the B.P. Konstantinov Petersburg Nuclear Physics Institute, Gatchina. A sample was placed at a distance of 5 m from the synchrocyclotron extraction window in the accelerator hall. The beam spot size at the irradiation point was 3×6 cm^2 with a flux density of up to 6.25×10^{10} cm^{-2} s^{-1}. The long-burst operation mode [8] was used during irradiation to ensure a uniform exposure over time. The time of exposure was 4.32×10^3 s.

The beam was monitored by the method of activated foils, using the reaction ^{27}Al(p, $3pn$)^{24}Na, whose cross section was assumed to be (10.5 ± 0.7) mbarn. The activity of ^{24}Na was measured with a gamma spectrometer calibrated against a standard ^{60}Co source whose intensity was known to within 3% at a 95% confidence level.

The detectivity of SiC diode structures was directly measured using alpha-particles with an average energy of 5.79 MeV from a ^{244}Cm preparation. The recorded energies (or the nonequilibrium charge created in SiC) were determined in relation to a reverse bias applied to the diode by amplitude analysis. The data on the structure capacitance were also used to determine the real size of the sensitive region and the hole diffusion length.

The parameters and concentrations of deep levels formed under irradiation were calculated from data furnished by deep-level transient spectroscopy (DLTS).

3. EXPERIMENTAL RESULTS

1. Figure 1 shows typical dependences of the measured energy E on the reverse bias U for three structures. The difference in E between the three samples is insignificant, indicating a sufficient uniformity of the SiC properties over the film area. Data of the type presented in Fig. 1 were used for further processing, these dependences being taken before and after irradiation with protons.

Data processing (Fig. 1) relied on the nonequilibrium charge generated in SiC by an alpha-particle being strictly calibrated. According to the known dependence of specific ionization losses by the alpha-particle on its path length in SiC (Bragg curve), energy loss is strictly related to the length of the sensitive region of the detector, W_{eff}. We used the Bragg curve obtained with TRIM software [9]. The curve was approximated (with the exception of its peak region) by a cubic polynomial in W_{eff}. Correspondingly, the calculated energy $E_{\text{th}}(W_{\text{eff}})$ released along the path W_{eff} was described by a fourth-order polynomial. The W_{eff} values were obtained by solving numerically the equation $E = E_{\text{th}}(W_{\text{eff}})$, where E is the measured quantity, with an accuracy of no less than 0.025 μm.

Figure 2 presents the $W_{\text{eff}}(U)$ dependences obtained as described above. The contact potential difference across the p^+–n-junction was taken into account by adding 1.5 V to the bias voltage. At 100 V, W_{eff} exceeds 7 μm, being equal to the sum of the space charge region width W and the hole diffusion length L_D:

$$W_{\text{eff}} = W + L_D. \qquad (1)$$

To distinguish between the contributions from the W and L_D terms to W_{eff}, we measured the dependence of the capacitance C on the bias U. However, the obtained C values were not used to calculate W directly, the stray

capacitance being significant for small-area structures. To exclude this error, we used the following expression for $W_{\text{eff}}(C)$

$$W_{\text{eff}} = \frac{A}{(C - P_1)} + P_2, \quad (2)$$

where the constant A is related to the structure area, and the parameters P_1 and P_2 correspond to stray capacitance and L_D. Figure 3 exemplifies a fitting calculation according to relation (2) for one of the samples before and after proton irradiation at a dose of 2.7×10^{14} cm^{-2}. The obtained L_D values are (1.658 ± 0.079) and (1.214 ± 0.098) μm, respectively.

2. Table 1 presents parameters of deep centers before and after irradiation from DLTS data. It can be seen that only the concentration of R centers changes significantly, and no new centers appear. Since the R centers are presumably associated with vacancies (see, e.g., [5]), we can estimate their rate of introduction by the number of primarily formed vacancies, determined from the calculations of proton deceleration using TRIM software. Computer simulation shows that the number ratio of vacancies is 110 : 1 for proton energies of 8 and 1000 MeV. This results from the decrease in the cross section of scattering of a proton on Si and C atoms with its increasing energy.

However, in the case under study the experiment gave a concentration of R centers approximately 400 times lower. Thus, the result expected in terms of the model of primary defects markedly differs from the concentration of "final" defects formed during physicochemical processes in SiC. This indicates that the defect formation processes at 8 and 1000 MeV are not identical. Apparently, this is due to a difference of two orders of magnitude in the energies transmitted to the primarily displaced out Si and C atoms.

4. DISCUSSION

The data presented in Figs. 1–3 allow the effect of irradiation on W_{eff} and L_D to be estimated. Table 2 lists the L_D values and illustrates the tendencies of W_{eff} variation for five samples. The span of W_{eff} variation can be judged from Figs. 2 and 3.

As can be seen, the hole diffusion lengths change by no more than 30% (except in sample no. 56). The variations in W_{eff} are even less pronounced. It seems reasonable to relate the decrease in W_{eff} for samples nos. 25 and 55 to decreasing L_D. At the same time, the invariability of W_{eff} for other samples (or even its increase for sample 36) is due to compensation occurring in SiC. As a result, the difference between the charges of ionized donor (N_D^+) and acceptor (N_A^-) impurities, $N_{\text{eff}} = |N_D^+ - N_A^-|$, determining the range of the electric field in the p^+–n structure, decreases. Correspondingly, the value of $W \propto |N_D^+ - N_A^-|^{-1/2}$ also increases.

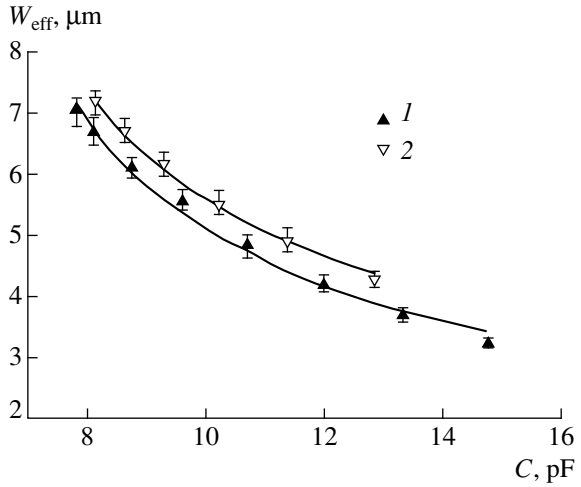

Fig. 3. Effective width of the sensitive region of the structure vs. measured capacitance for sample 25. Points, experiment; lines, approximation by relation (2). (*2*) As-grown and (*1*) irradiated sample.

The hole drift length in an electric field of strength F can be found as $L_F^p = (\mu\tau)_p F = (L_D)(Fe/kT)$. Here, e is the electron charge, k is the Boltzmann constant, T is the absolute temperature, and μ and τ are the carrier mobility and lifetime. Assuming that $F = 10^5$ V/cm and $L_D = 1$ μm, we obtain $L_F^p = 400$ μm for holes at room temperature.

Table 1. Deep centers according to DLTS data

Type of center	$E_c - E_t$, eV	Concentration, cm^{-3}	
		before irradiation	after irradiation
*E*1/*E*2	0.35–0.4	$(1–2) \times 10^{13}$	$(1–2) \times 10^{13}$
R	1.1–1.2	$<5 \times 10^{12}$	5×10^{13}

Table 2. Diffusion length and the effect of irradiation on the size of the sensitive region

Sample no.	L_D, μm, before irradiation	L_D, μm, after irradiation	Variation in W_{eff}
25	1.66	1.21	Decrease
36	1.80	1.24	Increasing
46	0.78	0.61	Const
55	0.92	–*	Decreasing
56	1.00	0.16	Const

* L_D for sample 55 after the irradiation is not presented because of the significant error in approximation by relation (2).

The electron drift length $L_F^n = (\mu\tau)_n F$ can be evaluated using the data from [6], where $(\mu\tau)_n = 7 \times 10^{-9}$ cm^2/V was obtained in the unipolar electron transport mode for 8 MeV protons with a dose of 8×10^{15} cm^{-2}. Assuming that *R* centers are responsible for the decrease in the lifetime and introducing a correction to the $(\mu\tau)_n$ value, accounting for the number of *R* centers formed, we obtain $L_F^n \leq 1$ cm for the conditions of the present study.

Thus, the carrier drift lengths are quite satisfactory for detectors with a working region several hundred micrometers long.

5. CONCLUSION

Comparing the results of this study with the data obtained in [5], where 8 MeV protons were used for irradiation, we conclude that the proton energy has no significant effect on the spectrum of centers formed upon irradiation. *R* centers with energies 1.1–1.2 eV below the bottom of the conduction band still play an essential role. However, the rate of introduction of the centers was lower than that predicted on the basis of the number of primarily introduced defects.

Direct studies of SiC detector properties have shown that the variation of parameters responsible for carrier transport can be classified as the initial stage of deterioration.

The width of the space charge region (with a high electric field) in the diode structure remains practically unchanged. This means that the effective charge of ionized impurities N_{eff} is conserved, despite the high concentration of primarily introduced vacancies (1.4×10^{15} cm^{-3}). The rate of introduction of *R*-centers is low, and their concentration is only 5×10^{13} cm^{-3}. Thus, the N_{eff} values are still determined by the initial impurity concentration.

REFERENCES

1. C. H. Carter, Jr., V. F. Tsvetkov, R. C. Glass, *et al.*, Mater. Sci. Eng. B **B51–B62**, 1 (1999).
2. N. S. Savkina, A. A. Lebedev, D. V. Davydov, *et al.*, Mater. Sci. Eng. B **B77**, 50 (2000).
3. N. B. Strokan, A. M. Ivanov, A. A. Lebedev, *et al.*, Fiz. Tekh. Poluprovodn. (St. Petersburg) **34**, 249 (2000) [Semiconductors **34**, 243 (2000)].
4. G. Lindstrom, M. Moll, and E. Fretwurst, Nucl. Instrum. Methods Phys. Res. A **426**, 1 (1999).
5. A. A. Lebedev, A. I. Veĭnger, D. V. Davydov, *et al.*, Fiz. Tekh. Poluprovodn. (St. Petersburg) **34**, 897 (2000) [Semiconductors **34**, 861 (2000)].
6. N. B. Strokan, A. M. Ivanov, A. A. Lebedev, *et al.*, Fiz. Tekh. Poluprovodn. (St. Petersburg) **34**, 1443 (2000) [Semiconductors **34**, 1386 (2000)].
7. M. M. Anikin, N. I. Kuznetsov, A. A. Lebedev, *et al.*, Fiz. Tekh. Poluprovodn. (St. Petersburg) **28**, 457 (1994) [Semiconductors **28**, 278 (1994)].
8. N. K. Abrossimov, R. P. Deviateriakov, A. G. Kotov, *et al.*, in *Proceedings of the III All-Union Conference on Charged Particle Accelerators, Moscow, 1973*, Vol. 2, p. 94.
9. *Ion Implantation: Science and Technology*, Ed. by J. F. Ziegler (Academic, Orlando, 1984).

Translated by D. Mashovets

Semiconductors, Vol. 35, No. 4, 2001, pp. 485–489. Translated from Fizika i Tekhnika Poluprovodnikov, Vol. 35, No. 4, 2001, pp. 499–503.

PHYSICS OF SEMICONDUCTORS DEVICES

The Thermal Cross-Interference Effects in the Arrays of Vertical-Cavity Surface-Emitting Lasers

S. M. Zakharov

Institute of High-Performance Computer Systems, Russian Academy of Sciences, Moscow, 117872 Russia

Submitted May 10, 2000; accepted for publication November 9, 2000

Abstract—Thermal interference effects in the arrays of vertical-cavity surface-emitting lasers are considered. Thermal resistances for various laser configurations in the array are estimated. © *2001 MAIK "Nauka/Interperiodica".*

1. INTRODUCTION

There are serious difficulties in solving thermal problems in injection lasers with vertical outcoupling of radiation (also called vertical-cavity surface-emitting lasers, VCSELs); these difficulties are primarily related to the complexity of the heat-source distribution in the laser bulk and to the two-dimensional pattern of the electric-current flow. A certain amount of experimental data related to thermal phenomena in the arrays of VCSELs have so far been accumulated [1–5].

In this context, it is important to study the issues related to the simulation of VCSEL array [6–12]. When simulating the VCSELs, it is necessary to devise a unified physical model that accounts for both the optical and the thermal (and electrical) properties of the surface-emitting lasers in general. In fact, the latter circumstance forces one to use numerical simulations, which make it possible to take adequately into account the totality of the above properties and make constructive decisions related to a complex structure of objects. In view of this, numerical simulations inevitably lead to the necessity of using large computational resources. Under these conditions, it is appropriate to apply simpler approaches, which make it possible first of all to assess the thermal parameters analytically.

In this study, we use the simplest model solutions for various configurations of operating lasers in an array to calculate the thermal resistance that accounts for the mutual or cross influence of the lasers on each other. In particular, an asymmetry in the thermal properties of central, corner, and edge lasers is noted. The results obtained were compared in detail with experimental data.

2. EFFECTIVE THERMAL RESISTANCES WITH A MUTUAL EFFECT FUNCTION

We define the thermal resistance R_{ij}^{th} with a mutual-effect function of any lasers as the ratio between the temperature increment ΔT_i of the ith laser and the thermal power P_j released during operation of the jth laser; i.e.,

$$R_{ij}^{\text{th}} = \frac{\Delta T_i}{P_j}. \quad (1)$$

We note that this definition is not rigorous, because, in the lasing zone, it is more appropriate to deal with the distribution of the temperature fields. However, thermal resistances are often used in engineering calculations because they make it possible to easily estimate the temperature increment (and, at the same time, the temperature of the active laser region) caused by the thermal-power dissipation [1–5].

In the model of an array of VCSELs under consideration, there are no thermal flux losses at the top (in contact with air) and lateral (in contact with passivating polyamide) laser surfaces. This means that the heat exchange between lasers is accomplished only via the substrate. In the substrate itself, a distribution of the heat flux between two mutually perpendicular directions occurs. As this takes place, a fraction of heat flux either goes to infinity (as in the case of a semi-infinite medium) or is lost at the contact with a cool heatsink (a body whose temperature is treated as constant); the latter occurs when the substrate is in the form of an unlimited layer with a finite thickness. Thus, the thermal problem is reduced to determining the thermal-field distribution over the semiconductor–substrate surface.

In this situation, it is convenient to use the simplest model solutions to thermal problems. For example, for a point heat source, the steady-state temperature of the surface ($z = 0$) varies following the $1/r$ law; therefore, we have

$$R_{ij}^{\text{th}}(r) = \frac{1}{2\pi\kappa r}, \quad (2)$$

where $r = |\mathbf{r}_i - \mathbf{r}_j|$. It is noteworthy that the variables $\{r, z\}$ are cylindrical coordinates.

If the heat flux is introduced with a constant density of $q = P/\pi R^2$ (a q model) into a circular region with a

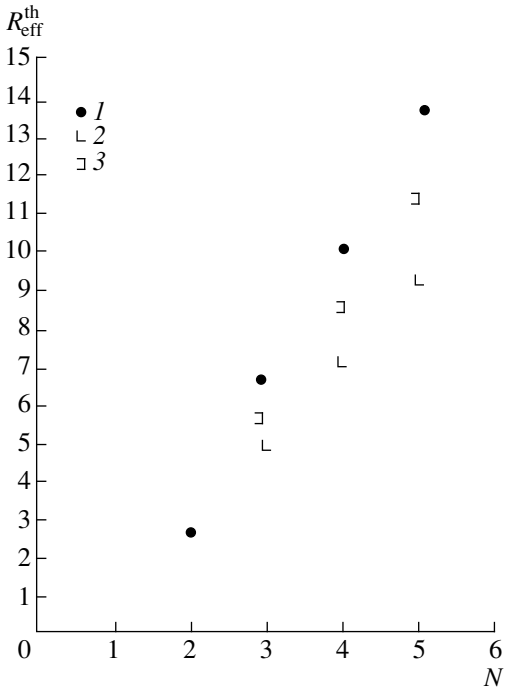

Fig. 1. Effective thermal resistance for cross interference effects of lasers as a function of the edge number N for lasers in the $N \times N$ array, where $N = 2$, 3, 4, and 5 (points *1* correspond to the central laser; symbols *2* refer to the corner lasers; and symbols *3* correspond to the edge lasers).

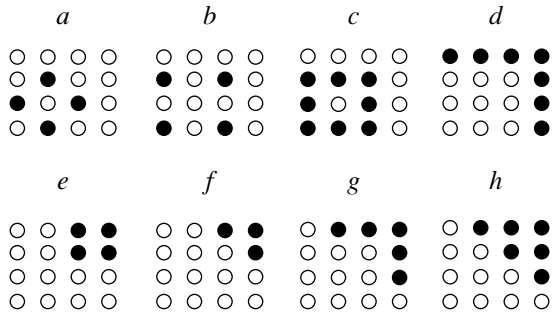

Fig. 2. Various configurations of operating lasers (shown by shaded circles) in the 4×4 array.

radius of R in the substrate with thickness l, we may use the analogy to [13] to obtain

$$T(r, 0) = \frac{P}{\pi\kappa R}\int_0^\infty \tanh(\lambda l) J_0(\lambda r) J_1(\lambda R)\frac{d\lambda}{\lambda}.$$

Thus, we have

$$R_{ij}^{\text{th}}(r) = R_0^{\text{th}}\int_0^\infty 2\tanh\left(\frac{l}{R}x\right)J_0\left(\frac{r}{R}x\right)J_1(x)\frac{dx}{x}, \qquad (3)$$

where $R_0^{\text{th}} = (2\pi\kappa R)^{-1}$.

For a distributed heat flux controlled by constant temperature T of a circular (with a radius of R) region (a T model), we obtain

$$R_{ij}^{\text{th}}(r) = R_0^{\text{th}}\int_0^\infty 2\tanh\left(\frac{l}{R}x\right)J_0\left(\frac{r}{R}x\right)\frac{\sin x}{x}dx. \qquad (4)$$

Integrals (3) and (4) can be analytically calculated for $l/R \gg 1$ since, in this case, the range of l/R where the function $\tanh[(l/R)x]$ differs from zero is narrow and does not make a significant contribution to the result. For $l/R \leq 1$, this function causes the result of integration to be undervalued. Physically, this means that effective thermal resistances for mutual (cross) effects and for a substrate with finite thickness l are lower than in a semi-infinite medium ($l \longrightarrow \infty$). Therefore, in what follows, we restrict ourselves to a consideration of thermal resistances in relation to the interference effects for a semi-infinite medium.

It is noteworthy that a solution described by expression (4) yields the value of the integral equal to $1.57 \approx \pi/2$ for $r = R$ ($l \gg R$), so that

$$R_{(f=R)}^{\text{th}} = \frac{\pi}{2}R_0^{\text{th}} = \frac{1}{2\kappa d}, \quad \text{where} \quad d = 2R.$$

Similarly, we may introduce the so-called effective thermal resistance for an array of lasers as

$$R_{\text{eff}}^{\text{th}} = \sum_{i \neq j} R_{ij}^{\text{th}} = \gamma_N R_0^{\text{th}}, \quad R_0^{\text{th}} = \frac{1}{2\pi\kappa r_s}, \qquad (5)$$

where r_s is the parameter (spacing) in the laser array, and the summation is performed over all operating lasers.

It is worth noting that the quantity γ_N depends heavily on the configuration of operating lasers and indicates to what extent the consideration of lasers in an array is more important than the thermal contribution of the nearest neighbor laser. Thus, the quantity γ_N makes it possible to take into account to what extent an individual operating laser is affected by other lasers in an array. As a result, the effective thermal resistance makes it possible to assess any variation in the temperature of a given laser when all the other lasers are operating; it is assumed that the same thermal power is released in each of the neighboring lasers.

Figure 1 shows the effective thermal resistance for cross interference as a function of dimension N ($N \times N$) of a laser array. It follows from Fig. 1 that the lasers located in the central region of the array are most affected; the effect exerted on the lasers located at the edge is less profound; and the lasers located at the corners of the arrays are less affected still. These results can be explained by the fact that the heat flux from neighboring lasers enhances the effective thermal resistance of other lasers in an array; therefore, the lasers located at the array center exhibit higher effective ther-

mal resistance because they are surrounded by a larger number of lasers.

The numerical results below refer to the 4×4 laser array. Effective thermal resistances in the case of interference effects on the laser with coordinates (3, 2) for various configurations of operating lasers in the 4×4 array were calculated. Various configurations are illustrated in Fig. 2 (the shaded circles correspond to operating lasers). The results of calculating the thermal resistances for interference effects in various configurations of operating lasers in a given laser are listed in the table.

3. ESTIMATION OF THE SUBSTRATE ELECTRICAL RESISTANCE

For the thermal models (the solutions to which were given above) to be valid, it is necessary that the bulk heat sources may be ignored in the substrate region. In other words, the resistance in the substrate region should be much lower than the active resistance of the laser.

In order to estimate the electrical resistance of the substrate, we use an analogy between the electrical and thermal parameters; thus, we find that the heat flux $Q(t)$ corresponds to the electric-current strength $I(t)$, the heat-flux density $\mathbf{q}$ corresponds to the electric-current density $\mathbf{j}$, the temperature T corresponds to the potential φ, the thermal-conductivity coefficient κ corresponds to the electrical conductivity σ, and the heat capacity C_p corresponds to the capacitance C.

For the sake of simplicity, we assume that an electric current is fed to the substrate region with a constant density. Using the analogy between the electrical and thermal quantities, we may immediately conclude that a solution for potentials in the region of $z \geq 0$ is given by the following expression similar to that reported previously [13] with q replaced with j_0 and κ replaced with $\sigma = 1/\rho_e$:

$$U_e(r, 0) = j_0 \rho_e R \int_0^\infty J_0(\lambda r) J_1(\lambda R) \frac{d\lambda}{\lambda}.$$

The mean potential is expressed as

$$\langle U_e \rangle = \frac{\int_0^R U_e(r) 2\pi r dr}{\pi R^2} = \frac{8 j_0 \rho_e R}{3\pi},$$

and the mean electrical resistance is given by

$$\langle R_e \rangle = \frac{\langle U_e \rangle}{I_{0e}} = \frac{8\rho_e}{3\pi^2 R} = \frac{16\rho_e}{3\pi^2 d}. \quad (6)$$

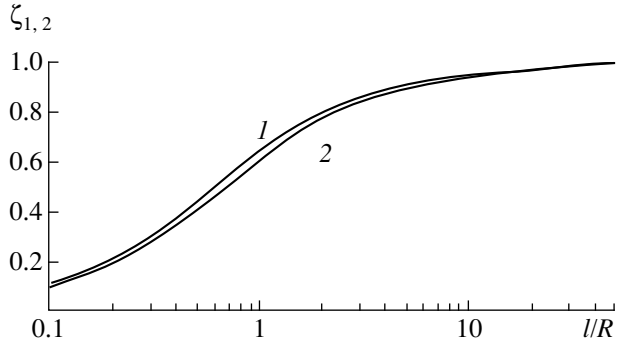

Fig. 3. Plots of the functions ζ_1 and ζ_2 characterizing the dependence of electrical resistance of the substrate on its thickness l.

If the substrate is a layer of finite thickness l, we have to use the solution to the thermal problem [13]; as a result, we obtain

$$\langle U_e \rangle = 2 j_0 \rho_e R \int_0^\infty \tanh\left(\frac{l}{R}x\right) J_1^2(x) \frac{dx}{x^2} = \frac{8 j_0 \rho_e R}{3\pi} \zeta_1\left(\frac{l}{R}\right),$$

where

$$\zeta_1\left(\frac{l}{R}\right) = \frac{3\pi}{4} \int_0^\infty \tanh\left(\frac{l}{R}x\right) J_1^2(x) \frac{dx}{x^2}.$$

Correspondingly,

$$\langle R_e \rangle = \frac{16\rho_e}{3\pi^2 d} \zeta_1\left(\frac{l}{R}\right). \quad (7)$$

A plot of the $\zeta_1(l/R)$ function is shown in Fig. 3. It can be seen that electrical resistance decreases with decreasing substrate thickness.

In order to estimate the substrate electrical resistance, we can also use another model solution for the potential being constant in a circular region in the $z = 0$

Thermal resistance of the laser with coordinates (3, 2) in the 4×4 array as a function of the configuration of operating lasers

The configuration type	The value of coefficient γ_N for thermal resistance
a	4
b	2.83
c	6.83
d	3.14
e	1.96
f	1.25
g	2.25
h	2.96

plane ($U_e(r) = U_{0e}$ = const, $r \le R$). The total current is then given by

$$I = \int_0^R j(r)2\pi r dr = \frac{4U_{0e}R}{\rho_e} = \frac{2U_{0e}d}{\rho_e},$$

and the resistance R_e is expressed as

$$R_e = \frac{U_{0e}}{I} = \frac{\rho_e}{2d}. \quad (8)$$

If the substrate is a layer of a finite thickness, we should use the following solution for the potential:

$$U_e(r, z) = \frac{2U_{0e}}{\pi}\int_0^\infty \frac{\sinh[\lambda(l-z)]}{\cosh(\lambda l)} J_0(\lambda r)\frac{\sin(\lambda R)}{\lambda} d\lambda.$$

The mean value of potential in the region with $z = 0$ and $r \le R$ is then given by

$$\langle U_e\rangle = \frac{\int_0^R U_e(r)2\pi r dr}{\pi R^2} = U_{0e}\zeta_2\left(\frac{l}{R}\right),$$

where

$$\zeta_2\left(\frac{l}{R}\right) = \frac{4}{\pi}\int_0^\infty \tanh\left(\frac{l}{R}x\right) J_1(x)\sin x\frac{dx}{x^2}.$$

As a result, the mean resistance is expressed as

$$\langle R_e\rangle = \frac{\rho_e}{2d}\zeta_2\left(\frac{l}{R}\right). \quad (9)$$

A plot of the function $\zeta_2(l/R)$ is also shown in Fig. 3.

We now estimate the electrical resistance under the condition of the current flowing in the substrate region. Using the numerical values of $\rho_e = 4.0 \times 10^{-5}\ \Omega$ m and $d \sim 10$ μm for GaAs and employing formula (6), we obtain $\langle R_e\rangle \sim 2.2\ \Omega$, which is much smaller than the laser electrical resistance ($R_L \sim 1$ kΩ) controlled mainly by the Bragg mirrors. A similar estimation based on formula (8) yields $R_e \sim 2\ \Omega$.

4. COMPARISON OF THE RESULTS OF CALCULATIONS WITH EXPERIMENTAL DATA

As was mentioned above, the manifestation of thermal effects in the VCSEL dynamics is related to temperature increase in the active region and to the extreme sensitivity of the threshold current to the active-region temperature. Thermal effects are especially important for lasers operating in continuous-wave mode. A temperature-related shift of the lasing wavelength to lower energies may be considered as another manifestation of thermal phenomena.

We now compare the estimates of thermal resistances with published experimental data [3–5]. Scientists of the University of California studied the interference effects on thermal properties for the 4×4 laser array with a characteristic spacing of 30 μm and a diameter of 7 μm [3]. The laser structure was grown on an *n*-GaAs wafer by molecular-beam epitaxy and consisted of Bragg mirrors (AlAs–GaAs layers) and an active region in the form of three $In_{0.18}Ga_{0.82}As$ quantum wells 80-Å thick. The lasers were fabricated by ion etching and were passivated with Si_3N_4 layers with a thickness of 2500 Å. The laser threshold current varied from 570 to 690 μA, and the mean value was $\langle I_{th}\rangle$ = 610 μA. The measured thermal-shift rate for the lasing wavelength of $\lambda_L = 975$ nm was $\Delta\lambda_L/\Delta T = 0.62$ Å/K.

It followed from experimental data reported previously [3] that thermal resistance of individual lasers was controlled to a large extent by the thermal-conductivity coefficient of the "lower" Bragg mirror in the direction perpendicular to the layer surfaces and amounted to 2720 K/W. Wipiejewski *et al.* [3] estimated the mean coefficient of the material's thermal conductivity at $\kappa = 0.28$ W cm^{-1} K^{-1}, which was much less than the bulk values of thermal conductivity in AlAs (0.91 W cm^{-1} K^{-1}) and in GaAs (0.45 W cm^{-1} K^{-1}). The above experimental value only slightly exceeds the corresponding value for GaAs–AlAs superlattices [14] and indicates that the thermal-conductivity coefficient in the multilayer Bragg mirrors cannot be determined from the properties of the bulk material; rather, it is bound to be controlled by the processes of scattering of phonons by interfaces.

In the 4×4 laser array, the effective thermal resistance was calculated [3] to be 4287, 4110, and 3970 K/W for the central, edge, and corner lasers, respectively. These values are about 50% larger than the measured value of the thermal resistance for an individual laser. Estimation of the thermal resistance of an individual laser using the formula $R^{th} = 1/2\kappa d$ yields $R^{th} \approx 2 \times 10^3$ K/W, which is about 30% smaller than the experimental value.

Let us estimate the thermal resistance for the mutual effect of two nearest neighbors on the basis of the data shown in Fig. 3 of paper [3]. For the 2×2 laser array, we obtain $R_1^{th} = 2720$ K/W and $R_{eff}^{th} = 3.2 \times 10^3$ K/W; thus, we have $R_0^{th} = 173$ K/W. Based on the data reported in [3] for the 4×4 laser array, we have $R_0^{th} = 157$ K/W for a central laser, 177 K/W for a corner laser, and 166 K/W for an edge laser. Thus, the mean value of R_0^{th} is 167 K/W. Using formula (5) in the estimation, we obtain $R_0^{th} = 1.2 \times 10^2$ K/W for $\kappa = 44$ W m^{-1} K^{-1} and $R_0^{th} = 1.5 \times 10^2$ K/W for $\kappa = 35.4$ W m^{-1} K^{-1}. The consistency between the experimental and theoretical results is reasonable if we set $\kappa = 35$ W m^{-1} K^{-1}; i.e., under actual conditions, thermal resistance is found to be lower than the calculated value.

It is also of interest to compare the estimates of thermal resistances with experimental data reported previously [4, 5]. An 8×8 VCSEL array fabricated by an "inverted crystal" technique was studied by Ohiso *et al.* [4]. Thermal resistances [4] were found to be 1210 and 660 K/W for the lasers with diameters of 16 and 26 μm, respectively. Let us estimate the thermal resistance for an individual laser. Since the $Al_{0.1}Ga_{0.9}As$ compound was used as the substrate [4], we should use the value of $\kappa = 44/(1 + 12.7x - 13.22x^2)$ W m^{-1} K^{-1}, where $x = 0.1$, for the thermal-conductivity coefficient. Thus, $\kappa = 20.6$ W m^{-1} K^{-1}, and we obtain 1.5×10^3 and 0.9×10^3 K/W for the thermal resistances of lasers with diameters of 16 and 26 μm, respectively. Thus, under actual conditions, the thermal resistance is found to be smaller than the expected one, which may be related to array mounting according to the inverted-crystal method.

Huffaker *et al.* [5] formed the 2×2 VCSEL array using selective oxidation. It was assumed that the thermal shift of the lasing wavelength was 0.56 Å/K. The measured thermal resistances were found to be 2550 and 2280 K/W for the lasers with characteristic dimensions of 2 and 3.5 μm. Estimations based on the formula $R^{th} = 1/2kd$ (2) yield 5.6×10^3 K/W ($d = 2$ μm) and 3.2×10^3 K/W ($d = 3.5$ μm).

The measured value of thermal resistance with allowance made for the mutual effect of nearest neighbors was [5] 140 K/W. If we estimate this resistance using formula (5) we obtain 3×10^2 K/W, so that the actual thermal resistance is about two times smaller than the expected one.

5. CONCLUSION

It follows from the above results that the thermal resistances of laser arrays are controlled to a large extent by structural features of both the lasers and the array as a whole. This refers primarily to the thermal resistances of individual lasers. Thermal resistances with an interference function are found to be less sensitive to structural features only if the lasers in an array are separated by characteristic distances which exceed the linear dimensions of the individual lasers. In addition, the local distribution of heat sources in the bulk of an individual laser is unimportant for the consideration and assessment of the thermal influence of lasers on each other. The suggested model solutions (undoubtedly, too inexact for an individual laser) may, nevertheless, yield a satisfactory agreement with the experimental data. In general, the considered approaches to solving the thermal problems yield results that are in qualitative agreement with the experimental data. Thus, the analytical solutions obtained may be used to estimate the thermal parameters.

ACKNOWLEDGMENTS

I am indebted to V.V. Bezotosnyĭ for his helpful participation in discussions of the issues considered in this paper.

REFERENCES

1. M. Kajita, T. Numai, K. Kurihara, *et al.*, Jpn. J. Appl. Phys., Part 1 **33**, 859 (1994).
2. Y. Ohiso, Y. Kohama, and T. Kurokawa, Electron. Lett. **30**, 1491 (1994).
3. T. Wipiejewski, D. B. Young, B. J. Thibeault, *et al.*, IEEE Photonics Technol. Lett. **8**, 980 (1996).
4. Y. Ohiso, K. Tateno, Y. Kohana, *et al.*, IEEE Photonics Technol. Lett. **8**, 1115 (1996).
5. D. L. Huffaker and D. G. Deppe, IEEE Photonics Technol. Lett. **8**, 858 (1996).
6. M. Simizu, D. I. Babic, J. J. Dudley, *et al.*, Microwave Opt. Technol. Lett. **6**, 455 (1993).
7. J. W. Scott, S. W. Corzine, D. B. Young, and L. A. Coldren, Appl. Phys. Lett. **62**, 1050 (1993).
8. J. W. Scott, R. S. Geels, S. W. Corzine, *et al.*, IEEE J. Quantum Electron. **29**, 1295 (1993).
9. J. Piprek and S. J. B. Yoo, Electron. Lett. **30**, 866 (1994).
10. J. Piprek, H. Wenzel, and G. Sztefka, IEEE Photonics Technol. Lett. **6**, 139 (1994).
11. G. H. Hadley, K. L. Lear, M. E. Warren, *et al.*, IEEE J. Quantum Electron. **32**, 607 (1996).
12. M. Osinski and W. Nakwaski, IEEE J. Sel. Top. Quantum Electron. **1**, 681 (1995).
13. H. S. Carslaw and J. C. Jaeger, *Conduction of Heat in Solids* (Clarendon Press, Oxford, 1959; Nauka, Moscow, 1964).
14. T. Yao, Appl. Phys. Lett. **51**, 1798 (1987).

Translated by A. Spitsyn